

Laser Additive Manufacturing of Bulk Shape Memory Alloy Structures: Numerical Modeling and Experimental Investigation

A THESIS

*Submitted in partial fulfillment of the
requirements for the award of the degree
of*
DOCTOR OF PHILOSOPHY

by
SHIVA. S



**DISCIPLINE OF MECHANICAL ENGINEERING
INDIAN INSTITUTE OF TECHNOLOGY
INDORE**

MAY 2017



INDIAN INSTITUTE OF TECHNOLOGY INDORE

CANDIDATE'S DECLARATION

I hereby certify that the work which is being presented in the thesis entitled **LASER ADDITIVE MANUFACTURING OF BULK SHAPE MEMORY ALLOY STRUCTURES: NUMERICAL MODELING AND EXPERIMENTAL INVESTIGATION** in the partial fulfillment of the requirements for the award of the degree of **DOCTOR OF PHILOSOPHY** and submitted in the **DISCIPLINE OF MECHANICAL ENGINEERING, Indian Institute of Technology Indore**, is an authentic record of my own work carried out during the time period from July 2013 to May 2017 under the supervision of **Dr. I. A. Palani**, Associate Professor, Discipline of Mechanical Engineering, Indian Institute of Technology Indore and **Dr. C. P. Paul**, Head, LAM lab, Laser Development Industrial Applications Division, Raja Ramanna Center for Advanced Technology Indore.

The content presented in this thesis has not been submitted by me for the award of any other degree of this or any other institute.

**Signature of the student with date
(SHIVA S)**

This is to certify that the above statement made by the candidate is correct to the best of our knowledge.

Signature of Thesis Supervisor #1 with date

Dr. I. A. Palani

Signature of Thesis Supervisor #2 with date

Dr. C. P. Paul

SHIVA S has successfully given his Ph.D. Oral Examination held on

Signature (s) of Thesis Supervisor (s)

Date:

Convener, DPGC

Date:

Signature of PSPC Member #1

Date:

Signature of PSPC Member #2 Signature of External Examiner

Date:

Date:

ACKNOWLEDGEMENTS

I would like to express my sincere gratitude to my research guides **Dr. I.A.Palani**, and **Dr. C.P. Paul** for their constant encouragement, guidance and support from the preliminary stage to the concluding level of this research work.

I express my sincere thanks to **Prof. P. Mathur**, Director, IIT Indore, **Dr. D. Deshmukh**, Head, Discipline of Mechanical Engineering and **Dr. Anil Kumar** former Head of the Discipline.

I wish to thank the doctoral committee members **Dr. M. Anbarasu**, **Dr. D. Deshmukh**, for their valuable suggestions right from the beginning of the course work. My Sincere thanks are also due to **Dr. B.K. Lad** and **Dr.I.A. Palani** for providing me an opportunity to work at Institute for manufacturing (IFM), University of Cambridge under Newton Bhabha project.

I also express my sincere thanks to **Sophisticated Instrumentation Centre (SIC)**, **IIT Indore** for providing me the necessary characterization facility throughout my research period.

I also express my deep gratitude to **Dr. S. Kanmani Subbu** of Mechanical Engineering, NIT Warangal for his constant encouragement and timely help.

I personally thank **Dr. C. P. Paul** also as Head of Laboratory, Laser additive manufacturing laboratory for giving me an opportunity to carry out PhD research work at, RRCAT, Indore and for providing me the necessary infrastructure. I would like to thank **Shri Pankaj Bhargava** and **Dr. Atul Kumar** for their constant support and suggestions throughout my PhD work. I also thank the technical officers of LAM Lab, RRCAT Indore **Mr. S.K. Mishra**, **Mr.Upendra Kumar** and **Mr. C.H. Prem Singh** for extending the laboratory facilities for this research work.

I would like to thank my colleagues in Mechatronics and Instrumentation Laboratory **Mr. Akash Kumar**, **Mr. Tameshwar Nath Tiwari**, and from Opto Mechatronics Laboratory **Mr. Ashish Shukla**, **Mr. Rajagopalan**, **Mr. Mani Prabhu**, **Ms. Nandini Patra**, and **Dr. Reena Disawal** for their suggestions and timely solutions for the problems encountered during the research work.

I would like to acknowledge my colleagues **Mr. Suryakanth Mishra** and **Mr. Sagar Nigam** for their valuable suggestion in numerical modeling.

I extend my cordial thanks to all staff members of SIC, Central workshop, Central Library, Academic Section, Accounts Section of IIT Indore for their kind cooperation.

On a special note I would like to acknowledge the affection, support and moral encouragement provided by my father **Dr. A.S.S. Sekar** and my mother **Mrs. S. Daisy Rani**. I am forever indebted to the mas they have spent their entire life, with lots of sacrifices and emotional hardships in giving me a better life. Thanks are also due to my sister **Mrs. S. Janani**, brother-in-law **Mr. T.Ranjith** and **Master R. Shiv Mithran** for their motivation and support in the course of my research.

Last but not least, I am eternally grateful to my wife **Mrs.L.Kalaimathy** and my kid **Master S. Sarvesh** for travelling with me throughout my research journey. Though I spent most of my time in my research being away from them, they constantly backed me during my tough days and supported me in achieving my goal.

Shiva S

Dedicated to My Family

SYNOPSIS

Shape memory alloys (SMA) are of great research interest for applications in various areas, such as active layers in thin film actuator, Micro Electro-Mechanical Systems (MEMS) devices, damping systems and vibration control systems. The current market for SMA is dominated by NiTi with maximum deployment in the form of thin films. The use of SMA in the form of bulk structures is very limited due to various defects, including high hysteresis and reducing in life cycle. The alloying with a third element Cu to the binary NiTi alloy overcomes these defects with the same system efficiency. However, building tailored structures of bulk binary and ternary SMA with same shape memory effect is a challenging task. Complex structures of SMA are very difficult to built using conventional tooling technologies. In order to address many of the existing issues, laser additive manufacturing (LAM) may deployed to build tailored complex structures of various compositions. Porosity and brittleness are two major concern in LAM built SMA structures and these can be addressed by post processing techniques, like- laser shock peening and laser annealing. To the best our knowledge, there are not published reports on laser based post processing on LAM built SMA structures. Hence new and interesting findings are expected

In the present study, LAM is deployed to build bulk structures of NiTi with three different compositions (Ni rich NiTi45, Ti rich NiTi55 and equiatomic composition of NiTi50) and TiNiCu ternary alloy with six different compositions (Ti percentage is maintained at 50% and the Cu is varied from 5-30% in the step 5%.) The built samples are subjected to two different types of post processing, i.e., laser shock peening and laser annealing is demonstrated using a solid state laser. A numerical simulation is carried out to estimate the temperature and residual stress developed on the samples during LAM and the results are compared with the experimental results. Also, the post processing effect of laser shock peening and laser annealing are simulated and validated with the experimental results.

The built samples are also investigated for surface morphological properties, mechanical properties, crystalline properties and phase transformation properties in the as manufactured state and after post processing technique. The samples are finally selected to study the shape memory properties to figure out the best combination of LAM sample.

LIST OF PUBLICATIONS

Peer Reviewed International Journals

1. **S. Shiva**, I.A. Palani, S.K. Mishra, C.P. Paul, L.M. Kukreja, “ *Investigations on the influence of composition in the development of NiTi shape memory alloy using laser based additive manufacturing*”, **Opt Laser Technol**, **69**, 44-51(2015). (I.F: 1.87)
2. **S. Shiva**, I.A. Palani, S.K. Mishra, C.P. Paul, B.Singh “*Investigations on phasetransformation and mechanicalcharacteristics of laser additive manufactured TiNiCu shape memoryalloy*” **J. Mater. Process. Technol.****238**, 142-151(2016). (I.F: 2.35)
3. **S. Shiva**, I.A. Palani, C.P. Paul, B. Singh, “*Laser Annealing of Laser AdditiveManufactured NiTi Structures: An Experimental – Numerical Investigation*”**P IMECH ENG B-J ENG**, DOI: 10.1177/0954405416661582. (2016) (I.F : 1)
4. **S. Shiva**, I.A. Palani, S.K. Mishra, C.P. Paul, L.M. Kukreja,, “*Influence of Cu Additionto Improve Shape Memory Properties in NiTi Alloys Developed by Laser Rapid Manufacturing*” **J Laser Micro NanoEng**, **11**, 153-157 (2016) (I.F : 0.75)
5. **S. Shiva**, I. A .Palani, C. P. Paul, B.Singh “*Experimental and numerical investigations of laser annealing on TiNiCu shape memory alloys structures developed by laser additive manufacturing*” on the phase transformation and mechanical characteristics of laser additive manufactured TiNiCu shape memory alloy structures” **Materials Letters (Under Communication)**. (I.F : 2.34)
6. **S. Shiva**, I. A .Palani, C. P. Paul, B.Singh , “*A prevision and experimental analyses of laser shock peening effects on the various properties of laser additive manufactured NiTi structures*” **Journal of manufacturing Science and Engineering (Under Communication)**.
7. **S. Shiva**, I. A. Palani, C. P. Paul, B.Singh “*Analyses of temperature distribution experimentally and numerically and their effects on various properties of TiNiCu shape memory alloy structures developed by laser additive manufacturing*” **International Journal of Advanced Manufacturing(Under Communication)**. (I.F : 1.56)

Book Chapter

S.Shiva, I.A Palani, C.P Paul, B.Singh “*Comparative Investigation on the effects of Laser Annealing and Laser Shock peening on the as manufactured NiTi Shape Memory Alloy Structures Developed by Laser Additive Manufacturing*” (to be communicated)

Refereed International Conferences

1. Shiva.S, FarhanBabu, I.A. Palani, “*Studies on Pulsed laser deposition of SMA thin films and laser assisted actuation for the development of micro-pump’s*” Conference on **Intelligent Robotics, Automation and Manufacturing(IRAM)**, 2013 held during 16th-18th December 2013,at IIT Indore.
2. Tameshwer Nath, S.Shiva, Akash K., Farhan Babu, I.A.Palani, "*Investigations on The Effect of Laser Actuation And Interaction On NiTi SMA Sheet For The Development Of Micro-Grippers*" **International Union of Material Research Societies- The IUMRS International Conference in Asia-2014** , held during August 24th -30th, 2014 at Fukoka Japan.
3. Shiva S, Aditya Singh, Suyash Bhangale, I A Palani, S K Mishra, C P Paul, L M Kukreja, A M Awasthi, “*Influence of Laser Annealing on Laser Additive Manufactured Shape Memory Structures of NiTi Alloys*” **Lasers and Plasma Application in Materials Science (LAPAMS)** 2015 held during January 15th-17th 2015 at Kolkata
4. Shiva S, I A Palani, S K Mishra, C P Paul, L M Kukreja, “*Influence of Cu addition on Laser Additive Manufactured Shape Memory Structures of NiTi Alloys*” **Laser Advanced Materials Processing (LAMP)** held during May 26th-29th 2015, at Fukoka, Japan
5. Shiva S, I A Palani, C P Paul “*Influence of conventional annealing and laser annealing on the surface morphology of NiTi structures developed by laser additive manufacturing*” **DAE BRNS National Laser Symposium (NLS-24)**. held during December2-5, 2015 at RRCAT, Indore.
6. S.Shiva, I.A Palani, C.P Paul, B.Singh “*Comparative Investigation on the effects of Laser Annealing and Laser Shock peening on the as manufactured NiTi Shape Memory Alloy Structures Developed by Laser Additive Manufacturing*” **All India Manufacturing Technology Design and Research (AIMTDR) Conference** held during December 16-18, 2016 at COEP, Pune.
7. S.Shiva, I.A Palani, C.P Paul, B.Singh, "*Comparing the effects of pulsed laser annealing and continuous wave laser annealing on the as manufactured NiTi shape memory alloy structures developed by laser additive manufacturing*" **Solid Freeform Fabrication Symposium 2016 (SFFSymposium2016)**to be held during August 8th- 10th, 2016 at The University of Texas in Austin, Austin, Texas, USA.

TABLE OF CONTENTS

LIST OF FIGURES

LIST OF TABLES

NOMENCLATURE

ACRONYMS

Chapter 1: Introduction

1.1	Shape Memory Alloys (SMA)	1
1.2	Shape Memory Phenomenon	3
1.2.1	Shape Memory Effect (SME)	3
1.3	NiTi	5
1.4	NiTi Characteristic Temperatures and transformation kinetics	7
1.5	NiTi Phase Diagram:	8
1.5.1	Super-elasticity	9
1.6	Thermo-elastic Transformations:	10
1.7	Shape Memory Alloy based Actuation:	11
1.8	NiTi SMA (Thin Films):	12
1.9	NiTi SMA (Bulk):	12
1.10	Applications of bulk NiTi Shape Memory Alloys	13
1.11	Applications of bulk TiNiCu Shape Memory Alloys	17
1.12	Need for Laser Additive Manufacturing in Developing SMA structures	18
1.13	Motivation	18
1.14	Objective and Scope	19
1.15	Outline of the Thesis	20

Chapter 2 : Overview of NiTi Bulk Structures Development and Laser Additive Manufacturing

2.1	Introduction	21
2.2	Influence of composition of SMA properties of NiTi	21
2.3	Development of tailor made NiTi and TiNiCu SMA Structures:	22
2.3.1	Ni rich NiTi	22
2.3.2	Ti rich NiTi	23
2.3.3	Cu tailored TiNiCu	25
2.4	NiTi Bulk Structure Development	27
2.5	Limitation of existing process LAM can provide the solution	30
2.6	LAM	30
2.7	Requirements for Laser Additive manufacturing System	34
2.7.1	High power laser system	35
2.7.2	Material Feeding System	36
2.7.2.1	Wire feeders	36
2.7.2.2	Pre-placed powder bed	36
2.7.2.3	Dynamic powder blowing	37
2.7.3	CNC workstation	40
2.8	Laser based Additive Manufacturing techniques used to develop bulk NiTi SMA	41
2.8.1	Selective laser sintering (SLS)	41
2.8.2	Selective laser melting (SLM)	42
2.8.3	Laser Engineered Net Shaping (LENS)	50
2.8.4	Electron beam melting (EBM)	51
2.9	Need for laser assisted surface post processing of additive manufactured samples	52

2.10	Methodology of development of bulk NiTi using LAM	53
2.11	Summary	54

Chapter 3: Development of Bulk Shape Memory Alloy Structures using Laser Additive Manufacturing: Numerical and Experimental Investigation

3.1	Introduction	55
3.2	Numerical Modeling and Experimental Procedure	55
3.2.1	Conduction mode heat transfer analysis	55
3.2.2	Solution Strategy	59
3.2.3	Thermo Mechanical Analysis	60
3.2.4	Solution Strategy for Thermal Analysis	63
3.3	Validation of numerical modeling	65
3.4	Experimental Procedure	72
3.5	Effects of processing parameters	75
3.6	Evaluation of Surface Morphology	79
3.6.1	Scanning Electron Microscopy Examination	79
3.6.2	Microstructure Analysis	82
3.6.3	Atomic Force Microscopy Examination	84
3.7	Mechanical Properties Evaluation	87
3.7.1	Micro-hardness Measurement	87
3.7.2	Compression Test	88
3.8	Crystalline Properties Property Evaluation Using X-Ray Diffraction Analysis	91
3.9	Summary	93

Chapter 4 : Laser Shock Peening of Bulk Shape Memory Alloy Structures using Laser Additive Manufacturing: Numerical and Experimental Investigation

4.1	Introduction	95
4.2	Numerical Modeling and validation of Laser Shock Peening	97
4.3	Laser shock peening of NiTi and TiNiCu bulk samples	99
4.4	Validation of numerical modeling	101
4.4.1	Simulation and finalization of parameters	101
4.5	Evaluation of surface morphology	105
4.5.1	Scanning electron microscopy examination	105
4.5.2	Microstructure analysis	107
4.5.3	Atomic force microscopy examination	108
4.6	Mechanical properties evaluation	112
4.6.1	Micro-hardness measurement	112
4.6.2	Compression test	114
4.7	Crystalline properties evaluation using X-Ray diffraction analysis	117
4.8	Summary	120

Chapter 5 : Laser Annealing of Bulk Shape Memory Alloy Structures using Laser Additive Manufacturing: Numerical and Experimental Investigation

5.1	Introduction	121
5.2	Numerical Simulation	122

5.3	Laser annealing of NiTi and TiNiCu bulk structures	123
5.4	Simulation and Validation	125
5.5	Surface morphology	130
5.5.1	Scanning electron microscopy examination	130
5.5.2	Microstructure analysis	131
5.5.3	Atomic force microscopy examination	133
5.6	Mechanical Properties Evaluation	135
5.6.1	Micro-hardness Measurement	135
5.6.2	Compression test	137
5.7	Crystalline Properties Property Evaluation Using X-Ray Diffraction Analysis	137
5.8	Influence of Laser annealing	141

Chapter 6 : Phase transformation and shape memory characteristics of the developed samples

6.1	Introduction to Dynamic Mechanical Analysis (DMA)	
6.2	Phase transformation property in as manufactured state	143
6.3	Phase transformation property after laser shock peening	147
6.4	Phase transformation property after laser annealing	149
6.5	Experimental Analysis Using DMA	151
6.6	Results and Discussion	152
6.7	Summary	153

Chapter 7: Conclusion and Future Scope of Work

7.1	Conclusions	155
7.1.1	Development of bulk NiTi and TiNiCu structures with numerical and experimental study	155
7.1.2	Laser shock peening of bulk NiTi and TiNiCu structures with numerical and experimental study	156
7.1.3	Laser annealing of bulk NiTi and TiNiCu structures with numerical and experimental study	156
7.1.4	Shape memory characteristics analysis on the developed samples	157
7.2	SCOPE OF FUTURE WORK	157

LIST OF FIGURES

Figure no.	Description	Page No.
Fig. 1.1	Basic shape memory effect (SME), schematically illustrated crystallographically (left), and macroscopically through the bending of a simple rod (right).	4
Fig. 1.2	The martensite fraction (ξ) vs. temperature (T) considering the chemical and non-chemical contributions.	7
Fig. 1.3	NiTi Phase diagram (Otsuka, 1994)	8
Fig. 1.4	Temperatures above the austenite finish temperature, A_f , but below the martensite deformation temperature, M_d , the super-elastic effect occurs in NiTi.	9
Fig. 1.5	The schematic diagram of the experimental set up for concrete re enforcement(Li et al. (2008))	14
Fig. 1.6	SMA clamping device: (a) solid model, (b) manufactured steel clamping element (spindle) and SMA rings. (Malukhin et al.2012)	15
Fig. 1.7	The schematic diagram of the developed SMA ring over the tool holder(Lee et al. 2016)	16
Fig 1.8	SMA impinged Ball Screw Drive(Drossel et al 2016)	16
Fig 1.9	Stewart Platform developed using TiNiCu springs (A. AbuZaider et al. 2015)	17
Fig. 2.1	Successful methodologies implemented in manufacturing NiTi SMA	28
Fig. 2.2	Successful methodologies implemented in manufacturing TiNiCu SMA	29
Fig.2.3	Block diagram of an entire LAM requirements	34
Fig. 2.4	Schematic diagram of Powder Bed Technology	37
Fig.2.5	Different types of feeding systems used in LAM	39
Fig.2.6	3D NiTi structures developed by SLS (Shishkovsky et al 2008)	42
Fig.2.7	Bulk NiTi structures developed by SLM (Shishkovsky et al 2012)	43
Fig.2.8	Bulk NiTi compression test samples developed by SLM (H. Meier and C. Haberland, 2012)	43
Fig. 2.9	Bulk NiTi actuators developed by SLM [Christoph Haberland et al. 2014]	44
Fig.2.10	Bulk NiTi ingots developed by SLM [Habijan et al.2013]	45
Fig.2.11	Bulk NiTi scaffolds developed by SLM from designed CAD model [Hoffmann et al 2014]	46
Fig.2.12	Bulk NiTi structures developed by SLM[Walker et	47

	al.2016]	
Fig. 2.13	Porous NiTi structures developed by SLM [Taheri Andani et al 2016]	48
Fig 2.14	Porous NiTi structures developed by SLM for various mechanical properties studies [Dadbakshet al. (2014)]	49
Fig 2.15	NiTi Cantilevers structures developed by SLM for actuation studies [Clare et al.2008]	49
Fig 2.16	Bulk NiTi structures developed by LENS [Gibson et al. 2010]	50
Fig 2.17	Implants developed using EBM method (a) as manufactured (b) after post processing (Elahinia et al.2012)	52
Fig 2.18	The work chart of the entire work process	53
Fig 2.19	The schematic diagram of the laser assisted surface post processing techniques	54
Fig. 3.1	Three dimensional solution geometry for the applied boundary conditions	59
Fig. 3.2	Overall procedure followed in conduction mode heat transfer analysis	60
Fig. 3.3	Overall procedure followed in thermo-mechanical analyses	64
Fig. 3.4	Simulation results for maximum temperatures generated for the samples in all three layers of vertical depositions	66
Fig. 3.5	Simulation results for maximum residual stress generated for the samples in all three layers of vertical depositions	67
Fig. 3.6	Comparison graph of simulated temperature and residual stress values with experimental data	69
Fig. 3.7	Simulation results for maximum temperatures generated for the samples in all three layers of horizontal depositions	70
Fig. 3.8	Simulation results for maximum residual stress generated for the samples in all three layers of horizontal depositions	71
Fig. 3.9	Comparison graph of simulated temperature and residual stress values with experimental data	72
Fig.3.10	Schematic diagram of 2 kW Fibre laser based Additive Manufacturing System fabricating NiTi and TiNiCu	73

	samples	
Fig.3.11	Powder Morphology of (a) Ti, (b) Cu and (c) Ni powders	76
Fig.3.12	Effect of Laser Energy per unit area (E_L) on Aspect Ratio (W/H)	77
Fig 3.13	(a) Deposition rate and (b) catchment efficiency as function of no. of layers	78
Fig.3.14	Laser additive manufactured NiTi ring and TiNiCu brick structures	79
Fig.3.15	SEM images of as manufactured (a) NiTi45 (b) NiTi50 (c) NiTi55 (d) TiNiCu5 (e) TiNiCu10 (f) TiNiCu15 (g) TiNiCu20 (h) TiNiCu25 (i) TiNiCu30 samples developed by LAM	81
Fig.3.16	Microstructure images of as manufactured (a) NiTi45 (b) NiTi50 (c) NiTi55 (d) TiNiCu5 (e) TiNiCu10 (f) TiNiCu15 (g) TiNiCu20 (h) TiNiCu25 (i) TiNiCu30 samples developed by LAM	83
Fig. 3.17	AFM images of as manufactured (a) NiTi45 (b) NiTi50 (c) NiTi55 (d) TiNiCu5 (e) TiNiCu10(f) TiNiCu15 (g) TiNiCu20 (h) TiNiCu25 (i) TiNiCu30 samples developed by LAM	86
Fig. 3.18	Micro-hardness values of (a) NiTi and (b) TiNiCu samples developed by LAM	87
Fig. 3.19	Stress Vs Strain graph of as manufactured (a) NiTi45(b) NiTi50 (c) NiTi55 samples developed by LAM	89
Fig. 3.20	Stress Vs Strain graph of as manufactured TiNiCu samples developed by LAM	90
Fig. 3.21	XRD graph of as manufactured NiTi45, NiTi50, NiTi55, TiNiCu5, TiNiCu10, TiNiCu15, TiNiCu20, TiNiCu25 and TiNiCu30 samples developed by LAM	93
Fig. 4.1	Types of laser shock peening being implemented successfully	96
Fig. 4.2	Schematic of laser shock peening functioning	99
Fig. 4.3	NiTi sample developed by LAM used for LSP	99
Fig. 4.4	Schematic diagram of the experimental setup used for LSP	100
Fig. 4.5	The residual stress distribution simulated for (a) NiTi (b) TiNiCu	102
Fig 4.6	Effects of various power of LSP on the surface of the sample	104
Fig. 4.7	Amount of residual stress distributed in NiTi and TiNiCu sample for 3 shot LSP	105
Fig. 4.8	SEM images of (a) NiTi55 (b) NiTi50 (c) NiTi45 (d) TiNiCu5, (e) TiNiCu10, (f) TiNiCu15 (g) TiNiCu20, (h)	107

	TiNiCu25 (i) TiNiCu30	
Fig. 4.9	Microstructure images of (a) NiTi55 (b) NiTi50 (c) NiTi45 (d) TiNiCu5, (e) TiNiCu10, (f) TiNiCu15 (g) TiNiCu20, (h) TiNiCu25 (i) TiNiCu30	108
Fig. 4.10	AFM images of (a) NiTi55 (b) NiTi50 (c) NiTi45 (d) TiNiCu5 (e) TiNiCu10 (f) TiNiCu15 (g) TiNiCu20 (h) TiNiCu25 (i) TiNiCu30 after LSP	110
Fig. 4.11	Micro-hardness values of NiTi55, NiTi50, NiTi45, TiNiCu5, TiNiCu10, TiNiCu15, TiNiCu20, TiNiCu25 and TiNiCu30 samples after LSP	113
Fig. 4.12	Compression test results of NiTi55, NiTi50 and NiTi45 samples after LSP	114
Fig.4.13	Compression test results of TiNiCu5, TiNiCu10, TiNiCu15, TiNiCu20, TiNiCu25 and TiNiCu30 samples developed by LAM	116
Fig. 4.14	XRD graph of NiTi and TiNiCu samples before and after LSP	119
Fig. 5.1	Schematic arrangement for laser annealing	123
Fig. 5.2	Typical laser additive manufactured sample used for laser annealing.	124
Fig.5.3	Experimental set up for laser annealing	125
Fig. 5.4	Simulated temperature profile of (a) 900 mJ/cm ² (c) 1000 mJ/cm ² (e) 1100 mJ/cm ² (g) 1200 mJ/cm ² and SEM images of (b) 900 mJ/cm ² , (d) 1000 mJ/cm ² , (f) 1100 mJ/cm ² , (h) 1200 mJ/cm ²	127
Fig. 5.5	Experimental set up for measuring the temperature generated by various laser energy densities	128
Fig. 5.6	Comparison between simulated and real time experimental temperature values for various laser energy densities	129

Fig. 5.7	SEM images of the NiTi and TiNiCu samples after laser annealing	130
Fig. 5.8	Microstructure images of the NiTi and TiNiCu samples after laser annealing	132
Fig. 5.9	AFM images of the NiTi and TiNiCu samples after laser annealing	134
Fig. 5.10	Micro-hardness values of NiTi and TiNiCu samples after laser annealing	136
Fig. 5.11	Stress Strain images of NiTi and TiNiCu samples after laser annealing	138
Fig. 5.12	XRD graphs of NiTi and TiNiCu samples after laser annealing	141
Fig. 6.1	DSC graph of as manufactured NiTi55, NiTi50, NiTi45 samples developed by LAM	145
Fig 6.2	DSC graph of as manufactured NiTi55, NiTi50, NiTi45 samples developed by LAM	147
Fig 6.3	DSC graph of NiTi50, NiTi45, TiNiCu5, TiNiCu10, TiNiCu15 and TiNiCu20 samples after LSP	148
Fig 6.4	DSC graphs of NiTi and TiNiCu samples after laser annealing	150
Fig 6.5	Geometry of the three-point mode DMA experiment	151
Fig 6.6	The DMA results of (a) NiTi50 (b) TiNiCu5 and (c) TiNiCu10 samples	154

LIST OF TABLES

Table No.	Description	Page No.
Table 1.1	List of SMA as reported by (Pons, 2005 and Liang, 1990)	1
Table 2.1	Redistribution of Laser Power during laser cladding	35
Table 2.2	Various Laser Rapid Manufacturing Systems	41
Table 3.1	Properties of the samples	64
Table 3.2	Parameters used for experiments	74
Table 3.3	EDS results of TiNiCu samples developed by LAM	80
Table 3.4	AFM measurements for the samples in as manufactured state	85
Table 4.1	Parameters used for LSP process	101
Table 4.2	EDS results of the formed NiTi and TiNiCu samples after LSP	106
Table 4.3	Grain size, surface roughness and kurtosis value of the samples from AFM	111
Table 4.4	Compression test results of NiTi55, NiTi50, NiTi45, TiNiCu5, TiNiCu10, TiNiCu15, TiNiCu20, TiNiCu25 and TiNiCu30 before and after LSP	117
Table 5.1	Processing Parameters used in the laser annealing experiments	124
Table 5.2	EDS results of NiTi and TiNiCu samples after laser annealing	131
Table 5.3	EDS results of the samples after laser annealing	135
Table 5.4	Mechanical properties after laser annealing	139

NOMENCLATURE

Symbol	Unit	Description
ξ		Martensite fraction
T	$^{\circ}\text{C}/\text{K}$	Temperature
E		Specific laser energy
P	W	Laser power
d	mm	Laser spot diameter
V	mm/sec	Scan velocity
m_p	g/min	Mass flow rate of the powder
ρ	Kg m^{-3}	Density of Powder Fed
t	mm	Distance between the hopper and disc
D	mm	Mean diameter of the slot
N	rpm	Rotation of the disc speed
k_m	$\text{W m}^{-1} \text{K}^{-1}$	Thermal Conductivity
k_o		Thermal conductivity of the material
T_m	$^{\circ}\text{C}/\text{K}$	Melting point of the material
\dot{Q}	W m^{-3}	Rate of heat generation per unit volume
C_p	$\text{J kg}^{-1} \text{K}^{-1}$	specific heat capacity of the material
σ	-	Stefan-Boltzmann constant
ε	-	emissivity
kn,	$\text{W m}^{-1} \text{K}^{-1}$	Thermal conductivity normal to the surface
q	W/m^2	Imposed heat flux onto the surface
h	$\text{W}/\text{m}^2\text{K}$	Convection heat transfer coefficient
T_o	$^{\circ}\text{C}/\text{K}$	Ambient temperature
η	-	Efficiency of heat source
U	-	stress tensor
F	N/m^3	Body force vector per unit volume
P	N/m	Pressure
μ	Poise	Viscosity of the molten metal
I	-	Identity matrix
g	kg/cm^2	Acceleration to gravity
β		Coefficient of thermal expansion
T	$^{\circ}\text{C}/\text{K}$	Reference temperature
F'	N	The electromagnetic body force
$\varepsilon_x, \varepsilon_y, \varepsilon_z$	N/m	Normal strains in x, y and z directions respectively
$\gamma_{xy}, \gamma_{yz}, \gamma_{zx}$	N/m	Shear strains in xy, yz and zx planes respectively
De	-	Elasticity matrix
G	N/m^2	Shear modulus
E_T	N/m^2	Slope between stress and plastic strain of specified material
σ_{av}	N/m	Average one dimensional stress
$\sigma_1, \sigma_2, \sigma_3$	N/mm^2	Principal stresses
Ω	m^2	Work piece surface area
Γ	m^2	Laser spot area
h_c	$\text{W}\cdot\text{m}^{-2} \text{K}^{-1}$	Heat transfer coefficient

L(t)	mm	Thickness of the plasma generated
P(t)	Pa	The pressure generated by the laser pulse impinged
I(t)	J	The laser energy
Z	$\text{g cm}^{-2} \text{s}^{-1}$	Combined shock impedance
D _L	mm	Least geometric dimension
r _l	mm	Radius of laser
I ₀	mJ/cm ²	Intensity of Laser
δ	GPa	Represents the laser on and off state in pulsed laser
E*	Gpa	Complex modulus
E'	Gpa	Elastic modulus
E''	Gpa	Imaginary loss modulus

ACRONYMS

S.No.	Acronyms	Expansion
1	SMA	Shape Memory Alloys
2	SME	Shape Memory Effect
3	TWSME	Two Way Shape Memory Effect
4	PE	Pseudo Elasticity
5	LSP	Laser Shock Peening
6	LA	Laser Annealing
7	M_s	Martensite Start
8	M_f	Martensite Finish
9	A_s	Austenite Start
10	A_f	Austenite Finish
11	MEMS	Micro Electro Mechanical Systems
12	M_d	Martensite Deformation
13	GP	Guinier–Preston
14	MT	Martensitic Transformation
15	AM	Additive manufacturing
16	NC	Numerically Controlled
17	CAD	Computer aided Design
18	CAE	Computer aided Engineering
19	FEA	Finite Element Analysis
20	NURBS	Non Uniform Rational Basis-Splines
21	GUIs	Graphical User Interfaces
22	LRM	Laser Rapid Manufacturing
23	SLS	Selective Laser Sintering
24	DMLS	Direct Metal Sintering
25	SLM	Selective Laser Melting
26	EBM	Electron Beam Melting
27	LENS	Laser Engineered Net Shaping
28	SEM	Scanning Electron Microscopy
29	EDS	Electron Dispersive Spectroscopy
30	AFM	Atomic Force Microscopy
31	VHN	Vicker’s Hardness Number
33	XRD	X-Ray Diffraction
34	DSC	Differential Scanning Calorimetry
35	DMA	Dynamic Mechanical Analyzer

Chapter 1

Introduction

1.1 Shape Memory Alloys (SMA)

Shape Memory Alloy secures a special place of being the first choice for manufacturing many micro electromechanical systems (MEMS) devices, like actuators in micro-pumps and valves. Owing to its maverick character of super elasticity and thermal shape memory effect [Laeng et al, 2007, Wu et al, 2008, Li et al, 2009 and Wu et al, 2007]. The effect caused by SMA deforms it into predefined shape in a controlled way. This is because SMA has two phases of different temperatures. The first is the martensite- low temperature phase, and second is the austenite-the high temperature phase. These phase transformations can be obtained only if the alloy components are blended perfectly under proper lattice arrangements leading to Shape Memory Effect (SME). SME is observed for many alloys including NiTi, Cu-Al-Ni, Cu-Zn-Al, Cu-Sn, Nb-Ti, Cu-Al-Be and Ti-Nb. Among the available options, NiTi has an edge over all the remaining due to its stability of retaining SME and prolong fatigue life as reported by (Pons, 2005 and Liang, 1990).

Table 1.1 : List of SMA as reported by (Pons, 2005 and Liang, 1990)

S.No.	Alloys	Composition (wt %)	Transformation Temperature Limits (°C)	Hysteresis Limit (°C) (Approx)
1	AgCd	Cd [(44-49)-x] Ag	-190 to 50	15
2	AuCd	Cd[(46.5-50)-x] Au	30 to 100	15
3	CuAlNi	CuAl (14-14.5)Ni (3-4.5)	-140 to 100	35
4	CuSn	Sn (Approx 1-14)	-120 to 30	
5	CuZn	Zn(38.5-41.5)	-180 to 10	10
6	CuZnX (X= Si,Sn,Al)	X= >2	-180 to 200	10
7	InTi	Ti(18-23)	60 to 100	4

8	NiAl	Al(36-38)	-180 to 100	10
9	NiTi (X) X= Pd,Pt	X= (0-50)	-200 to 700	30
10	TiNiCu	Ti- 50 Compulsory Cu= (1-30)	-150 to 100	100
11	NiTiNb	Nb (0-15)	-200 to 50	50
12	NiTiAu	Au (0-50)	20 to 610	125
13	TiPdX X= Cr,Fe	X=(0-15)	0 to 600	
14	MnCu	Cu= (5-35)	-250 to 180	25
15	FeMnSi	Mn=(0-32) Si= (0-6)	-200 to 150	100
16	FePt	Pt = (0-25)	-130 (Approx)	4
17	FePd	Pd = (0-30)	50 (Approx)	
18	FeNiX (X= C,Co,Cr)	X >2		

Some of the alloys which exhibit the SME are as listed in Table 1.1. Considerable efforts are still being put to discover new SMA materials. Out of these SMAs, only two alloy systems, Nickel-Titanium (NiTi) and copper based alloys (CuZnAl) and their combinations with minute quantities of dopants have promising technological advantages. The other alloys are ill-suited for industrial applications because, either the constituent elements are too expensive or they cannot be used as SMA unless they are in the form of single crystals as reported by (Pons, 2005 and Liang, 1990).

SMAs are capable of producing large recoverable strains. The major limitation of these materials are poor response behaviour, large thermal energy loss and limited temperature ranges. SMAs are the most promising materials for actuator/sensor applications and many researchers are trying to improve their capabilities to enhance their usefulness in technological applications. Any actuation mechanism

in smart structures is governed by the controlled production of work output or energy release. Comparisons of some of the important aspects of smart materials being used as actuators are presented in Table 1.1. The specific energy density involved in shape memory mechanism is of the order of 25 J/m^3 , which is an order of magnitude higher than any of the alternative mechanisms. The principle behind the SMA actuators is in the conversion of thermal energy into kinetic energy and work output. These actuators offer large range of motion at low operating voltages. An array of benefits, such as high recoverable forces, large recoverable output strains up to (8%), different actuation modes (linear, bending, torsion) and high work output per unit volume or mass, can be achieved by these actuators. Hence, SMA actuation mechanisms are one of the most preferred actuation mechanisms.

1.2 Shape Memory Phenomenon

SMA's are capable of changing their shape from one form to the other when initiated either by stress or temperature. If the transformation occurs due to change in temperature, it is known as 'temperature induced phase transformation' and the transformation caused by either load or stress is known as 'stress induced phase transformation'. On application of stress, these materials can deform plastically. When these materials are subjected to appropriate thermal or stress conditions, they will return back to their memorized shape. They can sustain large amount of strain without any permanent deformation. The above strains can be recovered upon either by changing the temperature or the load. A reversible, solid state phase transformation, known as 'martensitic transformation', is the main driving force behind SMA's.

1.2.1 Shape Memory Effect (SME)

As SMA materials are heated from low temperature phase to high temperature phase, shape memory effect (SME) occurs. It explains the effect of restoring the original shape of a plastically deformed material by heating it above transformation temperature. It involves the transition from one form of crystal structure to another. This phenomenon of changing from one crystalline phase to the other crystalline phase is known as "thermo-elastic martensitic transformation". At temperatures below the transformation temperature, SMA's are in martensite phase. In this condition, the SMA material is soft

and can be deformed quite easily by detwinning. The microstructure is characterized by self-accommodating twins. Heating above the transformation temperature recovers the original shape and converts the material to its high strength austenite phase [Tadaki et al, 1988]. The transformation from the austenite to martensite and the reverse transformation from the martensite to austenite do not take place at the same temperature.

One-way Shape Memory Effect:

At low temperature, a SMA material can be plastically deformed. This deformation involves the movement of highly mobile boundaries (twin boundaries, martensite / martensite interfaces). Upon heating, SMA material reaches Austenite phase with the initial orientation and so the specimen reverts to its original shape. While cooling, no additional shape change takes place; this effect is called “one-way shape memory effect”.

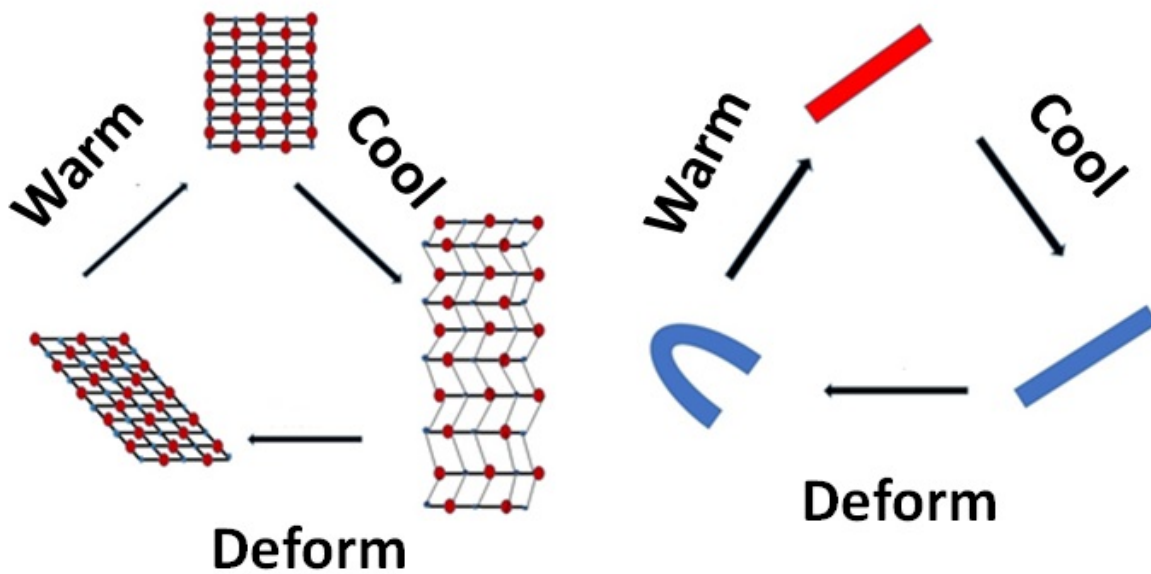


Fig. 1.1 :Basic shape memory effect (SME), schematically illustrated crystallographically (left), and macroscopically through the bending of a simple rod (right).

The one-way effect can be repeatedly induced by deforming SMA in the martensitic state. Initially, in a SMA material displaying one-way SME, there is no movement on heating. The shape change starts at A_s temperature and get completed in a small temperature range (e.g. 10 to 30 K). The A_s temperature of NiTi SMAs can be significantly tuned by suitable selection of the chemical composition of the alloy and dopants.

Two-way Shape Memory Effect:

SMAs with a two-way shape memory effect (TWSME), "remember" both a high temperature shape (austenite) and a low temperature shape (martensite). Though, TWSMAs can switch from their low temperature shape to their high temperature shape, their recoverable strain is usually about half of their corresponding one-way SMAs. To produce a two-way effect, it is necessary to induce a special mechanical/thermal treatment in a SMA. One method to produce a two-way effect is based on a severe deformation in the martensitic state. In addition to this, there are still some other methods to produce a TWSME. They are (1) SME training, (2) stress-induced martensite training, (3) combined training, (4) forces of inactive surface layers and etc[Cole et al, 2005].

During heating, the specimen will move towards its original shape and the high temperature shape gets formed. On cooling again, the pre-existing martensite plates will accommodate the stress field of the induced dislocation structure and preferred martensite variants forms, which give rise to the formation of low temperature shape. Thus, by temperature cycling one gets the two-way effect. This method of the production of the two-way effect can be used for training in the NiTi alloys, since it displays high ductility.

1.3 NiTi

Although SME was observed in early 1950s, the engineering importance of SMAs has not been well recognized till the equiatomic NiTi alloys (Nitinol), in 1963 as reported earlier [Otsuka, 1998, Moberly and Melton, 1990 and Kohl, 2004]. "Nitinol" derives its name from its chemical components and its finders: Ni (Nickel) + Ti (Titanium) + NOL (Naval Ordinance Lab). During last three decades, binary NiTi alloys are being intensively investigated to cater functional applications. Recently, NiTi based SMAs are the most important commercial SMAs because of their unique shape-memory performance, ease of processing, pseudo-elasticity and have the required mechanical

properties (Otsuka, 1994, Shaw and J. A. Shaw and S. Kyriakides, 1995, P. Tautzenberger, RAU, 1995). In addition, the alloy exhibits excellent corrosion resistance and is also bio-compatible in nature. The NiTi, inter-metallic compound is extraordinary because it has moderate solubility range for excess of nickel or titanium, as well as with other metallic elements. This solubility allows, alloying possibility with many other elements, to modify both the mechanical and phase transformation properties. These materials have exhibited some exciting application potentials in micro-electro-mechanical systems (MEMS), medical implants, intelligent materials and structural systems, either in the monolithic form or in combination with other materials. More detailed information about NiTi SMA basic properties is available in the literature presented by (Otsuka, 1994).

The SMA transformation can be explained based on a thermodynamic analysis, since it is driven either by the stress or the temperature. The heat interaction between the SMA sample and the surroundings, at specific temperature, decides the phase transition. The phase transformation temperature can be evaluated by the differential scanning calorimetry (DSC). A thermodynamic analysis provides an insight into SMA's unique characteristics such as hysteresis, super-elasticity, one-way effect, rubber elasticity, two-way effect and etc. Gases can be generally liquefied by a suitable application of pressure or stress. Similarly, a phase transition from the parent phase to martensite can be induced by the application of a stress. The thermodynamic analysis explains thermal and mechanical effects on the SME. Thermodynamics is a good tool to perform calculations on the thermal implications of the stress induced phase transition. It also explains the reversibility of the phase transition in certain SMAs and highlights energy contributions that control the hysteresis phenomenon (Peng et al, 2008).

Gibbs theory of thermodynamic stability is used to describe the phase transition, when an alloy system is considered to be under equilibrium condition. Based on the above consideration, it is evident that Gibbs theory is not suitable for systems that are not in equilibrium in which fluctuations are amplified to generate new structures. A martensitic transformation can be considered to be a succession of several equilibrium states [Mousavi et al, 2009 and Yinong Liu]. The martensitic transformation is a solid state transformation. The thermodynamic analysis based on internal variables (latent heat of the phase transformation, enthalpy and entropy) can be applied for a single crystal of SMA. The classical Clausius-Clayperon equation can be derived as it relates stress and

temperature. The analysis can be conducted for a single crystal of SMA, because it facilitates the investigation of the SMA specimen as a thermodynamic system with only one component.

1.4 NiTi Characteristic Temperatures and transformation kinetics:

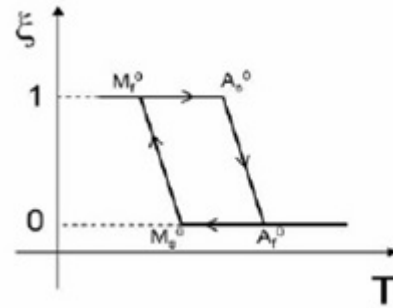


Fig. 1.2 The martensite fraction (ξ) vs. temperature (T) considering the chemical and non-chemical contributions.

The SMA transformation has the following characteristic temperatures. The complete transformation cycle in martensitic transformation is characterized by the following temperatures:

1. Austenite Start (A_s)
2. Austenite Finish (A_f)
3. Martensite Start (M_s)
4. Martensite Finish (M_f)

As shown in Fig1.2, the heating process of NiTi, evolves into austenite when temperature reaches (A_s) and completes the transformation process when it reaches A_f . While the cooling process, martensite at (M_s) and finishes at M_f . The difference between the transition temperatures is called hysteresis. These characteristic temperatures are in the order of $M_f < M_s < A_s < A_f$. The mentioned above relation is temperature induced stress. Martensitic transformations can also be stress induced it occurs at constant temperature, moderately above the austenite finish temperature leading to super elasticity to form stress induced transformation. Temperature induced transformations involve the deformation at low temperature phase (martensite phase).

1.5 NiTi Phase Diagram:

NiTi phase diagram is much like a typical binary phase diagram as shown in Fig. 1.3. It is useful to understand, the phase and precipitate formation in NiTi. NiTi in equiatomic phase can exist in solid state up to a temperature of 1310° C. The maximum solubility of Ni in NiTi is about 5 atomic % at 1118° C. The horizontal line at 1118° C represent a eutectic reaction where $L = \text{NiTi} + \text{Ni}_3\text{Ti}$. It is evident from phase diagram that for slightly Ti-rich (than equiatomic) composition, the phases will be $\text{Ti}_2\text{Ni} + \text{NiTi}$ (above 600° C) and for Ni-rich composition, $\text{NiTi} + \text{Ni}_3\text{Ti}$. These precipitates play an important role in strengthening the Ni-rich NiTi alloys. Kim et al reported the existence of additional meta-stable phases other than Ni_3Ti_2 and Ni_4Ti_3 . These phases are not equilibrium phases, but influence the transformation temperature and shape memory behaviors mentioned earlier by (Miyazaki, 2009). The deviation in NiTi alloy composition from stoichiometry increase the extent of precipitates formation, as seen for Ti-rich NiTi alloy. These precipitates have a significant effect on the hot workability of NiTi, particularly on the Titanium rich side; they are brittle and often result in cracking. These precipitates ultimately change the transition temperatures of the alloy. Therefore, it is important to have a sufficient understanding of the different precipitate formation that is created during a particular heat treatment.

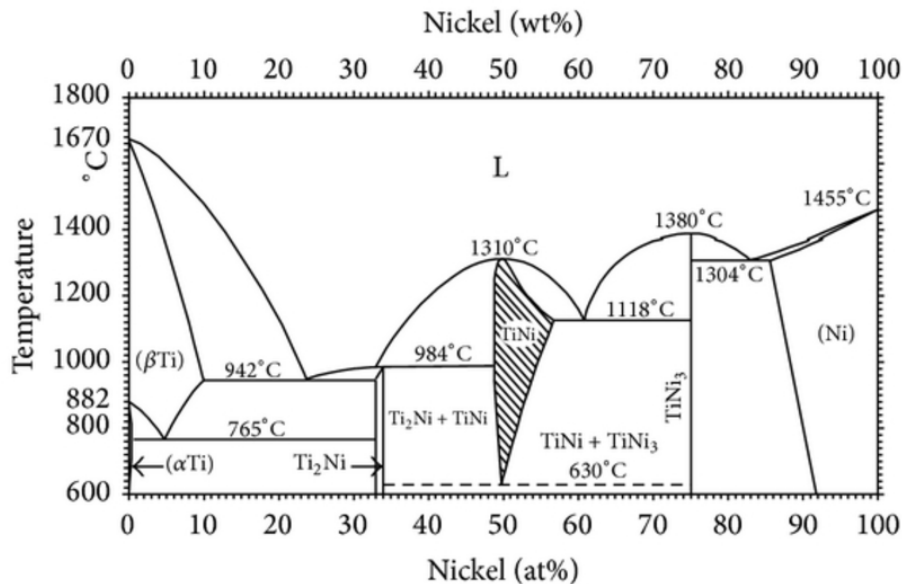


Fig 1.3 NiTi Phase diagram (Otsuka, 1994)

1.5.1 Super-elasticity:

Super-elasticity is simply a manifestation of the shape memory effect, when the material is deformed slightly above its transformation temperature. In this case, shape recovery occurs spontaneously as soon as the deforming stress is removed. At a temperature moderately greater than A_f , SMA is capable of showing superelastic properties. It means that these large strains produced by mechanical loadings are simply recovered upon unloading as reported by [Hou and Grumman, 1995].

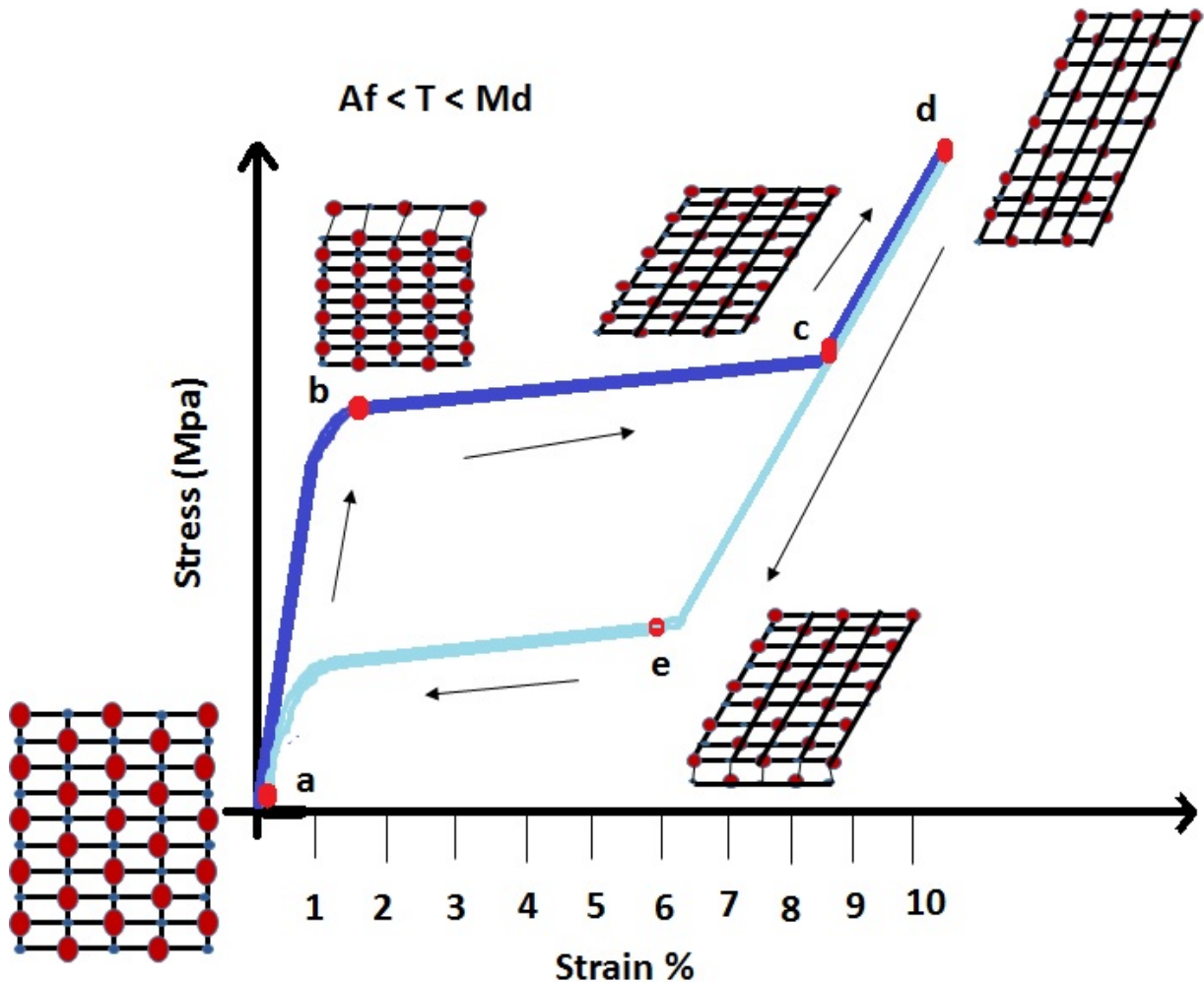


Fig. 1.4 Temperatures above the austenite finish temperature, A_f , but below the martensite deformation temperature, M_d , the super-elastic effect occurs in NiTi.

Starting at (a), the material is fully austenite. The austenite is elastically loaded to point (b) at which time transformation to martensite occurs (the martensite forms in twins, and instantaneously de-twins due to the high applied stresses). Further loading along a stress “plateau” to point (c), fully transforms

the material to martensite. Continued loading to (d) requires increased stress and elastically deforms the martensite. Unloading back through point (c) recovers the elastic strains in the martensite, and continued unloading to (e) forces the onset of the reverse transformation to austenite, with full reverse transformation upon complete unloading to (a). These strains can be as large as 8% in case of SMAs, while for conventional materials like steel, the yield strains are in the order of 0.2 to 0.3 %. It should be noted that super elastic applications are isothermal in nature with temperature being fixed with $T > A_f$. As described in SME, the residual strains caused due to Martensitic transformations can be recovered by heating the sample above A_f . In super elastic effect, the strain at temperature above A_f can be eliminated by removing the stress. Hence, in both shape memory effect and super elasticity, the shape recovery is driven by reverse martensitic transformation.

1.6 Thermo-elastic Transformations:

Temperature induced phase transformation is divided in to two categories: thermo elastic and non-thermo-elastic. In thermo-elastic transformations, the crystal has nucleation and growth steps to reach equilibrium condition and the crystal grows or shrinks with change in temperature, where as in non-thermo-elastic transformations, the crystal has only nucleation and it reaches to final size instantly and after that, it does not grow or shrink with change in temperature. In thermo-elastic transformations, the rate of growth and shrinkage is proportional to the applied heating or cooling rates. These transformations are reversible in nature and are important for shape memory effect to occur as reported by (Melton, Mercier, 1979, Grabe and Bruhns, 2009 and Craciunescu et al, 2003).

It is also observed that both heating and cooling thermal cycle does not follow the same path. The difference in the heating and cooling thermal cycles results in a hysteresis formation. Hence, a hysteresis always exists during the thermal cycling. The extent of hysteresis is measured by 'hysteresis temperature', which is defined as $(A_s - M_s)$. Hysteresis temperature is temperature specific. In general, it is high for non-thermoelastic transformations and relatively low for thermo-elastic transformations, which indicates that only thermo-elastic transformations can be responsible for highly reversible phenomenon of shape memory. In Martensite transformation of SMAs, the shear deformation involves very small volume change. The transformation proceeds without inducing any plastic deformation of surrounding parent phase, which may be the cause of thermo-elastic transformation in SMAs. Non-thermo-elastic transformations do not induce shape memory effect.

As discussed earlier the application of SMA are widely used as actuators MEMS. The primary requirement for being an actuator is the ability of the material to function with high frequency and fast response. Low hysteresis and narrow transformation temperatures help in becoming an efficient actuator. The NiTi in its binary state has a hysteresis value of 30°C. The inclusion of Cu with NiTi not only reduces hysteresis but also exhibits an equal amount of efficient actuation like NiTi [Zhu and Li, 2009]. Compared with TiNi binary alloy, TiNiCu alloys show less composition sensitivity in transformation temperatures, lower martensitic yield stress, and superior fatigue property, etc., which make them more suitable for microactuator application as stated by [Brenner, 1956].

1.7 Shape Memory Alloy based Actuation:

SMA's can be used in the actuator applications, depending on whether their SME is either one-way or two ways. Although, two-way SMA can perform action in both directions, the associated transformation strain is generally half of that of one-way SMA. An alternate approach is to put two one-way SMA actuators, one against the other, to generate two-way mechanical performance as well. It can be achieved by heating one SMA actuator to get forward motion and another SMA actuator in the reverse direction. The advantage of one-way actuator is higher motion and higher force than that of two-way actuator. At the same time the two-way actuator is simpler, compact and contains less number of elements. The SMA actuators function in three modes as mentioned below (shown in Fig. 1.2).

In the recent years, the use of SMA's has been proposed as an alternative approach to replace the existing conventional systems. The advantages of SMA structures over existing systems are:

1. **Mass and volume savings:** SMA actuators have the potential capability to achieve high output/weight ratio, as compared to traditional actuators.
2. **Minimum system complexity:** SMA actuators are always associated with spring structures. Hence, the need for dampers and overall system complexity of structures can be minimized.
3. **Retraction capability:** usually it is available only in motor-type structures.
4. **Noiseless operation:** SMA actuators remove the vibration disturbances to other payloads that are normally associated with motor-driven deployment.

5. **Sensing capability:** Both actuating and sensing functions can be combined by measuring changes in electrical resistance associated with the phase transformation.
6. **Higher reliability:** The movement is triggered by a phase transformation and the speed of movement is related to the temperature of the SMA element, which itself is determined by the thermal input and heat transfer. Therefore, it is possible to design systems with large torque margins.
7. **Large recoverable strains:** SMA actuators permit extremely long strokes and the application of large forces when deformation is restrained.
8. **High electrical resistivity:** It means that the shape transformation can be activated by passing an electrical current through a SMA element, thus avoiding the need for separate heaters.
9. **Design Flexibility:** SMA actuators can be linear, rotary, or combination of both, and can form an integral part of the component. Thus, it appears that SMA-actuator can combine practically all the advantages of controlled and free-movement.

1.8 NiTi SMA (Thin Films):

Generally, Bulk SMAs exhibit large strokes and high actuation forces and at the same time they suffer from poor response. However, thin film SMAs provide a larger energy density, higher frequency response and longer life time at microscopic level. NiTi thin films are the most appropriate material for micro-actuation mechanisms because of their extensive energy density, displacement, work output per unit volume and improved frequency response. At this level, smaller mass and larger surface to volume ratio enable significant increase in the heat transfer and low power requirements. Hence, large stresses and strains can be realized. These advantages make thin film NiTi SMA a very promising actuator material for micro-device applications such as micro-valves, micro-grippers, micro-pumps, micro-cage, micro-robotic, micro-sensors, micro-switch, micro-positioners and such other applications.

1.9 NiTi SMA (Bulk):

Recent progress in research, in the fabrication of SMAs, has opened new ways to develop novel actuators and systems, which are capable of performing smart functions by responding to their thermal, mechanical and magnetic environment in controllable way. Most commercial applications of

shape memory alloys can be grouped into three categories. They are (1) shape memory actuation devices, (2) super-elastic devices and (3) martensitic devices. Shape memory actuation devices utilize the shape memory effect and can be further sub-divided into three groups: viz. (a) free recovery, (b) constraint recovery and (c) partially constraint recovery. Super elastic device relies on the super-elasticity and provide a constant force over large strains. They exhibit larger torque and larger kink resistance. martensitic devices employ the deformation of SMA material in martensite phase and result in very high damping characteristics and remarkable fatigue strength. They can be easily deformed plastically, while strains can be recovered on heating.

Nickel Titanium (NiTi) SMAs have been developed for a broad range of applications, e.g., in the fields of aerospace, industrial and biomedical applications. This has been realized because of low manufacturing cost, good corrosion resistance, biocompatibility and tailorable material properties. The applications in aero space are fabrication of elevator and ailerons, transportation of large sophisticated equipments and quick connect-disconnect couplings. The industrial applications include connectors and fasteners, couplings, tweezers, monolithic micro-grippers, robotic actuators, micromanipulators and gas flow control valves and etc. In bio-medical field these are being used for orthodontic arch wires, blood clot filter, orthopedic, stents, bone anchor and implants in biomedical respectively.

1.10 Applications of bulk NiTi Shape Memory Alloys

Researchers have used bulk SMA structures are also of wide scope not only in MEMS but also in vibration absorption and other dampers applications. Similar type researches are analyzed below.

Li et al. (2008) have developed a new repair method for a simple reinforced concrete (RC) beam strengthened with carbon fiber reinforced polymer (CFRP) plates in combination with SMA wires is proposed in this study. Four specimens that are temporarily strengthened with SMA wires followed by permanent strengthening with CFRP plates are tested. The test results indicate that the SMA wires can reduce residual deformations of the specimens effectively when heated. An increase of the number of SMA wires leads to a greater reduction in residual deformation. The main steel reinforcing bars play a significant role in preventing the reduction of residual deformation and the closing of cracks. The small residual deformation obtained by heating SMA wires results in a relatively large stiffness of the specimen strengthened later by CFRP plate and a relatively small damage index at relatively low load levels. Therefore, RC structures temporarily strengthened by SMA wires followed

by permanent strengthening with CFRP plates presents an effective method to strengthen RC structures. The reduction of residual deformation has little impact on the ultimate capacity of the strengthened specimens. A linear relationship between mid-span deflection and change rate of electric resistance of SMA wires is also observed in this study, providing a potential tool to develop smart RC structures with integrated self-diagnosis and self-repairing functions.

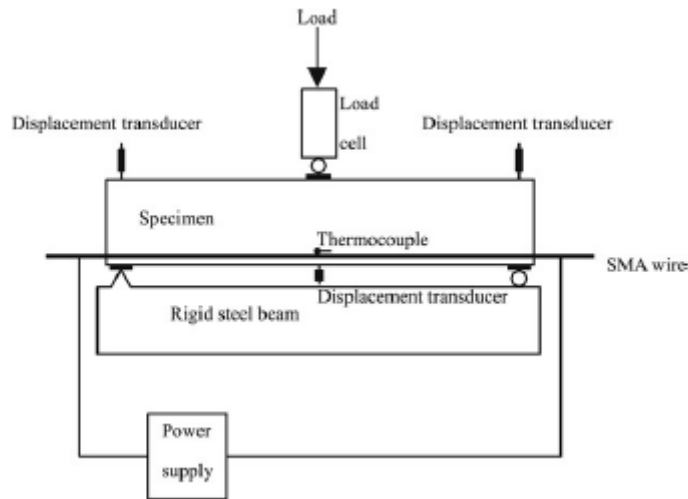


Fig 1.5The schematic diagram of the experimental set up for concrete re enforcement(Li et al. (2008))

Malukhin et al. (2012) have designed, manufactured, and tested and analysis of several SMA based clamping devices were undertaken. Two alternative designs of the SMA clamping devices have been considered from the point of view of their manufacturability and capability to produce and exert clamping forces on micro-tools at a desired level. Device topologies with an SMA ring and with monolithic SMA jaws Have been analyzed; FEM models of both types of the SMA clamping devices have been developed to estimate the clamping forces produced by the devices; Experimental prototypes of the SMA clamping devices with SMA rings have been designed, manufactured and tested; Experimental investigations have shown that the SME driven clamping force exerted by the SMA clamping device with the SMA ring on a micro-tool exceeds the required clamping force level expected in micro-cutting operations, and, therefore, can be used in micro-machining applications.

The formed SMA rings and clamping devices are as shown in Fig.1.6

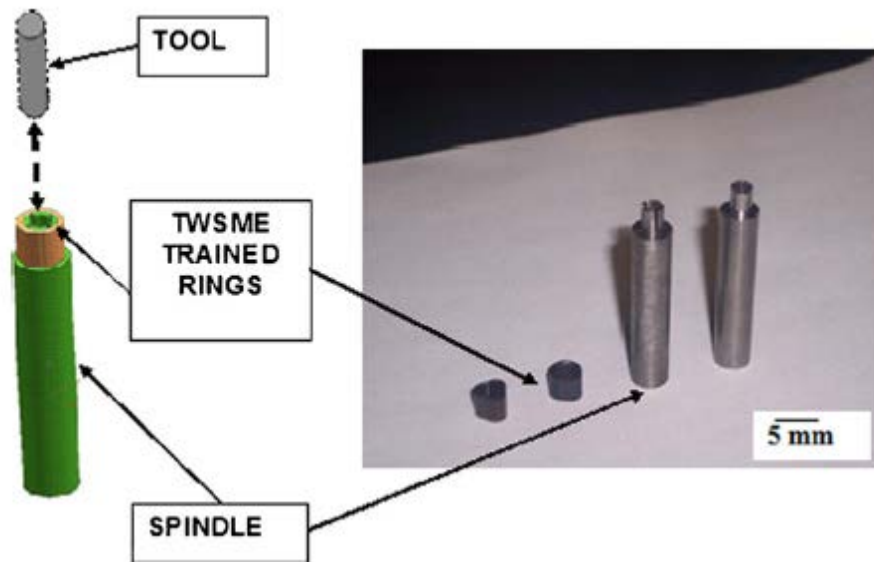


Fig 1.6 SMA clamping device: (a) solid model, (b) manufactured steel clamping element (spindle) and SMA rings. (Malukhin et al.2012)

Most recent research by (Lee et al. 2016) is about analyzing the deflection of a SMA tool holder by modeling the structure as a simple beam. The pressure applied to the holder was calculated based on an interference fit between the tool holder and the SMA ring, and the moment of inertia was obtained from the input parameters. The deflection curve and the constraints of the beam were determined using these parameters, and the inner diameter of the SMA tool holder was analyzed. Clamping and release occurred due to transitions between the austenitic and martensitic phases. The main function of the SMA tool holder is to clamp the tool in the austenitic phase and release it in the martensitic phase. Two kinds of tool holder were investigated. The first was a straight-type holder, and the second was a stepped holder.

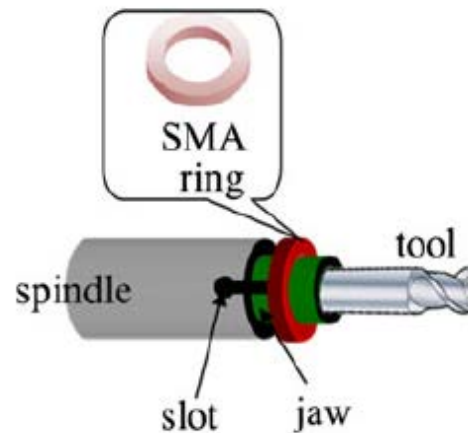


Fig 1.7 The schematic diagram of the developed SMA ring over the tool holder(Lee et al. 2016)

In the most recent research by (Drossel et al 2016), a component for Ball Screw Driver (BSD) is made of SMA to compensate wear. For actuation purposes actuators made from SMA were used. The described component consists of a mount, the actuators and a heating element. For assembling in a BSD, the whole system is placed between both nuts and replaces a conventionally used spacer without increased cross section. The heating element is activated from the outside by electrical current for a short period of time. Thermal energy causes the SMA to expand which causes a force and deformation between both nuts and increases the preload, which results in an increased accuracy. Such system enables machine tool users to increase the lifetime of the BSDs by a certain period without any major expenses. Since the current component design only allows to be used a single-time. Additional actuators with a higher transformation temperature could be used to implement more than one preload resetting operation.

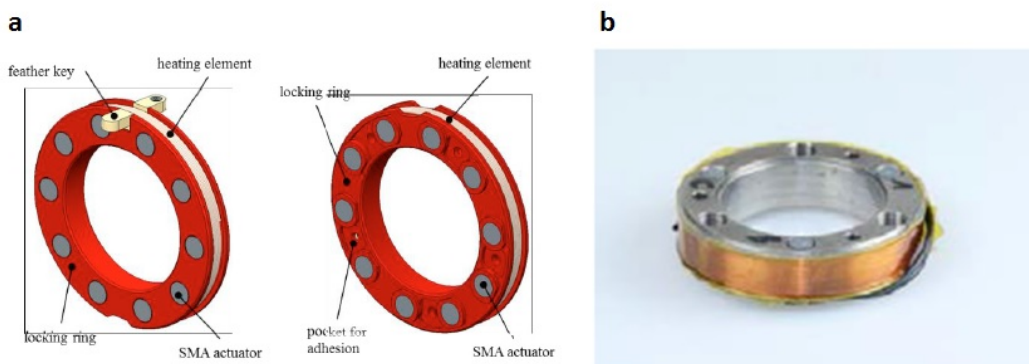


Fig 1.8 SMA impinged Ball Screw Drive(Drossel et al 2016)

1.11 Applications of bulk TiNiCu Shape Memory Alloys

A. AbuZaider et al. (2015) have recently developed a Stewart platform made of TiNiCu springs. A Stewart platform is a parallel manipulator robot that is able to perform three linear movements, lateral, longitudinal, and vertical, and three rotations, pitch, yaw, and roll. This paper reports a $30\text{mm} \times 30\text{mm} \times 34\text{mm}$ mini scale Stewart platform using TiNiCu shape-memory-alloy (SMA) actuators. The proposed Stewart platform possesses various advantages, such as large actuation force and high robustness with a simple mechanical structure. This Stewart platform uses four SMA actuators and four bias springs and performs a linear z -axis movement and tilting motions. The SMA actuators are activated by passing a current through the SMA wires using a heating circuit that generates a pulse width modulation (PWM) signal. This signal is varied to control the level of the displacement and tilting angle of the platform. The tilting direction depends on the SMA actuator that is activated, while all four SMA actuators are activated to achieve the linear z -axis movement. Each SMA actuator exerts a maximum force of 0.6N at PWM duty cycle of 100%. The fabricated miniature Stewart platform yields a full actuation of 12mm in the z -axis at 55°C , with a maximum tilting angle of 30°C in 4 s.

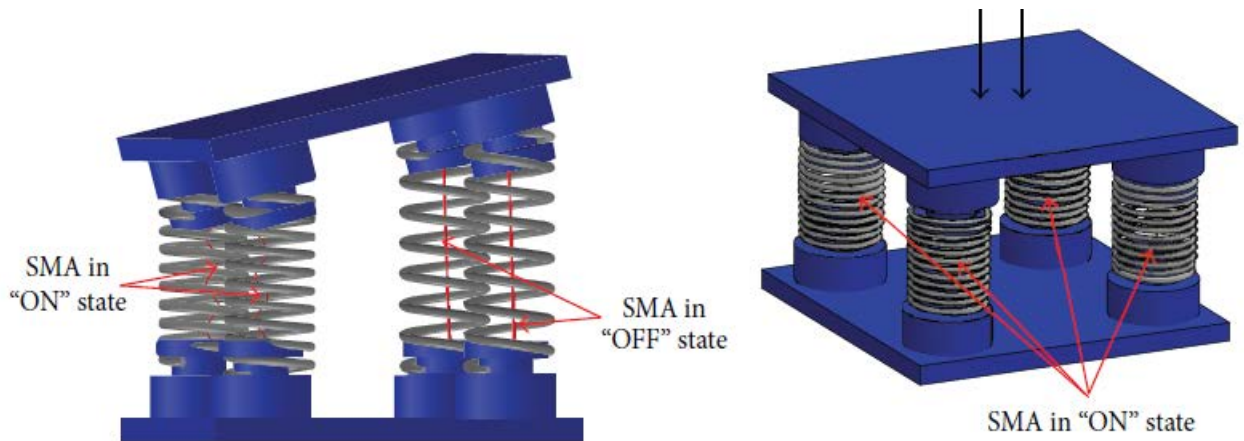


Fig 1.9 Stewart Platform developed using TiNiCu springs (A. AbuZaider et al. 2015)

1.12 Need for Laser Additive Manufacturing in Developing SMA structures

Laser Additive Manufacturing has revolutionized the manufacturing with a new concept “feature based design and manufacturing”. It is propelled with high power lasers computer aided design and manufacturing powder metallurgy and allied electronics and translated a 3D model into a three dimensional functional metallic part. This technology has provided five exclusive freedom to human race for the fabrication of components:

1. Material design freedom
2. Shape design freedom
3. Logistics freedom
4. Quality freedom
5. Post-processing freedom

1.13 Motivation

SMA's have drawn great attentions in performing as actuators for various applications in MEMS specifically, such as thin films in functioning of micro pumps and micro valves. The widely used SMA currently is NiTi for its maverick nature of getting adapted to all sought of environments. Most of the biomedical implants have also been developed using NiTi for its compatible nature. However NiTi has its own limitations in the aspect of hysteresis which sequentially reduces the life of the NiTi product. In order to overcome this issue, the birth of a ternary alloy TiNiCu came into picture. TiNiCu possess the same quality of NiTi and also the hysteresis temperature of the alloy is very less than the binary NiTi alloy. The tailor made NiTi structures have been successfully developed by researchers in the past and TiNiCu tailored structures have been developed as well.

The reports also make it very clear that much concentration has been given to thin films development, and bulk structures development have not been probed much. All the developed structures were developed in simple shapes and development of complex structures are yet to be achieved. It is vividly known from the results that the problems of porosity is yet to be addressed for samples developed by other additive manufacturing techniques. Hence post processing of the samples were the idea carried out in the current work to overcome the existing issues. In that accord laser shock peening and laser annealing were chosen. Since the samples developed are porous and brittle in nature, much care has to be given to maintain the physical and chemical nature of the metal. Hence

post processing techniques were implemented after much analyses was done on the nature of the experiment.

The laser shock peening process in general is done with high power and a sacrificing layer in order to impinge more residual stress to prevent any crack propagation on the samples. In the current work a low power laser shock peening without any sacrificing layer was carried out to prevent the sample from getting deteriorated. Also after the shock peening process, laser annealing with pulsed green laser was carried out in order to trim out the extra residual stress impinged in the samples. Hence the phase transformation in the sample can occur at ease. This sequentially results in good shape memory effect of the samples with good reliable life in them.

Limited work has been reported in development of bulk SMA structures of complex geometry using laser additive manufacturing. The motivation increased to probe into development of bulk SMA structures with post processing techniques in order to improve the quality of the samples developed. The final structures developed can be used as vibration dampers in real time applications as discussed above.

1.14 Objective and Scope

The objective and scope of the research work are as follows:

1. To develop bulk NiTi based SMA samples using laser additive manufacturing with addition of a third element Cu in different compositions to overcome issues, like - brittleness and porosity forming various composition of TiNiCu and to carryout numerical and experimental analyses to study the temperature and residual stress distribution.
2. To investigate the influence of compositions in the samples through studying the surface morphology, mechanical properties, crystalline properties and phase transformation properties.
3. To study the influence of LSP on laser additive manufactured samples through numerical and experimental analyses estimating the amount of residual stress.
4. To study the influence of laser annealing to overcome the amorphization effect due to LSP through numerical and experimental analyses.

5. To investigate the influence of post processing techniques in shape memory effects of the samples using dynamic mechanical analyzer (DMA) and its comparison with differential scanning calorimetry (DSC) curves.

1.15 Outline of the Thesis

The thesis is divided into seven chapters. Chapter 3 deals with the bulk SMA structures developed using LAM assisted with numerical and experimental studies. Both NiTi and TiNiCu samples of different compositions are brought under several characterizations to study the surface morphology, mechanical properties, crystalline properties and phase transformation properties of the samples.

Chapter 4 deals with experimental and numerical analyses of LSP to study the effects of LSP in residual stress distribution for both NiTi and TiNiCu samples. Similar characterizations as mentioned in chapter 3 are carried out for a comparative study of the properties before and after LSP.

Chapter 5 deals with the LA process with experimental and numerical analyses of the temperature distribution

In the samples during the process. Experimental analyses of residual stress distribution is also done in order to confirm the deduction in the amount of residual stress in the samples after LA. Characterizations done in chapter 4 and 5 are repeated to analyze the effects of LA in the samples.

Chapter 6 deals with the shape memory properties of the samples developed, which is the most important analyzes of the thesis. Based on the results obtained in this chapter the success of developing SMA using LAM relies.

Chapter 7 gives the conclusion of the current research work and scope of future work.

Chapter 2

Overview of NiTi Bulk Structures Development and Laser Additive Manufacturing

2.1 Introduction

In the past decade, Additive Manufacturing (AM) has gained significant attention for processing NiTi because they have circumvented many of the challenges associated with the conventional methods. These processes rely on the CAD data and entails adding material in consecutive layers made of powders and melted, in most cases by a laser. The AM techniques for NiTi are either powder-bed based technologies such as Selective Laser Melting (SLM), or flow-based methods such as Laser Engineered Net Shaping (LENS). The powder-bed based techniques deal with deposition of the powder through a roller, blade, or knife, while the flow-based technologies deposit the powder through one or more nozzles that directly feed the powder into the laser focus. Powder-bed based technologies are more common for creating complex parts.

2.2 Influence of composition of SMA properties of NiTi

These properties depend strongly on the exact chemical composition, processing history, and impurity level as stated by (Sawaguchi et al. 2003). Contaminants such as oxygen and carbon can dramatically affect the properties of the NiTi shape memory alloy. Their penetration occurs basically during production and processing of the alloy. Commercial production processes usually involve induction melting of the alloy under high vacuum. Vacuum induction melting usually yields SMAs with excellent chemical homogeneity as reported by (Zhang et al. 2005). The functional and structural properties of SMAs strongly depend on the appropriate casting parameters and the impurity level as well as the alloy composition. A major source of contaminants is the melting crucible, mould and environment, which need to be carefully controlled. In order to improve the quality of shape memory effect and mechanical properties under different conditions, various mechanisms have to be clarified and finally the conditions for establishing optimised properties to be deduced.

2.3 Development of tailor made NiTi and TiNiCu SMA Structures:

2.3.1 Ni rich NiTi

Figure presents the phase diagram near the equiatomic composition of the TiNi alloy system (Ishida et al, 1995). On the basis of this diagram, a solution aging treatment of Ni-rich TiNi films is applicable to suppress plastic deformation, which is the most common heat-treatment in bulk alloys. The film composition is Ti-51.3at%Ni. From the diffraction pattern, the precipitates are identified to be Ti_3Ni_4 . These precipitates are known to form on $\{111\}$ planes of the B2 matrix, having a lenticular shape, instead of $TiNi_3$, and play an important role in strengthening Ni-rich bulk alloys. Under low stresses, the film exhibits a two-stage elongation on cooling. The first small elongation arises from the R-phase transformation (B2 phase to R phase), whereas the second large one is from the martensitic transformation (R phase to B19' phase). The R-phase transformation is commonly observed in age-treated Ni-rich TiNi alloys, although it is not detected in solution-treated ones as stated by (Miyazaki and Ishida ,1994). The important features of SMA, suggesting that the performance of SMA actuators can or should be controlled by an applied stress called “bias stress”. In order to discuss the dependence of shape memory characteristics on stress, the temperatures for the R-phase transformation start (R_s), the M_s , and the A_f were measured by the tangential extrapolation method. All the transformation temperatures are found to increase with the increasing stress. This stress dependence is expected from the Clausius–Clapeyron equation as reported by (Miyazaki and Ishida ,1994). The M_s temperature shows stronger dependence on stress than the A_f temperature and, as a result, the temperature hysteresis between the forward and reverse transformations becomes small with increasing stress. The R_s temperature is also less sensitive to stress than the M_s temperature. This is the reason that the deformation mode changes from a two-stage deformation (B2-R-B19) to a single-stage deformation (B2-B19) when the stress is high. Basically, the R-phase transformation is less sensitive to stress than the martensitic transformation, since the lattice deformation associated with the former transformation is only one tenth of that of the latter transformation. The plastic strain is not detected under low stresses, but it appears at a certain stress. This stress is defined as “a critical stress for slip”. This critical stress is considered to correspond to the maximum generative stress of an SMA thin-film actuator in that it can recover its original shape up to this stress. As the stress increases, the transformation strain increases gradually and then levels off. Since the plastic strain increases above the critical stress, the recoverable strain decreases after reaching a maximum. Similar measurements were carried out for Ti-51.3at%Ni thin films aged at

various temperatures (573–773K) for three different times (3.6, 36 and 360 ks) after solution treatment at 973K for 3.6 ks [Ishida et al, 1996]. The R_s and M_s temperatures are obtained by extrapolating the temperature–stress. All the transformation temperatures increase with the increasing aging time, but their dependence on aging temperature is a little complicated. They increase with the increasing aging temperature from 573 to 723 K, but the further increase from 723 to 773K causes a decrease in the transformation temperatures. These effects are explained in terms of two factors, that is, the composition of the B2 matrix and the precipitation morphology of the second phase. As the precipitation process proceeds, the Ni content of the matrix decreases owing to the formation of Ti_3Ni_4 . The transformation temperature of a TiNi phase is known to decrease with increasing Ni content (Honma, 1987). Therefore the composition change of the matrix causes the transformation temperatures to increase. However, when the composition of the matrix approaches the equilibrium one after a long-time aging, the transformation temperatures of films aged at 773K can be lower than those of films aged at 723 K. This occurs because the equilibrium Ni content in the matrix phase increases with increasing temperature. The transformation temperatures are affected by the microstructure as well as the matrix composition. The fine precipitates strengthen the matrix and thus suppress the shape changes associated with the transformations. This results in lowering transformation temperatures. This effect is strong for the martensitic transformation compared with the R-phase transformation because of its large lattice deformation. As either aging temperature or time increases, the critical stress for slip decreases. The precipitation hardening due to the Ti_3Ni_4 phase plays an important role in increasing the critical stress for slip while the precipitate diameter is less than 100 nm. The maximum recoverable strain decreases with increasing aging temperature and time. The aging effects of Ni-rich films are almost the same as those reported in bulk alloys as mentioned by (Saburi et al, 1998).

2.3.2 Ti rich NiTi

In contrast to Ni-rich films, Ti-rich TiNi films exhibit different microstructures and shape memory behaviors from those of bulk alloys. This section discusses their microstructures and shape memory behaviors, which are peculiar to thin films. It has been known that Ti-rich NiTi alloys exhibit a high martensitic transformation temperature compared with Ni-rich TiNi alloys as reported by (Honma, 1987). This should be an advantage, but Ti-rich bulk alloys have not been used for practical applications and even the shape memory behavior has not been measured except for near equiatomic

compositions. The reason is their coarse structure formed by casting. In bulk alloys, coarse particles of Ti_2Ni form only along grain boundaries, leading to their brittleness as reported by (Lin et al, 1992). The steep solubility line on the Ti-rich side of the TiNi single-phase region prevents any heat treatment from changing this cast structure. However, the crystallization process of Ti-rich amorphous films produces various kinds of interesting microstructures effective in improving their shape memory behavior as mentioned by (Ishida and Martynov, 2002 and Kawamura et al, 2000). The microstructure in the B2 matrix evolves in the following sequence as reported by (Ishida et al, 1997): (a) plate precipitates of Guinier–Preston (GP) zones along $\{100\}$ planes of the matrix, (b) GP zones and spherical Ti_2Ni precipitates with Moire_fringes and (c) spherical Ti_2Ni precipitates alone. Prolonged annealing at a high temperature of the same film results in decreasing the density of the spherical Ti_2Ni precipitates in the grain interiors and enhancing grain boundary precipitation as reported by (Otsuka, 1998). This structure is similar to that of bulk alloys. High-resolution transmission electron microscopy reveals that the GP zone consists of several atomic layers and lies on $\{100\}$ planes with perfect coherency to the matrix as reported by (Kajiwara et al 1996). On the other hand, the spherical Ti_2Ni precipitates have the same orientation as that of the B2 matrix, but the interface between them is semi coherent. The microstructure of the Ti-rich films is affected by the crystallization process as well as the precipitation process. The homogeneous distribution of GP zones suggests that they were generated from a supersaturated B2 matrix with the same composition as that of the amorphous phase. However, when an annealing temperature is low, B2 phase with a near-equiatom composition nucleates from the amorphous matrix and grows, ejecting surplus Ti atoms into the surrounding matrix. This process results in localized distribution of GP zones. Furthermore, Ti_2Ni particles without any specific orientation relationship are found in films with higher Ti content. In this Ti-45.2at%Ni film, Ti_2Ni particles crystallize first, and then the B2 phase surrounding them crystallizes. The diversity in microstructure, affects the shape memory behavior of Ti-rich TiNi films. A two-stage elongation in the cooling curve and a two-stage contraction in the heating curve under constant stresses of 40 and 120MPa. These two-stage shape changes are explained by the R-phase and martensitic transformations. A two-stage elongation is still detected in the cooling curve, but a two-stage contraction does not occur on heating. This change in the transformation behavior results from the rise in the martensitic transformation temperature. A noticeable change in shape memory behavior is seen, the R-phase transformation disappears, resulting in a single-stage transformation attributable to the martensitic transformation. In this film

Ti₂Ni precipitates are observed along the grain boundaries, like bulk alloys. The absence of the R-phase transformation in this film agrees with the transformation behavior reported in bulk Ti-rich TiNi alloys as mentioned by (Lin et al, 1992). The R-phase transformations of Ti-rich TiNi thin films are, therefore, characteristic of thin films as stated by (Ishida et al, 1995). In addition to the difference in transformation behavior. The GP zones produce coherency strain fields around them and, as a result, suppress plastic deformation as reported by (Ishida et al, 1995). On the other hand, Ti₂Ni precipitates have semicoherent interfaces and the strengthening effect is not so high as that of GP zones. Compared with these two films, the film shows a considerably large plastic strain because of the preferential precipitation of Ti₂Ni along the grain boundaries. The large transformation strain of films containing GP zones can be understood by the effects of GP zones and Ti₂Ni precipitates on (001) twinning in the martensite, which is a dominant twinning mode in films with either a large amount of GP zones or Ti₂Ni precipitates as per (Zhang et al, 2005), The (001) twin plate intersects the existing GP zone, suggesting that GP zones can be elastically deformed by the shear deformation (Zhang et al, 2005). In contrast, it is clear that the Ti₂Ni precipitates can not deform by the shear deformation associated with the (001) twinning, implying a small transformation strain. The dependence of the shape memory characteristics on annealing temperature and Ni content for films with Ti₂Ni precipitates alone is summarized as follows: (1) Ms temperature decreases with decreasing Ni content and annealing temperature; (2) Rs temperature is almost constant irrespective of Ni content, but slightly increases with increasing annealing temperature; (3) critical stress for slip increases with decreasing Ni content and annealing temperature; (4) maximum recoverable strain decreases with decreasing Ni content and increasing annealing temperature. On the other hand, films containing GP zones show characteristic behaviors such as low transformation temperatures, a high critical stress for slip and a large maximum recoverable strain. The small temperature hysteresis of the R-phase transformation is of practical importance to increase the response speed of an actuator. Specifically the R-phase transformation of Ti-rich TiNi thin films is attractive, since their transformation temperatures are usually higher than those of Ni-rich Ti-Ni thin films.

2.3.3 Cu tailored TiNiCu

Similar to NiTi, TiNiCu also had lots of tailored structures being made for various other applications. Titanium-nickel alloys with a chemical composition close to equiatomic remain in the centre of interest due to the unique properties associated with shape memory effect (SME). In opposite to

polymers or ceramic, mechanism of the shape memory effect is strictly correlated to the thermoelastic reversible martensitic transformation (MT). Modification of the course of the martensitic transformation influences the shape memory effect. Generally, course of the martensitic transformation can be influenced, separately or simultaneously, by two ways:

Modification of chemical composition: addition and/or substitution of the alloying elements as reported by (Otsuka et al 1998; Van Humbeeck, 1997). Alloying elements such as aluminum, iron, cobalt, cause lowering temperatures of the martensitic transformation even down to -140°C . Addition of copper as reported by (Duerig et al.1990), hafnium or zirconium as reported by (Li et al. 2006) causes an increase of the transformation temperatures. In case of hafnium zirconium, it is possible to obtain high-temperature shape memory alloys, in which the reversible martensitic transformation occurs at temperatures between 300 and 400°C as stated by (Santamarta et al 1999).

Modification of microstructure: way of production and/or further alloy processing. The course of the martensitic transformation and its reversible nature is also affected by the structure of defects formed during the manufacturing or alloy processing. In order to change the transformation temperatures, in fact - the thermal range of the shape memory effect, mostly heat treatment or thermo-mechanical treatment is applied (Besseghini et al. 1999).

Ternary TiNiCu alloy belongs to a large family of NiTi alloys, which reveals shape memory effect (Mercier et al 1978). In the TiNiCu alloys content of titanium is close to 50at.% while nickel does not exceed 20at.%. The rest is copper as reported by (Melton et al. 1979). Substituting either nickel or titanium results in increasing the characteristic temperatures of the martensitic transformation, when compared to a binary NiTi alloy. In results of that, a thermal range of the shape memory effect moves from the room temperature up to approximately 800°C as stated by (Duerig et al 1990). Moreover, copper causes good stability of transformation temperatures as well as prevents from formation of Ti_3Ni_4 precipitation. However, the most important feature is appearance of the multistep martensitic transformation and formation of different type of the martensite structures. It results in receiving shape memory alloy, in which a hysteresis of the martensitic transformation can be narrowed from about 30 degrees down to 15 degrees. Dependently on the copper addition, the course of the martensitic transformation can be as follows.

The copper lower than 5-10 at% during cooling the parent phase B2 transforms directly to the B19' monoclinic martensite; thermal hysteresis is about 20 degrees for 10-15at% Cu - transformation occurs in two steps: first, from the B2 parent phase the orthorhombic martensite B19 is formed, next

the B19 martensite transforms to the B19' monoclinic martensite; thermal hysteresis is about 30 degrees; when the Cu content exceed 20%, again one-step transformation can be observed, however the B2 parent phase transforms directly to the B19 orthorhombic martensite; thermal hysteresis is about 10 degrees; Special attention was drawn by alloy with nickel content of 25 at. % Ni and copper also 25 at.%. It was due to the wide possibility of its potential application (Gil et al 2004) . The reason for this is the narrow thermal hysteresis loop of the martensitic transformation. Its width does not exceed 150°C.

Recently, for manufacturing of the NiTi-based alloys, intensive effort has been put to adoption of the nonconventional production techniques such as powder metallurgy as reported by (Goryczka at all 2005), melt-spinning as reported by (Santamarta at all 2004) or twin roll casting as reported by (Goryczka and Ochin 2005). This creates a wider possibility of the alloy applications. Despite the fact that these techniques have been successfully applied to metals and alloys production, their application for SMAs manufacturing is quite new.

The subtle nature of martensitic transformation and shape memory effect requires the selection of appropriate process conditions and parameters. In fact not many references about the influence of the processing parameters on the shape memory alloys and transformation behavior in TiNiCu alloy can be found.

2.4 NiTi Bulk Structure Development

Developing NiTi structures as reported in the literature that the manufacturing of SMA has been achieved through several methods, like pulsed laser deposition, sputtering process etc. These methods are successfully deployed but their usage is limited to the fabrication of thin sheets as reported by (Chung et al. 1997 and Constantinescu et al. 2007). These thin sheets are being used as actuators for various MEMS applications, especially in micro-pumps and micro-valves. Also, the fabrication route involving powder metallurgical processing, like- solid state-sintering, hot extrusion , hot pressing as reported in (Morris et al. 1989, hot isostatic pressing [Neese et al. 2000,Bram et al. 2002], metal injection molding (Bram et al. 2002), field activated- activated pressure- assisted synthesis (Locci et al. 2003), mechanical alloying as reported by (Maziam et al. 2004) are tried. But these processes have limitations like - formation of stable secondary phases affecting the elongation of NiTi material, fabrication of simple geometries, etc. (Vamsi Krishna et al. 2007). Almost all the above mentioned

techniques have been successful in manufacturing thin films. The thin films developed have been deployed in various functional device developments. Detailed characterizations have been done and the area has been well explored by researchers in the past. The next level of developing bulk structures have not been probed much by researchers in the past and also, the pros and cons of developing bulk structures using the above mentioned technique is not much explored and also the possibilities were very lean.

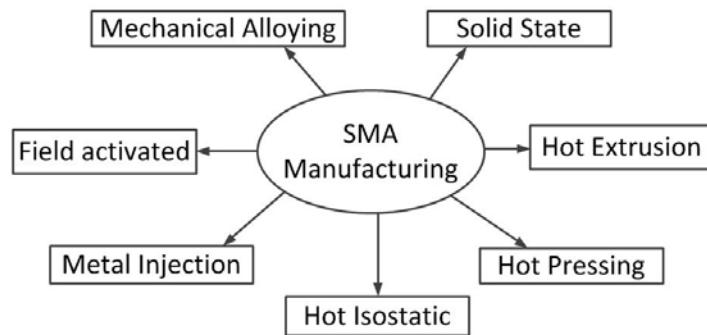


Fig. 2.1 Successful methodologies implemented in manufacturing NiTi SMA

For TiNiCu samples in published literature there are reports about the successful manufacturing of TiNiCu thin films using magnetron sputtering by direct deposition on various flexible substrates as well as glass substrates by (Ren et al.2000), (Zhang et al.2006) and (Cai et al.2007). TiNiCu ribbons by melt spin assisted with hot rolling was also successfully obtained by (Goryczka 2001). Gradually molecular beam epitaxy deployed by (Ralf Hassdorf et al. 2006) and flash evaporation by (Takashi Mineta 2007) also caught attentions in the list of TiNiCu manufacturing methodologies. (Valeanu et al. 2011) demonstrated promising results using powder metallurgy and vacuum plasma melting assisted with hot rolling was opted by (de Araújo et al. 2011), while (Fatemeh Alijani et al. 2014) demonstrated the manufacturing of TiNiCu using mechanical alloying. Fig.1 summarizes the the prevailing manufacturing technique of the fabrication of TiNiCu SMA.

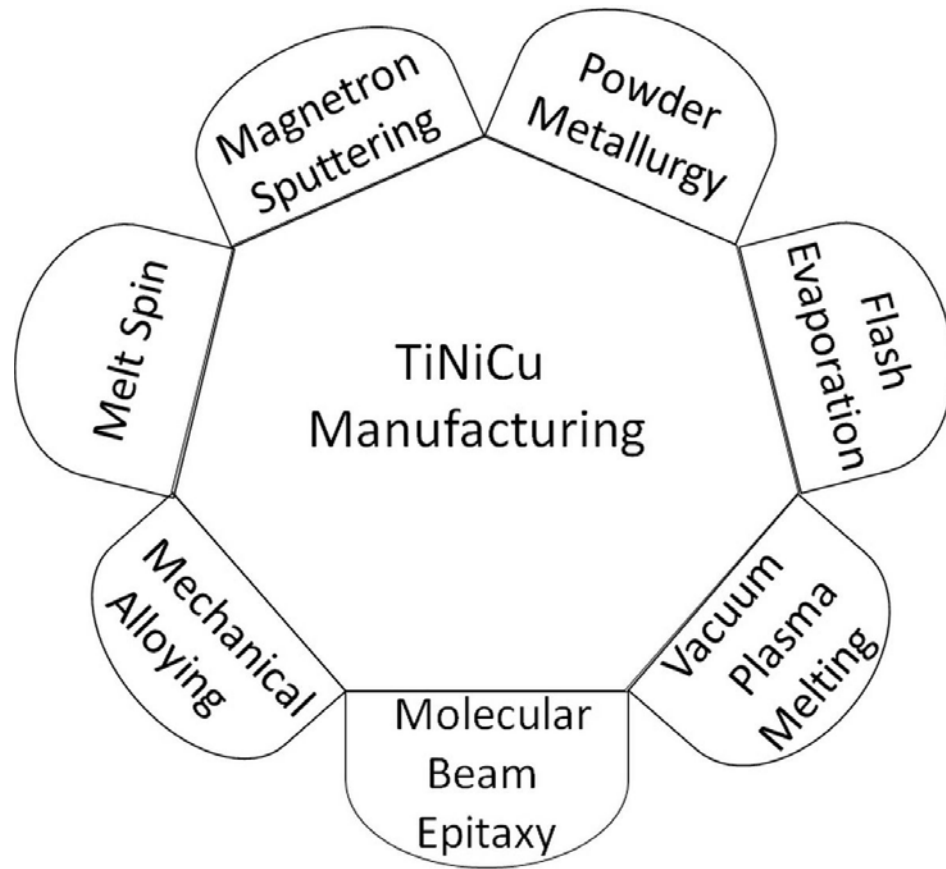


Fig. 2.2 Successful methodologies implemented in manufacturing TiNiCu SMA

The substitution of copper for nickel in the near equi-atomic NiTi alloys has many interesting effects on their transformation behavior, shape-memory characteristics and workability. The shape-recovery rate showed a slight decrease with increasing Cu content above 10 at. % and it became more brittle. At the same time, it is less composition sensitive for the martensitic transformation start temperature, M_s . The decrease in transformation hysteresis from 30 K to 10 K and increase in the dampening capacity have been observed, with increasing the Cu content. These features make the ternary TiNiCu alloys as most suitable alloy, as an actuator element for smart systems.

Du et al reported the effect of copper additions (1.3 at. %) on the crystallization of amorphous nickel-titanium thin films. The overall activation energy and crystallization temperatures have been found to be the same as that of pure NiTi. However, in situ transmission electron microscopy (TEM) showed the nucleation and growth behaviors to be markedly different (Du and Fu, 2004). Fu et al have deposited TiNiCu films by mix-sputtering of a NiTi target with a separated Cu target. They have investigated the influence of the process parameters on the crystalline structure, phase transformation

and shape memory effect of the TiNiCu films. The Cu compositions in the TiNiCu films have been found to depend on Cu target power. When these films were annealed, a two-way SME have been clearly observed (Fu et al, 2011). Krulevitch et al has demonstrated the mixed sputter deposition of Ti, Ni and Cu elemental targets for the deposition of TiNiCu films. This technique has enabled more composition flexibility for the deposition process (Fu et al, 2011). Miyazaki et al have shown the Martensite transformation temperatures of the TiNiCu films around 323 K. The hysteresis associated with the transformation showed a strong dependence on Cu content i.e., it decreases from 27 K to 10 K with Cu content increasing from 0 to 9.5 at.%. A single stage transformation has been observed when Cu content is less than 9.5 at.% in NiTi-Cu alloy. At the same time with increasing Cu at.% above 9.5, a two-stage transformation have been observed between the B2 and monoclinic phases [Miyazaki et al 1996, Hsu and Ting, 2002]

2.5 Limitation of existing process LAM can provide the solution

In the above discussed methods though the development of NiTi and TiNiCu have been successful, they are widely used to develop thin films. Development of bulk films using the existing methods is hardly possible and it has some draw backs like lots of time consumption, complex geometry not possible, almost importantly to maintain the composition of the samples homogeneously through the bulk structure is extremely unreliable. To overcome the issue laser additive manufacturing (LAM) can be opted. The details about LAM are as discussed below in the following session.

2.6 LAM

As lasers can heat, melt and vaporize any material, they are being exploited in manufacturing for cutting, welding, surface hardening, cladding, alloying, peening and additive manufacturing. In 1986, lasers stepped in the arena of additive manufacturing with the invention of Stereolithography-the first additive manufacturing process. In this process, UV laser beam is scanned on the surface of liquid UV-curable photopolymer "resin" to selectively cure and form a cross-section of indented object. A number of cross-sections are thus formed one over another to shape the whole object. It realized the concept of additive manufacturing into rapid prototyping process. Soon after the invention of stereolithography, the laser was deployed in "selective laser sintering" to fuse the polymer/polymer coated metal powders to shape the prototype components. The subsequent advances in the field of

high power lasers, computer aided design and manufacturing (CAD/CAM), powder metallurgy and allied electronics translated the rapid prototyping into three dimensional metallic components for various engineering applications. This propelled the research and development in the area of rapid manufacturing at various renowned universities and national laboratories. In this appendix list of rapid manufacturing, laser rapid manufacturing (LRM) is one of the leading manufacturing techniques. Additive Manufacturing technology primarily makes use of the output from mechanical engineering, 3D Solid Modeling CAD software. It is important to understand that this is only a branch of a much larger set of CAD systems and, therefore, not all CAD systems will produce output suitable for layer-based AM technology. Currently, AM technology focuses on reproducing geometric form; and so the better CAD systems to use are those that produce such forms in the most precise and effective way. Additive Manufacturing technology primarily makes use of the output from mechanical engineering, 3D Solid Modeling CAD software. It is important to understand that this is only a branch of a much larger set of CAD systems and,

therefore, not all CAD systems will produce output suitable for layer-based AM technology. Currently, AM technology focuses on reproducing geometric form; and so the better CAD systems to use are those that produce such forms in the most precise and effective way. Early CAD systems were extremely limited by the display technology. The first display systems had little or no capacity to produce anything other than alphanumeric text output. Some early computers had specialized graphic output devices that displayed graphics separate from the text commands used to drive them. Even so, the geometric forms were shown primarily in a vector form, displaying wire-frame output. As well as the heavy demand on the computing power required to display the graphics for such systems, this was because most displays were monochrome, making it very difficult to show 3D geometric forms on screen without lighting and shading effects. CAD would not have developed so quickly if it were not for the demands set by

Computer-Aided Manufacture (CAM). CAM represents a channel for converting the virtual images developed in CAD into the physical products that we use in our everyday lives. It is doubtful that without the demands associated with this conversion

from virtual to real that CAD would have developed so far or so quickly. This, in turn, was fuelled and driven by the developments in associated technologies, like processor, memory, and display technologies. CAM systems produce the code for numerically controlled (NC) machinery, essentially combining coordinate data with commands to select and actuate the cutting tools. Early NC

technologies would take CAM data relating to the location of machined features, like holes, slots, pockets, etc. These features would then be fabricated by machining from a stock material. As NC machines proved their value in their precise, automated functionality, so the sophistication of the features increased. This has now extended to the ability to machine highly complex, freeform surfaces. However, there are two key limitations to all NC machining: Almost every part must be made in stages, often requiring multiple passes for material removal and setups. All machining is performed from an approach direction (sometimes referred to as 2.5D rather than fully 3D manufacture). This requires that the stock material be held in a particular orientation and that not all the material can be accessible at any one stage in the process. NC machining, therefore, only requires surface modeling software. All early CAM systems were based on surface modeling CAD. AM technology was the first automated computer-aided manufacturing process that truly required 3D solid modeling CAD. It was necessary to have a fully enclosed surface to generate the driving coordinates for AM. This can be achieved using surface modeling systems, but because surfaces are described by boundary curves it is often difficult to precisely and seamlessly connect these together.

Even if the gaps are imperceptible, the resulting models may be difficult to build using AM. At the very least, any inaccuracies in the 3D model would be passed on to the AM part that was constructed. Early AM applications often displayed difficulties because of associated problems with surface modeling software. Since it is important for AM systems to have accurate models that are fully enclosed, the preference is for solid modeling CAD. Solid modeling CAD ensures that all models made have a volume and, therefore, by definition are fully enclosed surfaces. While surface modeling can be used in part construction, we can not always be sure that the final model is faithfully represented as a solid. Such models are generally necessary for Computer-Aided Engineering (CAE) tools like Finite Element Analysis (FEA), but are also very important for other CAM processes. Most CAD systems can now quite readily run on PCs. This is generally a result of the improvements in computer technology mentioned earlier, but is also a result in improvements in the way CAD data is presented, manipulated, and stored. Most CAD systems these days utilize Non-Uniform Rational Basis-Splines, or NURBS. NURBS are an excellent way of precisely defining the curves and surfaces that correspond to the outer shell of a CAD model. Since model definitions can include free form surfaces as well as simple geometric shapes, the representation must accommodate this and splines are complex enough to represent such shapes without making the files too large and unwieldy. They

are also easy to manipulate to modify the resulting shape. CAD technology has rapidly improved along the following lines:

Realism: With lighting and shading effects, ray tracing and other photorealistic imaging techniques, it is becoming possible to generate images of the CAD models that are difficult to distinguish from actual photographs. In some ways, this reduces the requirements on AM models for visualization purposes ability and user interface: Early CAD software required the input of text based instructions through a dialog box. Development of Windows-based graphical user interfaces (GUIs) has led to graphics-based dialogs and even direct manipulation of models within virtual 3D environments. Instructions are issued through the use of drop-down menu systems and context-related commands. To suit different user preferences and styles, it is often possible to execute the same instruction in different ways. Keyboards are still necessary for input of specific measurements, but the usability of CAD systems has improved dramatically. There is still some way to go to make CAD systems available to those without engineering knowledge or without training, however.

Engineering content: Since CAD is almost an essential part of a modern engineer's training, it is vital that the software includes as much engineering content as possible. With solid modeling CAD it is possible to calculate the volumes and masses of models, investigate fits and clearances according to tolerance variations, and to export files with mesh data for Finite Element Analysis. FEA is often even possible without having to leave the CAD system.

Speed:As mentioned previously, the use of NURBS assists in optimizing CAD data manipulation. CAD systems are constantly being optimized in various ways, mainly by exploiting the hardware developments of computers.

Accuracy: If high tolerances are expected for a design then it is important that calculations are precise. High precision can make heavy demands on processing time and memory.

Complexity: All of the above characteristics can lead to extremely complex systems. It is a challenge to software vendors to incorporate these features without making them unwieldy and unworkable.

Many CAD software vendors are focusing on producing highly integrated design environments that allow designers to work as teams and to share designs across different platforms and for different

departments. Industrial designers must work with sales and marketing, engineering designers, analysts, manufacturing engineers, and many other branches of an organization to bring a design to fruition as a product. Such branches may even be in different regions of the world and may be part of the same organization or acting as subcontractors. The Internet must therefore also be integrated with these software systems, with appropriate measures for fast and accurate transmission and protection of intellectual property. It is quite possible to directly manipulate the CAD file to generate the slice data that will drive an AM machine, and this is commonly referred to as direct slicing. However, this would mean every CAD system must have a direct slicing algorithm that would have to be compatible with all the different types of AM technology.

2.7 Requirements for Laser Additive manufacturing System

Laser Rapid Manufacturing system consists of the following three primary subsystems.

- 1) High power laser system
- 2) Material feeding system
- 3) Computerized Numerically Controlled (CNC) workstation.

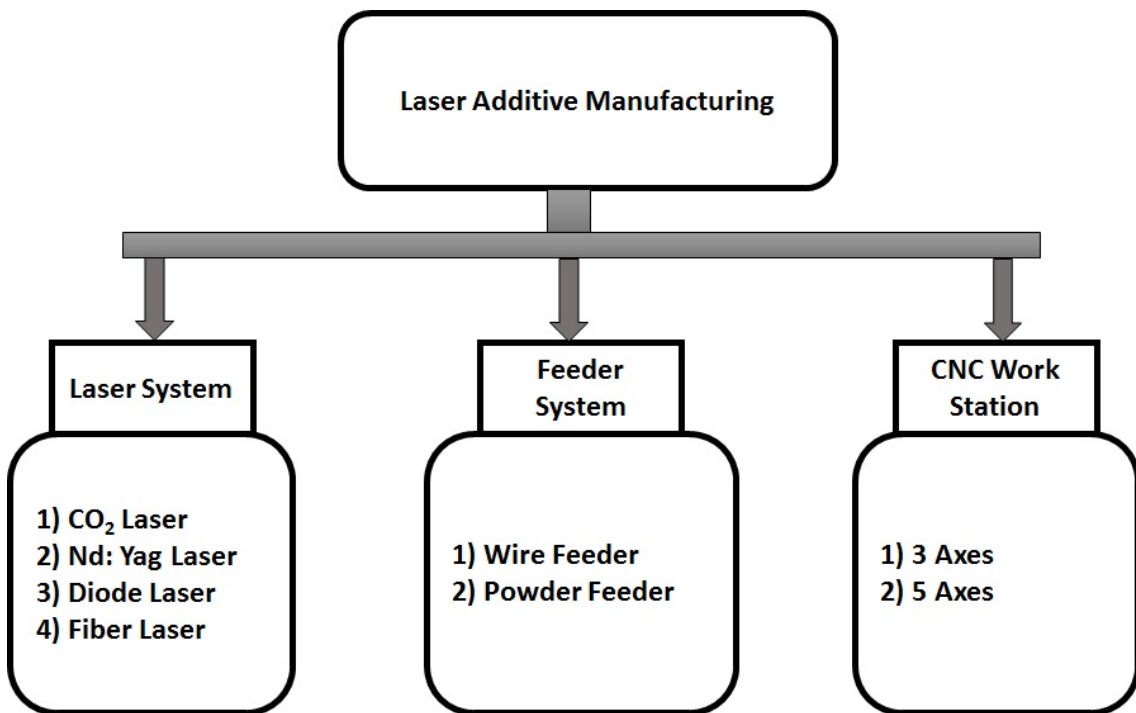


Fig. 2.3 Block diagram of an entire LAM requirements

2.7.1 High power laser system

In LRM, high power laser system is used as heat source to melt thin layer of substrate/previously deposited layer and fed material. CO₂ laser, Nd:YAG and diode lasers are most widely used for the application. High power fibre lasers are the new entrant in this application domain (Vetter et al. 1994). For laser material processing involving metals, Nd:YAG, diode and fibre lasers have better absorption due to shorter wavelength, but CO₂ lasers are still used due to established systems and procedures. Generally, laser energy intensity of 20 kW/cm² to 60 kW/cm² are used for CO₂ lasers, while it is 150 kW/cm² to 200 kW/cm² for pulsed Nd:YAG lasers (Sun et al. 2005). High energy intensity requirement for pulsed Nd:YAG lasers are attributed to remelting and solidification of molten pool during the processing. The basic pre-requisite for laser beam energy intensity distribution is symmetry along the axis of laser beam propagation. It allows uniform material deposition independent of direction of processing. Therefore, multimode laser beam with flat top distribution is most widely used. Gedda et al has studied the energy distribution during LRM process using CO₂ laser and Nd:YAG laser (Gedda et al. 2002). The observations are summarized in Table 2.1. The table clearly indicates that about 10% laser energy is utilized to melt substrate layer/previously deposited layer in case of CO₂ laser, while it is 20% in case of Nd:YAG laser due to increased absorption. When metals (such as SS316L) are in solid state, the laser energy utilization for Nd: YAG laser is more by a factor 1.3. This factor reduces as the temperature rises and is same for both the lasers in molten/liquid states. Thus, about 769 W of continuous wave Nd:YAG laser replaces 1 kW of continuous wave CO₂ laser of same beam product parameter for almost same results during LRM. Since the wave length of other commonly used lasers (diode and fibre) is close to Nd:YAG laser, a similar results as compared to CO₂ laser are pertinent.

Table 2.1:Redistribution of Laser Power during laser cladding

S.No.	Use of Laser Power	CO ₂ Laser	Nd:YAG Laser
1	Reflected off the cladding melt	50%	40%
2	Reflected off the powder cloud	10%	10%
3	Heat the substrate	30%	30%
4	Melt the substrate/previously deposited layer	10%	20%

2.7.2 Material Feeding System

Among material feeders, there are three main types of feeding techniques. They are wire feeding, pre-placed powder bed and dynamic powder blowing.

2.7.2.1 Wire feeders

Wire feeders are generally used in various industrial applications, including gas metal arc welding. These standard wire feeders are customized and used in many of LRM systems. Wire feeding is preferred for the fabrication of components involves continuous deposition (Hensal et al. 1992), as intermittent start/stops results in discontinuity in deposited material. In wire feeding, the wire is always in direct contact with the melt pool on the substrate. Any inaccuracy in wire positioning and wire-feed rate disturbs the shape and size of melt pool. This disturbance leads to non-uniform/unsymmetrical shape of deposited materials/tracks. Moreover, a definite ratio between beam diameter and wire diameter (>3) are used for good quality deposition. Here, good quality deposition means the deposited material has good bonding to the substrate and the fed material spreads out during deposition resulting in a uniform smooth surface. Therefore, the positioning of the wire to the substrate and its size is critical in wire feeder based LRM.

This method is not adopted as universal method, because of poor wire/laser coupling leading to poor energy efficiency, unavailability of various materials in wire forms and their cost.

2.7.2.2 Pre-placed powder bed

Figure 2.4 shows the schematic arrangement of LRM with pre-placed powder bed. In this scheme, the powder is spread over the substrate through a powder filled hopper and subsequently, it is uniformly leveled with a wiper. Thereafter, LRM is performed by scanning the laser beam over a pre-placed bed of the metal/ceramic powders. When laser beam heats the powder layer, melt-front advances through the low conductive powder layer, from the surface to the bulk. When the melt-front reaches the substrate, heat conduction increases sharply because of high conductivity of the substrate/previous deposited layer. If laser energy is sufficient to melt a thin layer of substrate/previous deposited layer, the melted powder is fused and deposited forming a metallurgical bond. Excessive energy causes

excessive remelting and thermal distortion, while insufficient energy causes poor adherence and incomplete melting of the powder. For any particular deposited height (h) of specific material, a specific laser energy (E) can be calculated by

$$E = \frac{P}{DV} \quad (2.1)$$

where P is the laser power, D is beam diameter and V is scan velocity. The value of specific laser energy (E) has to be within a certain range for controlled remelting of the substrate and achieving good powder consolidation for a specific material. This method needs some special laser scanning strategy to achieve nearly 100% density [Yusoff et al.2008].

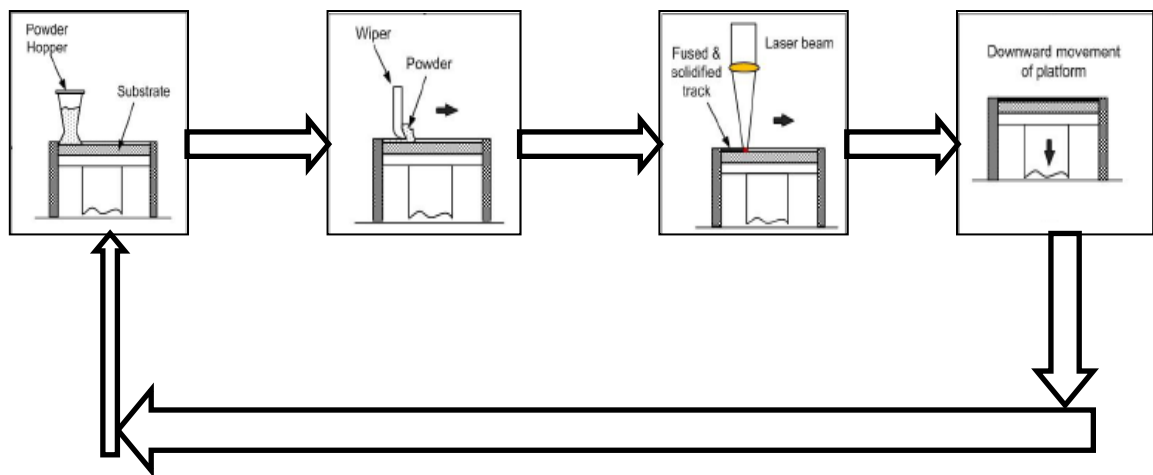


Fig. 2.4 Schematic diagram of Powder Bed Technology

2.7.2.3 Dynamic powder blowing

Dynamic powder blowing is convenient and most widely used approach for material feeding in LRM systems. It allows on-line variation in feed rate and multi-material feeding. Moreover, laser energy utilization is also more in dynamic powder blowing, as the laser beam passes through the powder

cloud to the substrate/previously deposited layer, resulting in preheating of powder particles by multiple reflections.

Various powder feeders are being used for this application. They are based on the following working principles:

- a. Pneumatic Screw Type Powder Feeder
- b. Vibration Assisted Gravity Powder Feeder
- c. Volumetric Controlled Powder Feeder

Pneumatic Screw Type Powder Feeder is one of oldest method. In this, the powder is fed by a rotating screw mounted at the bottom of the hopper as shown in Figure 2.5 (a). The controlled amount of the powder is fed into pneumatic line and transported to the powder nozzle with inert gas like- Argon (Ar), Helium (He) etc. The rotational speed and dimensions of the screw control the powder feed rate. Frequent choking and cleaning is one of the observed problems in this feeder.

In vibration assisted gravity powder feeder, a combination of pneumatic and vibration forces is used to feed the powder into pneumatic line (Paul etal 1997). The powder is taken in a hopper and some vibrating device, like- rotating wheel or standard ultrasonic vibrator, is fitted at the bottom of the hopper. The powder flows freely through an orifice. The dimension of orifice is controlled to regulate powder flow rate. The vibrating device generates the vibration and maintains the free flow of powder under gravity into pneumatic line. Thus, the powder is delivered to substrate with the help of inert gas as shown in Figure 2.5(b). This approach has limitations in regulating powder flow rate in finer steps and it is widely used for applications involving constant powder flow rate.

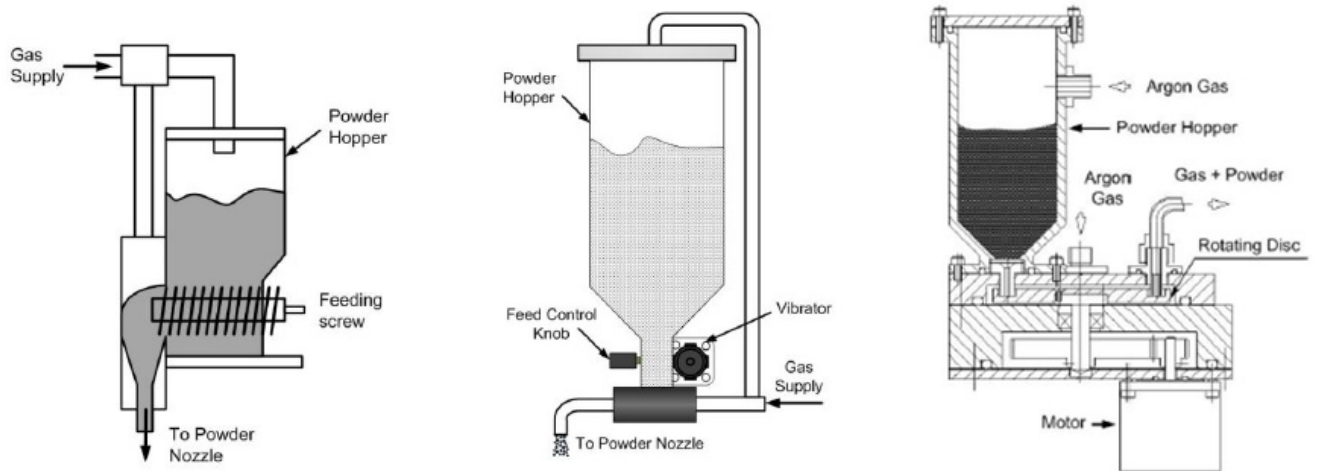


Fig. 2.5 Different types of feeding systems used in LAM

In volumetric controlled powder feeder, the powder is filled in the hopper and it falls on the annular slot of rotating disc. The hopper and the chamber enclosing the rotating disc are pressurized equally. The rotating disc carries the powder to an exit having a descending pressure gradient. This pressure gradient sucks the powder particles into pneumatic line and the powder is delivered to desired point. One such powder feeder is designed, fabricated and integrated at authors' laboratory for laser rapid manufacturing. Figure 2.6 (a) presents the schematic arrangement of developed volumetric controlled powder feeder. The pressure gradient resulting in a gas flow must exceed a minimum value to be able to suck the powder. This minimum gas flow rate is a function of powder material density and particle size. A higher gas flow rate does not increase the powder flow as the rotating disc is not able to deliver more powder. Moreover, a higher gas flow rate results in a higher gas velocity leading to a higher probability of the powder ricocheting at the impinging point. This results in lower powder catchment efficiency (=deposited material/fed material). In this system, the gap between the hopper and rotating disc, inside diameter of connecting tube, density of powder material and rotation speed of the rotating disc defines the volume of the powder displaced out to the feed tube from the rotating disc, i.e.,

$$m_p = \rho d t \pi D N \quad (2.2)$$

Where, m_p represents mass flow rate of the powder, ρ represents the density of the material feeded, t represents the distance between hopper and disc, d represents the inner diameter of the connecting tube, D represents the mean diameter of the slot and N represents the rotating disc speed.

In dynamic powder blowing method, there are two basic configurations for powder delivery to the substrate, i.e., lateral and co-axial powder feedings. Lateral feeding is very common in laser cladding. Since the powder stream is injected off-axis from the laser beam in lateral feeding, substrate movement determines different local deposition. For instance, a so-called “against-hill” deposition condition takes place when the powder stream is applied from the side from which the substrate moves. In this case, the powder is trapped temporarily in a corner formed between the molten track and the flat substrate. This leads to higher powder catchment efficiency as compared to that in the so-called “over-hill” deposition condition where the powder is from opposite side. In lateral powder feeding method, the nozzle is kept between 35° and 60° to the laser beam axis. Marsden et al has studied the effect of various parameters pertaining to nozzle geometry (Marsden et al. 1990).

When the powder is delivered coaxially with the laser beam, all the directions of the substrate movement in a plane perpendicular to the laser beam are equivalent. The coaxial feeding of powder is preferred in LRM due to advantages in terms of powder catchment efficiency and the omni directional material deposition. Various designs of co-axial nozzles have been reported in the literature. Vetter et al designed a co-axial nozzle that had a cone shaped nozzle with two concentric internal spaces. In the outer interstice, carrier or primary gas was used to blow the powder, while in inner space secondary gas jet was injected to shield the laser optics. This secondary gas also improved powder homogenization in the stream, insuring an optimum confinement of the powder stream along the beam axis. It prevented the deviation of the particles towards the focus, where breakdown could occur.

2.7.3 CNC workstation.

In CNC workstation, three-axis interpolation (X, Y and Z) is sufficient to reach to any point in the space, but two more axis (A and C) are required to orient particular direction to reach. Therefore, three-axis configuration is minimum system requirement and 5-axis is universal requirement without redundancy. Apart from axes-movement, laser workstation needs some more features, like- laser on/off, gas on/off, powder feeder on/off etc., for laser rapid manufacturing.

Table2.2 :Various Laser Rapid Manufacturing Systems

Process	Laser	Material Feeding	CNC Work Station
Laser Engineered Net Shaping (LENS)	2.4 kW CW Nd:YAG Laser	Co-axial	5-axis
Freeform Laser Consolidation	1 kW pulsed Nd:YAG Laser	Lateral	3- axis
Directed Light Fabrication	2 kW CW Nd:YAG Laser	Co-axial	5- axis
Shape Deposition Manufacturing	2.4 kW CW Nd:YAG Laser	Lateral	5-axis CNC mill
Laser Direct Casting (LDC)	2.8 kW CW Nd:YAG Laser	Co-axial	4-axis fully integrated CNC
Selective Laser Cladding (SLC)	5 kW CW CO ₂ Laser	Lateral	3- axis workstation
Automated Laser Fabrication	1 kW CW Fiber Laser	Lateral	5- axis workstation

2.8 Laser based Additive Manufacturing techniques used to develop bulk NiTi SMA

Additive manufacturing paved way for developing bulk NiTi structures. Successful reports have been reported claiming additive manufacturing methods like selective laser sintering (SLS), direct metal sintering (DMLS), selective laser melting (SLM), laser CUSING and electron beam melting (EBM).

2.8.1 Selective laser sintering (SLS)

Selective laser sintering (SLS), has been used by several researchers in the past to develop NiTi bulk structures. The following are the detail overview about NiTi structures developed by SLS

Shishkovsky et al 2008 have conducted an investigation of the technical aspects of producing sufficiently high strength porous biocompatible medical implants and tissue scaffolds from nitinol or pure titanium using selective laser sintering/melting (SLS/M) is presented. The developed material exhibited a martensitic transformation in the temperature range of -50 to 0 °C, which can be

interpreted as a SME. Production of the porous structure is desirable for further improvements in matching the elastic modulus to that of bone as the developed samples were much to be used for biomedical applications.



Fig.2.63D NiTi structures developed by SLS [Shishkovsky et al 2008]

2.8.2 Selective laser melting (SLM)

Shishkovsky et al 2012, had reported the solid nitinol samples obtained by two zone SLM process with the hatch distance of 100 μm , laser power of 50 W, laser beam diameter of 60 μm and with the scan velocities 100 and 160 mm/s under the additional heating up to nearly 500 $^{\circ}\text{C}$. The relative bulk density of the NiTi processed by the SLM was about 97% of the solid state. The additional hardening of the nitinol matrix ($\sim 540 - 735$ HV) after a high-speed laser cooling was achieved by the microhardness date. As a positive moment the absence of the free nickel and any NiTi intermetallic phase transformation during rapid solidification were also observed. Theformed product's area of applications are as scaffolds, stressed skeleton areas in maxillofacial surgery, orthopedics, and trauma recovery.

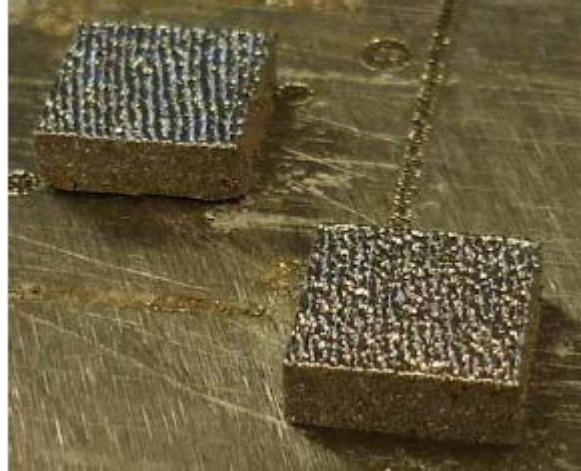


Fig. 2.7 Bulk NiTi structures developed by SLM [Shishkovsky et al 2012]

H. Meier and C. Haberland, 2012 have reported bulk NiTi shape memory alloy processed by SLM. The focus was on mechanical and functional properties of the material. The reports confirm SLM NiTi exhibits a similar stress-strain behavior than conventional NiTi for moderate strain up to 10% compression. Fracture strains and stresses of SLM NiTi are lower than for conventional NiTi (hot worked and straight annealed). Nevertheless, as SMAs belong to the class of functional materials, they usually are not exposed to high loads where cracking can occur during shape memory operations. The developed SLM NiTi showed a good functional stability during thermo mechanical testing. Also, higher reversible strains and less irreversible effects were observed than in the case of conventional NiTi. The authors had demonstrated that shape memory actuators can be produced by SLM, which exhibit a distinct pseudoplastic shape memory effect. The study shows that SLM offers a promising method for processing shape memory alloys. Moreover, this technology can provide a new scope for design of complex NiTi devices which hardly can be realized by conventional processing methods.

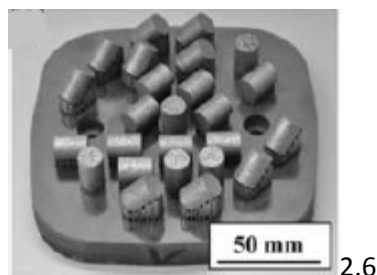


Fig.2.8 Bulk NiTi compression test samples developed by SLM [H. Meier and C. Haberland, 2012]

Christoph Haberland et al. 2014, have used SLM to produce high quality NiTi shape memory and superelastic parts. The work showed the parameters must be optimized such that a dense part fabricated, but impurity pick-up was minimized and the transformation temperatures were minimally affected. High quality NiTi had been additively manufactured which meets the requirements for impurity contents in medical grade NiTi. Furthermore, this work proves that the functional properties additive manufactured NiTi, include shape memory and pseudoelasticity, compare favorably with the properties of conventionally processed NiTi. Despite optimized conditions, and depending on alloy composition, a more or less pronounced shift of the phase transformation to higher temperatures after processing.

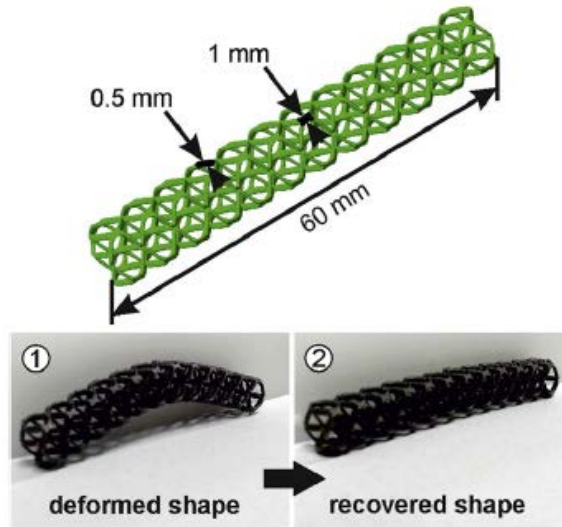


Fig. 2.9 Bulk NiTi actuators developed by SLM [Christoph Haberland et al. 2014]

Habijan et al. 2013 have developed porous SLM-NiTi samples. The reports suggest the variation in the diameter of laser beam the surface structure and volume of loose powder particles can be influenced significantly. By reducing the diameter of the laser beam, the mean nickel ion release decreases significantly. Although the nickel ion release of porous specimens was higher than the ion release of dense specimens, for all specimens the ion release was significantly below cytotoxic concentrations. The cytokine release profile on the NiTi specimens showed no sign of cell activation. Surface topography and cell morphology can be adjusted by varying the processing conditions. Reports also confirm SLM can provide an attractive technology to produce biocompatible NiTi implants. Hence the impact of process parameters optimization has been explored.



Fig.2.10 Bulk NiTi ingots developed by SLM [Habijan et al.2013]

Wild et al. 2013 have developed bulk NiTi structures for vibration damping applications SLM. The authors have shown that the damping ratio is characteristic for the phases that exist at specific temperature ranges. The results indicate that medical implants from conventional and SLM NiTi can be fabricated and can exhibit ultra-high mechanical damping properties. The damping properties of such NiTi parts were analyzed by the decay of cantilever vibrations in comparison to conventionally prepared NiTi. The dynamic modulus as a function of the temperature was derived from the resonant frequency. The results reveal two cantilevers showed a damping ratio of about 0.03 at temperatures below austenite start, maximal values of up to 0.04 in the transformation regions and low values of about 0.005 above austenite finish. The results also indicate that SLM developed NiTi qualifies for the fabrication of shock-absorbing medical implants in the same manner than conventionally produced NiTi.

Bormann et al. 2012 have demonstrated that the intentional modification of the applied energy during the SLM-process allows tailoring the transformation temperatures of NiTi entities within the entire construction. Differential scanning calorimetry, x-ray diffraction, and metallographic analysis were employed for the thermal and structural characterizations. In particular, the phase transformation temperatures, the related crystallographic phases, and the formed microstructures of SLM constructions were determined for a series of SLM-processing parameters. The SLM-NiTi exhibits pseudoelastic behavior. In this manner, the properties of NiTi implants can be tailored to build smart implants with pre-defined microarchitecture and advanced performance. The application of varied SLM process parameters, therefore, allows for the fabrication of pseudoelastic and pseudoplastic NiTi-structures from the same starting material. In addition, constructions consisting of several regions with distinct phase transformation temperatures can be built. This approach permits manufacturing implants with locally pre-defined anisotropic properties. SLM-produced implants

could, consist of pseudoelastic, shock-absorbing regions, on the one hand; pseudoplastic regions, on the other hand, would offer a reduced Young's modulus and the possibility to facilitate the one-way shape memory effect.

Hoffmann et al 2014 have demonstrated that Mesenchymal stromal cells (MSC) cultured on rapid-prototyped NiTi proliferated and differentiated along the osteogenic lineage to similar extents as on the clinically used reference titanium material. These results highlight the potential of SLM NiTi as a scaffold material for bone tissue engineering applications (i.e., in vitro engineering of osteogenic grafts) as well as regenerative medicine approaches (i.e., as a cell-free implant material). Moreover, the flexibility of the SLM technique, combined with the unique mechanical properties of NiTi, would allow for the design of grafts/implants better matching the mechanical requirements of a bone repair site than conventional Ti implants. Finally, the development of advanced NiTi shape memory implants, capable of applying regenerative mechanical stimuli at the site of implantation, could have profound consequences on implant integration periods leading to faster patient recoveries and to more successful clinical outcomes in the long term.

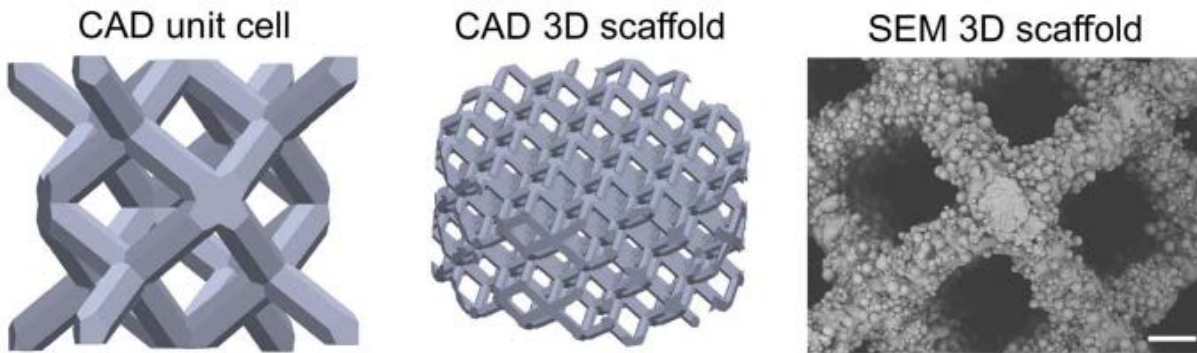


Fig.2.11 Bulk NiTi scaffolds developed by SLM from designed CAD model [Hoffmann et al 2014]

Saedi et al. [2016] revealed the effects of aging on the shape memory responses of SLM fabricated and solutionized NiTi alloys. It has been concluded that aging is an effective method to tailor the shape memory properties and obtain super elasticity of SLM fabricated Ni-rich NiTi alloys. SLM was used to fabricate complex-shaped NiTi parts for customized applications R-phase transformation was observed during the thermally cycling of 350°C-18h aged sample under constant stress. The “triangle type” behavior for shape memory effect was detected below 300 MPa while the behavior was symmetric at higher stress. The strength of the fabricated alloys increased after heat treatments.

Whereas 450°C aged samples did not show promising super elasticity, 350°C aged samples showed almost perfect super elasticity. 350°C-18h aging displayed 5.5% strain recovery and only 0.3% irrecoverable strain at first cycle under 1000 MPa loading. Super elastic responses of the samples were stabilized after cycling tests. Stress hysteresis and recoverable and irrecoverable strains were decreased with number of cycles. 350°C-18h and 450°C-10h aged samples demonstrated stable recoverable super elastic strains.

Walker et al.2016 have studied, the effects of processing parameters during SLM of NiTi. Compared with previously published studies on SLM of NiTi, The relationship between the track width and power is shown to be linear at constant scan velocities. Furthermore, it is demonstrated that laser parameters with a very high energy density result in parts with wavy surfaces, while too low energy density results in discontinuous melts, both of which are undesirable. With the optimal parameter setup, NiTi relative part density .98% can be achieved and shape memory functionality is demonstrated via cyclic compression testing. It is shown that impurity content and transformation temperatures both have a tendency to increase post-SLM. However, both effects can be minimized by operating at lower energy densities. Finally, NiTi structures with thin, cylindrical struts, and interconnected pores were manufactured to demonstrate SLM's ability to produce complex shape memory parts.

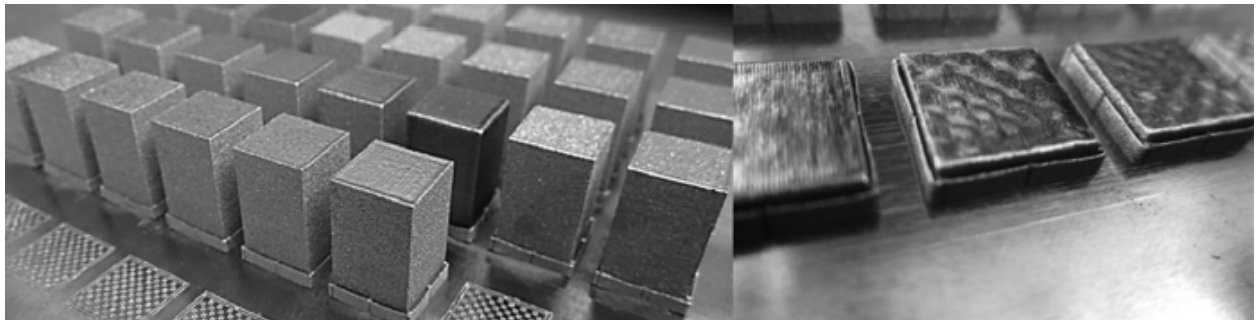


Fig. 2.12 Bulk NiTi structures developed by SLM[Walker et al.2016]

Andani et al 2016 have studied the feasibility of fabricating stiffness tailored porous NiTi parts was investigated. SLM was employed to fabricate solid and porous NiTi parts with predefined pore morphology. It was shown that it is possible to achieve the desired stiffness values by adjusting the percentage of the engineered porosity. A microplane constitutive modeling approach was adopted for the FE analyses of the produced shape memory components. Simulations and experiments showed similar trends in stiffness reduction as the percentage porosity increased. While only one type of unit

cell is studied in this work, many other unit cells can be implemented for this methodology. This approach paves the way for creating more effective bone implants and fixation hardware by providing both stability at the site of implantation and desirable mechanical properties. These two features facilitate bone healing and long-term implant success. Future fixation hardware will benefit from porosity at certain locations for optimal healing and stability properties.

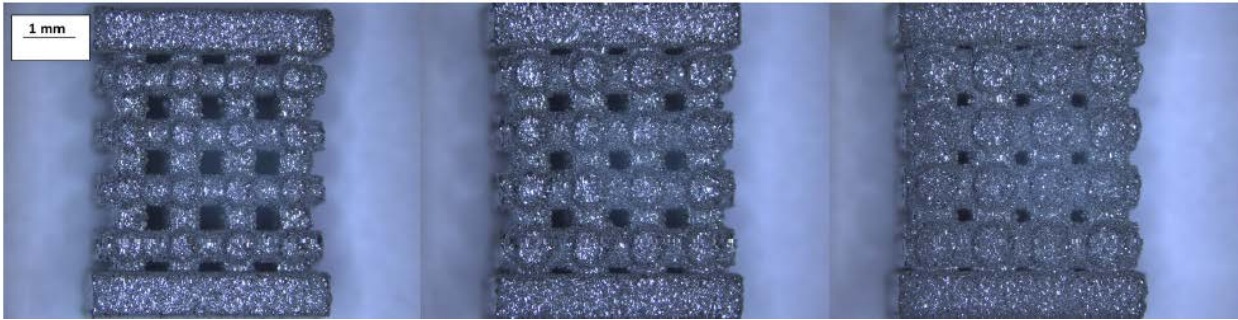


Fig.2.13 Porous NiTi structures developed by SLM [Taheri Andani et al 2016]

Dadbakshet al. (2014) have used SLM to manufacture dense nickel titanium (NiTi) parts. The reversible martensitic transformation of the NiTi parts is investigated with various SLM parameters. The parameters are in the same energy density range, composed of high laser parameters (HP: high laser power adjusted to high scanning speed) and low laser parameters (LP: low laser power adjusted to low scanning speed). The results are linked to the mechanical behavior and shape memory response achieved from compression and dilatometry tests. It is shown that the products may exhibit distinct transformation temperatures depending on the used SLM parameters. The atomized powders and the HP SLM parts with dominant pseudoelastic properties contain austenite at room temperature (due to their lower transformation temperatures), in contrast to the large thermal memory of the LP parts originating from martensitic phases (corresponding to higher transformation temperatures). The post-annealed samples undergo transformations in a comparable temperature range, implying no significant effect of SLM on composition of the originally used powder. The possible origin of the above findings is postulated and discussed.

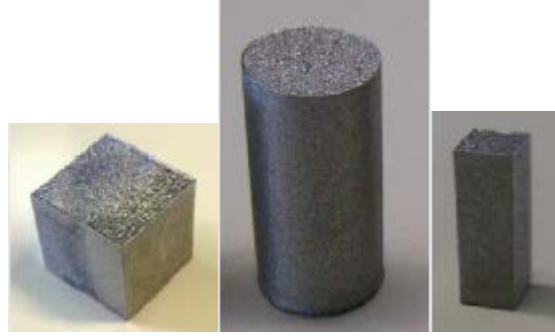


Fig.2.14 PorousNiTi structures developed by SLM for various mechanical properties studies

[Dadbakshet al. (2014)]

Clare et al. 2008 have used SLM process to the manufacture cantilever beams of NiTi shape memory alloys. The laser dwell time affected the phases present in built components. The dimension of build feature sizes and build quality is determined by the laser beam size, laser power, exposure time and powder properties. Although the X-ray diffraction pattern from the feed stock powder was consistent with the martensitic phase, the X-ray diffraction pattern from SLM processed material suggests that the process induces a mixture of the martensitic and rhombohedral Rphase in the alloy. The extent of the R-phase present in the SLM processed material varied with laser power although not monotonically suggesting that secondary parameters such as the cooling rate exerted some influence. The cooling rate was dependent on the size and shape of the SLM part. Generally the R-phase content tended to increase with laser power. NiTi cantilever beams produced by this method were two-way trained.

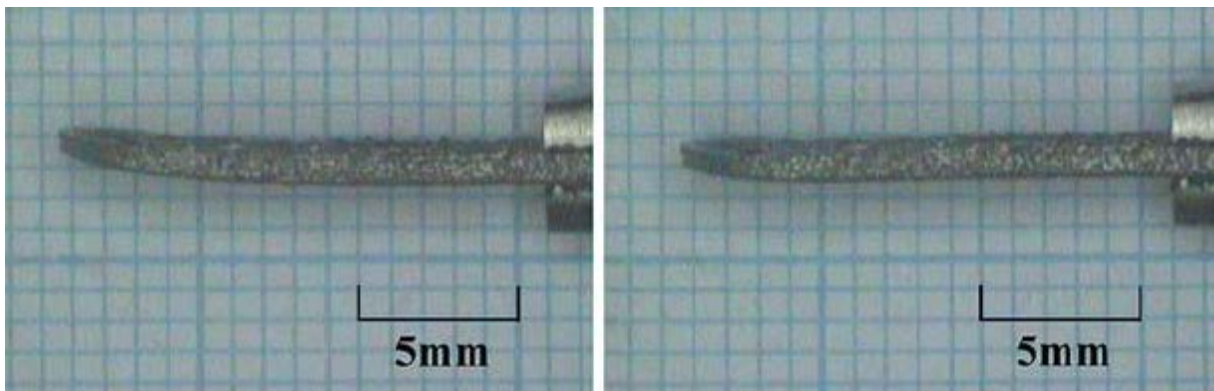


Fig.2.15NiTiCantilevers structures developed by SLM for actuation studies [Clare et al.2008]

2.8.3 Laser Engineered Net Shaping (LENS)

Gibson et al. 2010, have also reported about Laser Engineered Net Shaping (LENS) was developed by Sandia National Laboratories, and commercialized by Optomec Design Company. Optomec's machines originally used an Nd:YAG laser, but more recent machines utilize fiber laser. In a LENS machine, heat from a laser beam forms a small melt-pool. Simultaneously, metallic powder is injected into the molten pool, building up a feature. 3D CAD software is used to manipulate the marking head or the X/Y table holding the part to deposit the data matrix identification symbol (see Fig. 21). The head is moved up vertically as each layer is completed. Metal powders are delivered and distributed around the circumference of the head either by gravity or using a pressurized carrier gas. An inert gas is often used to shield the melt pool from atmospheric oxygen. The injected metallic material can be added to a structure made of different but compatible material

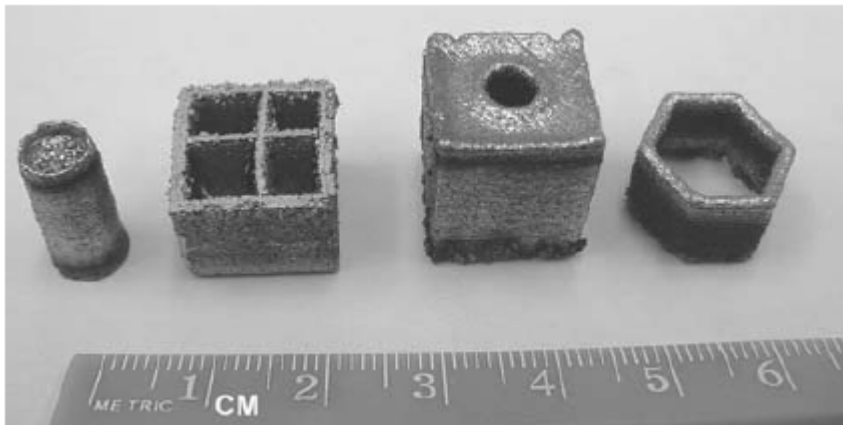


Fig 2.16 Bulk NiTi structures developed by LENS [Gibson et al. 2010]

Typically LENS is performed as a full melting process. It has ability to produce fully dense products containing strongly bonded particles. To fabricate a porous implant, the full melting of powders should be avoided. In that case, the particles are partially melted to create porosity. These surface melted particles join together due to the presence of liquid metal at the particle interfaces and bond well with the previous layers. However, there will always be some entrapped powder and loosely attached powder, especially at the surface of the implant. For the loose powders at the surface or in open pores, a simple chemical or mechanical treatment such as grit blasting can be used to remove them. For loose powders in the closed pores, powder removal is not possible.

The LENS system can produce parts in a wide variety of metals including titanium, nickel-base super alloys, stainless steels, and tool steels. In LENS, for instance, the nano/microstructure can be tailored (for example by locally modifying the laser power and scan rate) in a particular location by

controlling the size and cooling rate of the melt pool. The results from LENS consistently demonstrate better metallurgical and mechanical properties than other conventional processes due to an improved microstructure. For example, LENS-deposited Ti-6Al-4V has a yield strength, ultimate tensile strength, and elongation higher than those of conventionally processed and annealed samples. Any metallic, ceramic, or composite powder that is stable in a molten pool can be used for construction of parts using LENS. In general, metals with high reflectivities and thermal conductivities (such as gold and some alloys of aluminum and copper) are difficult to process. Most other metals are quite straightforward to process, provided that there is proper atmospheric preparation to avoid oxide formation. Generally, metallic materials that exhibit reasonably good weld ability are easy to process.

2.8.4 Electron beam melting (EBM)

Elahinia et al. (2012) reports Electron Beam Melting (EBM) a part is manufactured by melting metal powders layer by layer using an electron beam. The entire process takes place at temperatures around 1000 °C and in a high vacuum at 10^{-4} mbar in the chamber and 10^{-6} mbar in the electron beam producing gun. This makes EBM suitable for materials with a very high oxygen affinity. Arcam AB (Mölnadal, Sweden) developed the EBM approach. The Arcam A1 machine, shown in Fig. 26, is designated for additive manufacturing of orthopedic implants. It offers a beam power of 5–3000W with a scan speed of up to 8000 m/s. Currently, EBM process is capable of producing parts up to 200 X 200 X 200 mm with a dimensional accuracy of 0.4 mm. The device uses a thermionic emission gun that utilizes a Tungsten filament to make an electron beam, which selectively melts the metal powders with a thickness of 0.07–0.25 mm. A noticeable feature of both EBM and SLM layer manufacture is the significant reduction in waste material since the unused powder can be recycled. The lightly sintered powder surrounds the fabricated part and helps support its downward facing surfaces during the construction process. This powder is then broken down during the post-construction sifting process. This allows for most of the unmelted powder to be recovered and reused.

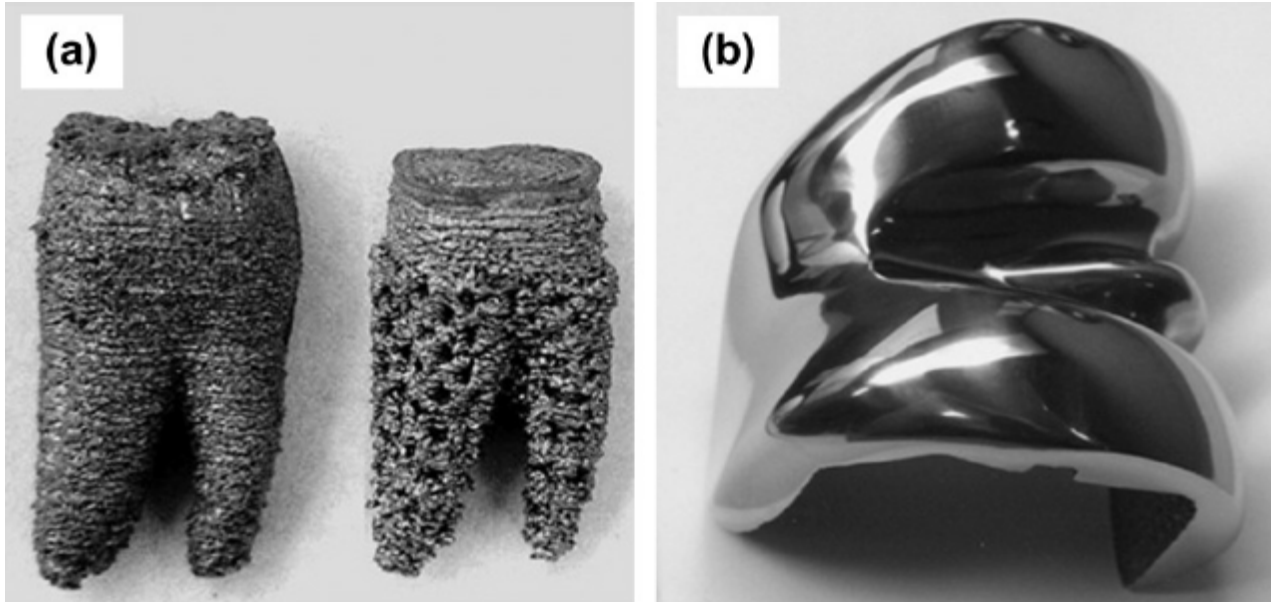


Fig 2.17Implants developed using EBM method (a) as manufactured (b) after post processing (Elahinia et al.2012)

2.9 Need for laser assisted surface post processing of additive manufactured samples

The additive manufactured NiTi structures in general have some problems in the physical and chemical nature as reported by researchers in the past. In case of SLS and DMLS manufactured NiTi the porosity is of a very big concern and the formation of secondary phases is totally uncontrollable in the entire process. Secondary phases like NiTi₂, Ni₃Ti and Ni₄Ti₃ are generally the main reason for embrittlement in the developed samples [Li et al. 2000]. Surface finish is very poor in samples developed by SLS and DMLS. The SLM process is renowned for imparting more stress in the samples. Similarly EBM method causes more porosity due to the negative charge generated during the process, also the surface finish is also very poor. As-cast microstructure and surface properties of NiTi products are not acceptable for medical applications and further processing is required. These post-processes can include hot working, cold working, machining, surface treatments, joining, and heat treatments. Hot working procedures include press forging, hot rolling, and rotary forging. Final product shapes such as wire, tubing, and sheet can be achieved via cold working. The average ductility of NiTi allows 30–50% of cold work. NiTi wires, the most widely available form of this

material, are produced via drawing. It is also possible to draw seamless tubing (mostly available in superelastic form). Rolled sheets and strips of NiTi have been used for photo chemically etched and stamped devices [Weinert et al. 2004 and Stockel et al. 2012].

As a solution to all the above mentioned problems, it is highly necessary to go for post processing techniques. Literature suggests shock peening and conventional annealing are the prominent solution for the existing problems. More efficiently giving considerations to the physical and chemical nature of the samples laser shock peening and laser annealing were to be carried out. Laser shock peening is efficiently expected to solve the problem of brittleness by preventing further dislocation in the lattice structure of the sample. Also laser annealing can trim out the excessive stress in the samples after laser shock peening is done.

2.10 Methodology of development of bulk NiTi using LAM

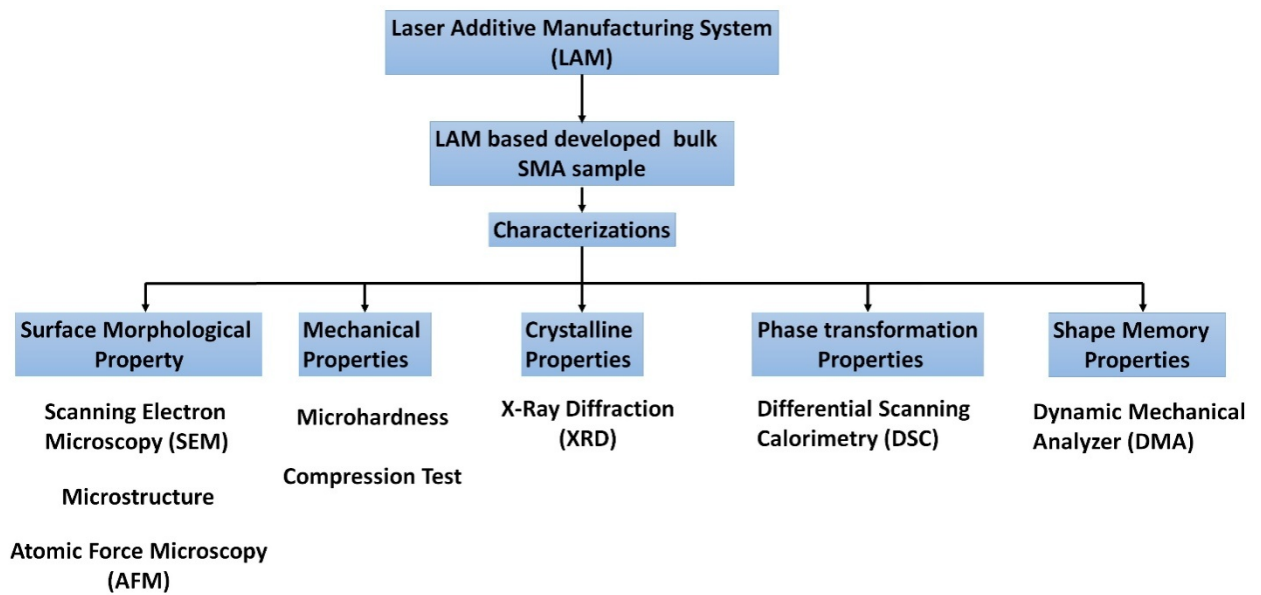
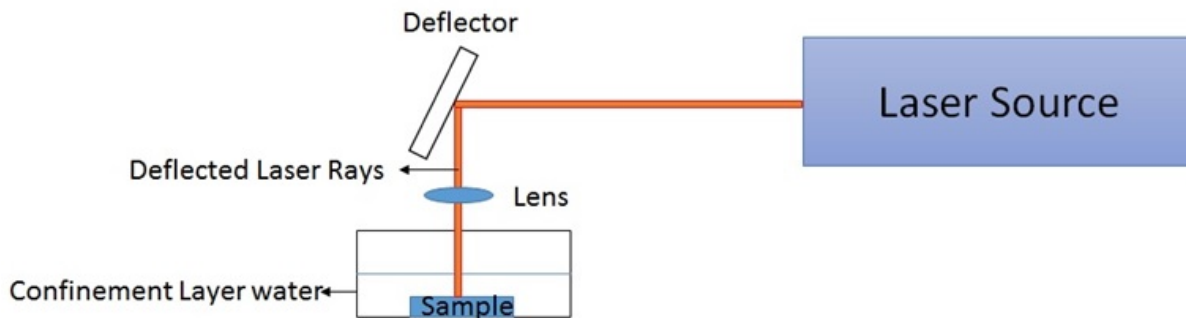


Fig 2.18 The work chart of the entire work process

Laser Shock Peening



Laser Annealing

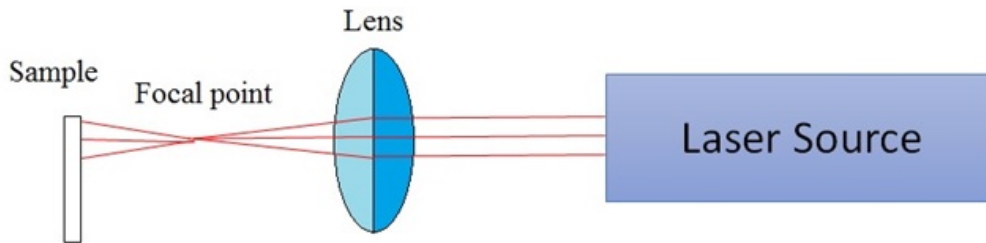


Fig 2.19 The schematic diagram of the laser assisted surface post processing techniques

2.11 Summary

Considering the inherent flexibility in process control, it is felt that some of the problems associated with fabrication, like - maintaining the physical and chemical nature of the formed product can be easily addressed if laser based additive manufacturing route is adopted. Moreover, laser based additive manufacturing can be deployed for the fabrication of complex geometries. To the best of our knowledge the deployment of laser based additive manufacturing for the fabrication of SMAs is not reported in the literature. Hence, the present study is focused on the feasibility of fabricating NiTi and TiNiCu SMA structures of various compositions are developed using laser based additive manufacturing. The study includes the surface morphology studies, microstructural analysis, micro-hardness measurement and shape memory effect analysis.

Chapter 3

Development of Bulk Shape Memory Alloy Structures using Laser Additive Manufacturing: Numerical and Experimental Investigation

3.1 Introduction

The laser additive manufacturing (LAM) process deals with complex physical phenomena that include heat transfer, material flow and distortion in developed structure after solidification. The theoretical basis of heat transfer, distortion and residual stress in LAM processes are illustrated in this chapter. A comprehensive numerical heat transfer model is developed based on finite element method using Gaussian distributed volumetric heat source. One of the most intricate phenomena in the LAM modeling is the model of 'heat source'. A well tested thermo-fluid model is utilized to investigate the influence of surface active elements in LAM process. A coupled thermo-mechanical analysis is performed to estimate the temperature and residual stress of the developed samples. One of the sensitive parts of LAM simulation is to identify the definite set of input parameters.

3.2 Numerical Modeling and Experimental Procedure

3.2.1 Conduction mode heat transfer analysis

The conduction mode heat transfer analysis is preferred due to reduced amount of computational time, ease of modeling and ease of coupling with stress analysis model. To approximate the influence of convective heat transfer within melt pool, the volumetric heat is used in conduction based heat transfer model. The thermal conductivity of the molten material is increased artificially in several folds to account the enhanced heat transfer due to high convective flow of liquid molten metal within the melt pool. In the present work, the conduction heat transfer, convective heat transfer and thermo mechanical models are developed in three-dimensional cartesian coordinate system. The integrated heat transfer and fluid flow process model is developed to investigate the influence of surface active elements in LAM process. In the present work conduction heat transfer based thermo-mechanical model is used to analyze the thermal and mechanical behavior of. It may be

pointed out that a pseudo-steady state heat transfer analysis is required for linear deposition using LAM processes, where the heat source moves at constant velocity with respect to the work-piece. The mathematical background and theoretical formulation to develop both the transient and steady-state heat transfer analysis using volumetric heat source is presented in the following sections. The corresponding formulation for the transport phenomena based convective heat transport analysis and thermo mechanical analysis are presented subsequently.

The governing equation and the boundary conditions that are followed for 3D transient conduction heat transfer analysis and their discretization using finite element method are presented in this chapter. The following assumptions are made for the development of a numerical heat transfer model:

Model Assumptions and Simplifications

- The heat source is considered as Gaussian distributed source due to TEM₀₀ laser beam source.
- Material properties like thermal conductivity and specific heat, constant density and emissivity are considered for simulation.
- The initial temperature of the work piece is assumed as room temperature.
- The convection and radiation heat losses from the surfaces of work piece are taken into account by considering lumped heat transfer coefficient .
- To avoid computation complexity for free surface modeling, the top surface of the developed sample is considered as flat.

For Y-axis the considered moving coordinate axis of laser beam at a velocity (v) the heat conduction equation can be stated in a cartesian coordinate system as:

$$k_m = \left(\frac{\partial^2 T}{\partial x^2} + \frac{\partial^2 T}{\partial y^2} + \frac{\partial^2 T}{\partial z^2} \right) + \dot{Q} = \rho C_p \left(\frac{\partial T}{\partial t} - V \frac{\partial T}{\partial y} \right) \quad (3.1)$$

where (x, y, z) is coordinate system attached to the heat source, k_m is the thermal conductivity of the material ($W m^{-1} K^{-1}$) and is given by the following equation to compensate the fluid flow of the molten material as

$$k_m = \begin{cases} k_0, & T < T_m \\ k_0 + k', & T \geq T_m \end{cases} \quad (3.2)$$

where k_o is the thermal conductivity of the material used; k' is the additional value by which the convection heat transfer capability is considered in the thermal model; T_m is the melting point of the material used. T is the temperature variable (K), \dot{Q} is the rate of heat generation per unit volume ($W m^{-3}$), ρ is the density of the material ($kg m^{-3}$), C_p is the specific heat capacity of the material ($J kg^{-1} K^{-1}$), t is time variable (s) and v is the deposition velocity ($m s^{-1}$). The first three terms on the left side of equation (3.1) refer to the conductive heat transfer in x , y and z direction, respectively. The term on the right side of equation (3.1) depicts the transient nature of the heat transfer process.

The temperature gradient normal to the sample interface is zero. The top surface of the plate is subjected to heat flux which is due to LAM heat source (laser beam) and rest of the surfaces are subjected to convection and radiation heat losses. The natural boundary condition can be represented mathematically as:

$$k_n \frac{\partial T}{\partial n} - q + h (T - T_o) + \sigma \varepsilon (T^4 - T_o^4) = 0 \quad (3.3)$$

where σ , ε , k_n , q , h , and T_o illustrates Stefan-Boltzmann constant, emissivity, thermal conductivity normal to the surface, imposed heat flux onto the surface, convection heat transfer coefficient, and ambient temperature respectively.

The initial condition for the transient heat transfer analysis of the LAM process is stated at time $t = 0$

$$T(x, y, z, 0) = T_o \quad (3.4)$$

where T_o is the initial temperature of the work piece.

The heat distribution in the formed sample is assumed to be distributed in a Gaussian manner. On the symmetric surface, the temperature gradient normal to the surface is zero. The rest of the work piece surfaces are subjected to convection and radiation heat losses. The dragging force exerted on the top surface of the samples developed by LAM is usually much smaller in comparison to the surface tension driven forces and hence, neglected. The distribution of heat flux on the top surface considering Gaussian distribution is mathematically expressed as

$$q_s = \frac{P \eta d}{\pi r^2} \exp \left(-\frac{d \cdot x^2}{r^2} - \frac{d \cdot y^2}{r^2} \right) \quad (3.5)$$

where P refers to the power of heat source, η is laser source efficiency, r is the laser spot radius of the heat source, and d is the power density distribution factor of heat source.

The conservation of momentum and mass are expressed mathematically as (J.N.Reddy et al. 2000)

$$\rho \left(\frac{\partial u}{\partial t} + U \cdot \nabla U \right) = \nabla \cdot \sigma_s + F \quad (3.6)$$

$$\nabla \cdot U = 0 \quad (3.7)$$

where U is the total stress tensor, ρ is the density of the material, F corresponds to the body force vector per unit volume and t is the time variable. The total stress tensor in equation (3.8) is expressed using Stoke's law as (J.N.Reddy et al. 2000)

$$\sigma_s = \mu [(\nabla U) + (\nabla U)^T] - P I \quad (3.8)$$

where P is the pressure, μ is the viscosity of the molten metal and I is the identity matrix. From equations (3.6) and (3.8) along with suitable modification due to laser beam movement, the momentum conservation equation is simplified as

$$P \left(\frac{\partial U}{\partial t} + U \cdot \nabla U \right) = -\nabla P + \mu \nabla \cdot [(\nabla U) + (\nabla U)^T] + \rho V \cdot (\nabla U) + F' + \rho g \beta (T - T_0) \quad (3.9)$$

where P depicts the pressure, μ represents the viscosity of the molten metal, g is acceleration due to gravity, β is the coefficient of thermal expansion, T_0 is the reference temperature and F' represents the electromagnetic body force. The last term of equation (3.9) indicates the buoyancy force (Boussinesq approximation) distributed over the volume.

Figure 3.1 schematically presents the boundary conditions applied for the heat transfer and fluid flow analysis. Since, the deformation of free surface is small and it requires extra computational cost, the free surface of melt pool is assumed as flat. During LAM deposition, the liquid metal is assumed as isotropic, Newtonian, viscous, and incompressible fluid. The flow of liquid metal within the melt pool is assumed as laminar. The solution boundaries for both mass and momentum equations are defined by the solid-liquid interface and the free surface of the melt pool. It may be noted that the solution domain for fluid flow analysis is separated from whole geometry which considerably saves computational time since fluid flow domain is generally less as compared to whole geometry for thermal analysis.

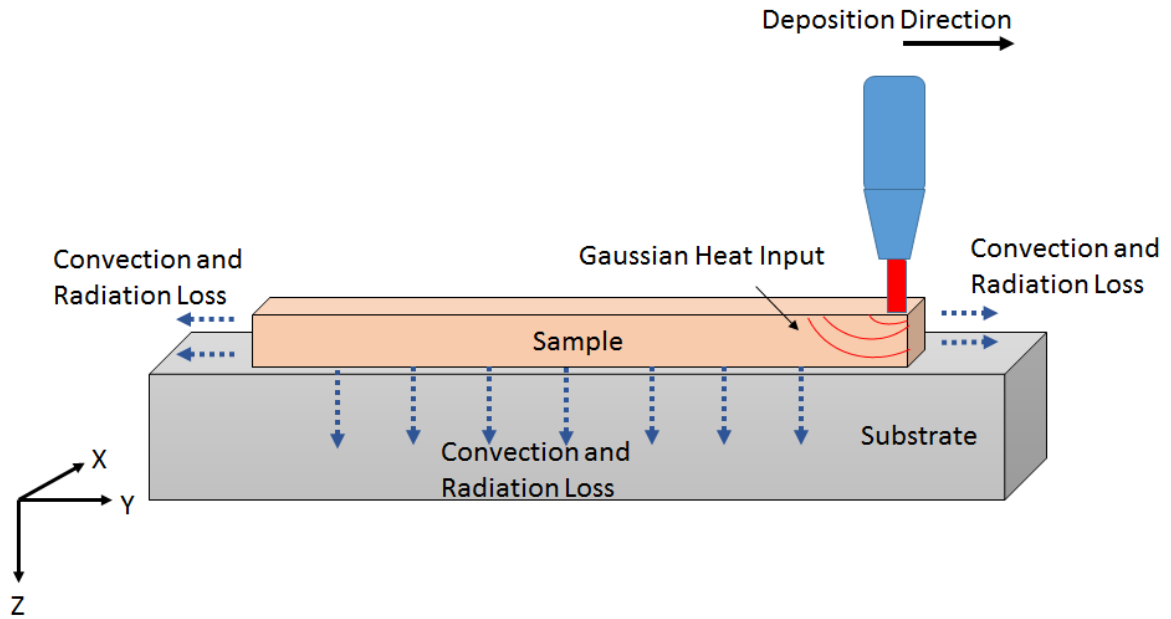


Fig. 3.1 Three dimensional solution geometry for the applied boundary conditions

3.2.2 Solution Strategy

Figure 3.8 outlines the overall solution procedure of the conduction heat transfer model of LAM process considering volumetric heat source. The procedure is implemented using commercially available FEM software ANSYS 14.0. Few of the significant steps as are described as follows

- o The CAD model of solution domain is created first and is discretized into a finite number of elements (SOLID70) in such a manner that a very fine mesh near to the heat source.
- o All the process parameters (laser power, track speed, etc.,) and model parameters (material properties, initial and boundary conditions along with volumetric heat source model, etc., are defined next.
- o In transient analysis, the total deposition time is divided into small timesteps, and then the heat transfer analysis is implemented for each time step explicitly.
- o The output of the model is finally obtained to compare with experimental values.

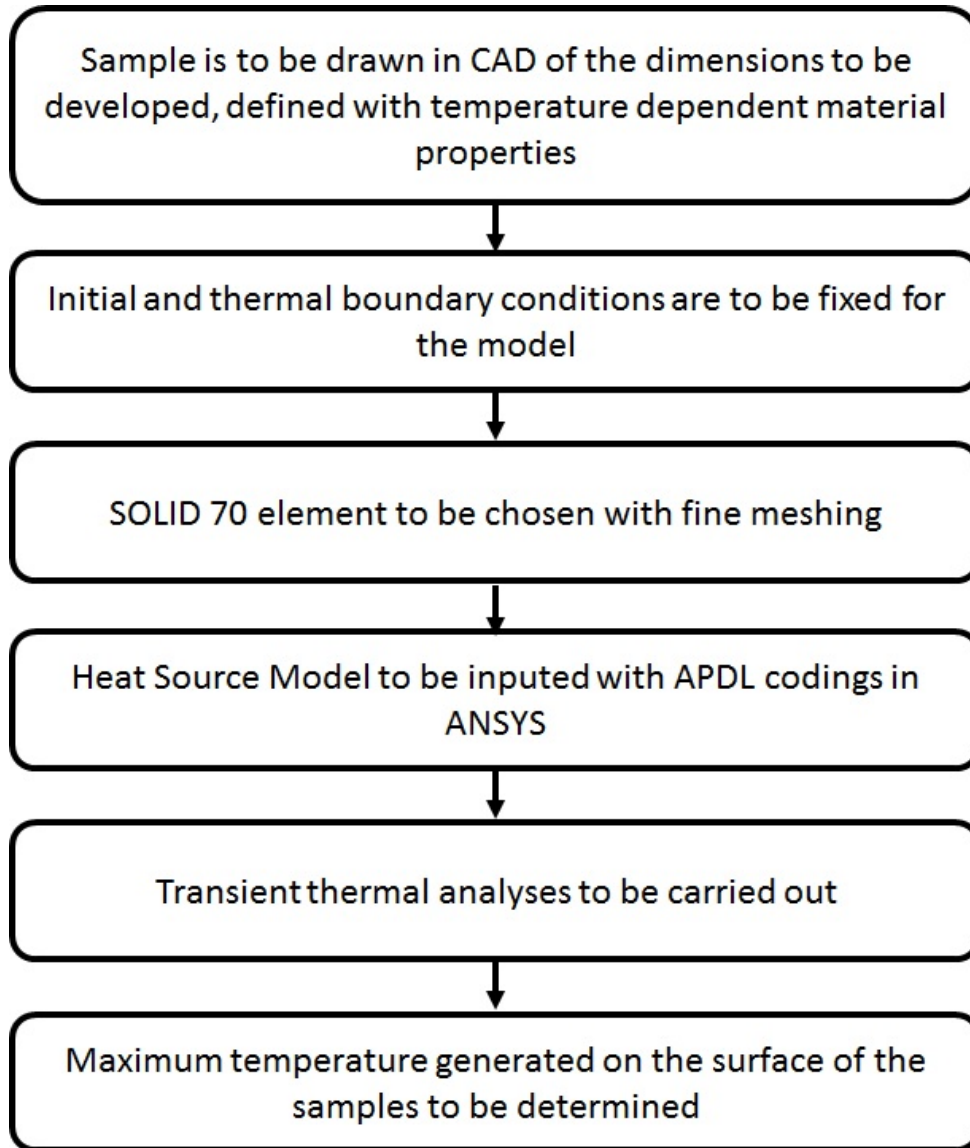


Fig. 3.2 Overall procedure followed in conduction mode heat transfer analysis

3.2.3 Thermo Mechanical Analysis

In the present work, a thermo-mechanical analysis is carried out to calculate the induced distortions and residual stresses in the samples during LAM. The present section describes the theoretical background of mechanical analysis. It includes the mechanical boundary conditions along with material model. The nodal temperature values are estimated from the conduction heat transfer analysis are integrated as a predefined field. The material was assumed to follow an elasto-plastic law with isotropic hardening behaviour (von Mises plasticity model). The detailed mathematical

background of this mechanical analysis is given in the subsequent sections. Figure 3.11 shows the elements used in thermal and mechanical analysis in the present work.

Governing Equations and Boundary Conditions

In the present work, the material response is assumed as thermo-elasto-plastic along with mechanical properties. The elasto-plastic analysis is generally performed by incremental mode of stress and strain. Rate independent plasticity is considered followed by von-Mises criterion, the associated flow rule and bilinear isotropic hardening behaviour. In Cartesian coordinate system, the strain-displacement relation can be written as (Bang et al. 2003, Gupta 2003).

$$\epsilon_x = \frac{\partial u}{\partial x}; \epsilon_y = \frac{\partial v}{\partial y}; \epsilon_z = \frac{\partial w}{\partial z} \quad (3.10)$$

$$\gamma_{xy} = \frac{\partial u}{\partial y} + \frac{\partial v}{\partial x}; \gamma_{yz} = \frac{\partial v}{\partial z} + \frac{\partial w}{\partial y}; \gamma_{zx} = \frac{\partial w}{\partial x} + \frac{\partial u}{\partial z} \quad (3.11)$$

where u, v and w represents displacements in x, y, z directions respectively; ϵ_x , ϵ_y and ϵ_z refer to the normal strains in x, y and z directions respectively; and γ_{xy} , γ_{yz} and γ_{zx} represents shear strains in xy, yz and zx planes respectively. Assuming the isotropic material, the thermal strain remains same in three directions and the increment of the total strain is sum of the incremental plastic strain, incremental thermal strain and incremental elastic strain, represented as

$$\{d\epsilon\} = \{d\epsilon^t\} + \{d\epsilon^p\} + \{d\epsilon^e\} \quad (3.12)$$

Following Prandtl-Reuss flow rule and Von-Mise's yield criteria, the incremental stress can be represented as

$$\{d\sigma\} = [D_{ep}]\{d\epsilon\} - [D^e]\{\alpha\}(\Delta T) \quad (3.13)$$

$$\text{Where } [D_{ep}] = \left([D^e] - [D^e] \left\{ \frac{\partial f}{\partial \sigma} \right\} \left\{ \frac{\partial f}{\partial \sigma} \right\}^T [D^e] \frac{1}{3G + E_T} \right) \quad (3.14)$$

where $[D_e]$ depict the elasticity matrix which consists of mechanical properties like Young's modulus E and Poisson's ratio μ . G is shear modulus and E_T is local slope between stress and plastic strain of specified material. The last term of equation (3.13) represents the thermal strain which may vary depending upon the temperature distribution. $[D_{ep}]$ is some sort of elasto-plastic matrix where the first term in equation (3.14) is due to elastic response of material or recovery of elastic response when the material is in plastic zone. The second term of the equation (3.14) is due to plastic flow of material which is zero when the material is elastic zone only. The evolution of the yield surface are governed by the hardening rule. In present case, Von-Mises yield surface is considered and bilinear isotropic hardening rule is assumed that may be appropriate for the selected material.

Material Model

In the present work, the numerical analysis is performed by considering the material properties. An elastic-plastic material model is used in the mechanical analysis module. The isotropic hardening rule is selected to consider the plasticity using the ANSYS APDL code. The elasticity is defined by Young's modulus and Poisson's ratio, and the plasticity is defined by yield stress and the elastic-plastic tangent modulus. Moreover, the Von Mises stress is used to predict yielding of the samples.

Computational Aspects

In the present work, the thermal and mechanical properties are used for thermo mechanical analysis. Thermal properties such as specific heat and thermal conductivity are considered. The latent heat of fusion is considered for the simulation through an artificial increase or decrease in the specific heat of the material (Trivedi et al. 2007). The governing equation along with boundary conditions for heat conduction, the linear system of equations for an element is written as

$$[C(T)]\{T\} + [K(T)]\{T\} + [V(T)]\{T\} = [Q(T)] \quad 3.15$$

where $[K]$ refers to the conductivity matrix, $[C]$ is the capacitance or specific heat matrix, $\{T\}$ is nodal temperatures vector, $[V]$ is the velocity matrix due to moving beam and $\{Q\}$ is the nodal heat flow vector.

The material behavior is considered as elasto-plastic in nature. In the present work, the influence of micro-structural changes, creep and transformation induced plasticity are not considered. The plasticity is assumed as rate independent and is modeled by assuming bilinear isotropic hardening behaviour along with associated flow rule. The von-Mises yield criteria is followed as

$$\sigma_{av} = \sqrt{1/2 [(\sigma_1 - \sigma_2)^2 + (\sigma_2 - \sigma_3)^2 + (\sigma_3 - \sigma_1)^2]} \quad 3.16$$

where, $\sigma_1, \sigma_2, \sigma_3$ are principal stresses and σ_{av} is the average one dimensional stress.

3.2.4 Solution Strategy for Thermal Analysis

Figure 3.13 shows the step by step procedure (flow chart) followed in a thermo mechanical analysis based on finite element method using FE software ANSYS 14.0. Few important steps are described below.

- In mechanical analysis, the similar FE model used in thermal analysis is considered other than type of element. SOLID 45 element is used which is defined by eight nodes having three degrees of freedom at each node, translation in the nodal X, Y, and Z directions.
- Next, the material properties are defined.
- The reading of nodal temperatures is considered for overall thermal analysis at different time steps.
- Structural analysis performed and estimate the distortion and residual stresses at different sections of the samples developed by LAM.

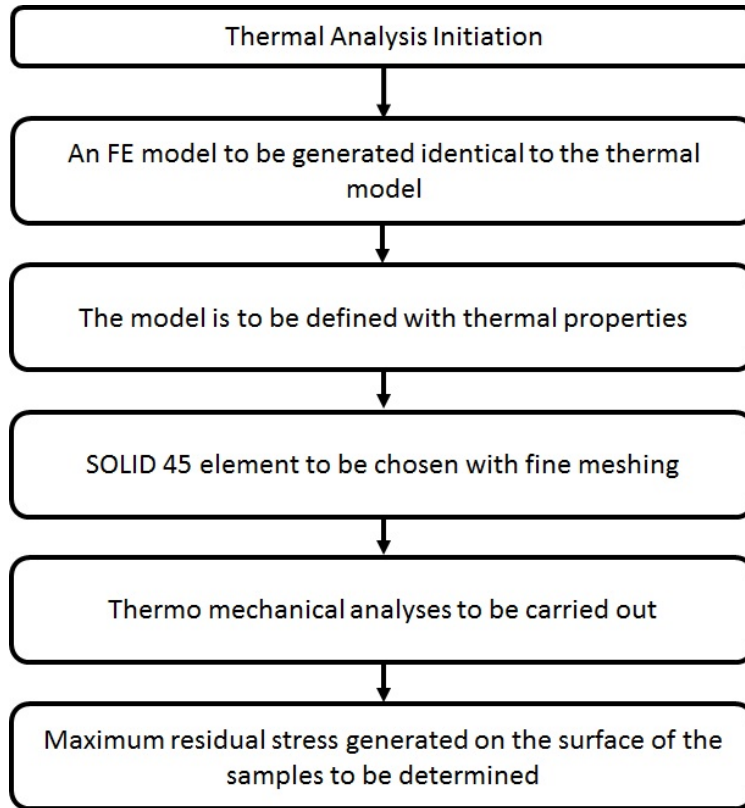


Fig. 3.3 Overall procedure followed in thermo-mechanical analyses

The material properties used for the above describes simulations for the materials to be deposited are as shown in Table 3.1 (Otsuka, 1998).

Table 3.1 Properties of the samples

Properties	Unit	NiTi	TiNiCu
Density	kg/m ³	6450	6450
Specific Heat	J/kg°C	320.451	460
Melting Point	°C	1300	1300
Poisson Ratio	-	0.3	0.3
Emissivity	-	0.4	0.4
Thermal	W/m°C	0.086	0.13

Conductivity			
Young's Modulus	GPa	41	78
Thermal Expansion Coefficient	-	6.6×10^{-6}	15.4×10^{-6}

3.3 Validation of numerical modeling

In order to finalize the nature of depositing the samples a numerical study was carried out based on the material properties in order to reduce the trial of experiments to obtain the best samples. A thermal model was generated to study the amount of temperature and residual stress distribution during the development of the process. Hence the simulation was carried out to build the samples vertically and horizontally to compare the temperature and stress distribution during the sample development. Initially the entire sample was finely meshed and converted into small elements. The heat input was based on the laser input energy. The convective boundary conditions were chosen as discussed earlier. The maximum temperature and residual stress distribution was calculated for both the way of depositions to determine the best way to deposit the final sample.

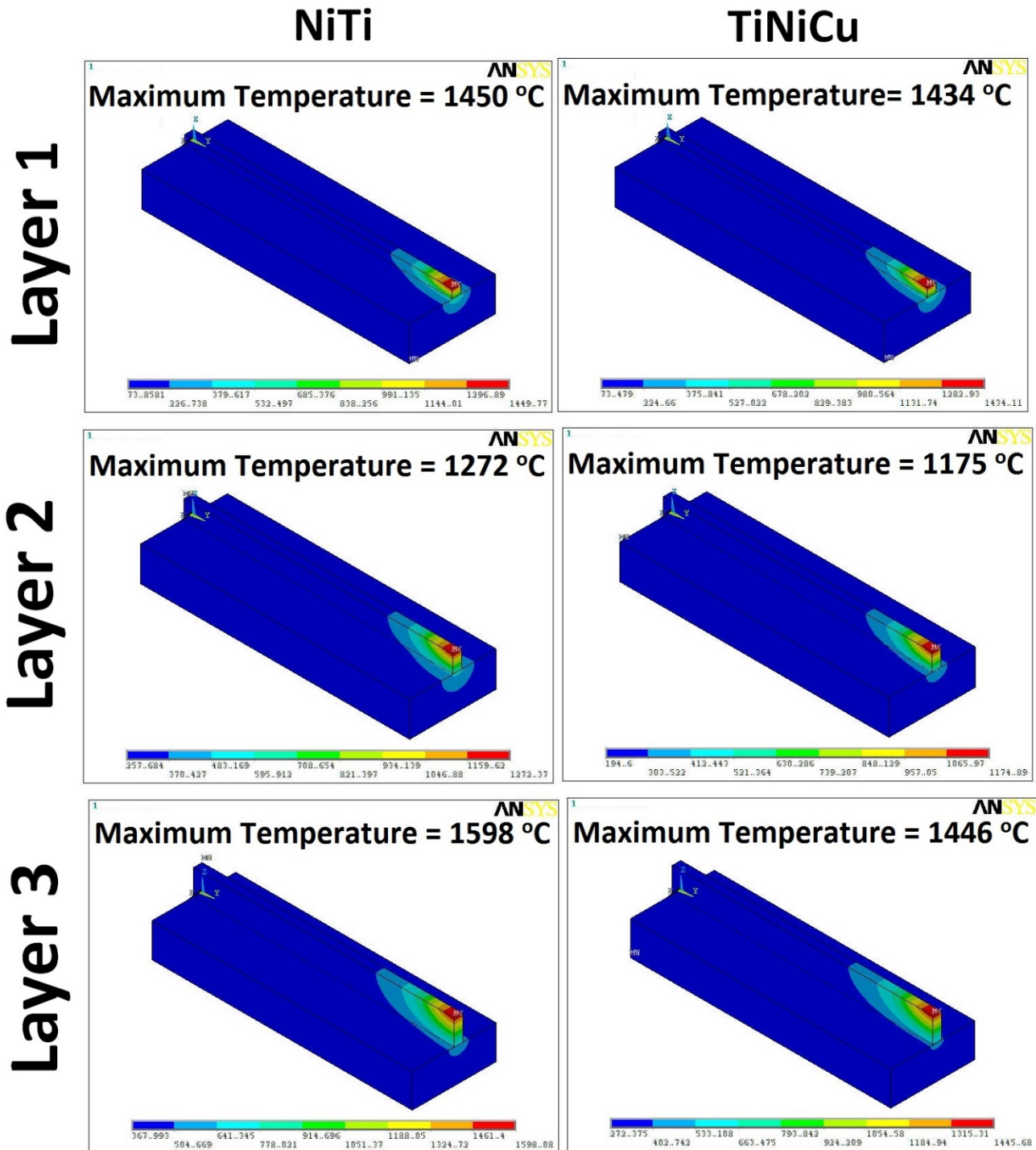


Fig. 3.4 Simulation results for maximum temperatures generated for the samples in all three layers of vertical depositions

Figure 3.4 shows the complete set of simulations developed for vertically developed samples. The simulated models have been fed with the material properties of NiTi in austenite, martensite phase,

and TiNiCu. From the figure it is vividly seen that the temperature distribution in the samples gradually decrease as the number of layers mounting on each other have a small decrease. This may be attributed to the temperature distributed into the beneath layer of the samples. Similarly Fig. 3.5 shows the overall residual stress generated on the three layers using the above mentioned properties and equations in the previous sections. The residual stress distribution seems to be widely distributed on the developed samples similar to the temperature distribution. This nature of distribution have high chances of influencing the SME properties of the developed samples.

To validate the simulated results a real time experiment was conducted using a thermo couple to measure the temperature distributed on the surface of the samples immediately after deposition, and XRD method was deployed to measure the residual stress distribution.

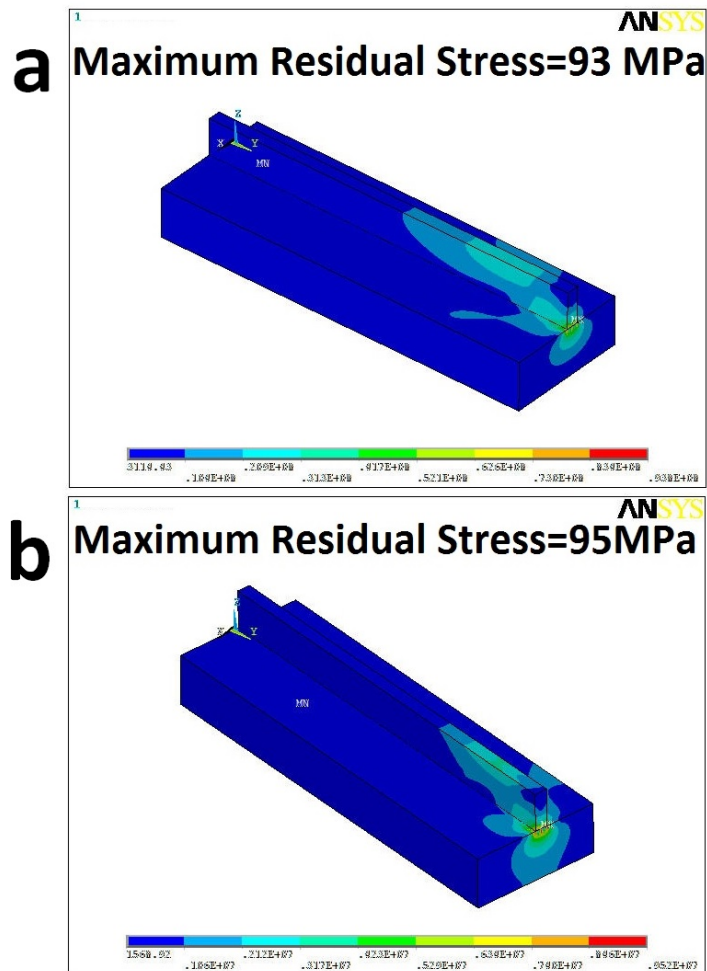


Fig. 3.5 Simulation results for maximum residual stress generated for (a) NiTi and (b) TiNiCu samples in all three layers of vertical depositions

The measured values are plotted as graph as shown in the Fig. 3.6 and Fig. 3.9. From the graph it is vivid that the simulated values are a bit higher than the real time experimentation values. The decrease in the real time experimentation values are attributed to the radiation losses. Similar impact is observed in the residual stress distribution as well. Also the prime factor of wetting on the surface of the samples due to high temperature are to be considered when the samples are developed vertically. This brings change in dimension of the deposited samples. Hence in a scope to overcome this issue, simulations were again simulated to check the effect of horizontal deposition of samples. Same governing equations, boundary conditions and material properties were used. In horizontal deposition the samples had uniform temperature and stress distribution.

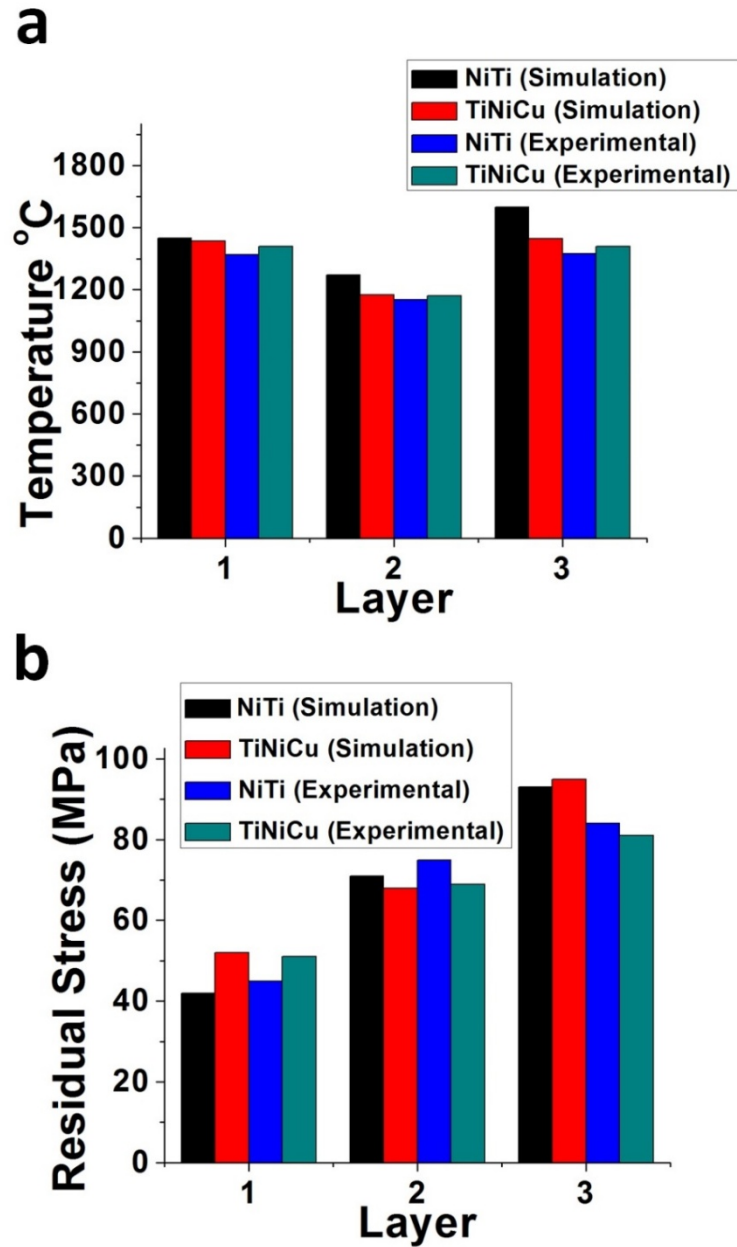


Fig. 3.6 Comparison graph of simulated temperature and residual stress values with experimental data

The temperature distribution within the formed samples in parallel deposition is high and evenly gets distributed throughout the surface of deposition including the substrate. In case of vertical developed samples the temperature distribution takes place within the samples only. Hence the formation of high residual stress generation within the sample is possible. The irregular temperature distribution within the samples leads to the formation of many secondary phases which spoils the SME in the

sample. Also gradual wetting process happens in vertical development that deforms the dimension of the developed samples due to the effect of temperature and residual stress accumulation.

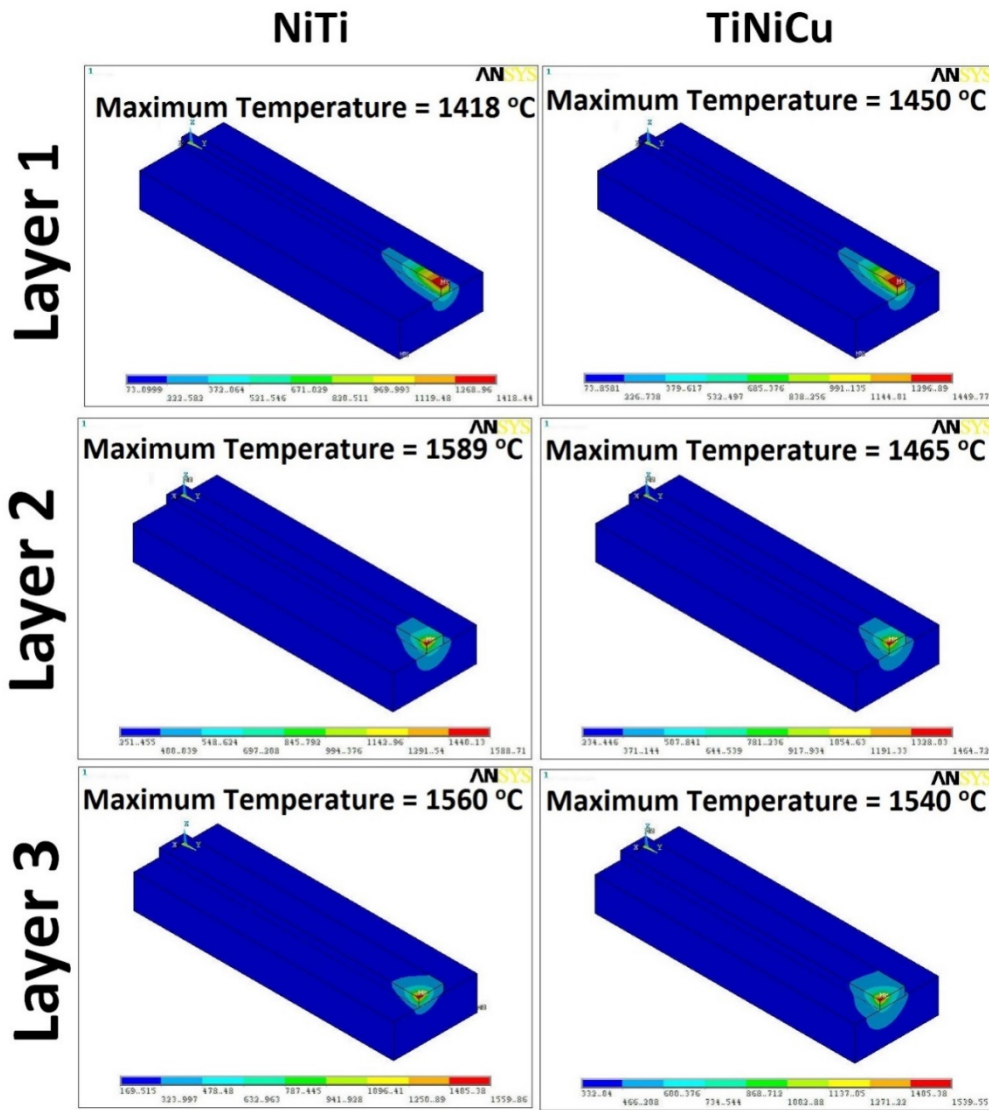


Fig. 3.7 Simulation results for maximum temperatures generated for the samples in all three layers of horizontal depositions

In case of parallel deposition the above mentioned problems don't occur as the temperature and stress gets uniformly distributed and chances of accumulation in the samples is comparatively less. Hence the risk of secondary phase formation can also be overcome. The simulation results and experimental results show the parallel developed samples generate high temperature on the surface and that simultaneously reflects in reducing the residual stress level in the samples.

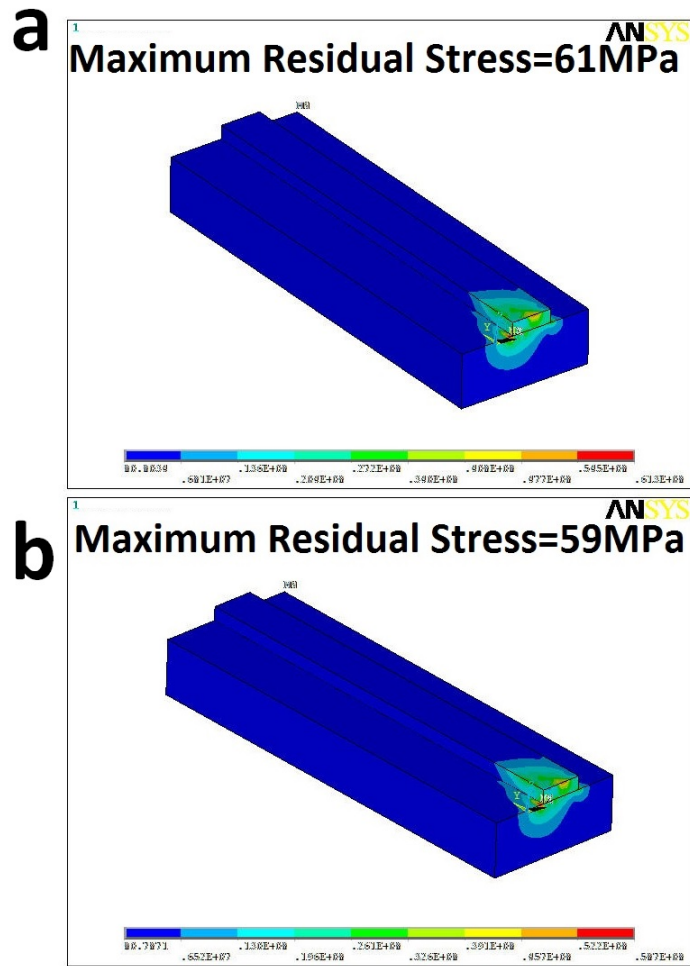


Fig. 3.8 Simulation results for maximum residual stress generated for (a) NiTi and (b) TiNiCu samples in all three layers of horizontal depositions

In vertically built samples show high residual stress values in Fig. 3.5. This may be attributed to the non-uniform temperature flow within the samples. While comparing the graphs in Fig. 3.9 and Fig. 3.6 we find the parallel developed sample have no much variation in numerical and experimental results while comparing to the vertically developed samples. Hence considering the factors mentioned above the samples developed for the current research were made sure to be developed parallelly for both NiTi and TiNiCu samples.

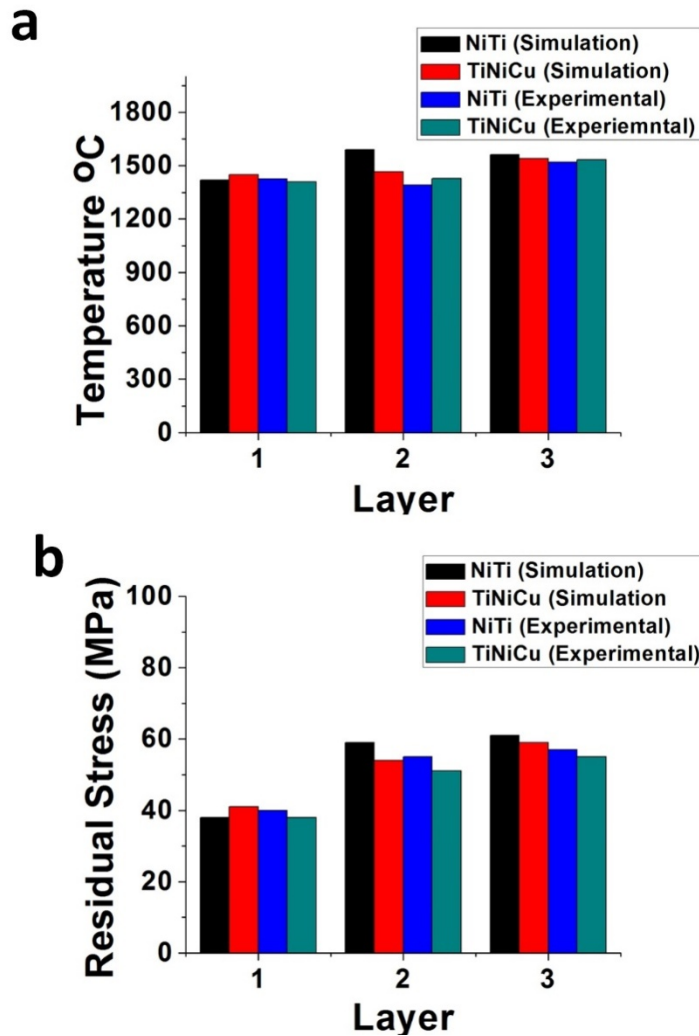


Fig. 3.9 Comparison graph of simulated (a) temperature and (b) residual stress values with experimental data

3.4 Experimental Procedure

In the present study, a 2 kW fibre laser based additive manufacturing (LAM) system (Bhargava et al. 2003) was deployed for laser rapid manufacturing of various deposits involving Ni and Ti. It consisted of a 2 kW fibre laser, a 5 axis workstation in a glove box, a computerized numerical controller, a coaxial nozzle and a twin powder feeder. The laser beam was transferred to 5-axis CNC laser workstation through optical fibre and Quartz lens (focal length = 200 mm) to focus the beam at the laser workstation. A defocused beam of diameter about 2 mm was delivered at the substrate surface. Pure Ti plate of size 100 mm x 100 mm x 10 mm thick was used as substrate. Titanium

substrate is chosen for our experiment expecting an easy debonding, as the thermal expansion coefficients are different for NiTi and Ti (Paul et al, 2012). Prior to the experiments, the substrates were sand-blasted to roughen the machined surface so as to increase the laser absorption. Argon gas was used as shielding and carrier gas and it prevented the oxidation. It was reported that near 1:1 ratio of Ni and Ti compositions have very good shape memory effect (Wirth et al. 2005). Therefore, three different Ni and Ti compositions with powders in three different weight percentages (Ni-45%Ti-55%, Ni-50%Ti-50%, Ni-55%Ti-45%), and six different compositions of TiNiCu Ti-50 % Ni- (50- X) % Cu- (X=5,10,15,20,25,30) are selected for the deposition process. The powders were pre-mixed using ball milling for 48 hours to ensure uniform mixing of powders. In the following sections, the different ratios of Nickel and Titanium, i.e., Ni-45%Ti-55%, Ni-50%Ti-50%, Ni-55%Ti-45% are designated as NiTi55, NiTi50, NiTi45, respectively and Ti-50 % Ni - (50- X) % Cu- (X=5,10,15,20,25,30) are designated as TiNiCu5, TiNiCu10, TiNiCu15, TiNiCu20, TiNiCu25 and TiNiCu30 respectively. The final parameters chosen for the experiment are summarized in Table 3.2.

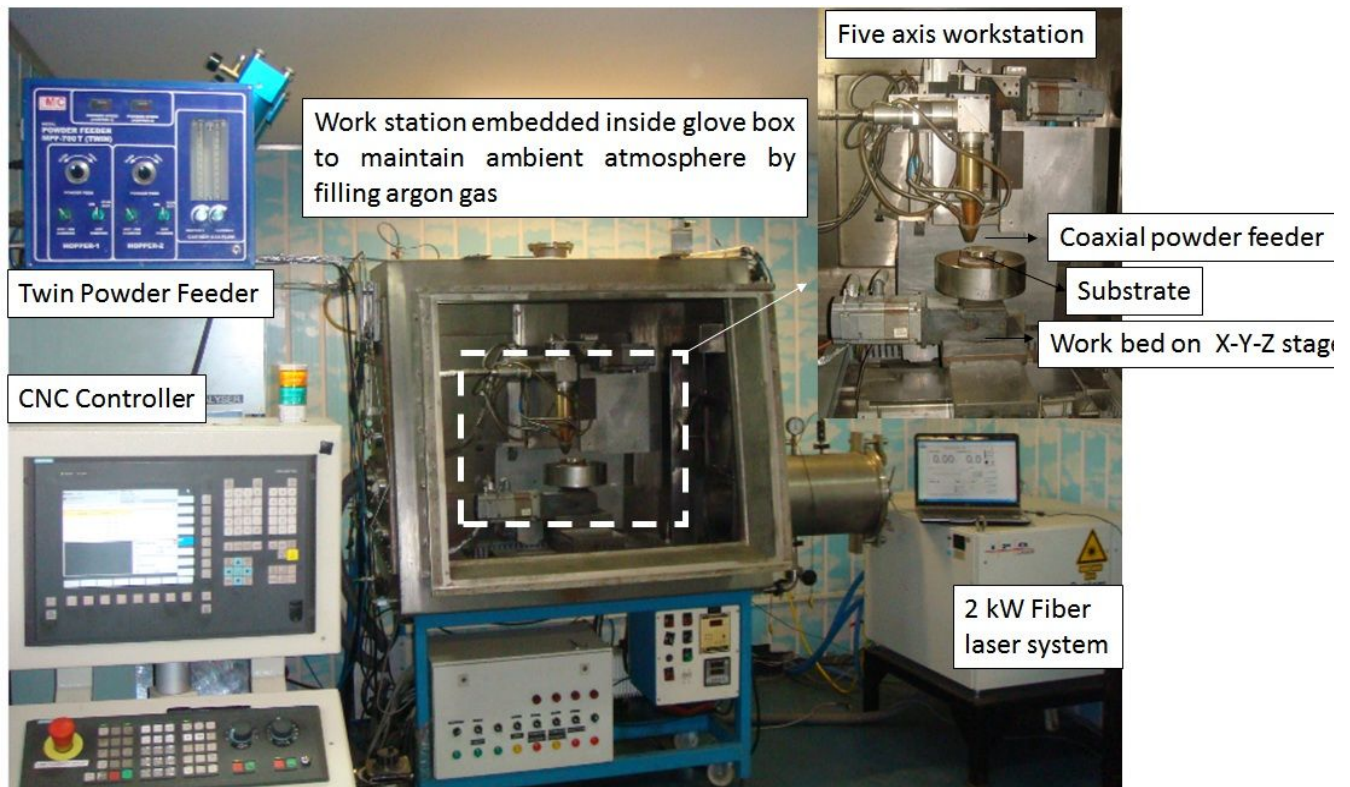


Fig.3.10 Schematic diagram of 2 kW Fibre laser based Additive Manufacturing System fabricating NiTi and TiNiCu samples

In order to optimize the process, a number of tracks were deposited at different process parameters. After deposition, the deposited tracks were examined visually. The uniform tracks without visual defects (like porosity and carbon deposition adjacent to the tracks) were selected and their cross sections were examined. The process parameters, leading to deposits with track aspect ratio (i.e. ratio between width and height) more than five, were chosen. These parameters have the range: laser power 1.0 – 1.5 kW; scan speed 0.2 – 0.5 m/min; and powder feed rate 5 – 8 g/min with Argon gas flow rate at 10 l/min.

Table 3.2 Parameters used for experiments

Parameter	Unit	Values
Laser Power	kW	1-1.5
Laser Diameter	mm	2
Scanning Speed	m/min	0.2 - 0.5
Powder Feed rate	g/min	5 - 8
Argon Gas gushing rate	l/min	10

The powders (Make: MEC, India) (Ni, Ti and Cu) were procured for LAM. Ni and Cu powders had powder particle size in the range of 45-106 μm , whereas it was in the range of 75 – 150 μm for Ti. These range of powder particles were selected as our preliminary experiments showed that the powder particle size smaller to this range tends to flew away in uncontrolled way due to higher surface area to weight ratio. The powder particles having size bigger than the above specified range result in semi-fused particles due to smaller absorbed laser energy per unit volume. The powder particles chosen were spherical in shape as shown in Fig 3.11, as the spherical powder particles are yields good density with no porosity in comparison of irregular and flake shaped powder particles (reported by Hirschhorn 1969).

3.5 Effects of processing parameters

LAM process is governed by parameters like laser power (P_L), beam diameter at the substrate (D_L), material feed per flow rate (m_p) and the scan speed (V_S) as explained by Paul et al. (2012). As reported in our earlier work Shiva et al. (2015), the shape and deposition pattern of the tracks are governed by the two combined parameters laser energy per unit area and powder feed per unit area. The laser energy per unit area (E_L) and powder feed per unit area (F) are defined as follows

$$\text{Laser energy per unit area, } E_L = \frac{60 \times P_L}{V_S \times D_L} \text{ kJ/mm}^2 \quad (3.17)$$

$$\text{Power feed per unit area, } F = \frac{m_p}{V_s \times D_L} \text{ g/mm}^2 \quad (3.18)$$

The shapes of track geometry were investigated in terms of aspect ratio as a function of deposition per unit area. Experimental observations confirmed the formation of non-uniform discontinuous tracks, under certain onset values of powder feed per unit area. It is just because some minimum amount of laser energy is needed to assist two physical processes during the laser-material interaction. These processes are the melting of fed powder and the wetting of thin layer of substrate/previously deposited material. For the LAM of brick shaped structures, only process parameters yielding uniform and regular shape were screened-in. In the current investigation, it was observed that some minimum laser energy per unit area is required for uniform and regular deposition of tracks. The similar observation was also reported by Paul et al. (2012). The laser energy per unit area was found to be 0.1 kJ/mm² for all the values of powder fed under investigation. As the powder feed increases the laser energy also need to be increased as more laser energy is required to melt the powder fed at higher quantity fed per unit area. It was also observed that various outputs in cross sections of track geometry were obtained with different combinations of laser energy and powders fed at per unit area. Fig. 3.12 shows the cross track geometry is presented in the form of aspect ratio, which represents the ratio of width and height of the track.

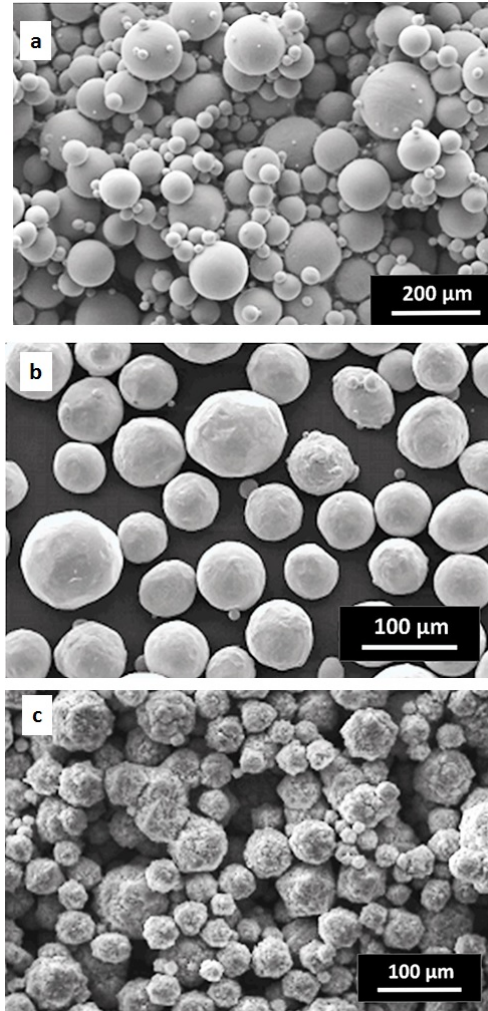


Fig.3.11 Powder Morphology of (a) Ti, (b) Cu and (c) Ni powders

It was also observed from the graph that the aspect ratio above five were capable of depositing defect-free tracks, as it avoided inter-run porosities generated at the base of two tracks due to the lack of fusion zone. Hence, the process parameters yielding aspect ratio more than five were chosen for the experiments. In order to investigate the efficiency of laser energy per unit area and powder feed per unit area in developing a single wall by a number of layers an experimental study was carried out. Fig 3.13(a) and Fig 3.13(b) present the deposition per unit length and catchment efficiency respectively in various layers for different laser energy per unit area and powder feed per unit area.

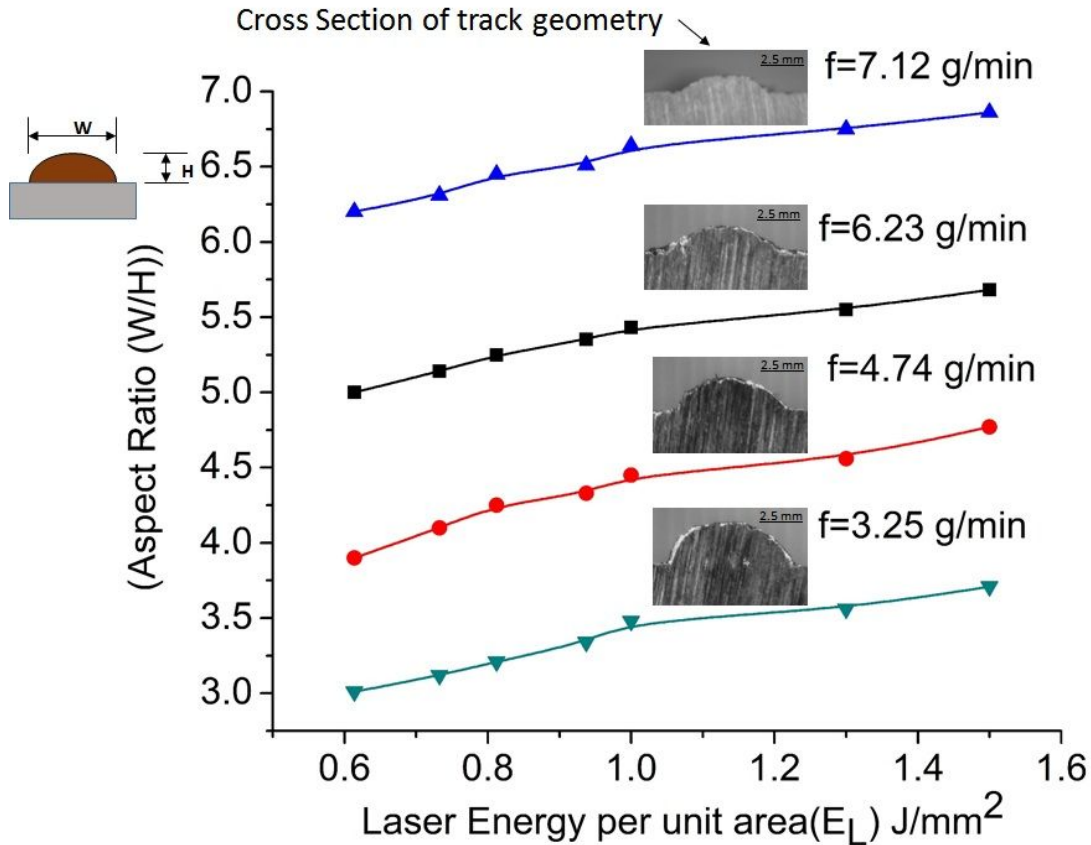


Fig.3.12 Effect of Laser Energy per unit area (E_L) on Aspect Ratio (W/H)

The catchment efficiency was measured by taking the ratio of powder fed to the material deposited during LAM. These experiments were carried out for NiTi50 and TiNiCu5 alloy. The similar trend was observed for binary and ternary compositions. It may be seen in Fig. 3.13(a) that the deposition rate gradually increases from layer to layer and subsequently gets saturated. The initial increment in the deposition rate is due to preheating effect causing higher powder catchment efficiency. The effect of powder catchment efficiency with respect to the number of layers is presented in Fig. 3.13 (b). It may be seen in figure that the catchment efficiency initially increases and it falls after certain number of layers. After the fall, it tends to saturate except for the parameters 5 kJ/m & 15.4 g/m. The increase in the catchment efficiency is due to preheating effect generated during the LAM of previous layers. After certain number of layers, other factors (like- ricocheting of powder particles, local fluid dynamics caused by the local shape of the tracks etc.) start dominating. The change in catching efficiency from layer to layer can also be attributed to the shift of the working plane for each layer since the layer thickness increases/decreases. Assuming that the vertical offset for each layer was

constant, this means that the process can leave its initial deposition plane regarding powder gas stream focus and laser beam focus moving in your case towards a higher efficiency and then drops down again. After certain layers for the selected process window, the process gets stabilizing itself.

A number of NiTi and TiNiCu structures were fabricated at optimum parameters. Fig. 3.14 presents a typical ring structure and TiNiCu brick structure fabricated using laser based additive manufacturing. Preparation of samples for examining the micro-hardness was as follows. Samples were cut into small pieces and cold mounted. The upper surfaces of the cold mounted samples were polished continuously in order to get a smooth surface finish. Once after the polishing is done they were placed on the machine to test their corresponding micro-hardness of all the four specimens including the commercially bought NiTi structure, which has been used as reference.

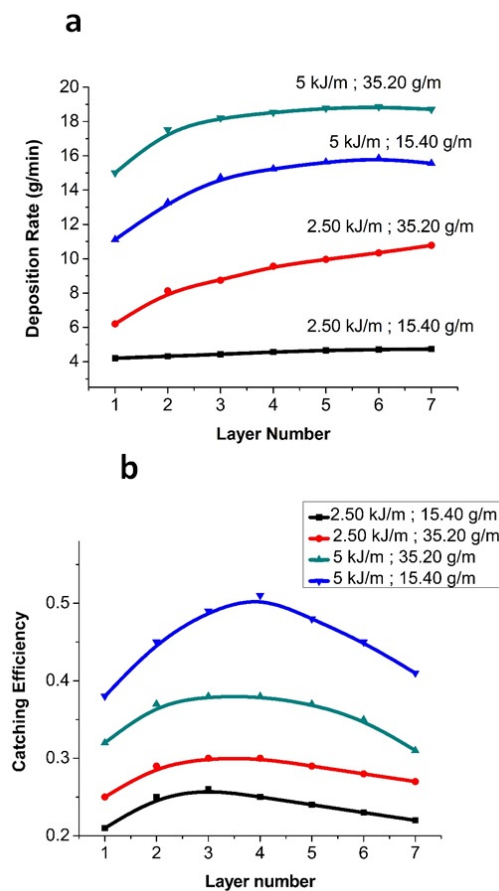


Fig 3.13 (a) Deposition rate and (b) catchment efficiency as function of no. of layers

For each samples ten load test readings were taken. The fabricated samples were further prepared using standard metallography techniques for various examinations. The surface morphological

analyses of the samples was carried out using scanning electron microscopy (Make: Zeiss, Model: Supra55) attached with Energy dispersive spectrograph (Make: Oxford Instruments, Model: X-mas) and the micro structure analyses by optical microscope (Make: Leica DFC295). Surface roughness measurements were done by optical profilometer (Make: Veeco NT9080). The structural analysis was carried out by X-ray diffractor (Make: Rigaku Model: Smart lab Automated Multipurpose). The shape memory effect was characterized using Differential Scanning Calorimetry (Make: TA Instruments, Model DSC 2910). The micro-hardness of the samples was measured by (Make: UHL, Model: VMH 002).

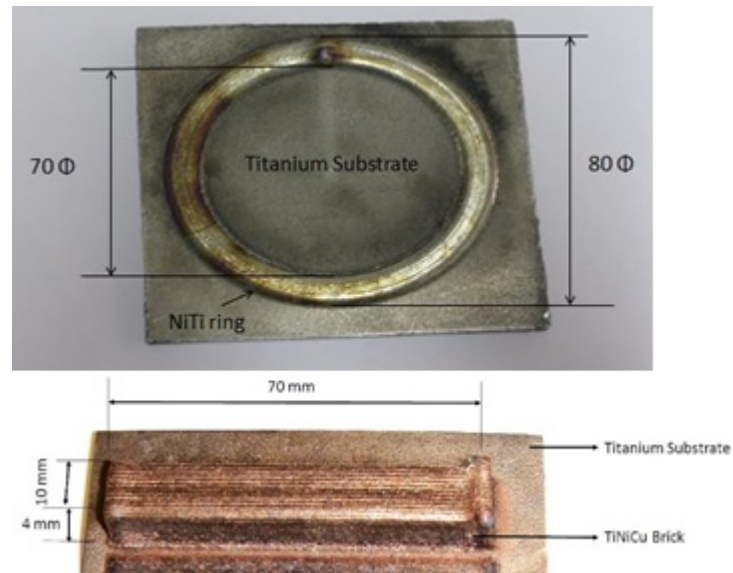


Fig.3.14 Laser additive manufactured NiTi ring and TiNiCu brick structures

3.6 Evaluation of Surface Morphology

3.6.1 Scanning Electron Microscopy Examination

Fig. 3.15(a) presents the surface topography of NiTi55 sample. It may be observed that there is non-uniform distribution of peaks and valleys at various locations. A number of pores and improper inter-bonding of NiTi particles are also observed. It may be attributed to the presence of Carbon and Oxygen leading to decrease of impurities of Fe and Cr found in NiTi alloys, also as discussed earlier the bigger grain size of this sample will have an impact. Energy Dispersive Spectroscopy (EDS) analysis indicated that this combination has Ni-30.46% and Ti-69.54%. However in the case of NiTi50 alloy, the bonding between the grains of the structure seems to be strong and there is no much free space found between the grains. As shown in Fig. 3.15(b) this closely packed nature is due to the

perfect amount of Ni and Ti which has given a perfect required lattice structure of standard NiTi. The EDS shows Ni-51.69% and Ti-48.31% in for this combination. Reason behind the increase in Ni weight percentage is due to the formation of NiTi₂ phases in the product and this combination can exhibit good shape memory effect as mentioned by (Shu-Young et al. 2012). Fig. 3.15(c) presents the surface topography of NiTi45. It shows fine structures similar to that are formed in dry wax. This is due to the effect of variation in the composition of Ni and Ti. The EDS shows the presence of Ni-38.01% and Ti-61.99%. In the above mentioned both samples, we found that there is an increase in the weight percentage of Ti, because of the diffusion of the substrate metal into the SMA alloy.

Table 3.3 EDS results of TiNiCu samples developed by LAM

Samples	Ti (Wt %)	Ni (Wt %)	Cu (Wt %)
TiNiCu5	54.35	39.87	5.78
TiNiCu10	58.27	38.65	3.08
TiNiCu15	60.89	32.07	7.05
TiNiCu20	57.56	28.24	14.2
TiNiCu25	63.41	15.37	21.23
TiNiCu30	55.28	23.98	20.74

In Fig. 3.15 (d) the surface morphology of TiNiCu5 is shown and it is smooth surface with a few random peaks of buried particles and no pores. Comparatively in Fig 3.15 (e) it is seen that the surface of the samples are free from porosity holes but the peaks of buried particles were seen yet. Fig. 3.15(f) shows the surface of TiNiCu15, which has a irregular surface with many particles scattered with bonding. Some pores are also visible in image. For TiNiCu20 samples the surface roughness is expected to be very high in the as manufactured state as the amount of particle impingements on the surface is very high as shown in Fig. 3.15 (g). In Fig. 3.15(h) the results of TiNiCu25 sampleis presented. It is a relatively smooth surface (as compared other TiNiCu samples) with some scattered particles. Among all the samples made TiNiCu30 has the best surface finish as shown in Fig. 3.15 (i). Not much scattered particles or pores are visible. From the above it can be concluded that 25% and 30 % Cu in the NiTi matrix contributes to the formation of uniform regular surface. The reason for the improvement might be impact of the equal amount of Ni and Cu atoms bonded with. The EDS results too showed some closeness in weight % between Ni and Cu in the Ti dominated alloy. The results of energy dispersive spectroscopy (EDS) are presented in Table 3.3. For

the compositions an increase in Ti composition as compared to fed composition was observed. It may be attributed to the better catchment of Ti particles from the substrate during LAM. Generally, a little amount of atoms with low atomic number (like – O, N, C, H etc.) are present on the surface of the sample, which is highly inevitable. As observed by Mohammad H Elahinia et al. (2012), these are built-in residues in the powder from the time of their manufacture/mixing. The effect of these elements with low atomic number is not seen much in TiNiCu5 and TiNiCu25, as the percentage of materials obtained are closer to the targeted compositions. But in TiNiCu15, the impact is more as we see large difference in the composition from Table 3.3.

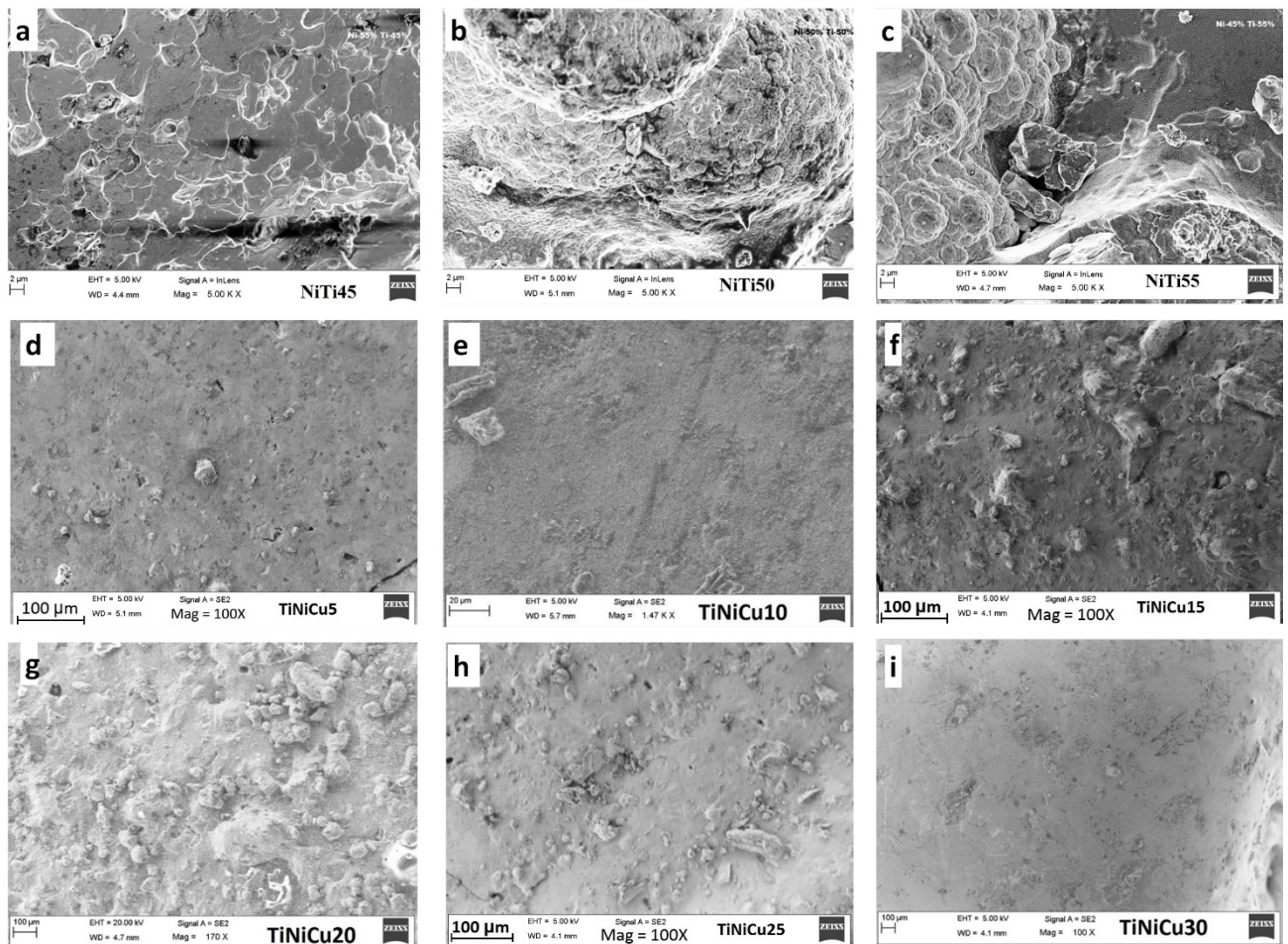


Fig. 3.15 SEM images of as manufactured (a) NiTi45 (b) NiTi50 (c) NiTi55 (d) TiNiCu5 (e) TiNiCu10 (f) TiNiCu15 (g) TiNicu20 (h) TiNiCu25 (i) TiNiCu30 samples developed by LAM

3.6.2 Microstructure Analysis

The samples were as usual prepared using the standard metallographic technique to cold mount, followed by a micro polishing and using an etchant the surface is mildly etched to have a better view of the grain size and structure under an optical microscope. The etchant used for the samples are HF-HNO₃-CH₃COOH, in the ratio 2:5:5. Fig. 3.16 (a) exhibits the micro structure of NiTi55. The grains are closely packed and are uniformly distributed. The grain size seems to be very large while comparing to the remaining two samples. This can be confirmed by the grain size data produced by using scherrer formula calculation in section where XRD analysis is done. The grain structures are irregular in shape throughout the sample. However from Fig. 3.16 (b) it is very clear that the combination of NiTi50 samples have much closely packed grain structures than the remaining two samples. They are also very fine in nature and the uniformity in grain size is observed to be more homogeneous throughout the surface, which is not found in the remaining two combinations. From Fig. 3.16(c) the microstructure of NiTi45 seems to be unlike NiTi55, as they have lots of uniform round shaped grain structures in them. The grain size is comparatively lesser than NiTi55 and a little greater than NiTi50. They are closely packed and presence of any pores or cracks are not found.

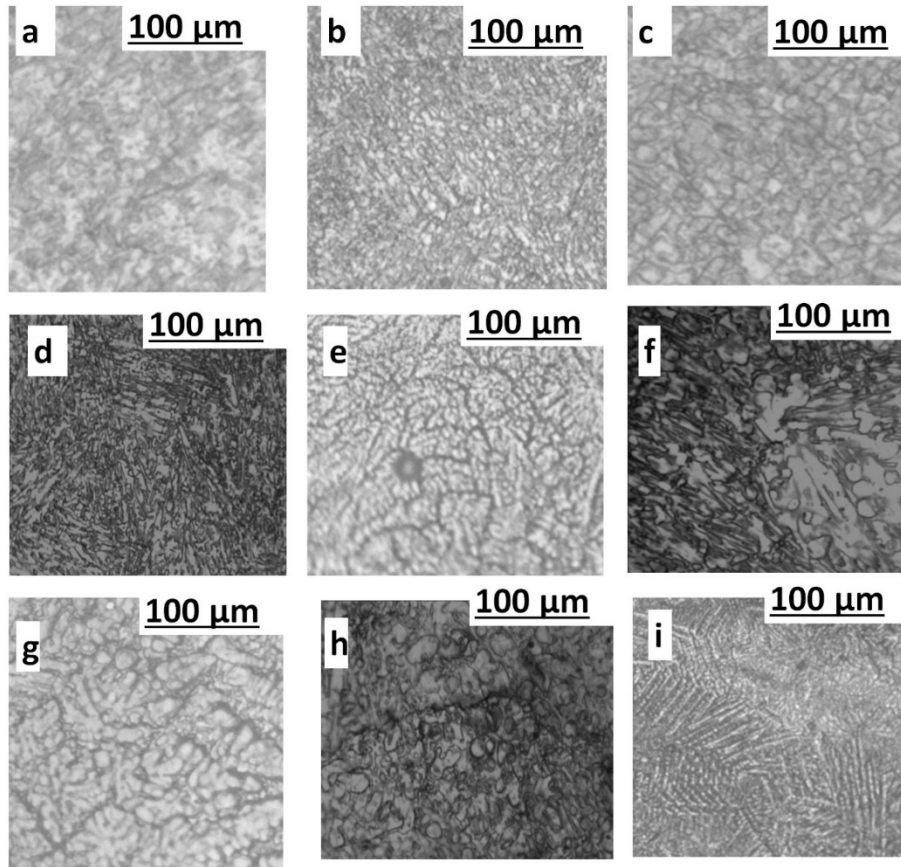


Fig. 3.16 Microstructure images of as manufactured (a) NiTi45 (b) NiTi50 (c) NiTi55 (d) TiNiCu5 (e) TiNiCu10 (f) TiNiCu15 (g) TiNiCu20 (h) TiNiCu25 (i) TiNiCu30 samples developed by LAM

Fig. 3.16 also presents the microstructure of TiNiCu samples developed by LAM in different compositions. The images provided are the cross section of the sample. The etchant used was HF, HNO₃ and H₂O in the ratio 1:12:4, respectively. The samples were cold mounted and polished. Subsequently, they were dipped into the etchant for a time of 3 seconds and rinsed in running water, as reported by Takashi Mineta et al. (2011). Subsequently, images were obtained using an optical microscope. It can be seen that the structure of the grains is different for all the samples with different compositions. Fig. 3.16(d) shows the microstructure for TiNiCu5. It is uniform and has a dendritic microstructure which is due to higher cooling rate. Fig. 3.16 (e) shows the microstructure of TiNiCu10 which gradually gets bigger than TiNiCu5. Mild deposition of precipitates like structures are visible which might be due to improper powder melting. Fig. 3.16(f) shows TiNiCu15 has very large while comparing to the previous two samples. The presence of pores at isolated locations are observed for this sample. This may be due to improper melting of powder particles during LAM. Fig.

3.16 (g) shows the microstructure of TiNiCu20 where the microstructure is getting collectively large in grain size. Clusters of dendrites are visible on the surface as well. Fig. 3.16 (h) shows the microstructure of TiNiCu25. In this composition the grains are in equiaxed structure due to dynamic recrystallization. Dynamic recrystallization happens when the crystal nucleus formed are unable to grow in time due to slow deformation velocity as reported by Jiang Shuyong et al. (2012). The above observations may be attributed to the composition of the powders as all other parameters during LAM are same. Fig. 3.16 (i) shows the microstructure of TiNiCu30, where needle like structures which indicate the presence of martensite phase are scattered heterogeneously on the surface of the samples. Not much precipitate formation or pores are visible. Hence the TiNiCu30 composition is expected to have a good lattice formation. Things can be made clearer once after verifying the results with X-ray diffraction test in the following section.

3.6.3 Atomic Force Microscopy Examination

Fig 3.17 shows the AFM images of all the samples. NiTi55, NiTi50 and NiTi45, were represented at a magnification of $1\mu\text{m} \times 1\mu\text{m}$. The magnifications of TiNiCu5, TiNiCu10 and TiNiCu25 were $1\mu\text{m} \times 1\mu\text{m}$ and TiNiCu15 and TiNiCu30 was $500\text{ nm} \times 500\text{ nm}$. The detected grain size and surface roughness are as mentioned in Table 3.2. The surface of binary alloys are filled with fine grains and not much of hillocks were found. In case of ternary alloy TiNiCu5 and TiNiCu10 had no hillocks, but smooth surface with large grains and blunt rounded tips. But for TiNiCu15 and TiNiCu20 have large hillocks with pointed structures. The grain size distribution was also not homogeneous. TiNiCu25 and TiNiCu30 were different from each other. TiNiCu25 had very fine grain structures as seen in Fig 3.17 (h) and TiNiCu30 had very large grain size. The observations with the image correlated with the grain size of the samples. To confirm the value of grain size calculated the values in Table can be compared with the values obtained from X-Ray Diffraction analysis in the forth coming session.

Table 3.4 AFM measurements for the samples in as manufactured state

Sample	Grain Size (nm)	Surface Roughness (nm)
NiTi55	55.45	5.76
NiTi50	31.73	3.16
NiTi45	40.39	5.63
TiNiCu5	18.41	3.22
TiNiCu10	20.12	3.97
TiNiCu15	38.26	6.21
TiNiCu20	33.57	5.83
TiNiCu25	21.61	4.76
TiNiCu30	25.51	4.25

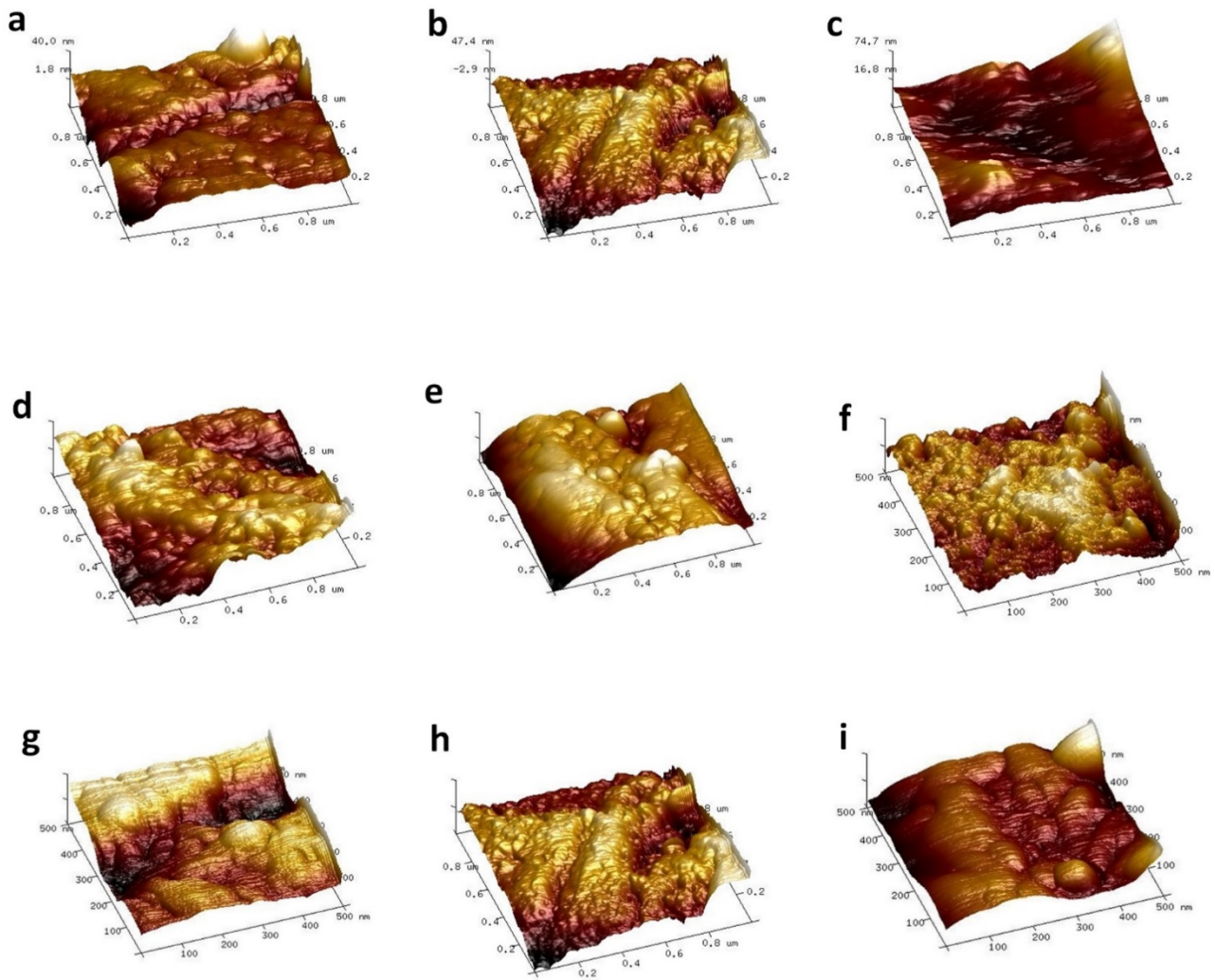


Fig. 3.17 AFM images of as manufactured (a) NiTi45 (b) NiTi50 (c) NiTi55 (d) TiNiCu5 (e) TiNiCu10 (f) TiNiCu15 (g) TiNiCu20 (h) TiNiCu25 (i) TiNiCu30 samples developed by LAM

3.7 Mechanical Properties Evaluation

3.7.1 Micro-hardness Measurement

The samples made by LAM were cut transverse to the direction of laying and prepared using standard metallographic techniques and micro-hardness measurement was carried out at an incremental distance of 25 μm at a load of 500 g. Fig. 3.18 presents the results of micro-hardness measurements. The average value of micro-hardness is found to be 380, 440 and 525 VHN for NiTi50, NiTi45 and NiTi55, respectively. The value of average micro-hardness is more for Ti-rich samples. This may be due to the formation of hard phases caused by the increased Ti content. Since the micro-hardness is more for NiTi55 samples, the ductility is likely to be less. A similar observation is seen for the Ni rich sample NiTi45. As per the indications earlier in the EDS results this because of the Ti weight percentage's impact in the alloys. From the results obtained in the graph shown in Fig. 6, it's very clear the Ni and Ti rich samples have high micro-hardness. For the other Ni and Ti rich alloys the hardness lies between 400-700 VHN. This makes them rigid and brittle in nature. The standard deviation bar indicates not much of variation for the NiTi50 alloy which is a primary indication about the homogeneity in the deposition process.

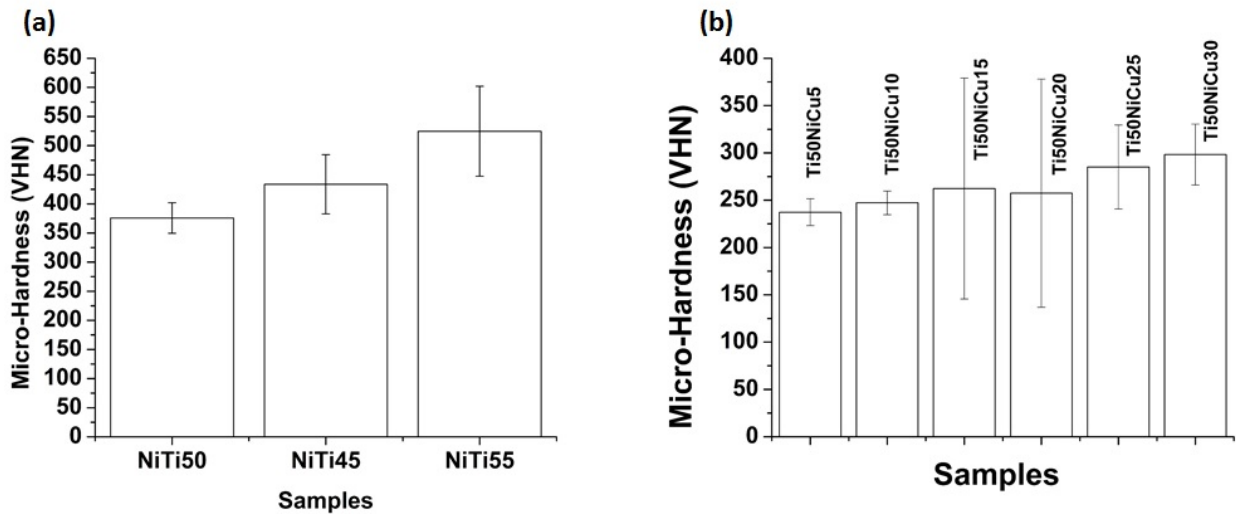


Fig. 3.18 Micro-hardness values of (a) NiTi and (b) TiNiCu samples developed by LAM

When it comes to the ternary alloy formation the formed TiNiCu samples fabricated by LAM technique the average value of micro-hardness is found to be 237, 242, 262, 278, 285 and 297 VHN for TiNiCu5, TiNiCu10, TiNiCu15, TiNiCu20, TiNiCu25 and TiNiCu30, respectively. The micro-

hardness in LAM samples increase with the increase of Cu concentration in the TiNiCu alloy.. The higher concentration Cu causes the formation of precipitate like $Ti(NiCu)_2$ in TiNiCu system and is the major attribute to the increment of micro-hardness due to internal stress. In case of a binary NiTi alloy the micro-hardness values should have been excessively high. But in the ternary alloy with the inclusion of Cu the problem could be overcome as the variation in hardness is not much and it is uniform across the sample. This is a clear indication that a good alloy formation has been obtained during LAM.

3.7.2 Compression Test

The mechanical properties of the samples a compression test was carried out. The sample size was as per ASTM 9 with dimensions of 5 mm diameter and 10 mm length. At least three samples were tested for each set of parameters to ensure the reproducibility. From the Fig. 3.19, results its very vivid that the elasticity of the materials formed are low due to their brittle nature, and all the three samples are comparatively uniform. As the percentage of Ti increases in the alloy, the elasticity gradually decreases. The amount of ultimate strength increases as the percentage of Ni increases in the alloy. Thus from the above discussion it is clear that the NiTi50 has better elasticity among the three binary alloys. The ultimate strength of NiTi55, NiTi50 and NiTi45 are 296, 315, 320 MPa respectively. The calculated elastic moduli are 20,21,21 for NiTi55, NiTi50 and NiTi45 respectively.

For the ternary alloy, it is very clear that the elasticity of all the samples formed have reasonably improved comparing to that of the binary NiTi alloy developed using LAM. There is a uniform and smooth growth of the curve initially for all the samples. Gradually for TiNiCu5 and TiNiCu10 after reaching the yield strength level the formation of plateau is seen which is quite similar to the results reported by Dongyun Zhang et al. (2015). The presence of martensite orientation drives the transition curve to plateau formation in the sample. Impact of residual stress generated by slip prevents the stress strain curve from attaining the maximum ultimate strength limit to be attained. The remaining four samples had very low ultimate strength, due to the defects of precipitates formed in them. As a result the impact of dislocations during the compression test is also expected to be high for TiNiCu15, TiNiCu20, TiNiCu25 and TiNiCu30. Lehto et al. (2014) reports Hall-Petch relation reveals the role of grain size playing a major role in the yield strength. Among the six samples formed from the images of optical microscope and AFM images it is very clear TiNiCu5 and

TiNiCu10 had the finest grain size. Also the lowest percentage of Cu had the maximum elasticity and ultimate strength, and as the Cu weight % increases the elasticity and ultimate strength had a dip gradually. For samples exceeding 10% of Cu, had higher micro-hardness values and their corresponding engineering stress strain curve too confirms the brittle nature. Earlier reports confirm a dip in the mechanical properties, as the weight % of Cu exceeds 12.5 in a ternary TiNiCu alloy. The ultimate strength of TiNiCu5, TiNiCu10, TiNiCu15, TiNiCu20, TiNiCu25 and TiNiCu30 are 451, 430, 412, 402, 397, 386 respectively. The elastic modulus for TiNicu5 and TiNicu10 was 25, 24 respectively. Hence the results of the compression test and micro-hardness are inter related with each other. Both results are in favor of TiNiCu5 and TiNiCu10 to be the best in choice of ternary alloys.

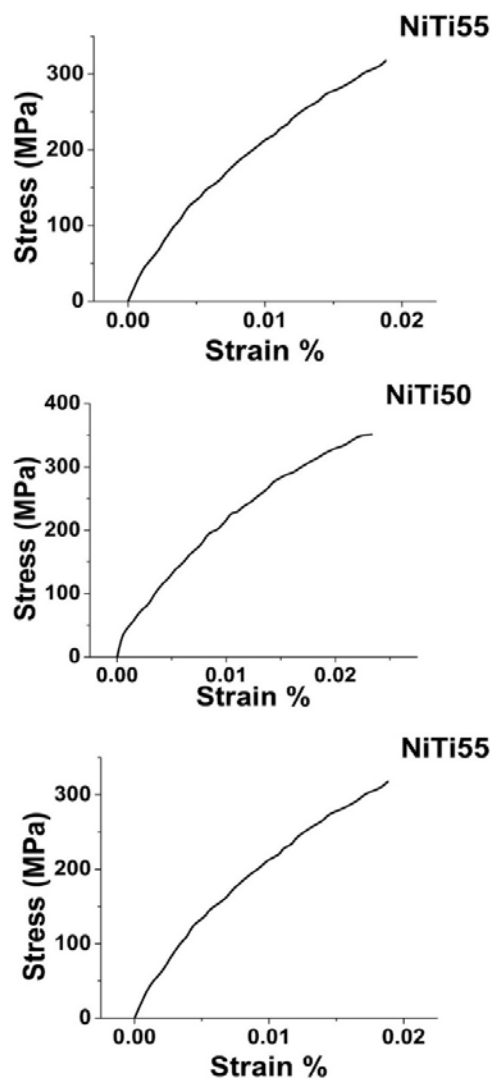


Fig. 3.19 Stress Vs Strain graph of as manufactured (a) NiTi45 (b) NiTi50 (c) NiTi55 samples developed by LAM

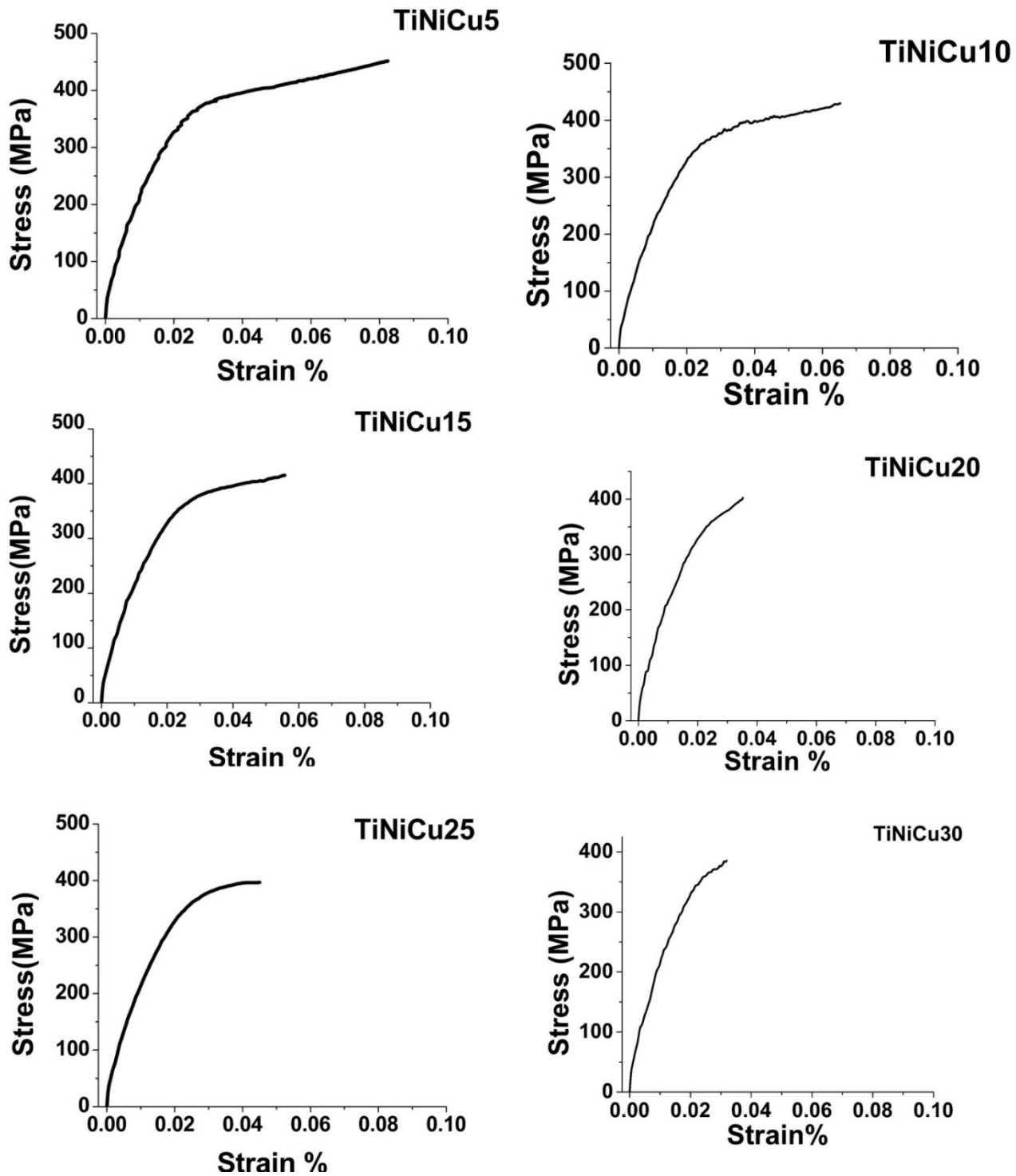


Fig. 3.20 Stress Vs Strain graph of as manufactured TiNiCu samples developed by LAM

3.8 Crystalline Properties Property Evaluation Using X-Ray Diffraction Analysis

In Fig. 3.20, the XRD peaks of NiTi55 reveals the presence of martensite phase at $2\theta = 41^{\circ}3'$ in monoclinic structure and the austenite phase takes a high peak at $2\theta = 44^{\circ}45'$, in which the material remains in cubic structure. Even a small change in the Ni content of the NiTi alloy can give a huge difference in its properties. The NiTi50 composition, the graph shows some presence of R phase as already shown earlier in Fig. 6(c). There are two visible peaks formed next to next in cubic structured austenite and monoclinic structured martensite phase at $2\theta = 40^{\circ}05'$ and $2\theta = 41^{\circ}25'$ respectively and is followed by a cubic structured austenite peak B2 at $2\theta = 44^{\circ}4'$. In the same figure the combination NiTi45 has its martensite peak B19' at $2\theta = 41^{\circ}34'$ and austenite peak B2 only upto a remarkable elevation at $2\theta = 44^{\circ}4'$ as shown. The presence of two phases austenite and martensite are vivid. The patterns of theseformed samples have peaks which are broad, which clearly intimates that, the grain structure of the all three samples formed are very small, almost uniform.

NiTi in general has three structures. They are Cubic structure in austenite phase, monoclinic structure in austenite phase and rhombohedral structure in R phase (if they exist). The presence of R phase increases the presence of two way shape memory effect in NiTi [28]. Lehto et al. (2014) demonstrated the weight % of Cu is at 5 in a TiNiCu alloy, then its phase transformation should be in a single step from monoclinic to cubic (B19'-B2). Similar observations weremade in samples TiNiCu5. There were three monoclinic structure martensite peaks B19' at $2\theta = 42^{\circ}7'$, $2\theta = 46^{\circ}56'$ and $2\theta = 51^{\circ}86'$ and the cubic structured austenite phase at a peak for $2\theta = 44^{\circ}5'$. For TiNiCu10 samples as well the phase transformation has taken single step transformation. B19' at $2\theta = 43^{\circ}1'$, and two B2 peaks at $2\theta = 44^{\circ}5'$ and $2\theta = 52^{\circ}5'$. The cubic peak has shifted two degrees ahead from the actual position from where it should have been. The increment in peak shift in general happens as a result of reduction in the d spacing between the lattice planes. The reduction in d spacing may be attributed to the following three reasons. First is the formation of solid solubility in every phase of the sample due to the less interaction time of the laser and the powders during the process of development as presented by Sun et al. (2010). Second is the internal stress developed due to the solidification process in the samples. As the chilling effect climbs from bottom to the top of the sample, it faces the temperature generated by the laser during the deposition process in the opposite direction from top to bottom, as described by Ocelík et al. (2009). Third reason is due to the residual stresses generated by the competing physical phenomena, like solidification, thermal expansion, molten metal flow, etc. during

LAM. The combination TiNiCu15 and TiNiCu20 are expected to have two step phase transformation as an orthorhombic phase (B19) comes in between the monoclinic (B19') and the cubic phase (B2) as reported by Yeon-Wook Kim et al. (2007). For both the samples the orthorhombic peak B19 have taken its place at $2\theta = 41^{\circ}79'$ and $2\theta = 43^{\circ}10'$ just before the B2 peak. The martensite peak of both the samples, B19' is seen at $2\theta = 38^{\circ}94'$ and $2\theta = 45^{\circ}24'$. The austenite peak B2 is raised at an elevation of $2\theta = 42^{\circ}25'$ and $2\theta = 61^{\circ}12'$. For TiNiCu20 the peak at $2\theta = 61^{\circ}12'$, is of less intensity. It is in line with the observation by Goryczka et al. (2001). In general, the martensite phase of TiNiCu25 and TiNiCu30 are in orthorhombic structure (B19), and austenite phase in cubic structure B2. The LAM developed samples TiNiCu25 has its martensite peak B19 at $2\theta = 39^{\circ}67'$, $2\theta = 43^{\circ}09'$ and $2\theta = 58^{\circ}33'$. The martensite peak B2 at $2\theta = 42^{\circ}62'$ and $2\theta = 58^{\circ}88'$. For TiNiCu30 both the B2 peaks have shifted forward by 2 degrees. Similar results have been witnessed by Rösner et al. (2000). The patterns of TiNiCu15 and TiNiCu25 samples have broader peaks as compared to that of TiNiCu5 and TiNiCu10. Crystallite size can be calculated by measuring the Bragg peak width at half the maximum intensity and using the Scherrer formula:

$$d = \frac{0.9 \lambda}{B \cos \theta} \quad (3.19)$$

Where d is for crystallite size, λ stands for wavelength of the X-Ray radiation used, B is the peak width at half the intensity, and θ is the Bragg angle (Suryanraya 2000). By using the Scherrer formula the calculated grain size of NiTi55, NiTi50 and NiTi45 from their corresponding peak width, has been found to be 55.46nm, 32.81nm and 41.62nm respectively. For ternary alloy samples the calculated grain size are TiNiCu5, TiNiCu10, TiNiCu15, TiNiCu20, TiNiCu25 and TiNiCu30 has been found to be 18.41nm, 19.56 nm, 37.55nm, 32.73 nm, 21.69 nm and 24.62nm, respectively. The calculated grain sizes are at par with the values obtained from AFM results discussed earlier.

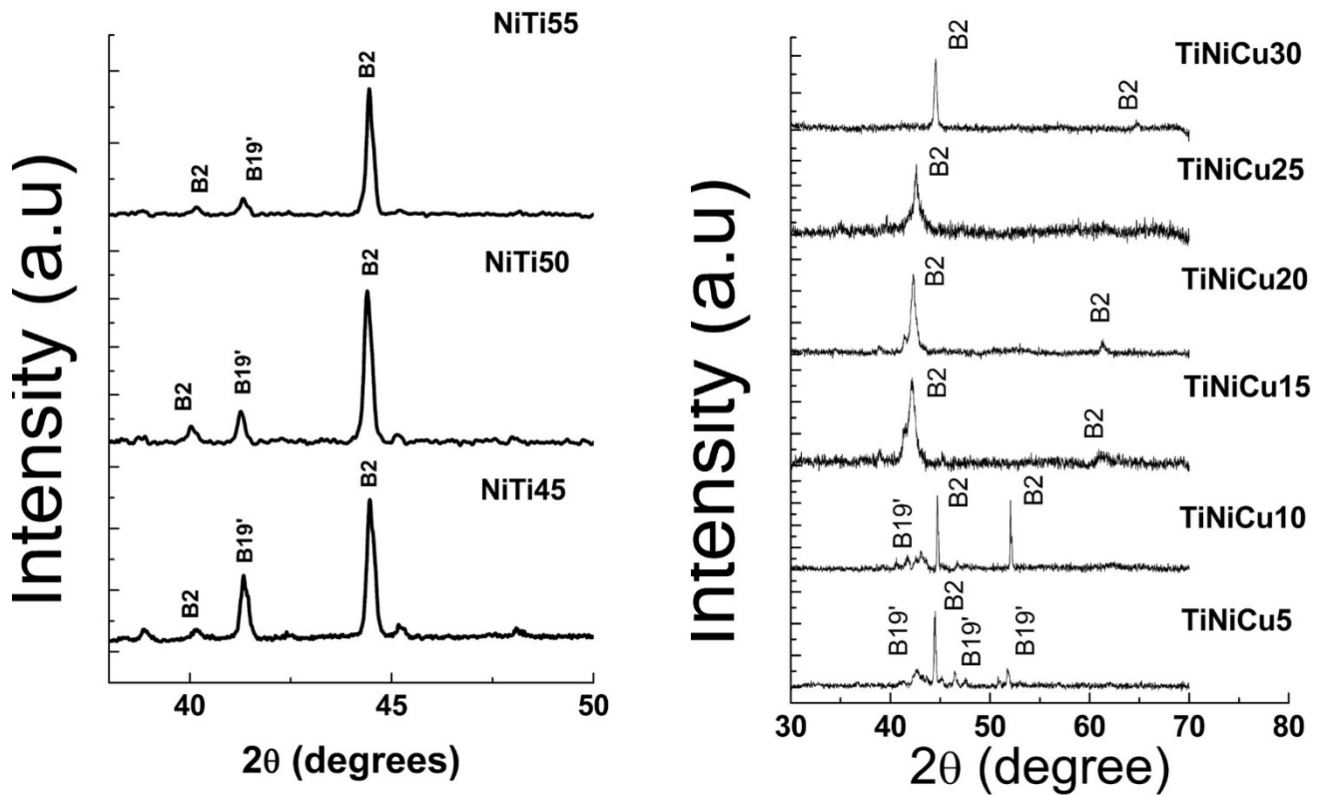


Fig. 3.21 XRD graph of as manufactured NiTi45, NiTi50, NiTi55, TiNiCu5, TiNiCu10, TiNiCu15, TiNiCu20, TiNiCu25 and TiNiCu30 samples developed by LAM

3.9 Summary

SEM of the surface texture of the samples reveals the nonporous NiTi50 which enhances good shape memory effect. However, presence of porosity is observed in NiTi55 and NiTi45 samples. The surface of NiTi50 was smoother than the other two compositions. This is assured by the corresponding surface roughness values of the samples. The surface roughness values of NiTi55 and NiTi45 are measured to be 5.76 μm and 5.63 μm respectively. Whereas NiTi50 has the lowest surface roughness value of 3.16 μm . In all the samples from the EDS it is found very clear that mild traces of C and O exist. They are in a negligible amount. This is due to the residual air content in the Ni and Ti powders initially before the mixing. These impurities exhibit the property change of the NiTi materials in NiTi55 and NiTi45 in their corresponding XRD graphs also. The martensite peaks are not much found for NiTi55 and NiTi45 compositions as shown in Fig 3.21. Among the formed three samples produced its found NiTi50, TiNiCu5 and TiNiCu10 have good properties.

Chapter 4

Laser Shock Peening of Bulk Shape Memory Alloy Structures using Laser Additive Manufacturing: Numerical and Experimental Investigation

4.1 Introduction

Though binary and ternary SMAs have been successfully developed by LAM, problems like porosity are yet to be addressed. A technique which has been successfully improving the surface quality of materials without bringing harm to the physical and chemical nature is laser shock peening (LSP). As the generated shock pressure by the laser pulse, rises higher than the Hugoniot elastic limit (HEL), it tends to produce high strain rate deformation on the surface of the sample which leads to maximum magnitude, compressive residual stress and strain hardening on the samples higher than the conventional methodologies like shot peening and deep rolling (Montross et al. 2002). The work hardened layer formed by LSP injects compressive stress that stops the crack propagation on the surface of the samples during the cyclic loading process with the help of pinning effect. Pinning effect is formed by the nano precipitates generated on the surface of the samples as a result of plastic deformation and high strain rate. The pinning effect is also capable of increasing the surface hardness, corrosion resistance and wear resistance (Liao et al. 2011). The researchers in the past have successfully studied with several experimentation and modelling that dislocation in the matrix overcome the hindrances up to a small radius with low volume density by shearing mechanism. The unsharable obstacles are surrounded by pinned dislocation loops, which holds them fixed at particular location preventing them from further dislocations. Adding to these effects the nano precipitates formed also contribute strengthening in the adjacent layers of dislocation. The efficiency of strengthening by nano precipitates completely depends on their morphology and distributed positions. Researchers in the past have been successfully improving the fatigue life of the samples using different types of LSP techniques as shown in Fig. 4.1. Warm LSP is used for very hard materials. In this type of LSP sacrificing layer is a must and widely silicon oil is used as the confining layer for this process. The entire process takes place at higher temperature (Liao et al. 2011). When it comes to Cryogenic LSP, it is widely used for ductile materials and the entire atmosphere of the experiment is maintained at very low temperature using liquid nitrogen, additionally the confining medium used is also water. In this type of LSP too, like warm LSP, sacrificing layer is a must (Ye et al. 2011). Normal LSP can be done with and without sacrificing layer. Many varieties of confining

layers can be used for this type of LSP (Kruusing 2008). The entire process is carried out under room temperature and it is suitable for any type of materials. Though a lot of LSP investigations have been explored for hard metals and alloys, LSP effects on smart material alloys like NiTi and TiNiCu are of less exploration. Also LSP effects on NiTi and TiNiCu developed by LAM is a novel approach. Since the samples developed are brittle in nature a minimum power of 1 GW/cm^2 is chosen for the experiments. Moreover for SMA besides improvement in various mechanical and surface properties the preservation of shape memory effect is a must for its application. In this motive multiple shots low power LSP is opted to improve the nature of samples in a better and homogeneous way. Thus the treated structures were subjected to surface morphology, microstructural analysis, micro-hardness measurement, mechanical property evaluation and phase transformation analysis.

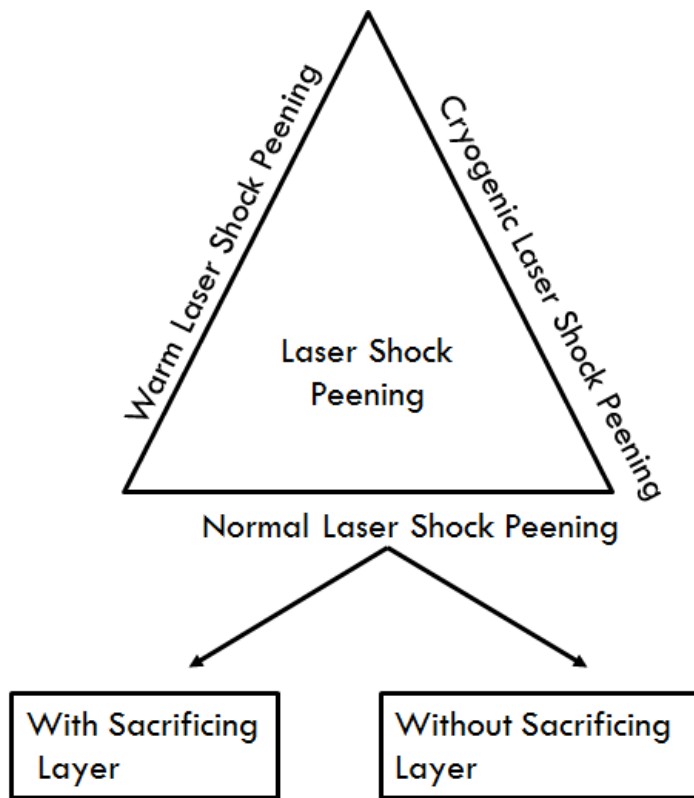


Fig. 4.1 Types of laser shock peening being implemented successfully

4.2 Numerical Modelling and validation of Laser Shock Peening

LSP process is primarily governed by heating rate, plasma generation and compressive stress impingement. The heating and cooling rate are predominantly governed by laser parameters and confinement properties. A finite element software was deployed to simulate the process and estimate the induced stress distribution at different processing parameters. Subsequently, these distributions were extrapolated to understand the mechanism of LSP. The simulation is carried out the software ANSYS and in-house developed APDL codes with the followings:

Governing Equation:

Following equation presents generalized heat equation applicable for laser shock processing process.

$$\rho C_p \left(\frac{\partial T}{\partial t} \right) - \nabla (k \nabla T) = 0 \quad (4.1)$$

Where k ($\text{W m}^{-1} \text{K}^{-1}$) is the thermal conductivity, C_p ($\text{J kg}^{-1} \text{K}^{-1}$) is the specific heat capacity, ρ (kg m^{-3}) is the density, and t (s) is the time.

Boundary conditions and associated simplifications

The initial temperature of the entire LSP set up is room temperature (T_0). So the initial and final conditions are

$$T(x, z, t) = T_0, \quad \text{when } t=0 \text{ and } t = \infty \quad (4.2)$$

The effect of the various processes is modelled using Lagrangian formulation and the associated boundary condition are expressed as

$$\begin{aligned} -K (\nabla T \cdot n) \Big|_{\Omega} &= [\beta I(x, z, t) - h_c (T - T_0)]_{\Omega} & \text{if } \Omega \in \Gamma \\ &= [-h_c (T - T_0)]_{\Omega} & \text{if } \Omega \notin \Gamma \end{aligned}$$

where, n is the normal vector of the surface, β is the absorption factor, I (W.m^{-2}) is the laser intensity, h_c is the heat convection coefficient ($\text{W.m}^{-2} \text{K}^{-1}$), Ω (m^2) is the area of work piece surface, Γ (m^2) is the laser spot area, and T_0 (K) is the ambient temperature. Ω and Γ are shown in Fig.1. The absorption factor is β , and heat transfer coefficient is h_c .

As the laser pulse of high intensity is impinged on the surface of the sample, plasma is generated, and the generated plasma expands and injects shock waves on the sample. The confined medium used for the entire process enhances the intensity of pressure generated multiple times. So the entire LSP process is governed by a shock pressure and plasma thickness. The relation between shock pressure and plasma thickness are being governed by the following equation as reported by (Fabro et al. 1990)

$$\frac{dL(t)}{dt} = \frac{2P(t)}{Z} \quad (4.3)$$

Where L (t) stands for thickness of the plasma generated, P(t) stands for the pressure generated by the laser pulse impinged. The laser energy, I(t) distributed on the surface of the sample is mathematically given as follows:

$$I(t) = P(t) \frac{dL(t)}{dt} + \frac{3}{2\alpha} \frac{d}{dt} [P(t) L(t)] \quad (4.4)$$

The pressure generated by the laser pulse on the surface of the sample is calculated using Fabbro's model as shown below [12]:

$$P = 0.01 \sqrt{\frac{\alpha}{2\alpha+3}} \sqrt{Z_1 I_0} \quad (4.6)$$

Where P (GPa) stands for peak pressure generated, α stands for absorption coefficient and for NiTi, Z (g cm⁻² s⁻¹) represents the combined shock impedance and it is obtained from the following formula $Z = \frac{2}{\frac{1}{z_1} + \frac{1}{z_2}}$, Z₁ stands for the shock impedance of NiTi (3.44 x 10⁶ g cm⁻² s⁻¹) (Millet et 2002) and Z₂ stands for the shock impedance of the confining medium water (1.45 x 10⁵ g cm⁻² s⁻¹) (Wang et al. 2013). Since the properties of TiNiCu is not available in literature it was given the value of NiTi as both have similar properties. The residual stress generated by the shock pressure is simulated and compared with the experimental values. In the entire process the growth of plasma is considered to be only in axial direction.

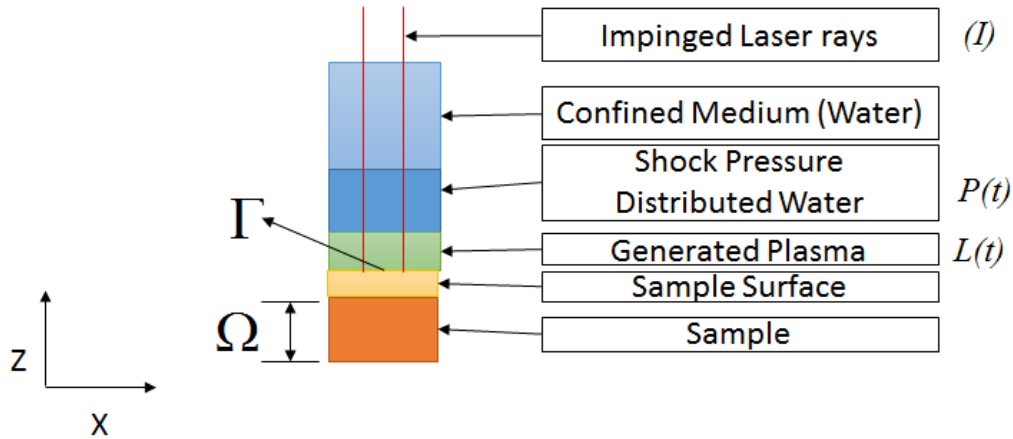


Fig. 4.2 Schematic of laser shock peening functioning

The developed numerical methodology was deployed to study the effect of multiple shot low power LSP by predicting the residual stress distribution and their effects on the surface of the sample.

4.3 Laser shock peening of NiTi and TiNiCu bulk samples

The dimensions of SMA structures fabricated using laser additive manufacturing chosen for LSP process was 25 mm length, 10 mm width and 1 mm thickness. The LSP experiments were carried out by using the third harmonic wavelength at Q-Switched mode of Nd:YAG laser (Quanta-Ray INDI) on the NiTi structure mounted on computer controlled X-Y manipulator. The schematic arrangement of LSP set up is presented in Fig. 4.4.

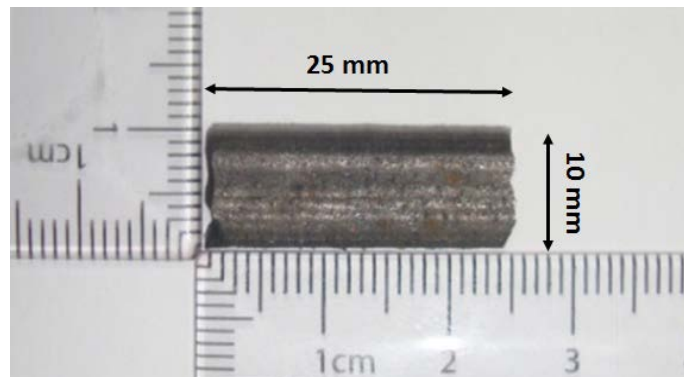


Fig. 4.3 NiTi sample developed by LAM used for LSP

The third harmonic of Nd:YAG laser was used, expecting an improved performance in LSP. The process parameters used for LSP experiments are presented in Table 4.1. The sample was fixed inside the LSP set up which had the water as the confining layer. Water was chosen as the confining medium, since the water generally breaks down the plasma after certain limit that sequentially reduces the intensity of pressure acting on the sample. Also the energy density of the laser can also be significantly reduced, as the breakdown of plasma, has the tendency of absorbing maximum laser energy density (Wu et al. 2006). As the sample taken for the study was brittle in nature, hence the plasma breakdown prevents it from getting damaged by high pressure generated by high laser energy density. This advantage can be availed only when water is used as the confining medium.

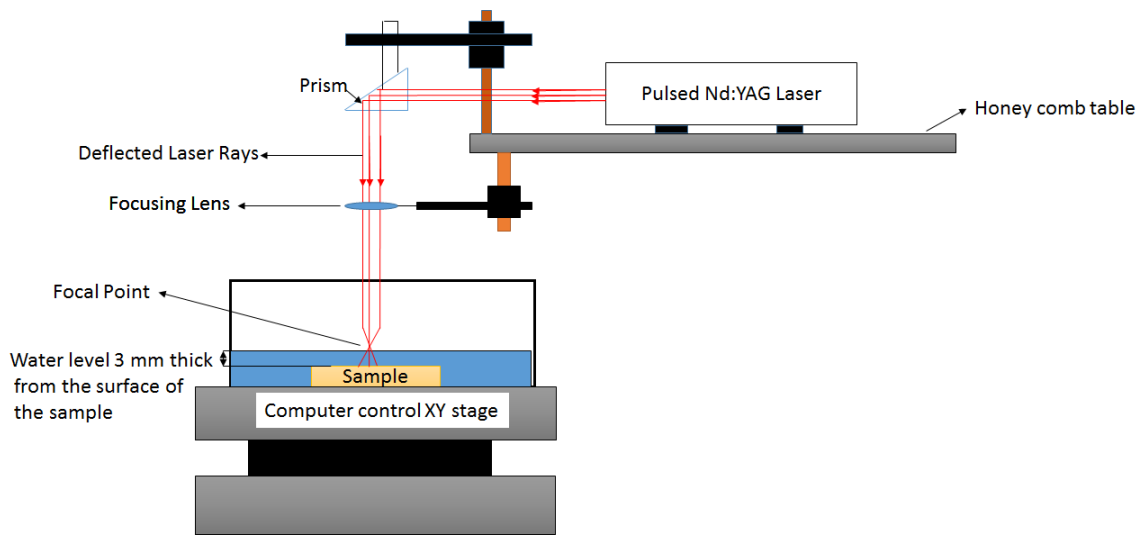


Fig. 4.4 Schematic diagram of the experimental setup used for LSP

As the laser pulse generates the pressure and plasma on the surface of the samples, a coating layer (generally black paint or black tape) is used as a medium to accumulate plasma formed and induce high compressive stress on the samples. In this study as mentioned earlier, considering the brittleness in the sample and to prevent excess of pressure accumulation on the surface of the samples, considering no harm to the physical nature of the sample the coating layer was not used in our experiments as reported by researchers in the past (Kalainathan et al. 2012). The laser light was deflected using a prism as shown in Fig. 4.5 and indented directly on the surface of the sample. Using the computer controlled manipulator the multiple impingement was carried on the surface of sample the surface of the sample.

Table 4.1 Parameters used for LSP process

Parameter	Unit	Value
Laser wavelength	nm	1064
Mode of operation	-	Q-switched
Laser energy per pulse	GW/cm ²	1
Laser pulse duration	ns	9
Laser pulse frequency	Hz	1
Laser spot size	mm	2
Overlap	%	20

The frequency and the spot repetition are the parameters that affect the reduced cooling rate and uniform plasma generation during LSP. They, also, result in reduced dilution and crack elimination. In general, a minimum laser energy density of 1 GW/cm² is a must for an effective LSP (Morales et al. 2008). After LSP the samples were characterized for the same characterizations using the same devices to investigate the impact of LSP on the SMA samples.

4.4 Validation of numerical modelling

4.4.1 Simulation and finalization of parameters

Based on the theoretical studies mentioned in our initial works a laser diameter of 2 mm was chosen as the best option for distributing the intensity of laser uniformly and effectively on the sample surface on the top. Using the above mentioned modelling equation using ANSYS 14.0 software and self-made APDL codes implementing the above chosen equation a simulation was carried out to study the amount of residual stress generated on the sample from the surface to its depth by a single pulse of 1 GW/cm² laser energy density was simulated. The materials properties of NiTi as quoted in Table 3.1 were used for the study to increase the preciseness of stress to be

generated by LSP. In order to validate the simulation the conventional method of measuring the residual stress by X-ray Diffraction was deployed. The simulated results for NiTi in martensite and austenite phase and TiNiCu are as follows in Fig 4.5

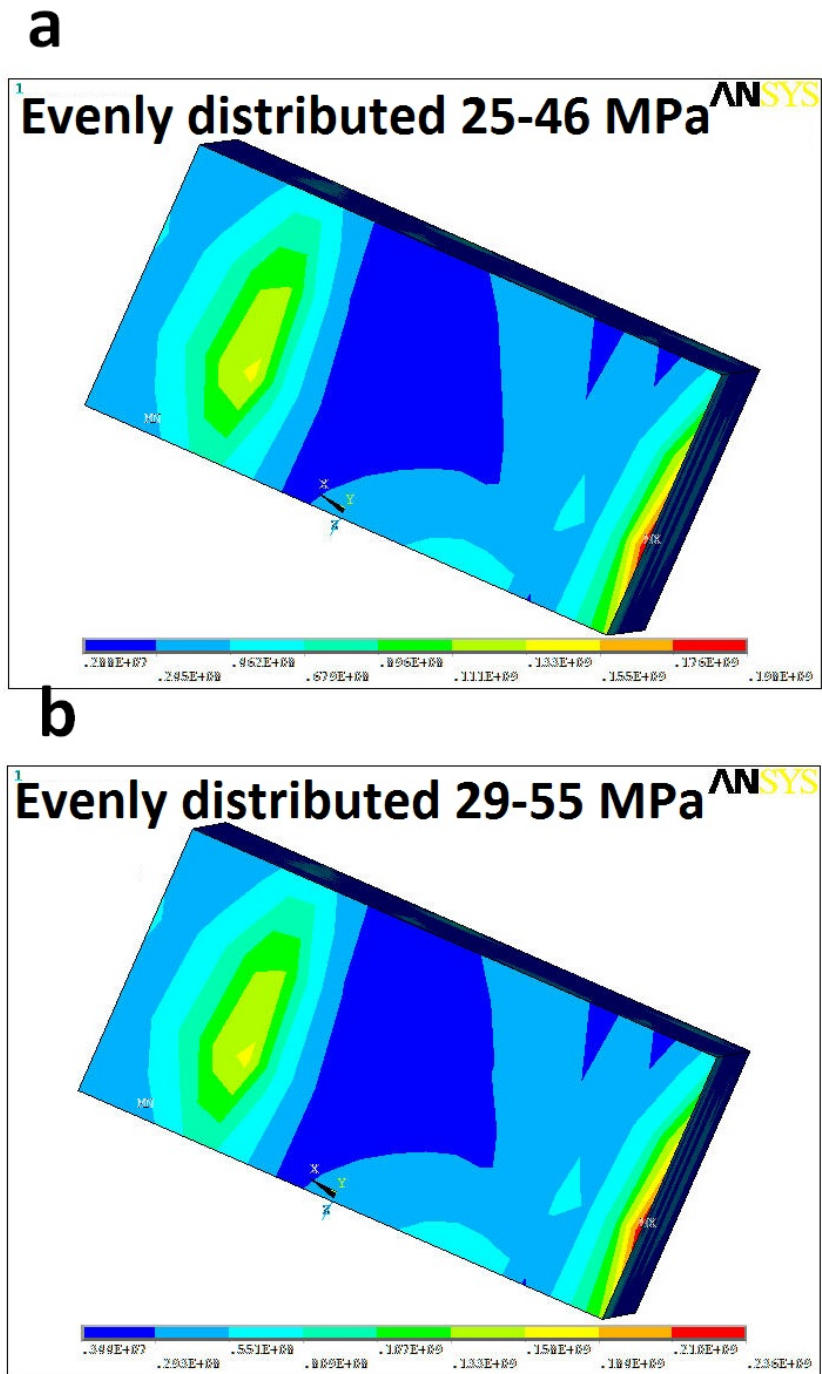
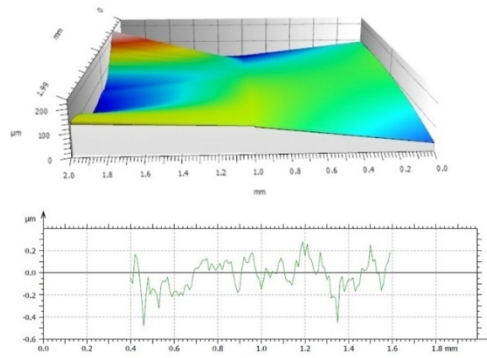
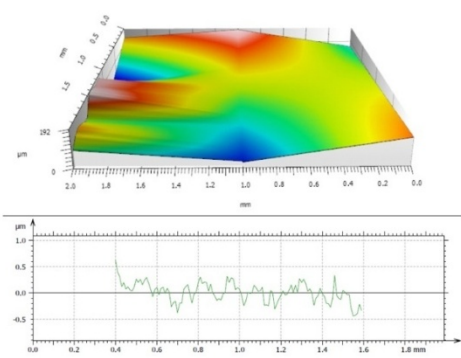
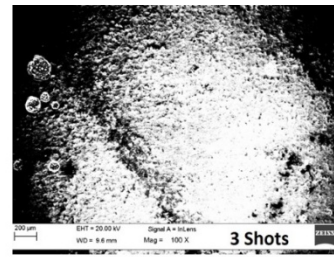
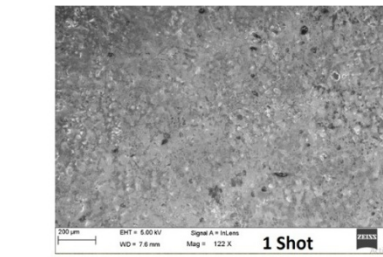


Fig4.5 The residual stress distribution simulated for (a) NiTi (b) TiNiCu

Figure 4.5 shows the residual stress generated on the surface of the samples for both NiTi and TiNiCu. The study shows the evenly distributed residual stress on the surface of the samples. Since the evenly distributed residual stress is of very less amount, the shock peening was to be carried out with multiple shots of 1 GW/cm^2 . In order to determine the number of shots to be used for the final experimentation a visual inspection was carried out on the surface of the samples and the results are as shown in Fig. 4.6. The SEM images of various number of laser shots and their corresponding surface roughness profiles are shown. In case of a single shot as shown in Fig. 4.6 hardly any change on the surface of the sample and not much fluctuation is seen in the surface profile graph. Whereas in Fig. 4.6 in case of 3 shots, changes were observed on the surface of the samples. No harm was seen in the physical nature of the sample. The surface profile graph did not have much fluctuations. In Fig. 4.6 the effect of 5 shots show clear ablation on the surface of the sample. The removal of layers on the surface of the sample may lead to other problems of crack propagation etc... Severe ablation accompanied with mild cracks propagation was observed on the surface of the samples when 7 shots were impinged on the surface as shown in Fig. 4.6 the surface profile was too rough as shown in Fig. 4.6 (h), the surface profile graph shows huge fluctuations in Fig. 4.6. Hence 3 shots of LSP was opted for the entire experimental procedures.

SEM
Surface Roughness Profile
and Image



SEM
Surface Roughness Profile
and Image

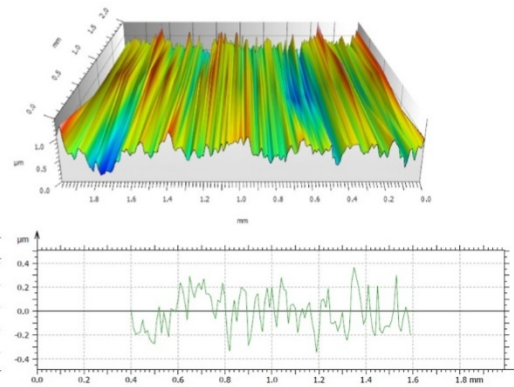
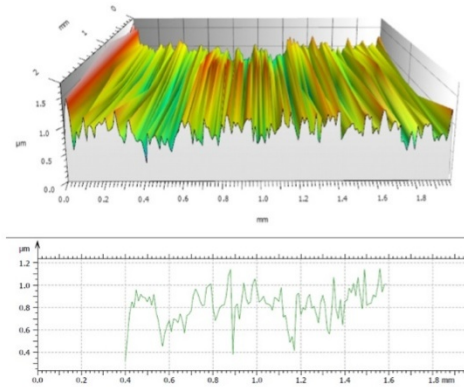
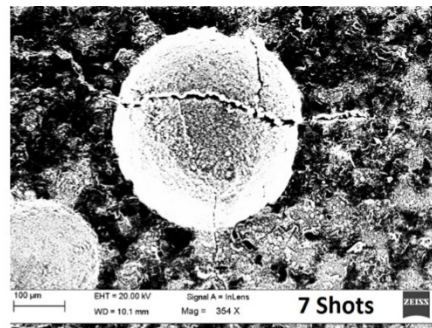
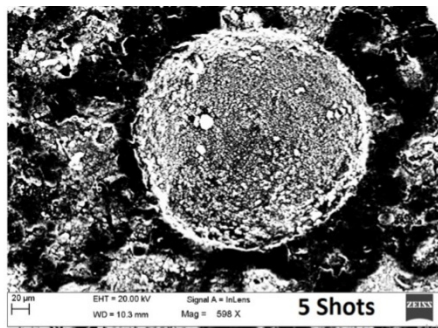


Fig. 4.6 Effects of various power of LSP on the surface of the sample

Hence from the above observation 3 shots were chosen topeen the surface of the samples and in order to homogeneously distribute the LSP effect throughout the sample the LSP was carried out on all the six surfaces of the samples. After the experimentation a reasonable increase in the amount of residual stress in the samples of NiTi and TiNiCu and are plotted in **Fig. 4.7**

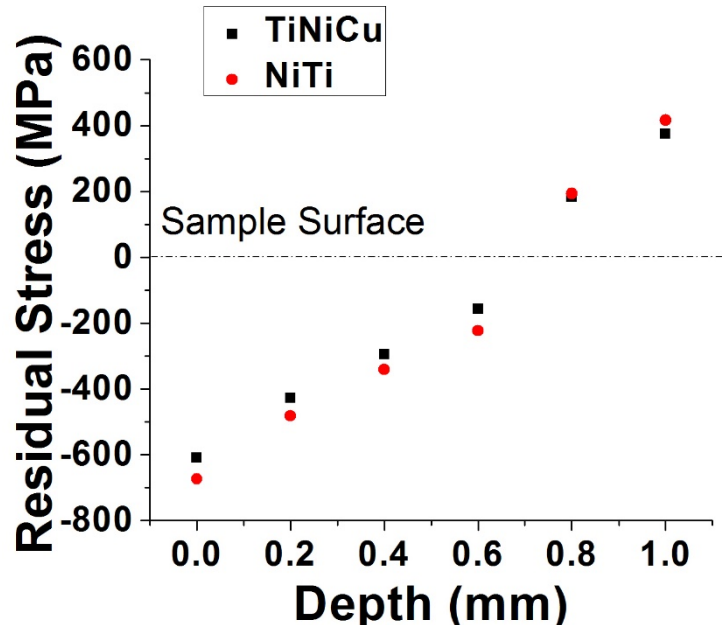


Fig. 4.7 Amount of residual stress distributed in NiTi and TiNiCu sample for 3 shot LSP

The samples chosen for the practical experimentation of 3 shot LSP are NiTi50 and TiNiCu5. So similar experimentations were carried on all other samples manufactured. After carrying out the following characterizations were performed to investigate the influence of 3 shot LSP on the samples.

4.5 Evaluation of surface morphology

4.5.1 Scanning electron microscopy examination

The analyses about the surface morphological studies were initiated with the scanning electron microscopy (SEM). The SEM images of NiTi55, NiTi50, NiTi45, TiNiCu5, TiNiCu10, TiNiCu15, TiNiCu20, TiNiCu25 and TiNiCu30 are shown in Fig. 4.8 for comparison. The figures show the effects of LSP well impinged on the surface. The surface topography of NiTi55 in Fig. 4.8(a) and Fig. 4.8(c) show the images of NiTi55 and NiTi45 it is seen very clear that the surface is not uniformly flat and peaks can be seen. The images show formation of cracks on the surface of the samples after

LSP. The surface is uniformly scattered, with no much pitting effects visible. The cavities formation are found randomly on the surface. Craters are formed along the cracks generated. NiTi50, TiNiCu5 and TiNiCu10 have a closely deposited particles without any pores or much dent. After LSP almost the entire surface got flat, and the particles went even closer with not much peaks and valleys visible. Mild traces of oxygen is visible but they are in a highly negligible state. The Fig. 4.8(h) shows the presence of molten wax like structures on the surface of TiNiCu25. Sequentially small craters accompanied with mild cracks have been generated on TiNiCu15, TiNiCu20 in Fig. 4.8 (f), (g) . Fig 4.8 (i) shows mixed presence of molten wax structures an mild pores in TiNiCu30. This may be attributed to the precipitates accumulation and other phases formed on the samples after LSP. To study the variation in the composition of the samples due to the effect of LSP energy dispersive spectroscopy (EDS) was carried out and the results are as plotted in Table 4.2The results show not much variation in the composition of the samples before and after LSP. The mild variation is due to the influence of micro-galvanic coupling which acts a prime factor for material dissolution. The reason behind the variation of composition of the binary alloys is the presence of TiNi₂ secondary phase and also the titanium substrate plays a bit of role in the composition as discussed in the previous chapter.

Table 4.2 EDS results of the formed NiTiand TiNiCu samples after LSP

Samples	Ti (Wt %)	Ni (Wt %)	Cu (Wt %)
NiTi55	68.37	31.63	
NiTi50	50.21	49.79	
NiTi45	55.28	44.72	
TiNiCu5	57.37	36.35	6.28
TiNiCu10	55.07	41.15	3.78
TiNiCu15	58.67	30.81	10.52
TiNiCu20	55.47	32.12	12.41
TiNiCu25	65.16	10.1	24.74
TiNiCu30	52.47	25.88	21.65

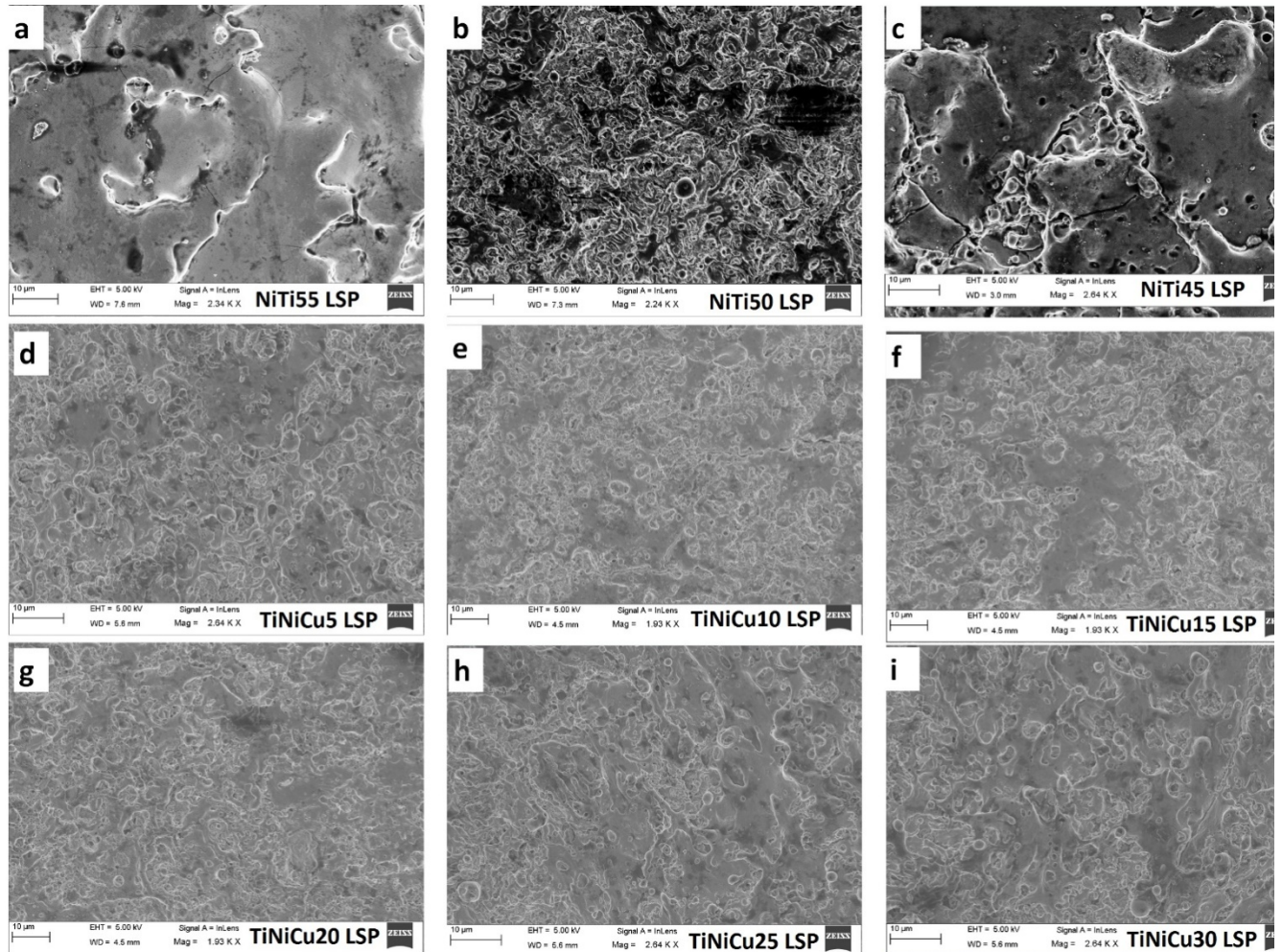


Fig. 4.8 SEM images of (a) NiTi55 (b) NiTi50 (c) NiTi45 (d) TiNiCu5, (e) TiNiCu10, (f) TiNiCu15 (g) TiNiCu20, (h) TiNiCu25 (i) TiNiCu30

4.5.2 Microstructure analysis

To improve the analyses further more deeply microstructures of the samples were used taken for comparison between before and after LSP. The Fig. 4.10 shows the microstructure of NiTi and TiNiCu samples after LSP. It is very clearly seen that the images show some lamellar microstructure after LSP. This shows the impact of LSP been done on the samples. The grain sizes have become smaller in size for all samples than the as manufactured state exhibiting the influence of effective LSP. In Fig 4.9 the presence of amorphous nature on the surface of the samples is almost present in all

samples. The amorphization is comparatively less for NiTi50, TiNiCu5 and TiNiCu10. During LSP tremendous amount of free energy and chemical disorder happens as an effect of dislocation accumulation. The free energy of crystalline phase reaches a critical level and sequentially leads to amorphization as reported by (Sun et al. 2010). This amorphization can badly affect the shape memory nature of the samples as the crystallinity is very much needed for its shape memory effect. For Cu% for than 20% the amorphization effects are seen high in Fig (g), (h) and (i) for samples TiNiCu20, TiNiCu25 and TiNiCu30.

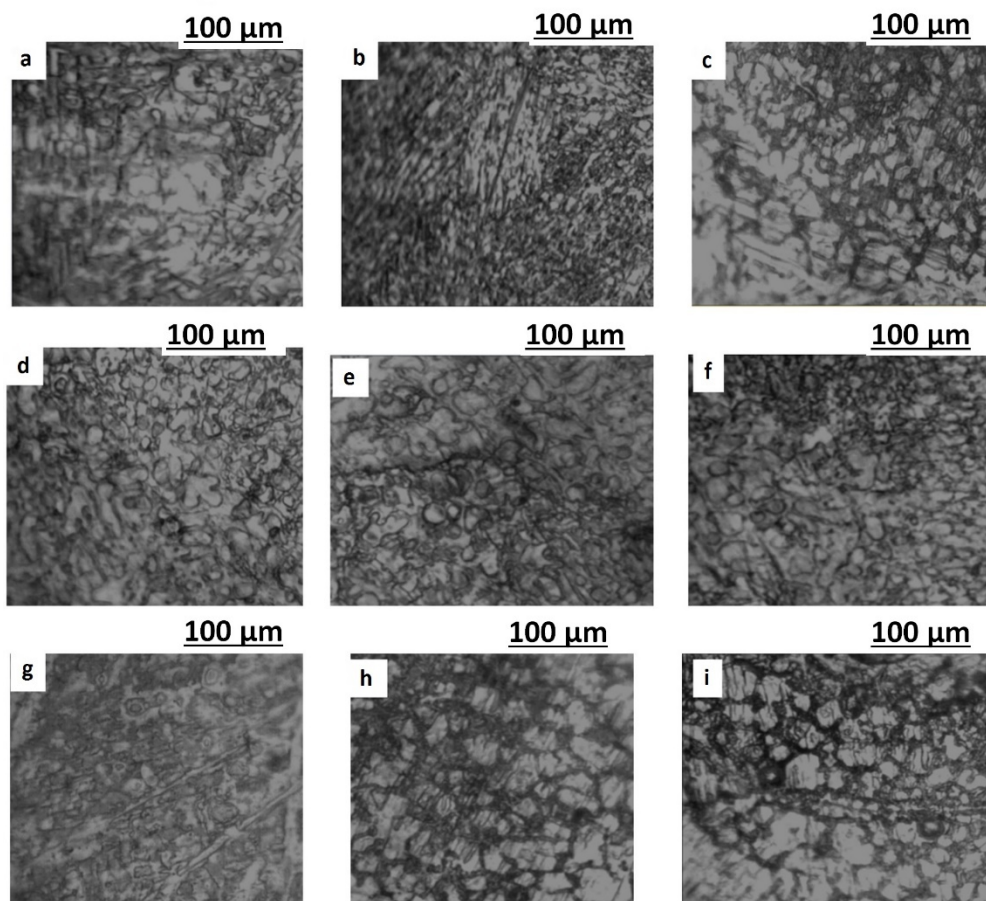


Fig. 4.9 Microstructure images of (a) NiTi55 (b) NiTi50 (c) NiTi45 (d) TiNiCu5, (e) TiNiCu10, (f) TiNiCu15 (g) TiNiCu20, (h) TiNiCu25 (i) TiNiCu30

4.5.3 Atomic force microscopy examination

In order to have a better analyses through the grain size and surface roughness values in nano level, the samples were characterized using atomic force microscopy (AFM). In General after LSP the grain size decreases after LSP and similar effects have been observed for our samples as well. In

Fig. 4.10, the AFM images of all samples after LSP process are shown. The dimensions of NiTi55, TiNiCu15 and TiNiCu30 samples are $1\ \mu\text{m} \times 1\ \mu\text{m}$ and NiTi50, TiNiCu20 and TiNiCu25 images at $10\ \mu\text{m} \times 10\ \mu\text{m}$. Finally dimensions of NiTi45, TiNiCu5 and TiNiCu10 images are $2\ \mu\text{m} \times 2\ \mu\text{m}$ respectively. The detected results of the samples out of AFM are as quoted in Table 4.3. The grain sizes show NiTi50 to have the finer grains and NiTi45 has the biggest grains among the three samples. Generally as an effect of LSP samples are expected to have finer grains and since NiTi45 and NiTi55 have not got much change in the grain size after LSP, it is very obvious that the equi atomic composition has got the tendency to absorb the amount of external stress acting on it. The surface roughness values almost are at par with the readings obtained by the surface profilometer. Similarly NiTi50 has got the best smoothest surface. Kurtosis values help us determine the surface sharpness of the samples. It is determined using the Nano Scope Analysis software (synchronized with the machine) simultaneously, as the images were captured. When the Kurtosis value is lower than 3 it indicates the surface of the sample is flat with less peaks, and when it is higher than 3 it indicates the valleys are less and peaks are predominant. From the results as well as from the image it is very clear NiTi50 has a flat surface with almost no peak. Hence this is a clear indication that the LSP effect has produced fine results with NiTi50 as concluded with SEM and microstructure images previously.

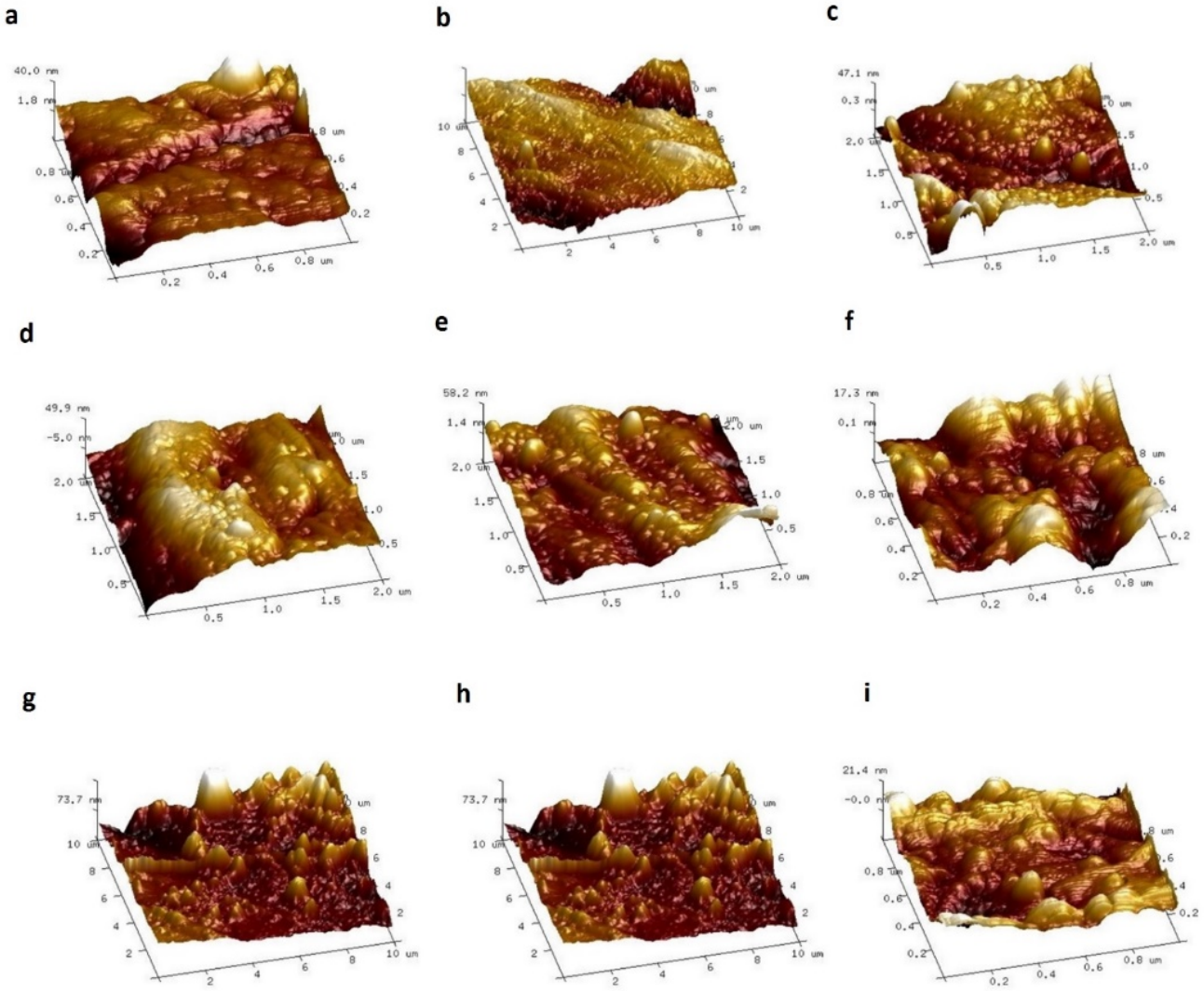


Fig. 4.10 AFM images of (a) NiTi55 (b) NiTi50 (c) NiTi45 (d) TiNiCu5 (e) TiNiCu10 (f) TiNiCu15 (g) TiNiCu20 (h) TiNiCu25 (i) TiNiCu30 after LSP

Table 4.3 Grain size, surface roughness and kurtosis value of the samples from AFM

Samples	Grain Size (nm)		Surface Roughness (nm)		Kurtosis Value	
	Before LSP	After LSP	Before LSP	After LSP	Before LSP	After LSP
NiTi55	55.45	48.49	31.73	28.76	3.39	3.83
NiTi50	5.76	28.76	3.16	4.73	3.63	3.89
NiTi45	3.12	35.43	2.57	2.83	3.45	3.76
TiNiCu5	18.41	16.12	3.22	3.89	2.25	2.90
TiNiCu10	20.12	21.08	3.97	4.36	2.88	3.09
TiNiCu15	38.26	35.64	6.21	6.97	3.74	3.95
TiNiCu20	33.57	31.47	5.83	6.17	2.94	3.35
TiNiCu25	21.61	18.75	4.76	5.28	3.04	3.17
TiNiCu30	25.51	20.13	4.25	4.91	3.54	3.92

4.6 Mechanical properties evaluation

4.6.1 Micro-hardness measurement

The samples after LSP were bisected to the direction of laying and prepared using standard metallographic techniques for micro-hardness measurement. The measurement was carried out at an incremental distance of 25 mm at a load of 500g. Figure 4.11, presents the micro-hardness distribution on the samples after LSP. It is very clearly seen that after LSP the micro-hardness has drastically increased. As discussed in the earlier sections the pinning effect plays a vital role in accumulating the dislocations and preventing them from proceeding further. The driving force of this pinning effect is exerted by the precipitates generally formed on the surface of the samples due to LSP. Mild traces of precipitates were visible in the SEM images shown in Fig. 4.8 as well. The precipitates resist the dislocations from proceeding further, leading to pin them down which sequentially leads to improved micro-hardness values. The precipitate hardening also leads to a gradual increase in the material strength. From the graph we can see the error percentage for all three samples are comparatively very less, which clearly indicates a homogeneous LSP been done on the samples with effective parameters. The grain boundary has remarkable influence in the obtained micro-hardness value. As the indentations were randomly done on the surface of the sample, possibilities of indenting on the grain boundary is also liable. Indentations on the grain boundary can fluctuate the values drastically. But the minimum value of standard deviation makes it clear that the influence of indentation on the micro-hardness values of the samples is very little. Hence the obtained values are purely based on the volume of materials below the indentation and the LSP effects on the samples. Among the increased values NiTi50 , TiNiCu5 and TiNicu10 are 390, 270, 280 VHN respectively.

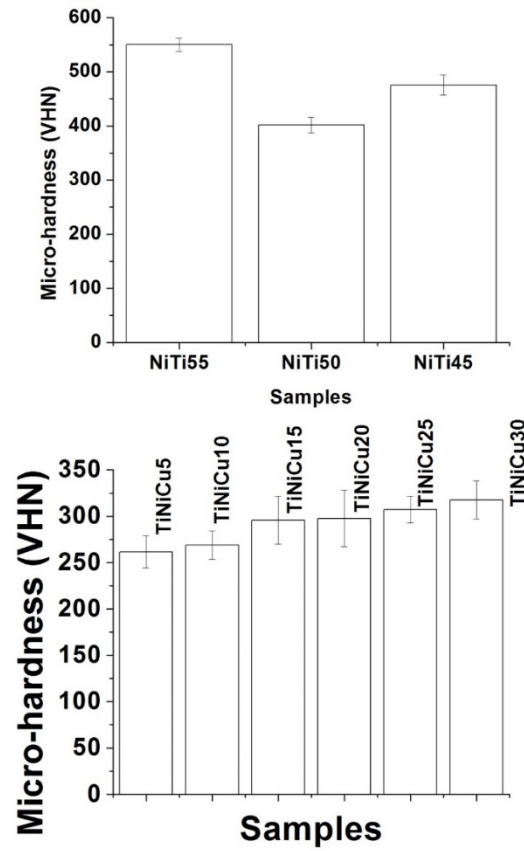


Fig. 4.11 Micro-hardness values of NiTi55, NiTi50, NiTi45, TiNiCu5, TiNiCu10, TiNiCu15, TiNiCu20, TiNiCu25 and TiNiCu30 samples after LSP

4.6.2 Compression test

Strength and ductility are very much essential properties of a metal, but in most of the commonly used metals both the properties are incompatible to each other. In case of SMA both ductility and strength are closely aligns with each other for an effective functioning. A material's ductility becomes higher as the strain hardening capacity of the material is high, which has the capability to accommodate maximum amount of dislocations due to plastic deformation. In the process of plastic deformation series of dislocations are generated and simultaneously becomes extinct. Once the dislocation density is high during plastic deformation the ductility of the samples are high as well. In the samples after LSP, during the compression test the plastic deformation happens and the density dislocation are being compressed in the lattice structures of the NiTi samples that are being capable of delivering increased ductility than the samples before LSP.

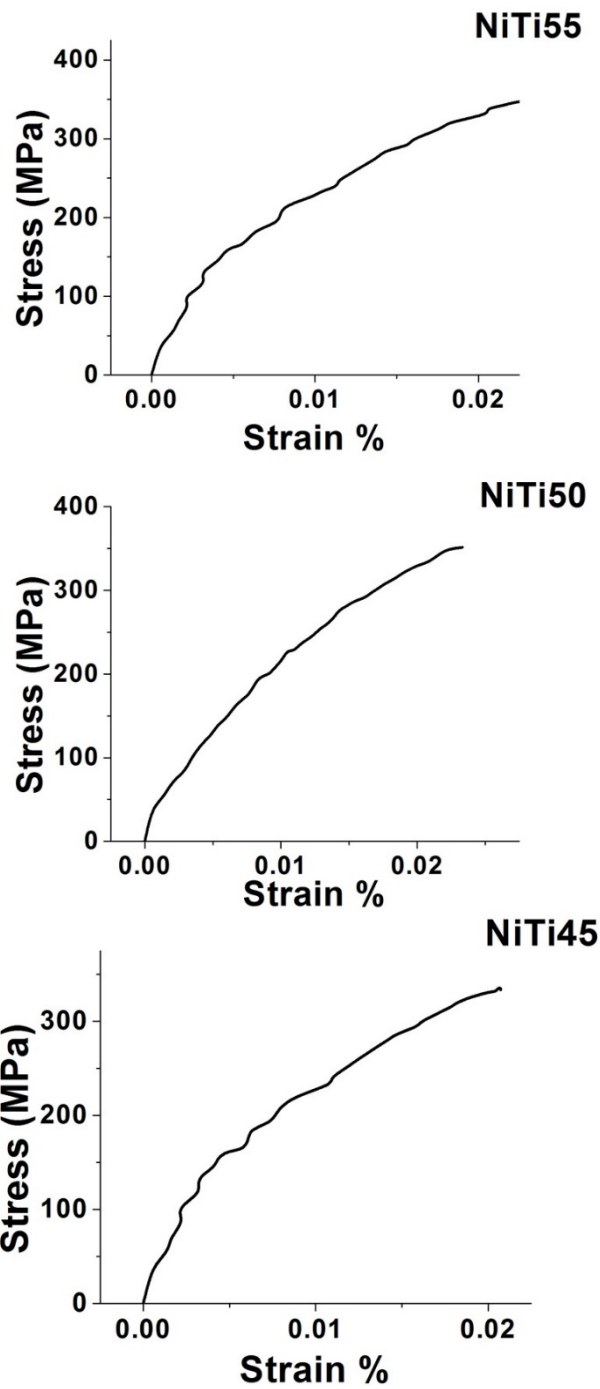


Fig.4.12 Compression test results of NiTi55, NiTi50 and NiTi45 samples after LSP

The young's modulus values quoted in the table shows it vividly. All the samples before LSP were badly affected by porous nature, due to which the capability of accumulating dislocations had been very less, that sequentially lead to the fracture of lattice structures very easily. Hence the ultimate strength and the young's modulus values had to be very low. As discussed earlier, due to the

pinning effect generated by the precipitates formed during LSP the sample structures developed by LAM have an increased strength and ductility while comparing to the samples in the as manufactured state. From Fig. 4.12 the martensite plateau which indicates the phase transformation of martensite to austenite phase, is clearly seen for NiTi50. Whereas the strength values of other two samples were hardly able reach the plateau level. For NiTi50 as an effect of continuous loading, from the martensite plateau the elastic deformation moves ahead till the ultimate strength value. Though the improvement in ultimate strength and young's modulus have been achieved for all the three samples after LSP, NiTi50 has got the best results, which closely aligns with the results of other surface morphological characterizations previously obtained. Similarly for ternary alloys TiNiCu5, TiNiCu10, TiNiCu15 and TiNiCu20 have successfully displayed martensite peak formation in the diagram at around 400 MPa. The TiNiCu25 and TiNiCu30 have failed to raise up the ultimate strength value inspite of LSP because the two samples were un able to succumb the pressure impinged by LSP. As an effect the total distortion of the lattice structure has led to the failure of the samples evolution into better shape. Similar to the surface morphological results TiNiCu5 and TiNiCu10 have remarkable betterment in the mechanical properties after LSP. Also TiNiCu15 and TiNiCu20 have showed some improvement as shown in Fig. 4.13. For both binary and ternary alloys the crookedness of the line generated is high comparative to the lines generated in the as manufactured state. This may be attributed to the pinning effect induced by LSP.

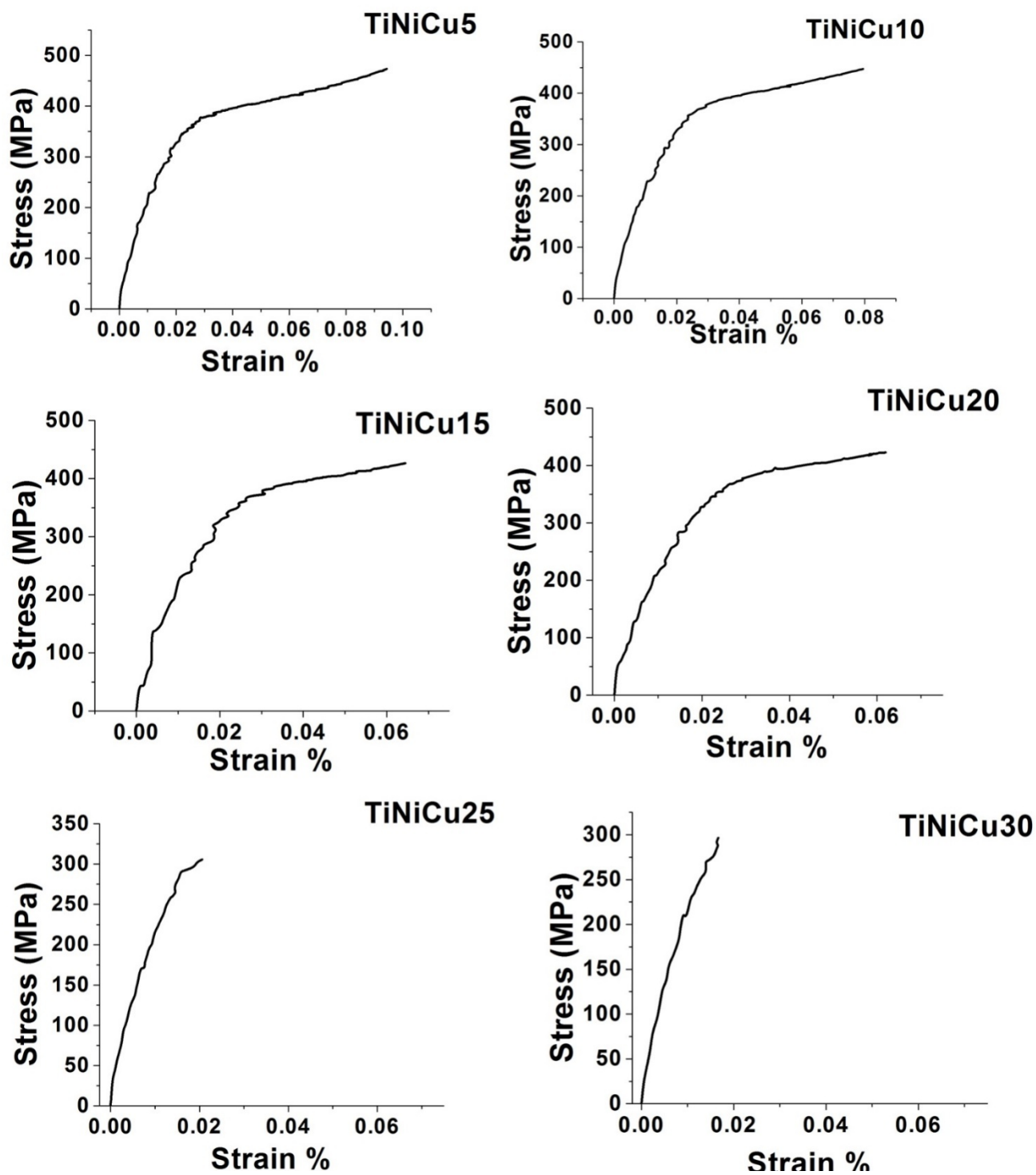


Fig. 4.13 Compression test results of TiNiCu5, TiNiCu10, TiNiCu15, TiNiCu20, TiNiCu25 and TiNiCu30 samples developed by LAM

Table 4.4 Compression test results of NiTi55, NiTi50, NiTi45, TiNiCu5, TiNiCu10, TiNiCu15, TiNiCu20, TiNiCu25 and TiNiCu30 before and after LSP

Parameter	Ultimate Strength (MPa)		Youngs Modulus	
	Before LSP	After LSP	Before LSP	After LSP
NiTi55	296	333	20	15
NiTi50	315	403	21	22
NiTi45	320	378	21	21
TiNiCu5	451	473	28	25
TiNiCu10	430	448	28	26
TiNiCu15	412	427	26	25
TiNiCu20	402	423	24	21
TiNiCu25	397	306	25	22
TiNiCu30	386	296	22	21

Figure 4.14, presents the XRD graph of all the three NiTi and TiNiCu samples after LSP. From Fig 4.14, after LSP it is seen that lots of martensite peaks have disappeared for both NiTi and TiNiCu samples. Also the peak width seems to be broadened than in the as manufactured stage. The peak broadening is a clear indication that the particle sizes have become smaller in size than at the as

made state. This aligns with the results obtained with AFM as well. The disappearance of certain martensite peaks may be attributed to the effect of amorphization, discussed earlier with the results of microstructure. The amorphization is clearly seen in TiNiCu samples. The peak position of all samples seem to be shifted front and back from their actual position in which they should have been. The cubic peak has shifted outstandingly for all samples, ahead from the actual position from where it should have been. The increment in peak shift in general happens as a result of reduction and increment in the d spacing between the lattice planes, depending upon the side of the shift.. TiNi45 has its martensite peak at $41^{\circ}27'$ and austenite peak at $46^{\circ}07'$. The peaks ascending two degrees ahead, is a clear indication of compressive residual stress bestowed in the samples [24]. Similarly from Fig.14 for NiTi50 it is seen that the martensite peak in the as made state has disappeared after LSP. This may be attributed to the effect of amorphization that happens due to LSP as discussed earlier. The monoclinic and cubic peak of NiTi50 after LSP is at $41^{\circ}37'$ and $46^{\circ}11'$ respectively. The Ni rich NiTi45 has its martensite peak at $42^{\circ}27'$ and two austenite peaks at $41^{\circ}27'$ and $44^{\circ}71'$ respectively. NiTi45 has its peak reverse shift as well. For ternary alloys the peaks of TiNiCu5 and TiNiCu10 have become slightly broader, whereas for other samples the half width maximum peak have become very much broader. For TiNiCu15 and TiNiCu20 the B2 spectrum is of very low intensity and lots of B19' peaks have disappeared. TiNiCu25 and TiNiCu30 samples have B2 peaks that are hardly visible in the figure. This can be attributed to the complete distortion of lattice structure as discussed earlier.

Crystallite size can be calculated using the Scherrer formula Using the Scherrer formula, the calculated grain size of all binary and ternary alloys show some decrease in the grain size than in the as manufactured state. The grain size using Scherrer formula shows NiTi55, NiTi50, NiTi45, TiNiCu5, TiNiCu10, TiNiCu15, TiNiCu20, TiNiCu25 and TiNiCu30 are 46.24 nm, 27.35 nm, 33.74 nm, 16.25 nm, 20.86 nm, 32.48 nm, 29.46 nm, 17.62 nm and 19.65 nm respectively. These values are almost very near to the values of grain size obtained through AFM as reported in Section 4.5.3.

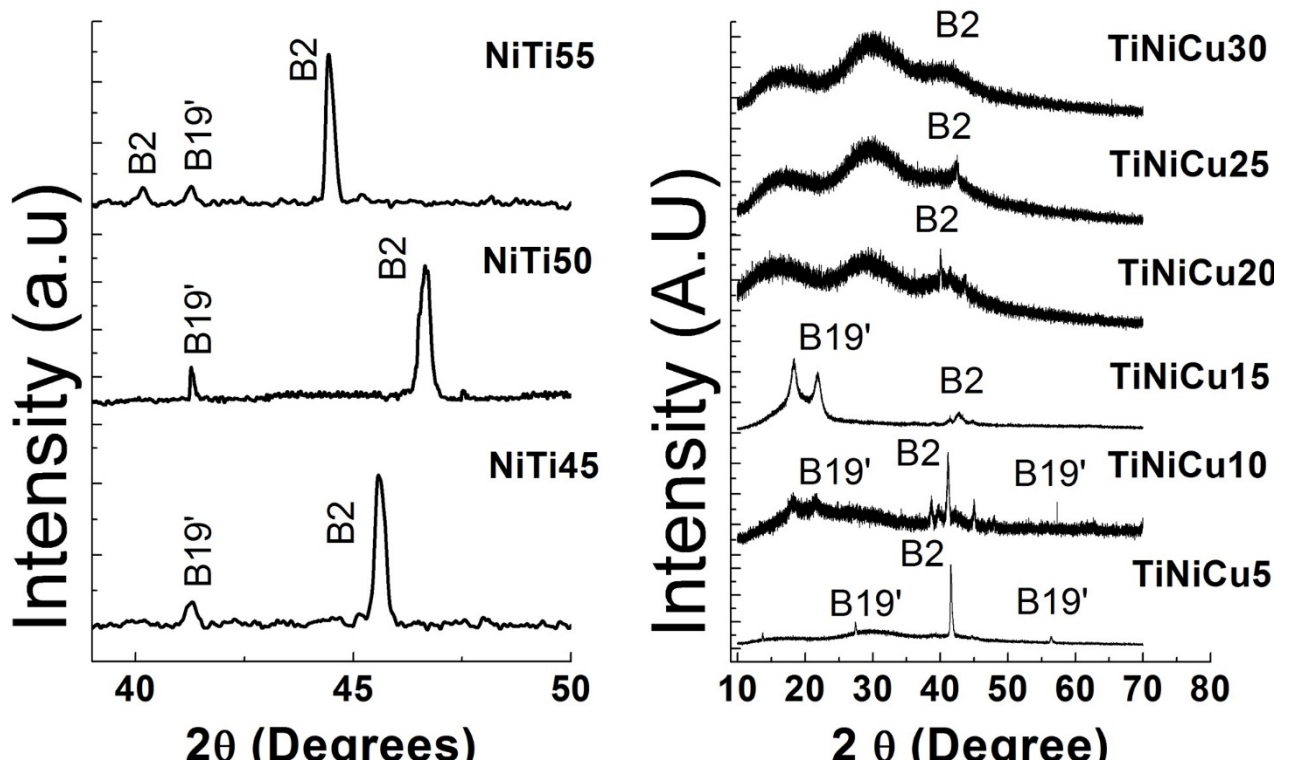


Fig. 4.14 XRD graph of NiTi and TiNiCu samples before and after LSP

4.9 Summary

The effect of LSP was very clearly observed on all samples. The behavior of samples varied due to the compositional variations. The surface morphology showed general changes like increment in surface roughness and decrement in lots of peak structures. The microstructures were closely bonded for NiTi50 and sub sequentially there were no cracks formed on the surface due to LSP, which was not the case for NiTi55 and NiTi45. A mild increase in the elastic modulus was also observed for NiTi50, TiNiCu5 and TiNiCu10, where as it had drastically decreased for NiTi55, NiTi4 and remained the same for TiNiCu samples while comparing with the as manufactured state. The XRD graphs showed the effect of amorphization within the samples as the peak intensity got highly reduced and peak width got broader after LSP. Similar to XRD, Similar to as manufactured state NiTi50, TiNiCu5 and TiNiCu10 can be circled out as the best composition among the three samples developed by LAM.

Chapter 5

Laser Annealing of Bulk Shape Memory Alloy Structures using Laser Additive Manufacturing: Numerical and Experimental Investigation

5.1 Introduction

Though LAM is one of the best options in fabricating the complex shapes, process control yielding homogenous microstructure is difficult due to in-situ alloying and local heating-cooling, the problems of brittleness and porosity existed. By opting LSP the problem of brittleness has been overcome, but as an effect of LSP the amorphization has been taking place on the samples tremendously. Since the alloys we are dealing with are shape memory alloys, crystallinity of the samples developed are of very much importance in order to imply them in real time applications. As conventional furnace annealing yields limited surface homogeneity for varying thicknesses, local annealing is opted as better option for developing complex shaped micro-devices (Bellouard et al. 1999). Earlier researchers have demonstrated annealing by continuous wave CO₂ laser of sputtering deposited NiTi thin films using a zero-contact line scan approach (Liu et al. 2005). Wang et al. (2015) investigated crystallization on NiTi shape memory thin films in which amorphous films are annealed by a scanning laser and found that the laser annealing process produces polycrystalline films with a random crystallographic texture. Annealing of NiTi structures by diode laser yielded remarkable stress recovery effects as reported by (Li et al. 2004). Also, there are some published literature reporting laser annealing of NiTi structure by repeated scanning of continuous wave infrared lasers systems (Mullenix et al. 2007 and Wang et al. 2008). There are also reports that pulsed Nd:YAG laser is deployed for annealing NiTi thin film with various power spots at a wavelength of 1064 nm developed by sputtering on silicone substrate as reported by (Sadrnezhaad et al. 2009).

During the literature survey, it is found that there are no published reports on usage of Nd:YAG laser at 532 nm wavelength for annealing bulk NiTi structures developed using laser additive manufacturing. In this work, an attempt has been made for the first time to investigate the influence of laser assisted annealing using spot overlap and its effect on the shape memory effect. This methodology achieved the homogeneity of crystallization over the entire sample surface. To the best of our knowledge, the laser annealing of laser additive manufactured NiTi structures has not been investigated. As laser annealing of laser additive manufactured structures is important for shape memory effect, we undertook a comprehensive investigation of laser annealing of three different

compositions of NiTi structures. The temperature distribution during laser annealing was simulated using ANSYS 14.0 executed with self-developed APDL codes, to get a better process insight. Subsequently, the laser annealed laser additive manufactured samples were subjected to the same characterizations performed in the previous chapters.

5.2 Numerical Simulation

Annealing process is primarily governed by heating rate, soaking period and cooling rates. In laser annealing, there is no soaking period due to self-quenching of the substrate/object and the heating and cooling rate are predominantly governed by laser parameters and substrate properties. We deployed finite element software to simulate the process and estimate the local temperature distribution at different processing parameters. Subsequently, these distributions were extrapolated to understand the mechanism of laser annealing. The simulation is carried out the software ANSYS14.0 and in-house developed APDL code with the same governing equation, initial final conditions and boundary condition with discussed in chapter 4 with the equation no. (4.1), (4.2) and (4.3) respectively.

A. Laser energy distribution is assumed to Gaussian (Ya et al. 2016). It is mathematically presented as

$$I = \delta I_0 * e^{-\left[2r^2/r_l^2\right]} \quad (5.1)$$

where, r_l stands for radius of laser (m) and $r = \sqrt{x^2 + y^2}$. The MKS units were followed while determining constants in Eq.(5.1).The value of I_0 (Toyserkani et al. 2004) can be derived by the formula $I_0 = \frac{2P}{\pi r^2}$, where P stands for laser beam power. The value of $\delta = 1$ when the laser is on, and $\delta = 0$ when the laser is off. The changes in the value of δ depends on the laser pulse shaping parameters like frequency F and pulse width.

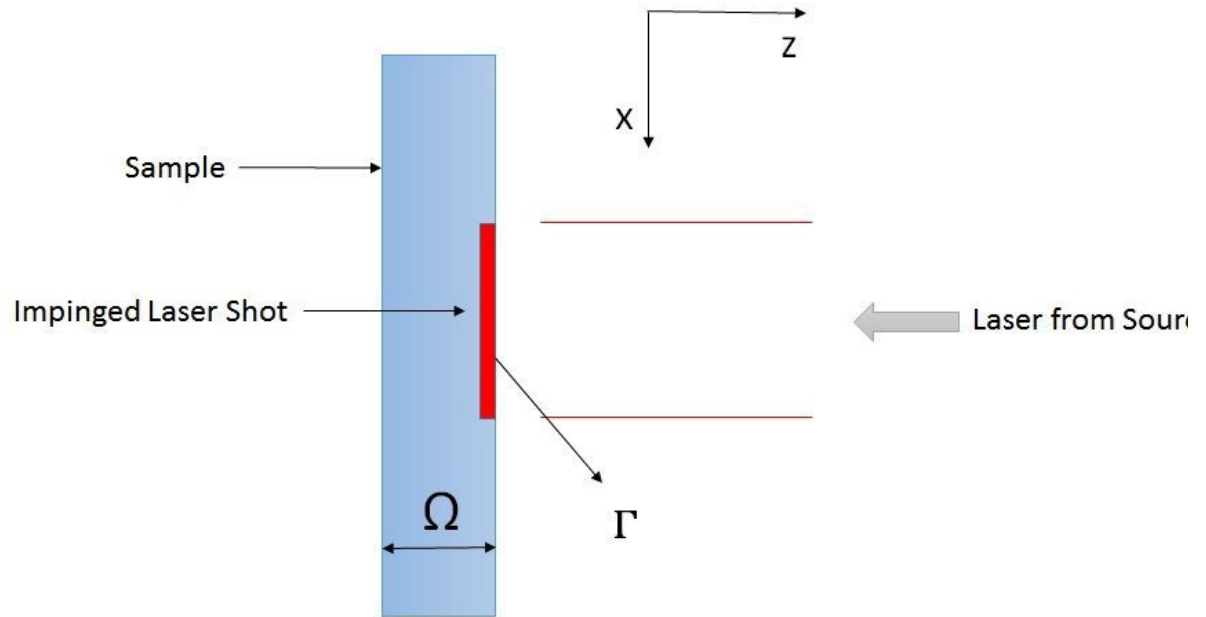


Fig. 5.1 Schematic arrangement for laser annealing

- B. The material properties are assumed to be constant for the all the temperature. The values used for the calculations are tabulated in Table 3.1
- C. The wall thickness is assumed to be equal to the laser beam diameter, which in turn is much less than the length and height, so that heat conduction is restricted to the (x, z) plane. It converts the simulation into two dimensional analyses.

The developed numerical methodology was deployed to study the effect of various laser intensity levels on annealing by predicting the temperature distribution.

5.3 Laser annealing of NiTi and TiNiCu bulk structures

Fig. 5.2 presents a typical structure that used for annealing. The dimensions of NiTi structures fabricated using laser additive manufacturing were 200mm length, 75 mm width and 1 mm thickness. The substrate used was a titanium plate of 100 mm x 100 mm x 10 mm, as it is earlier reported that the de-bonding coefficient between NiTi and titanium is very small and it enables easy partition of deposit during manufacturing.

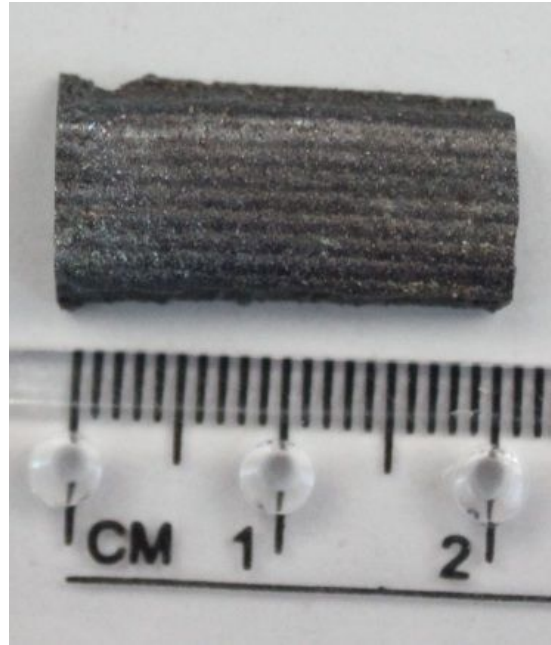


Fig. 5.2 Typical laser additive manufactured sample used for laser annealing.

The laser annealing experiments were carried out by shining the second harmonic of Nd:YAG laser (Quanta-Ray INDI) on the sample mounted on X-Y manipulator. The schematic arrangement of laser annealing set up is presented in Fig. 5.3. The second harmonic of Nd:YAG laser was used, as it yields improved performance due to shorter wavelength as reported by (Palani et al. 2008). The process parameters used for laser annealing experiments are presented in Table 5.1.

Table 5.1 Processing Parameters used in the laser annealing experiments

Parameter	Unit	Value
Laser wavelength	nm	532
Mode of operation	-	Q-switched
Laser energy per pulse	mJ	10
Laser pulse duration	ns	9
Laser pulse frequency	Hz	1
Laser spot size	mm	2
Spot overlap	%	90

The frequency and the spot overlap are the parameters that affect the reduced cooling rate and uniform heat absorbing zone during laser annealing. They, also, result in reduced dilution and crack elimination. In general, the frequency of 1 Hz and spot overlap of 90% indicated good laser annealing as reported by (Palani et al. 2008) .The annealed samples were characterized using a number the same techniques discussed previously to study the influence of laser annealing in the developed NiTi and TiNiCu samples.

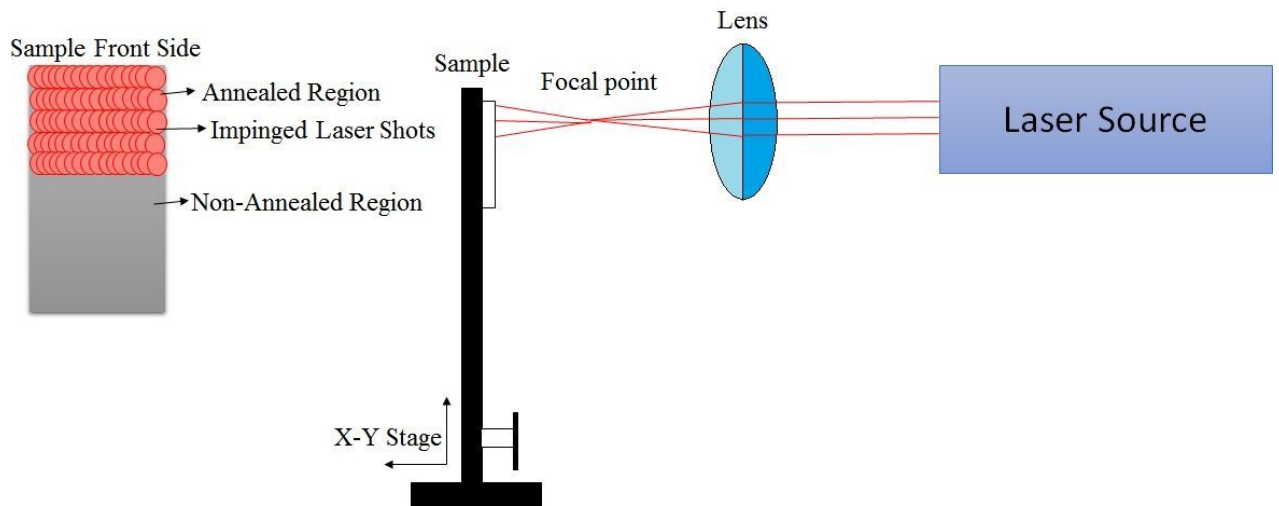


Fig.5.3 Experimental set up for laser annealing

5.4 Simulation and Validation:

As the effect of laser processing of NiTi and TiNiCu structures are predominantly governed by processing parameters and substrate properties, it was attempted to simulate the process condition to reduce the number of experimental trials. A thermal model was simulated to find the impact of laser wavelengths and laser beam intensity profiles on the formed NiTi thick film, in order to implement the best parameter for TiNiCu as well. First, the entire sample was meshed and converted into smaller elements. The heat flux was fed based on the laser input energy. The convective boundary conditions were considered as described above. The temperature distribution was calculated in the NiTi deposit and part of the substrate. The starting of the phase transformation was considered when local temperature is 50 °C above the recrystallization temperature.

The temperature profile of various laser intensities were simulated with the spot diameter of 2 mm and their impact on the sample was analysed, in parallel, using SEM. Figure 5.4 presents the temperature distribution for various laser energy density 900 mJ/cm^2 , 1000 mJ/cm^2 , 1100 mJ/cm^2 and 1200 mJ/cm^2 . The SEM images of NiTi samples after facing a single laser shot at the mentioned laser energy density. The predominant effect of varying intensities was seen in the SEM images. The maximum temperatures observed in these simulation results were $489 \text{ }^\circ\text{C}$, $530 \text{ }^\circ\text{C}$, $566 \text{ }^\circ\text{C}$ and $614 \text{ }^\circ\text{C}$. It was seen that the temperature difference increases with the increase in the laser energy density, but there is no visible change in the depth of temperature distribution. At laser energy density of 900 mJ/cm^2 , there was no visible effect on the specimen surface.

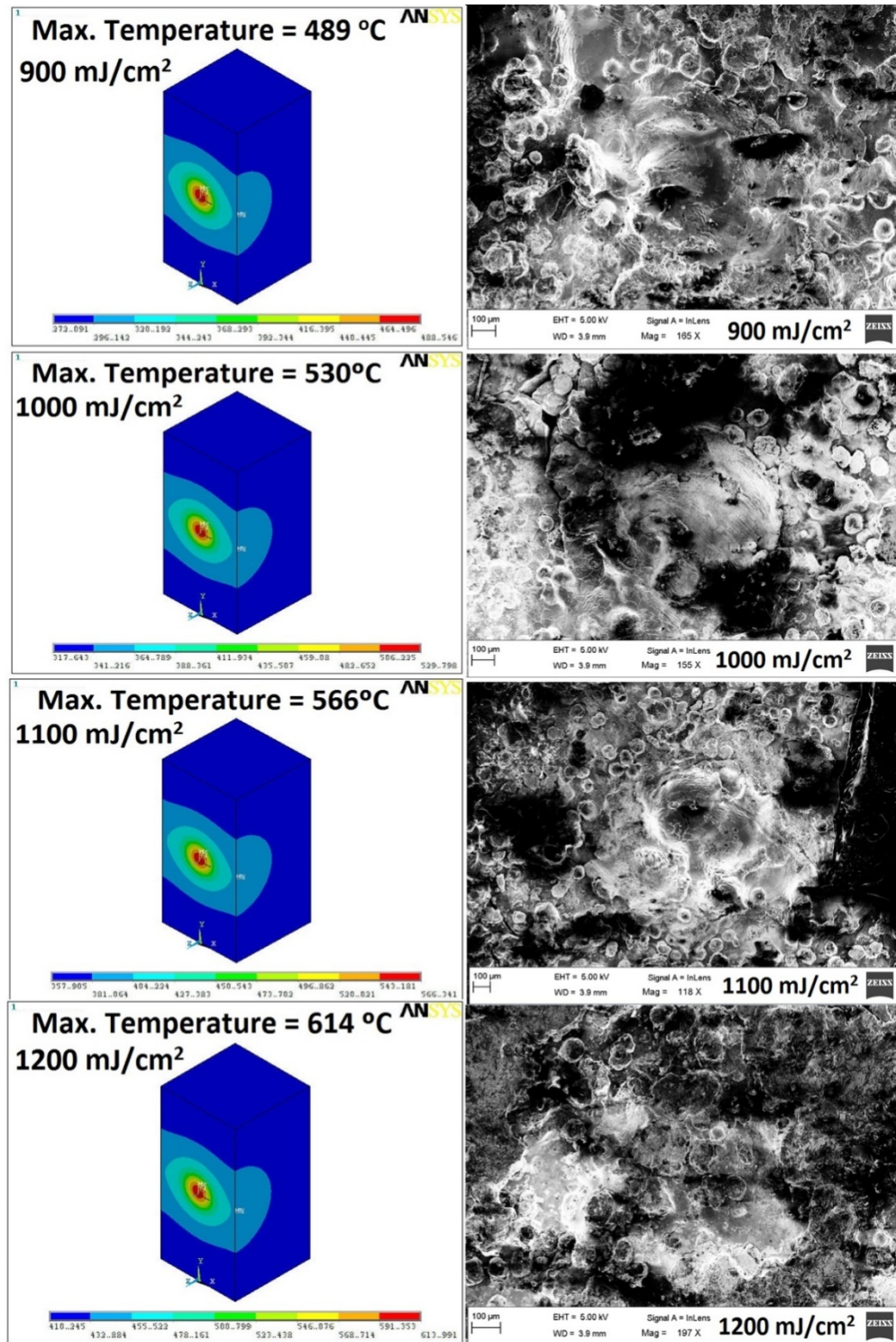


Fig. 5.4 Simulated temperature profile of (a) 900 mJ/cm² (c) 1000 mJ/cm² (e) 1100 mJ/cm² (g) 1200 mJ/cm² and SEM images of (b) 900 mJ/cm², (d) 1000 mJ/cm², (f) 1100 mJ/cm², (h) 1200 mJ/cm²

Laser energy density of 1000 mJ/cm^2 showed a blend of partial annealing and impact of laser as a thin layer of NiTi material which was in excess at the outer surface has formed a paste like structure evenly spread on the specimen. Likewise for laser energy density of 1100 mJ/cm^2 revealed a complete blend of the materials on the surface which had formed a pool of lava like structures with molten NiTi surface material. When the laser energy density was more than 1100 mJ/cm^2 , the dark patch was observed, confirming complete ablation at 1200 mJ/cm^2 .

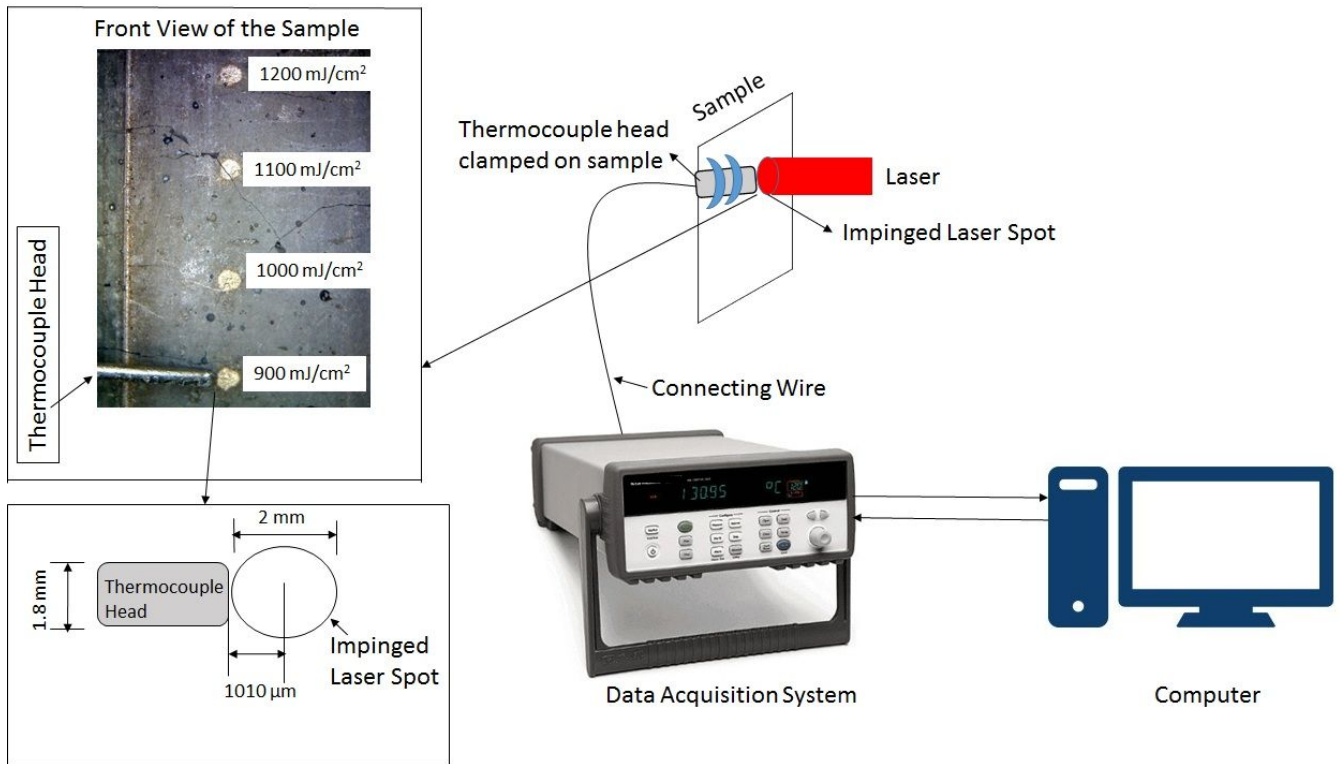


Fig. 5.5 Experimental set up for measuring the temperature generated by various laser energy densities

To validate the simulation, temperature measurement experiments were carried out using set up shown in Fig. 5.5. The setup consisted of a 'K' type thermocouple connected to a data acquisition system (Agilent, Model no. 34970A) and a computer using a general purpose interface bus (GPIB). The sample of equiatomic composition (NiTi50) for binary and TiNiCu5 for ternary alloy was chosen for the experiment as it displayed better results in the previous processing as well. The thermocouple was clamped on the sample exactly at minimum distance of $10 \mu\text{m}$ from the laser impinging spot to avoid the laser spot's direct contact with the thermocouple head. The diameter of the thermocouple head (1.8 mm) was less than the diameter of the laser spot (2 mm) for obtaining precise results. The

temperature of the work-piece was measured using the above setup for various laser energy density and compared with the simulated results (refer in Fig. 5.6). It is seen that the simulated and experimental results are fairly close ($\pm 20\text{ }^{\circ}\text{C}$). The variation may be attributed to the other heat losses during the real time experiments. As per the simulation results and the SEM images shown in Fig.5.4 laser energy density of laser energy density of 1000 mJ/cm^2 shows improper annealing and laser energy density of 1200 mJ/cm^2 confirmed ablation. Since the annealing temperature of NiTi is in the range of $500\text{ }^{\circ}\text{C}$ and the results in Fig. 5.4 showed good annealing by laser energy density of 1100 mJ/cm^2 . This value was opted for the annealing process of NiTi and TiNiCu samples.

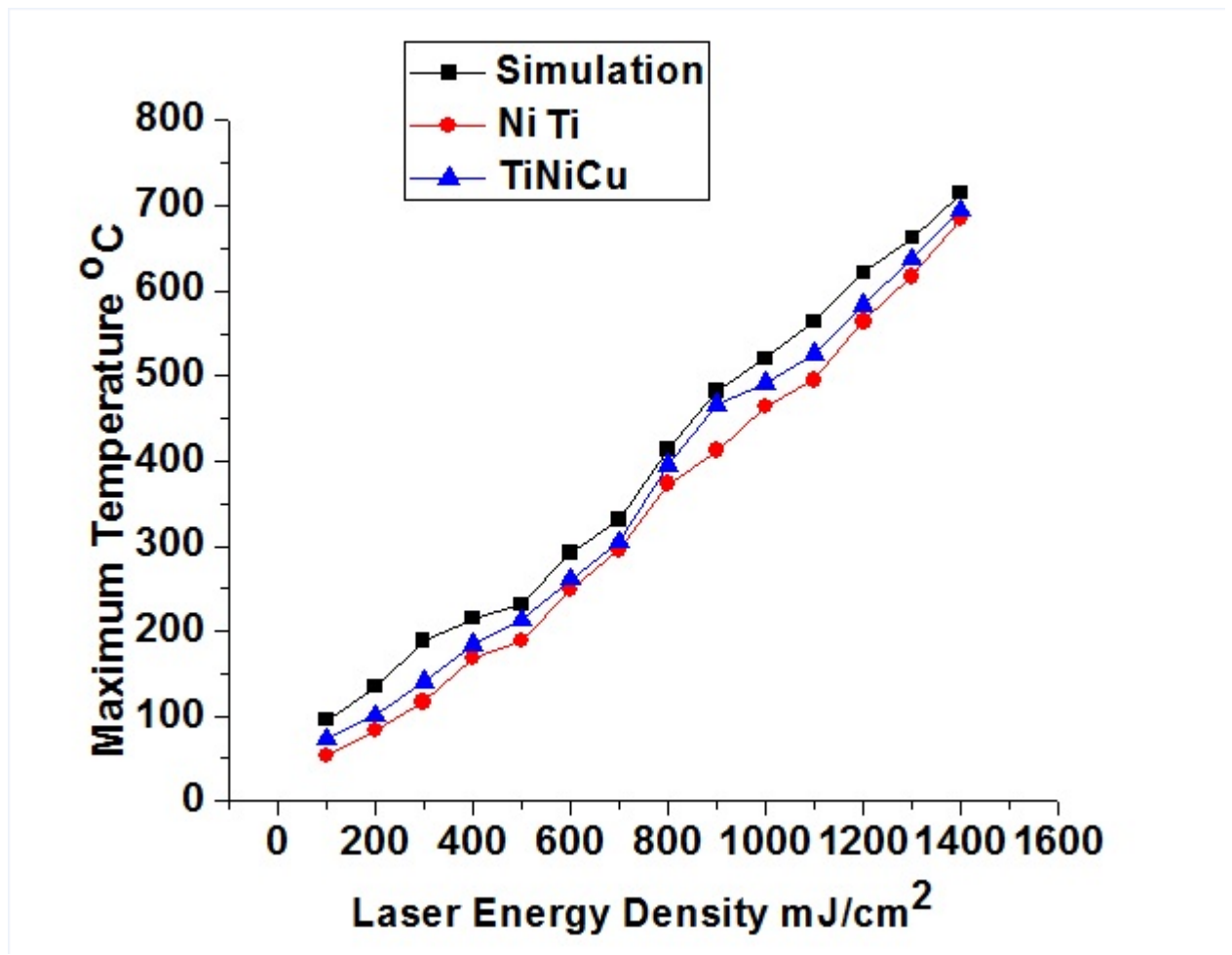


Fig. 5.6 Comparison between simulated and real time experimental temperature values for various laser energy densities

5.5 Surface morphology

5.5.1 Scanning electron microscopy examination

Figure 5.7 shows the SEM images of laser annealed samples, and it was noted that the surface of all the samples have become smoother. This variation is due to the impact of interaction between impinged laser spots and the surface of the formed samples. Very few pores were observed on the surface of TiNiCu15 and TiNiCu20. Presence of mild oxide layer was found on the surface of NiTi45 sample. In case of NiTi, TiO₂ oxide layer formation is a very common. Also among the two elements in the alloy Ti tends to form the oxide layer as the diffusion rate of Ti with oxygen is higher than Ni. In case of TiNiCu hardly any oxide layer is formed on the surface of the samples. The reason is when Cu is present in an alloy, the oxide layer tends to form on the surface actively when the environment goes above 600°C. In the current work the temperature is maintained below 600°C, hence the chance of oxide layer formation becomes very less. But still things can be more clearly confirmed with XRD results in the sessions ahead. The results of EDS after laser annealing are quoted in the table

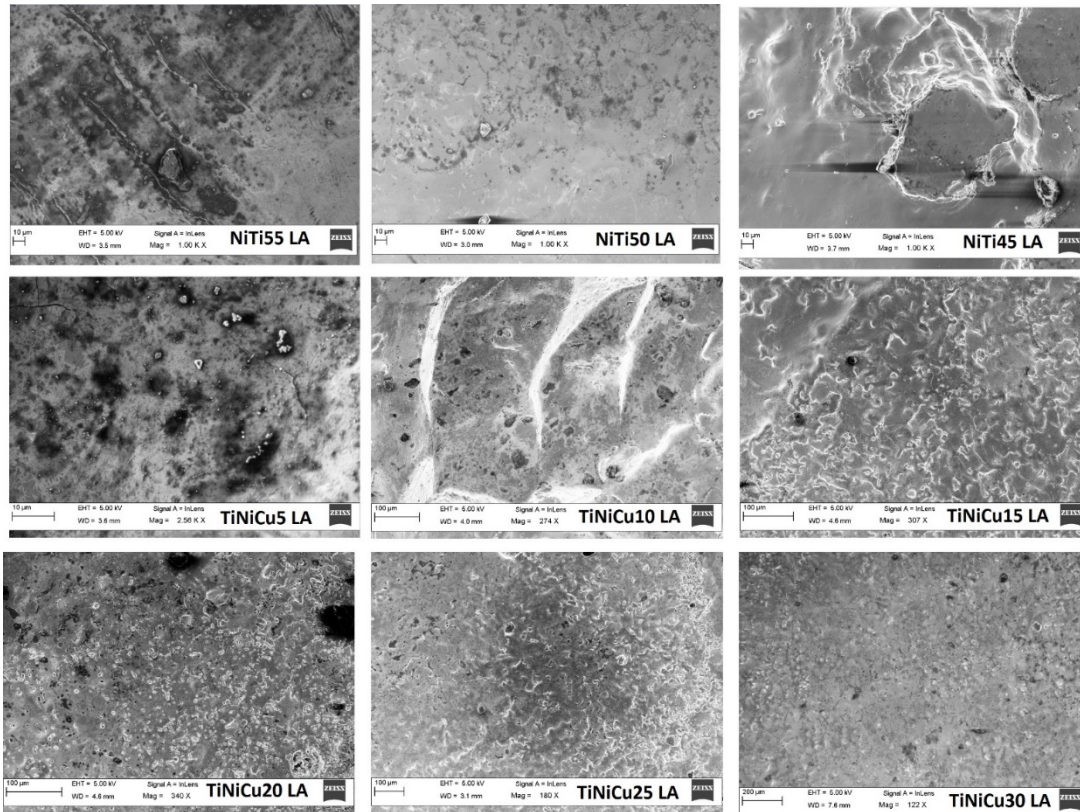


Fig. 5.7 SEM images of the NiTi and TiNiCu samples after laser annealing

NiTi55 and TiNiCu5 showed some pimple like structures on the surface as a result of re-melting of the sample after laser annealing. The dark region on the surface of the sample is Ti. It was found Ti has uniformly accumulated in particular regions rather than getting uniformly distributed throughout the surface. For NiTi45 and TiNiCu30 show there is not much Ti accumulation but mild settlements were seen here and there almost throughout the sample, spread uniformly. But NiTi50 and TiNiCu10 it was so clearly seen that the blend between nickel and titanium is so uniform throughout the sample. EDS results confirm the amount of nickel and titanium present in this mixture is very close to each other almost for all samples.

Table 5.2EDS results of NiTi and TiNiCu samples after laser annealing

Samples	Ti (Wt %)	Ni (Wt %)	Cu (Wt %)
NiTi55	42.36	57.64	
NiTi50	51.14	48.86	
NiTi45	52.	47.66	
TiNiCu5	55.47	40.21	4.32
TiNiCu10	56.17	38.56	5.27
TiNiCu15	57.75	30.82	11.43
TiNiCu20	52.37	32.76	14.87
TiNiCu25	59.29	27.20	13.51
TiNiCu30	48.95	27.98	23.07

5.5.2 Microstructure analysis

Figure 5.8 shows the microstructure of annealed NiTi and TiNiCu samples. The grain size seemed to be quite similar with little increase to the samples before they were annealed as shown in previous chapter. Most importantly the amorphization has been completely eliminated for all the samples microstructure seems to be tightly packed and well organised with much of irregularity in their shape. From the Fig. 5.8, it is clear that the grain size of all samples show they are arrayed in such a way that there is no much space between each other and most importantly they are uniform in size and shape. All the samples have a grain size in spherical structure. In both NiTi and TiNiCu alloys have

fine grain structure due to the suppression of the Ni_4Ti_3 and $\text{Ti}_3(\text{NiCu})_4$ precipitates during the development of the samples. On the other hand the is bigger grain size due to the rise of Ti_2Ni and $\text{Ti}_2(\text{NiCu})$ precipitate which forms due to difference in diffusivity between Cu, Ni and Ti during the fabrication process. Though the increase in grain size is directly proportional to the increase in surface roughness, in our case the surface roughness of the samples have considerably improved than after LSP. This can more clearly be confirmed by comparing the values of grain size obtained by AFM results in the following section with the surface roughness results quoted in Table 3. After annealing the microstructure image seems to have gained an organised alignment because image shows more uniform structures than before they were annealed. From Fig. 5.8 it is so clear that it has the finest microstructures among all the three. NiTi50 seems to be the best combination with good qualities of SMA as reported earlier with SEM image.

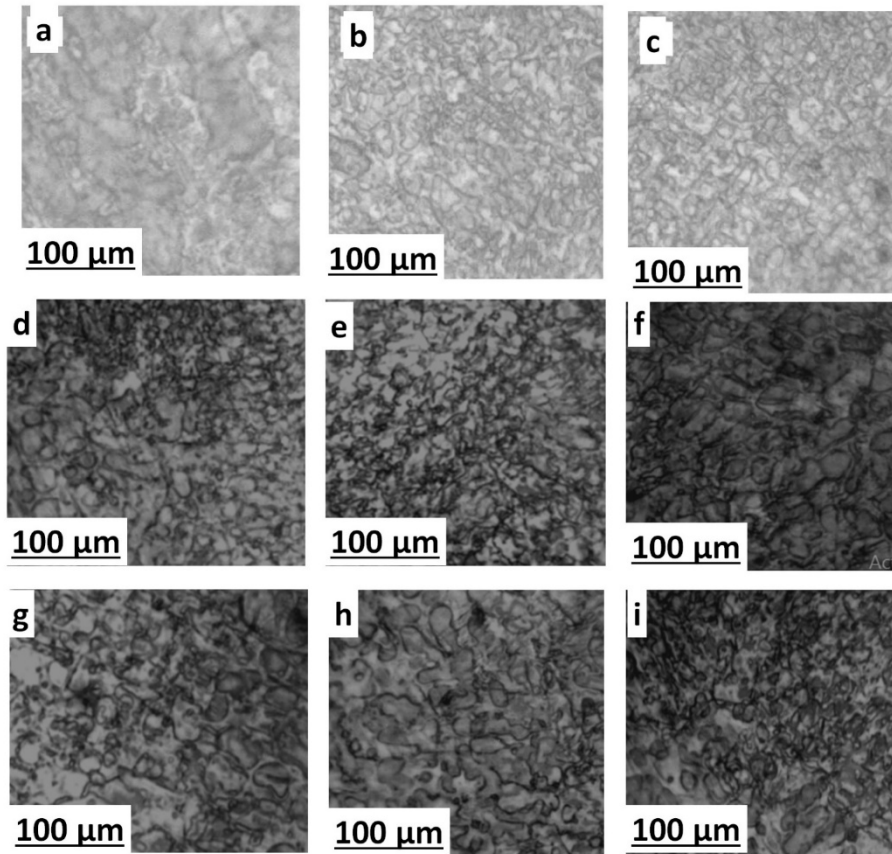


Fig. 5.8 Microstructure images of the NiTi and TiNiCu samples after laser annealing

5.5.3 Atomic force microscopy examination

Figure 5.9 shows the three dimensional AFM images recorded for the annealed samples. NiTi55 and NiTi50 are of dimension 2 μm X 2 μm . NiTi45, TiNiCu10, TiNiCu15 and TiNiCu30 are of dimension 1 μm X 1 μm . TiNicu5, TiNiCu20 and TiNiCu25 are of dimension 500 nm X 500 nm. Globular microstructures were arrayed uniformly throughout the sample is seen in all images. This indicates good quality of deposition and homogeneity of annealing with laser. The average height difference lies between 10 to 20 nm. The uniqueness of the samples is seen from their corresponding surface roughness values and grain size values. Since the globular structures are present high the kurtosis values are also expected to be less than 3. The measured grain size , surface roughness and kurtosis values are as quoted in the Table 5.3. The variations in the grain size values and surface roughness are completely attributed to the effective laser annealing.

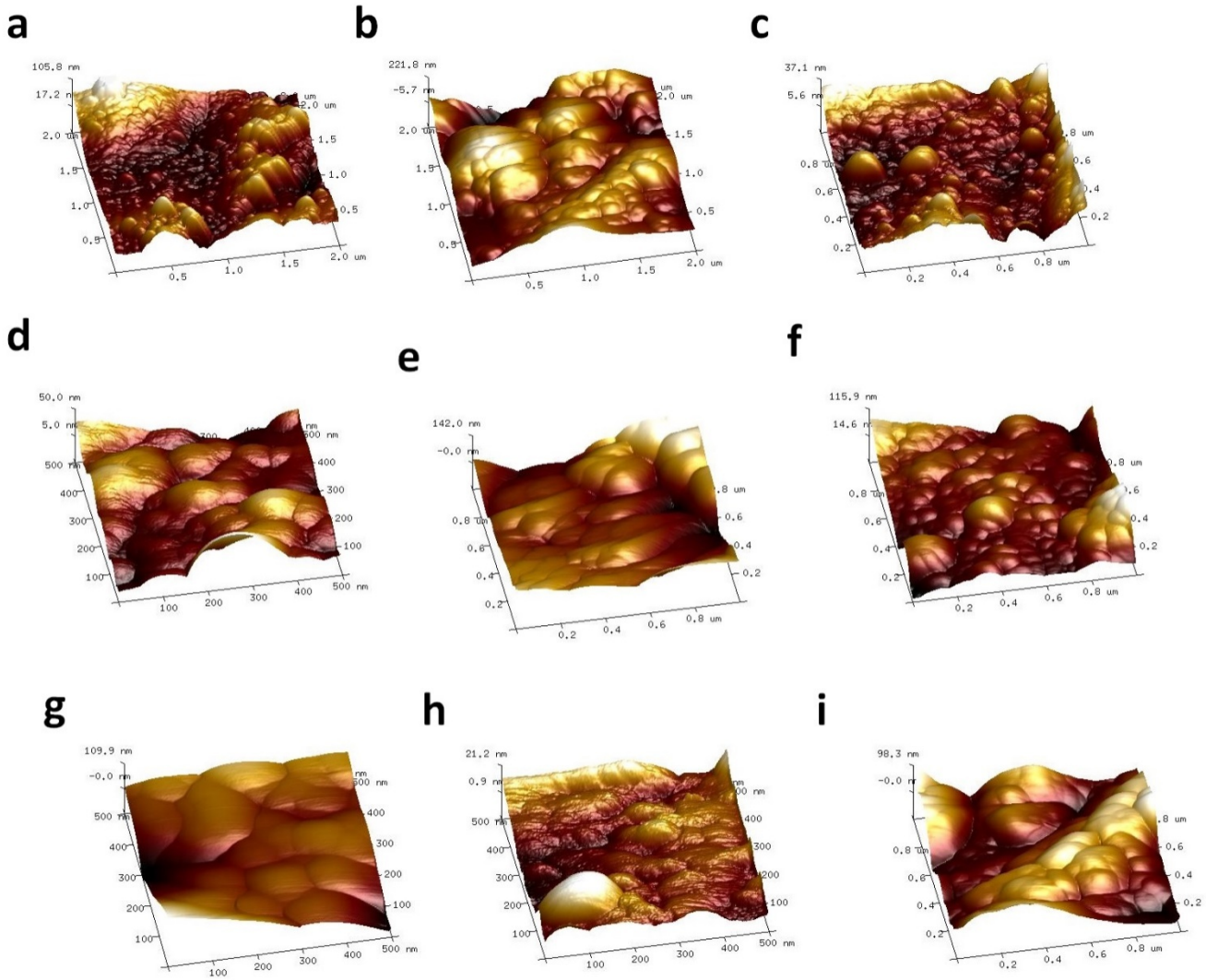


Fig. 5.9 AFM images of the NiTi and TiNiCu samples after laser annealing

Table 5.3 AFM results of the samples after laser annealing

Samples	Grain Size (nm)			Surface Roughness (nm)			Kurtosis Value		
	Before LSP	After LSP	After LA	Before LSP	After LSP	After LA	Before LSP	After LSP	After LA
NiTi55	55.45	48.49	55.18	3.73	2.76	3.97	3.39	3.83	3.12
NiTi50	31.73	28.76	34.69	3.16	4.73	3.22	3.63	3.89	2.87
NiTi45	39.12	35.43	37.23	2.57	2.83	2.08	3.45	3.76	3.25
TiNiCu5	18.41	16.12	19.05	3.22	3.89	3.52	2.25	2.90	2.64
TiNiCu10	20.12	21.08	22.57	3.97	4.36	4.27	2.88	3.09	2.95
TiNiCu15	38.26	35.64	38.41	6.21	6.97	6.54	3.74	3.95	3.37
TiNiCu20	33.57	31.47	34.39	5.83	6.17	6.24	2.94	3.35	2.98
TiNiCu25	21.61	18.75	23.86	4.76	5.28	4.98	3.04	3.17	3.09
TiNiCu30	25.51	20.13	24.92	4.25	4.91	4.35	3.54	3.92	3.27

5.6 Mechanical Properties Evaluation

5.6.1 Micro-hardness Measurement

The laser annealed samples were bisected transversely to the direction of lying and prepared using standard metallographic techniques and micro-hardness measurement was carried out at an incremental distance of 25 μm at a load of 500 g. Fig. 5.10 presents the results of micro-hardness

measurements of both NiTi and TiNiCu samples. The average value of micro-hardness was found to be 397, 342 and 382 VHN for annealed NiTi55, NiTi50 and NiTi45, respectively. The values for TiNiCu are 223, 237, 248, 252, 244 and 273 VHN respectively. The value of average micro-hardness was more for NiTi55 and TiNiCu30. As per the indications earlier in the EDS results this because of the Ti weight percentage's impact in the alloys, resulting in the formation of hard phases. Since the micro-hardness is more for NiTi55 and TiNiCu30 samples, the ductility is likely to be less. From the results obtained in the graph shown in Fig. 5.10, it's very clear that the VHN values for TiNiCu samples are almost very close to each other, than NiTi samples.

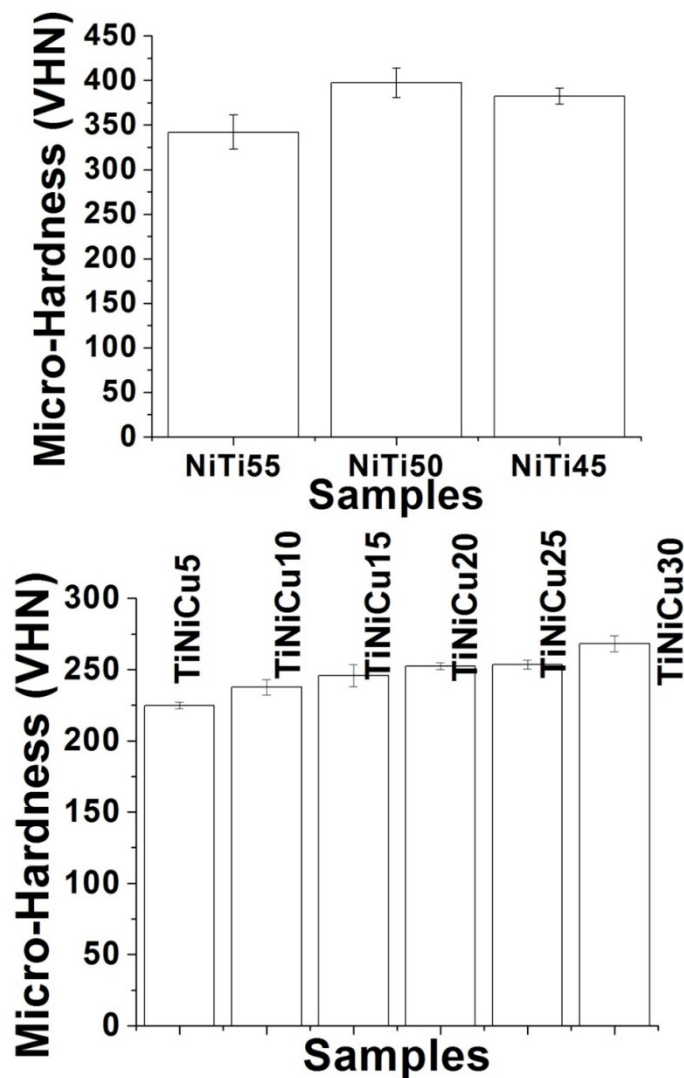
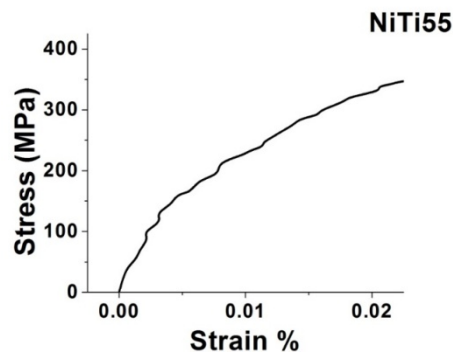
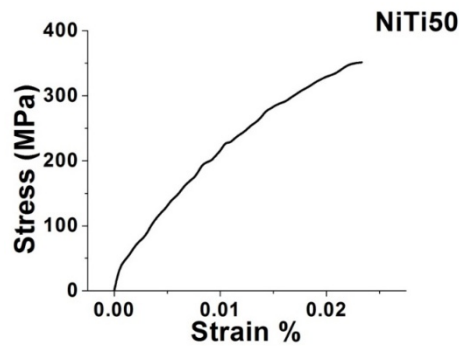
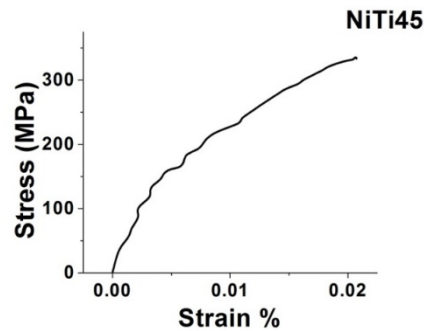


Fig. 5.10 Micro-hardness values of NiTi and TiNiCu samples after laser annealing

5.6.2 Compression test

The compressive strength and the corresponding modulus values of laser annealed and non-annealed samples are quoted in Table 5.4. The values of non-annealed samples were taken from our previous work. From the Fig.5.11, mild variations in the engineering stress strain curve before and after annealing can be seen. After annealing the samples have faced an increase in ultimate strength and elastic modulus obtained by tensile tests. In spite of brittleness being a hindrance to ductility, mild improvement was observed uniformly for all samples as a result of laser annealing. The elasticity and ultimate tensile strength were found to be good for the equi-atomic composition and TiNiCu5 and TiNiCu10 in ternary alloys. Thus the impact of laser annealing is clearly visible in both NiTi and TiNiCu samples.



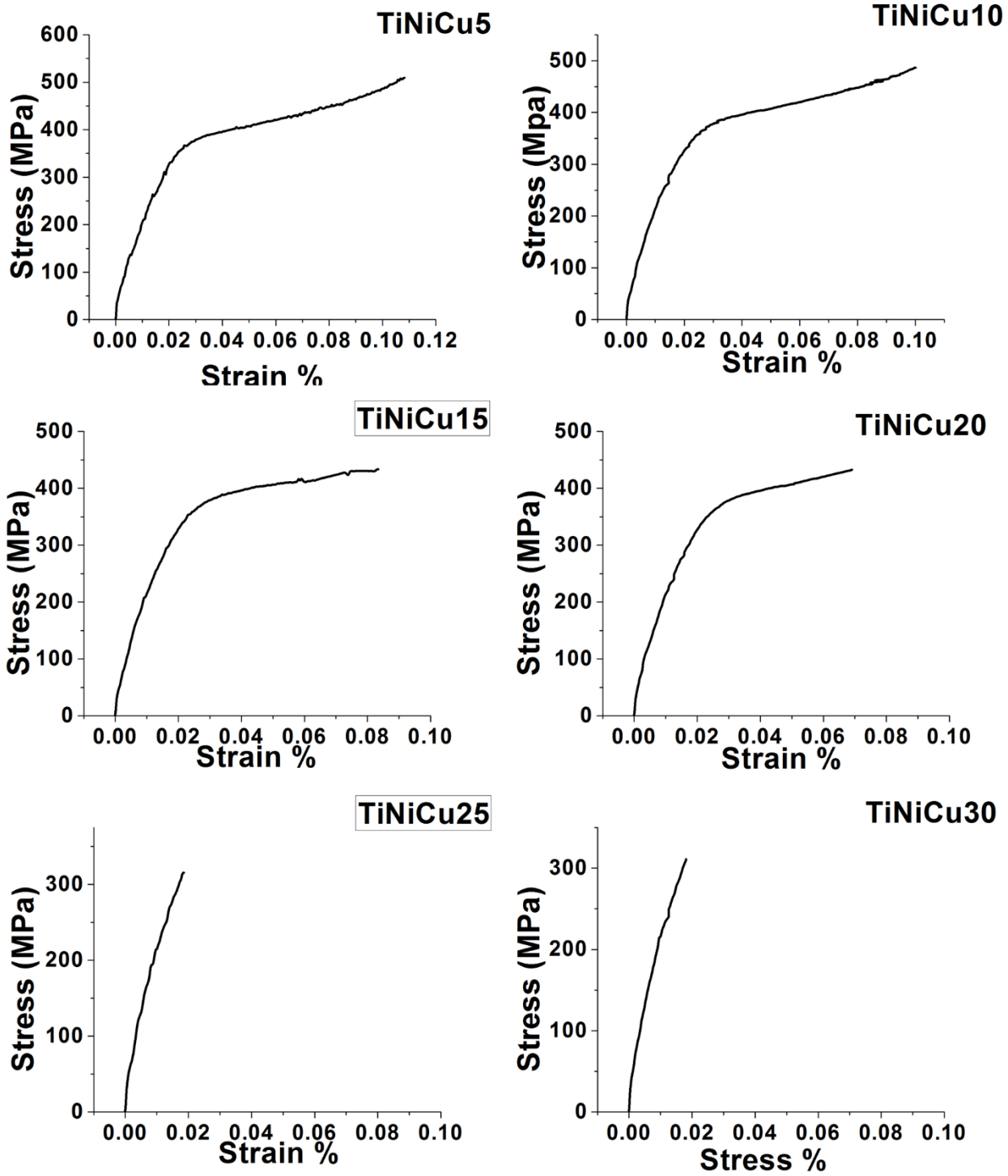


Fig. 5.11 Stress Strain images of NiTi and TiNiCu samples after laser annealing

Table 5.4 Mechanical properties after laser annealing

Samples	Ultimate Strength (MPa)			Youngs Modulus		
	Before	After	After	Before	After	After
	LSP	LSP	LA	LSP	LSP	LA
NiTi55	296	333	350	20	15	18
NiTi50	315	403	422	21	22	21
NiTi45	320	378	396	21	21	23
TiNiCu5	451	473	510	28	25	28
TiNiCu10	430	448	486	28	26	25
TiNiCu15	412	427	433	26	25	27
TiNiCu20	402	423	430	24	21	24
TiNiCu25	397	306	315	25	22	26
TiNiCu30	386	296	310	22	21	23

5.7 Crystalline Properties Property Evaluation Using X-Ray Diffraction Analysis

Fig. 15 shows the XRD spectrum of the formed samples. The presence of two phases, i.e., austenite and martensite were obtained. All the patterns of the samples had narrow peaks which clearly intimate the presence of well crystallized grains in fine sizes. There are lots of incomplete martensite

peaks formed and also all these peaks are split. Lots of spectrums had emerged after laser annealing clearly indicating the impact of efficient laser annealing. The untransformed martensite peaks formed on the annealed samples were because of the Ni rich layer which gets developed right under the oxide layer as an effect of laser annealing which are absent in samples after LSP. Absence of precipitates in the annealed sample is due to the less time of contact between the laser and the surface of the specimen, whereas in conventional annealing enough time is available for the NiTi alloy to react with heat to form precipitates. From the XRD graphs we can conclude the samples of NiTi have been finely processed by the laser annealing which had converted it crystalline nature. Laser annealing through the opted laser energy density level has also brought no harm to the nature of the material physically and chemically.

From Fig.5.12 it's known that NiTi55 has its austenite peak in cubic structure at $2\theta = 41^{\circ}24'$ and its parallelly accompanied by martensite peaks with monoclinic structure at $2\theta = 38^{\circ}78'$ and $2\theta = 42^{\circ}25'$ on either sides. NiTi50 has its cubic structured austenite peak at $2\theta = 41^{\circ}38'$ and its monoclinic structured martensite peaks at $2\theta = 38^{\circ}94'$ and $2\theta = 42^{\circ}44'$ on either sides parallelly. The NiTi45 sample has its austenite peak at $2\theta = 41^{\circ}26'$ and martensite peaks at $2\theta = 38^{\circ}78'$ and $2\theta = 42^{\circ}60'$. By using these XRD spectrums the crystallite size of the samples can be obtained using Scherrer's formula as discussed earlier. The calculated grain size values of NiTi55, NiTi50 and NiTi45 are 60.94nm, 37.21nm and 43.57nm respectively. The values obtained were quite close to the values of AFM experiments and also supported by the microstructure image results in section 4.2. From the curves of ternary alloy it is very clear that TiNiCu5 and TiNiCu10 have the peaks at the exact position of $2\theta = 42^{\circ}44'$. Also the influence of laser annealing was able to re appear the peaks that had disappeared due to LSP.

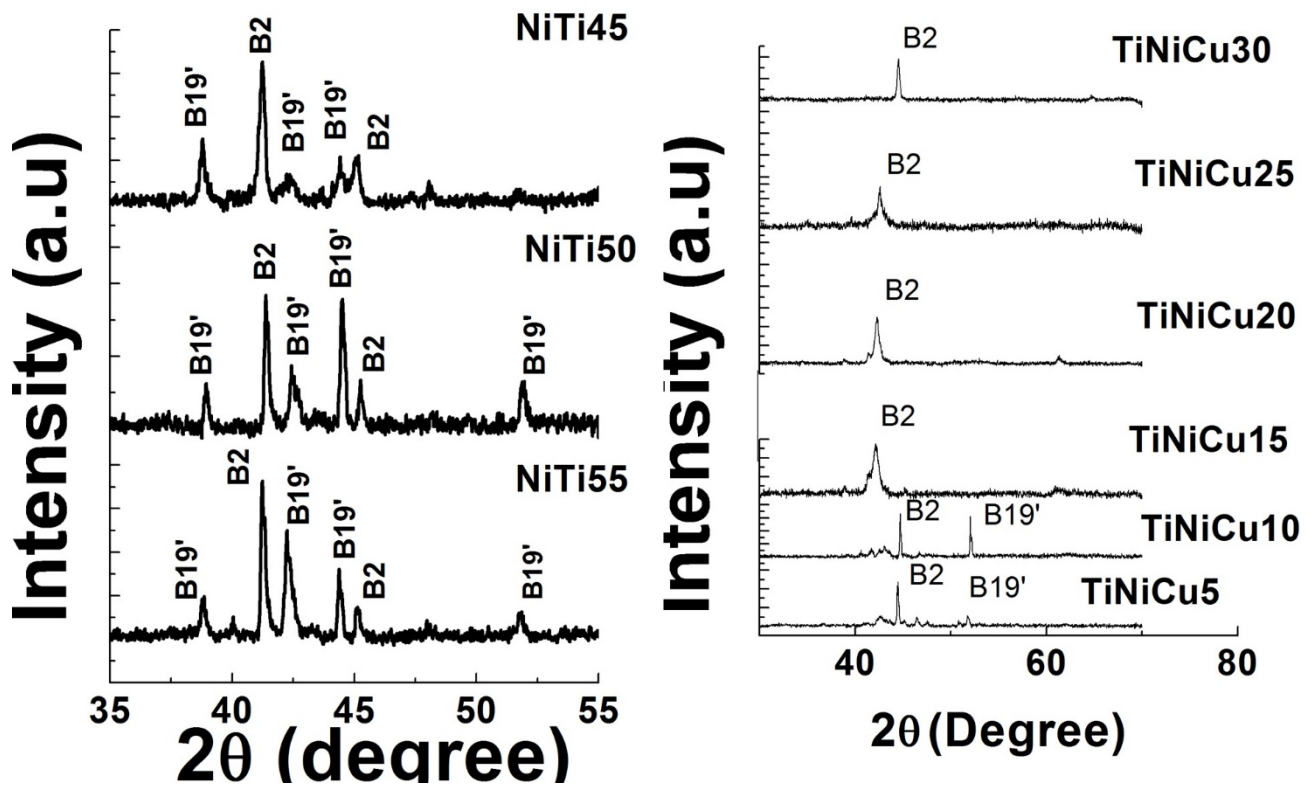


Fig. 5.12 XRD graphs of NiTi and TiNiCu samples after laser annealing

5.8 Influence of Laser annealing

The main reason behind deploying laser annealing for the samples is, too much of heating can spoil NiTi's SMA characteristics. That's because heating NiTi more than 630°C due to eutectic decomposition lots of Ni₃Ti precipitates will form. Moreover in conventional furnace annealing heat is completely distributed right from bottom to the top of the thick film with no control on selectiveness of the surface. Hence, higher loss of heat energy becomes inevitable. In order to prevent all these types of loss laser annealing was chosen and it has given some exceptionally good results. Nd:YAG laser annealing at 532nm wavelength has revealed some unique advantages over the remaining laser annealing as well. AFM results show a smoother surface morphology than the results of samples annealed with CO₂ laser as reported in earlier works [9,10]. Results of scanning laser [11] show the presence of cracks on the surface of the samples which is not the case in the current work. Increase in grain size the general effect of annealing is clearly visible in Nd:YAG laser annealing

than the diode laser annealing [12]. Risk of ablation is high while using Infra-red laser for annealing [13,14], whereas in Nd:YAG laser annealing the risk of ablation is under control. The same Nd:YAG laser is not able to produce smoother surface morphology revealed by SEM when 1064 nm wavelength annealing is done [15]. Just like the results of as manufactured samples [20], the NiTi50 combination continues to dominate the other two samples. SEM results flaunt the NiTi50 structure's improvement to good shape after annealing. The micro-hardness values also show some slight variation towards increment. That has led to its decrease in ultimate strength and elastic modulus. XRD shows good peaks in martensite phase as well as austenite phase. Especially in NiTi50 spectrum shows the position of its martensite peak and austenite peak have shifted towards higher angle. This is actually indicating compression and reduction in space between the lattice planes. So this confirms the efficiency of the laser annealing done and also indicates good crystalline nature of the sample. DSC graphs also support this point as the phase transformation peaks have become steeper after annealing than the remaining two samples.

From the above consolidated results it's very clear that NiTi50 has improved itself in many correlations in their characteristics like surface morphology, structure and shape memory effect than the remaining two samples. Most interesting thing was NiTi45 has also gathered itself into better shape through laser annealing giving some improved results, than they were in the as-made state. Similarly the nature of TiNiCu5, TiNiCu10 showed good results after Laser annealing.

Chapter 6

Phase transformation and shape memory characteristics of the developed samples

6.1 Introduction to Dynamic Mechanical Analysis (DMA)

Dynamic Mechanical Analysis (DMA) can be simply described as applying an oscillating force to a sample and analyzing the material's response to that force (Figure 1.1). From this, one calculates properties like the tendency to flow (called viscosity) from the phase lag and the stiffness (modulus) from the sample recovery. These properties are often described as the ability to lose energy as heat (damping) and the ability to recover from deformation (elasticity). The above mentioned property of the materials are used to study the shape memory characteristics of SMA by researchers in the past. The applied force is called stress and is denoted by the Greek letter σ . When subjected to a stress, a material will exhibit a deformation or strain, γ . The modulus is dependent on the temperature and the applied stress. The modulus indicates how well a material will work in a specific application in the real world. One advantage of DMA is that we can obtain a modulus each time a sine wave is applied, allowing us to sweep across a temperature or frequency range. So if we were to run an experiment at 1 hertz (Hz) or 1 cycle/second, we would be able to record a modulus value every second. This can be done while varying temperature at some rate like $5^{\circ}\text{C}-10^{\circ}\text{C}/\text{min}$ so that the temperature change per cycle is not significant. The modulus measured in DMA is, however, not exactly the same as the Young's modulus of the classic stress-strain curve. Young's modulus is the slope of a stress-strain curve in the initial linear region. In DMA, a complex modulus (E^*), an elastic modulus (E') and an imaginary (loss) modulus (E'') are calculated from the material response to the sine wave. These different moduli allow better characterization of the material because we can now examine the ability of the material to return energy (E'), to lose energy (E''), and the ratio of these effects ($\tan \delta$), which is called damping. Materials also exhibit some sort of flow behavior, even materials we think of as solid and rigid.

6.2 Phase transformation property in as manufactured state

Phase transformation property is a primary requirement for SME. The presence of phase transformation confirms the ability of the formed samples to poses SME. In order to analyze this property in detail, differential scanning calorimetry (DSC) was used. Fig. 6.1 presents the DSC

curves of NiTi55, which indicates the formation of some improper NiTi structures. This is clearly visualized in the DSC curves as there are no phase transformation curves visually seen. The Austenite start temperature (A_s) = 2°C and Austenite finish temperature(A_f) =21°C likewise Martensite start temperature(M_s) = 5°C and Martensite finish temperature(M_f) = -15°C are not clearly visible in the plot, this might be, due to the lattice mismatch. Fig. 8(b) shows the corresponding DSC graph of NiTi45, in which the plots of M_s = -38°C and M_f = -45°C similarly A_s = - 40°C and A_f = -21°C. The curves in both heating and cooling are mildly visible. In Fig. 6.1 NiTi50 composition's graph shows some presence of R phase. Details about R phase are elaborated in the forthcoming XRD analysis session. In the combination of NiTi50 actuation curves obtained are visible. In the DSC A_s = 2°C and A_f =21°C likewise M_s = 5°C and M_f = -15°C. This is clearly visible in the graph. Like SEM, EDS and micro-hardness test, DSC also gives positive results for the NiTi50 combination.

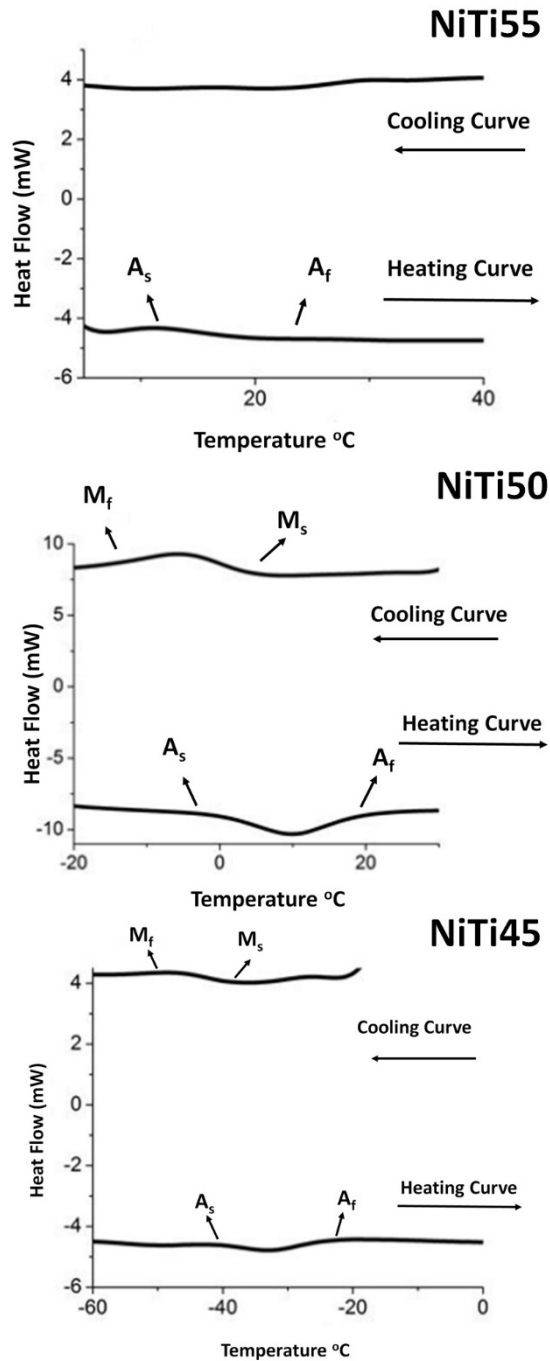


Fig. 6.1 DSC graph of as manufactured NiTi55, NiTi50, NiTi45 samples developed by LAM

Fig. 6.2 presents the DSC curves of TiNiCu5, which reveals the presence of two phases which is highly necessary for SMA structures. The single stage transformation was observed in both heating and cooling cycle of all samples, but a non-uniformity prevailed among all sample's martensite start temperature (M_s), martensite finish temperature (M_f), austenite start temperature (A_s) and austenite

finish temperature (A_f). For TiNiCu5 the $A_s = 23.81^\circ\text{C}$ and $A_f = 24.55^\circ\text{C}$ and the $M_s = 23.07^\circ\text{C}$ and $M_f = 22.07^\circ\text{C}$ are clearly visible in the plot, this can be considered as a perfect lattice structure alignment formed in the formed samples. In general Cu% at 5% in TiNiCu alloy lessens the impact of Ti's effect in transformation temperature. Figure 6.2 reveals the corresponding DSC graph of TiNiCu15, in which the $M_s = 50.09^\circ\text{C}$ and $M_f = 49.25^\circ\text{C}$ similarly $A_s = 49.92^\circ\text{C}$ and $A_f = 51.75^\circ\text{C}$ are seen. The curves in both heating and cooling are clearly visible. In all the graphs presence of R phase is detected. As discussed in detail in section 3.4 about the importance of R phase, and its existence in the structures developed through LAM flaunts the efficiency and ability of this new process to develop SMA. In the combination of TiNiCu25 phase transformation curves obtained are visible as shown in Fig. 6.2. The $A_s = 59.45^\circ\text{C}$ and $A_f = 60.29^\circ\text{C}$ likewise $M_s = 58.02^\circ\text{C}$ and $M_f = 57.32^\circ\text{C}$ can be spotted in the graph. Similar to SEM, EDS and micro-hardness test, DSC also gives positive results for the TiNiCu5 combination.

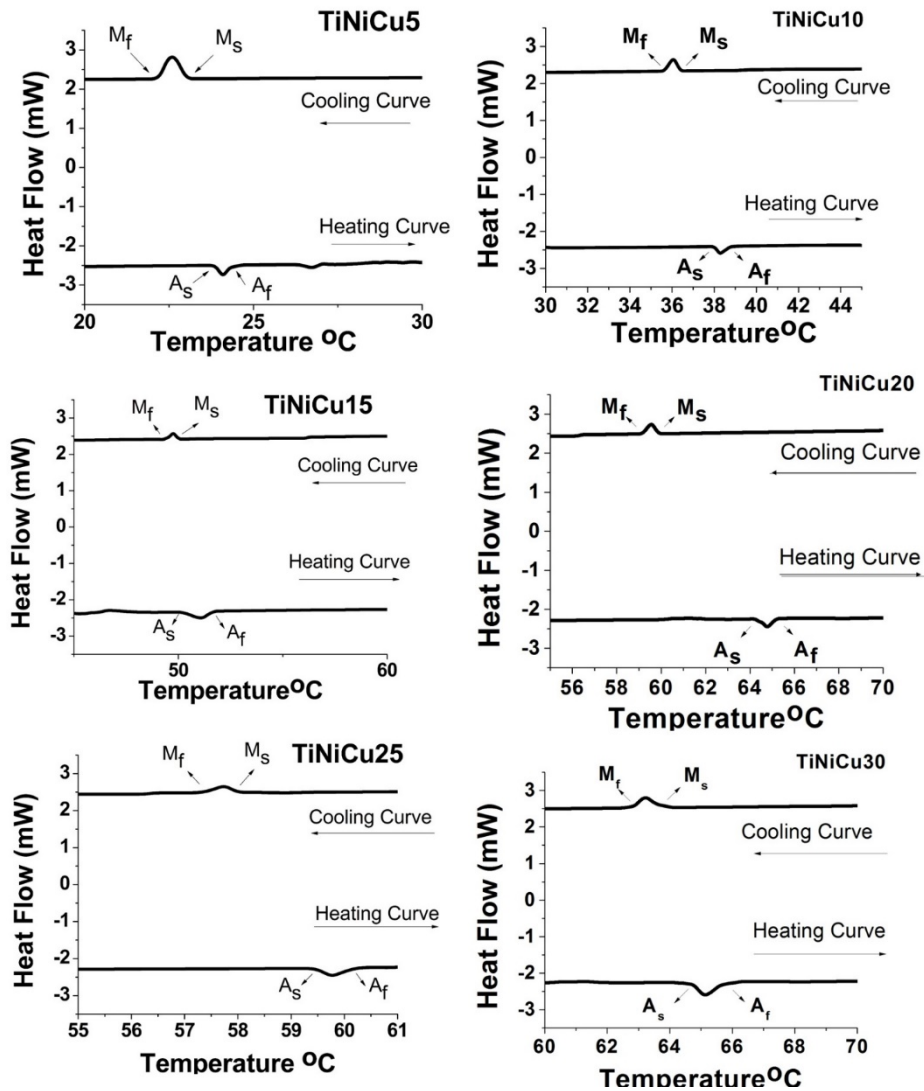


Fig. 6.2 DSC graph of as manufactured NiTi55, NiTi50, NiTi45 samples developed by LAM

6.3 Phase transformation property after laser shock peening

Figure 6.3 shows the DSC curves of NiTi55, NiTi50 and NiTi45 respectively after LSP. Among the formed curves NiTi50 had visible peaks in both, heating and cooling curves. For NiTi45 the visible peaks were obtained in the cooling curve but failed to display in the heating curve. NiTi55 failed to show in both the curves. The NiTi50 sample had the martensite start (M_s) temperature at 40°C , and martensite finish (M_f) temperature at 28°C . The austenite start (A_s) temperature and austenite finish (A_f) were at 42°C and 57°C respectively.

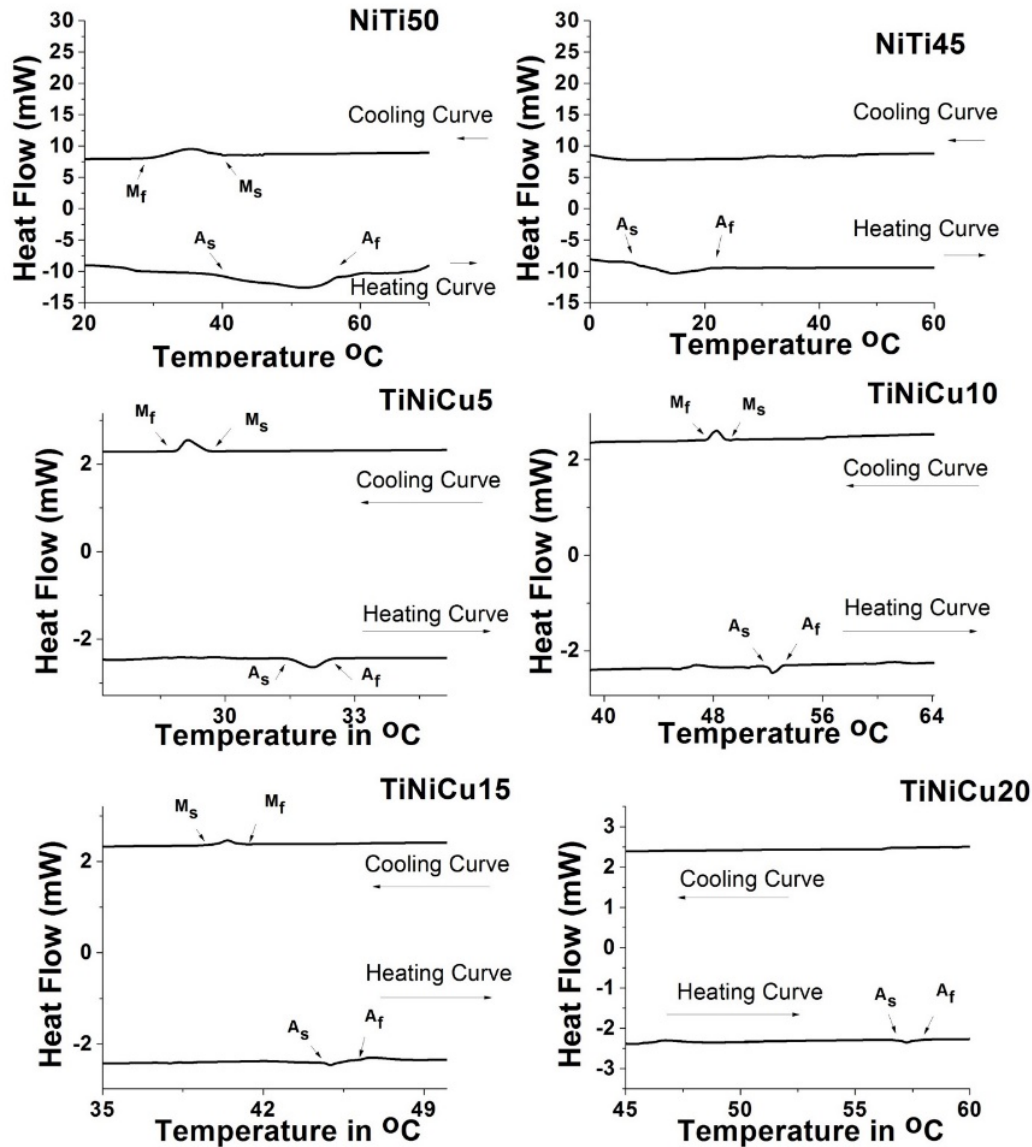


Fig. 6.3 DSC graph of NiTi50, NiTi45, TiNiCu5, TiNiCu10, TiNiCu15 and TiNiCu20 samples after LSP

A mild increase in the NiTi50 sample's (M_s) For this sample both were observed and also the peaks got wider and a bit sharper than the results obtained in as manufactured state. This is attributed to the effect of compressive residual stress stored in the samples due to LSP. The NiTi55 curves had totally destroyed after LSP and that is vividly seen while comparing to the curve in as manufactured state in the previous chapter. The reason may be attributed to the effect of excessive compressive stress injected on the samples. A mixed effect was found in NiTi45 samples. From Fig. 6.3 it is found that visible curves were obtained only in the cooling curve, with A_s at 7°C and A_f at 21°C . The reason for

the absence of curves visible in the cooling curve may be attributed to the effects of precipitates formed during LSP or the due to the amorphization formed as an effect of LSP, which was clearly seen in the microstructures of this sample. Figure 6.3 shows the DSC curves of TiNiCu5, TiNiCu10, TiNiCu15 and TiNiCu20 respectively after LSP. Among the formed curves TiNiCu5 and TiNiCu10 have very good visible peaks in both, heating and cooling curves, whereas TiNiCu15 has peaks of very less visibility and TiNiCu20 has peaks only in the heating curve. The peaks are very broad for samples as Cu% exceeds 10%. TiNiCu25 and TiNiCu30 failed to display peaks at both cycles just like NiTi55.

The TiNiCu5 has the M_s at 29 °C, M_f at 28 °C and the A_s and A_f at 31°C and 32 °C respectively. TiNiCu10 had both martensite and austenite temperatures a bit higher than TiNiCu5. The M_s and M_f of TiNiCu10 are at 49 °C and 47 °C respectively. The A_s and A_f lie at 51 °C and 52°C respectively for TiNiCu10. TiNiCu15 has the M_s at 41 °C and M_f at 39 °C, the A_s at 44 °C and M_f at 47 °C. The TiNiCu20 sample has the A_s of 57 °C and A_f 59 °C at respectively.

6.4 Phase transformation property after laser annealing

The presence of two phases have been confirmed in the laser annealed products, through XRD graphs. To confirm things more clearly and precisely differential scanning calorimetry (DSC) had been carried for the samples. From Fig. 16, NiTi55 sample's curve has totally not played any visible curves in heating and in cooling they show their (M_s) at 25°C and (M_f) at 16°C. Before annealing both in heating and cooling curves no visible results were obtained. The samples of NiTi45 and NiTi50 after annealing the samples we find visible curves are obtained. Also they have good steep transition curve in both heating and cooling process. The M_s and M_f of NiTi45 is -35 °C and -50 °C, whereas its Austenite start temperature (A_s) = -38 °C and Austenite finish temperature (A_f) = 20 °C. NiTi50 sample has its M_s at -5 °C and M_f at -20 °C. The same sample has its A_s at -16 °C and A_f at 10 °C. Researches in the past claim the stress induced during annealing has a great impact on the increase of austenite temperatures. This indicates stabilized martensite phase due to laser annealing. Rapid cooling of the material after laser annealing is liable of generating locked in internal stress, dislocation or vacancies. These defects induce reverse martensitic transformation due to frictional stress generated on the parent phase (martensite). So in the results presented here too we can find the martensite start and finish temperature of the laser annealed sample has decreased comparing to the as-made sample's results. There is an increase in the austenite start and finish temperature of the laser

annealed samples as they need additional energy to overcome the generated frictional stresses produced. The decrease in the M_s temperature can also happen due to the increase of Ni in the alloy as it was in the case of NiTi45, which has already been confirmed by the EDS and XRD results shown earlier. TiNiCu5 has sharp visible peaks in both heating and cooling curves, the M_s at 22°C and M_f at 21°C and A_s at 27°C and A_f at 31°C and TiNiCu10 had better results as well having M_s at 31 °C and M_f at 28°C. The A_s at 27°C and A_f at 31°C in heating and cooling cycles. TiNicu15 showed some mild peaks at M_s at 34 °C and M_f at 32°C. The A_s at 38°C and A_f at 41°C . While comparing the results of conventional available NiTi , TiNiCu5 and TiNiCu10 were at par with good phase transformation curves.

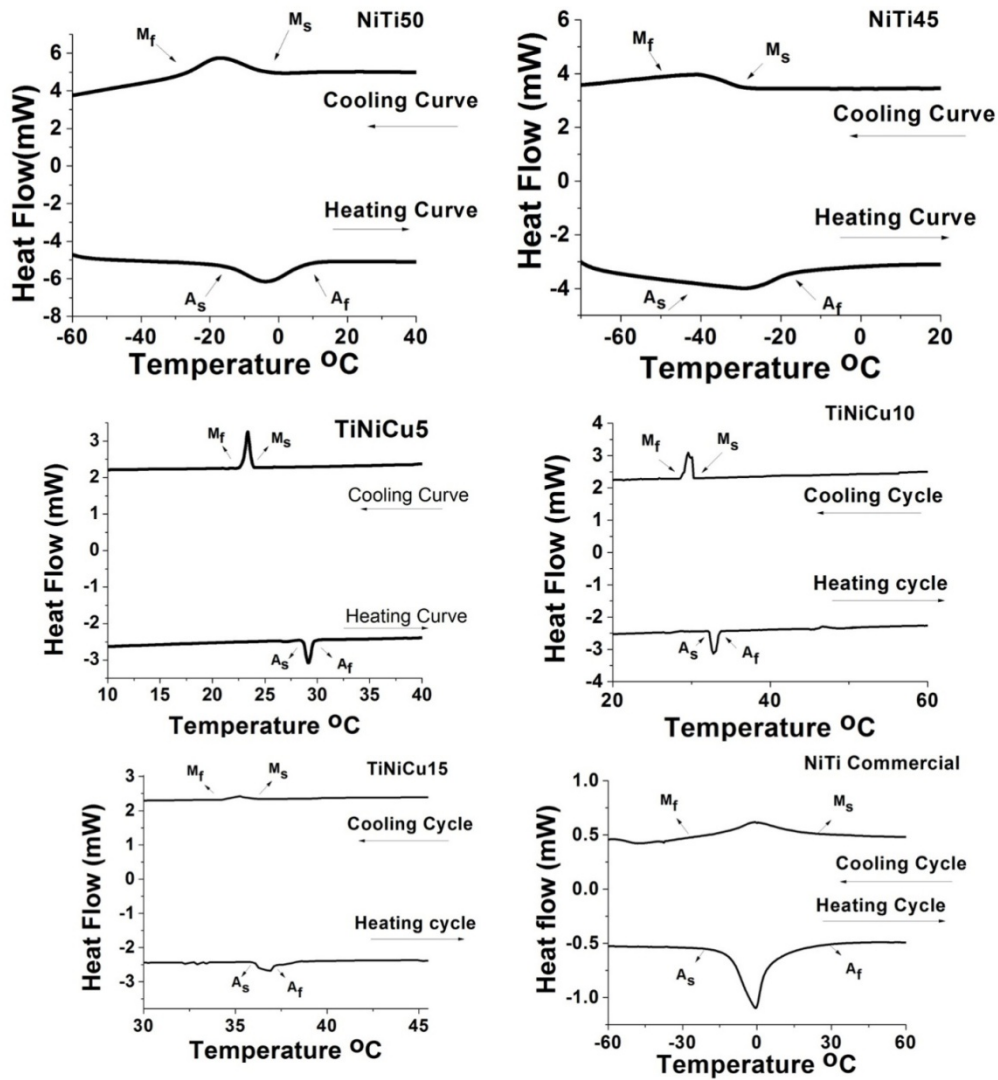


Fig. 6.4 DSC graphs of NiTi and TiNiCu samples after laser annealing

6.5 Experimental Analysis Using DMA

Taking shape memory characteristics into account the prospective industrial applications of these materials, the dynamic aspect of the elasticity can be more interesting. The storage modulus E' was determined by the dynamic mechanical analysis (DMA). Considering the elastic energy, the value of E' characterizes the storing properties of materials. The properties mentioned above were analyzed on cooling/ on heating measurements by using several frequencies of applied dynamic force. The elastic properties were measured on cooling/on heating for several frequencies of the dynamic force applied. The aim of this work is to determine properties such as the range of temperature hysteresis, the frequency-dependent evolution of storage modulus and damping capacity with temperature. Moreover the influence of oscillating force on such values as A_s , A_f , M_s , M_f and E' is taken into consideration.

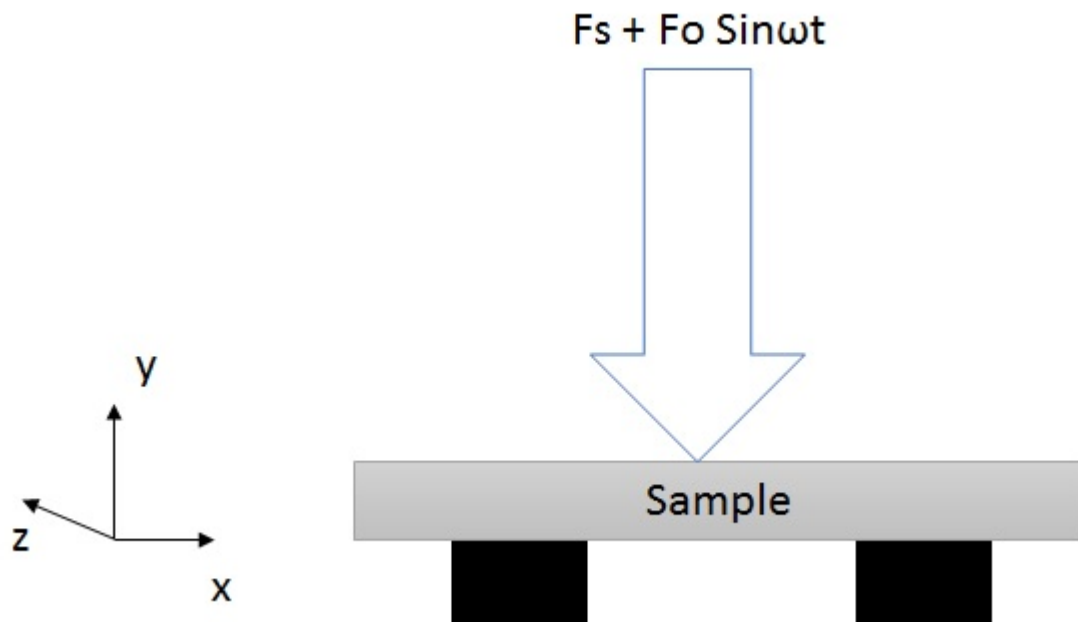


Fig. 6.5 Geometry of the three-point mode DMA experiment

As discussed in previous chapters the DSC shows good result only for three samples. So those three samples were taken for DMA testing in order to confirm and shape memory effect in the sample. The chosen samples are NiTi50, TiNiCu5 and TiNiCu10. The samples were chosen at a dimension of 40 mm X 10 mm X 3 mm. The DMA can be described as applying an oscillating force and analyzing the material's reaction. However, the modulus measured in the DMA is not exactly the same as the

Young's modulus, which can be evaluated as the slope of a stress–strain curve. The storage modulus E' gives information about the capability of the material to return or store energy.

The measurements were performed using the three-point bending configuration (figure 6.1). The deformation of the material can be looked at as a combination of an extension and compressive strain. The measurements of elastic properties were performed for MT and RT. The frequencies of the applied dynamic force were set at 1, 2, 5, 10 and 20 Hz in the dynamic temperature experiments. The heating rate was $3\text{ }^{\circ}\text{C min}^{-1}$. Additionally, the modification of elastic properties with ageing at constant temperature was determined. The frequency for the static temperature analysis was set at 10 Hz. All measurements were performed at the maximum dynamic force of $F_0 = 2\text{ N}$ with the proportionality factor 1, 2, which means that there was add-on static force $FS = 0, 4\text{ N}$. Forces larger than $\sim 3\text{ N}$ produced stress larger than critical for detwinning of martensite and caused a durable deformation of the samples at low temperatures.

6.6 Results and Discussion

Among the formed samples, from the phase transformation properties analyses using DSC, it is very clear three samples showed good results of SMA after all the post processing as well. One of the binary alloy and two ternary alloys TiNi50, TiNiCu5 and TiNiCu10. Hence the three samples were characterized using the DMA analyses to investigate the SME in them. The Fig Shows the DMA results of the three samples. The storage modulus E' was measured in the temperature range from -30 to $30\text{ }^{\circ}\text{C}$ for all three samples. The measurements were performed at single cooling–heating cycles. To ensure that there was no mechanical loading history of the materials, the initial temperatures for all measurements were set at $T = AS + 75\text{ }^{\circ}\text{C}$. The storage modulus E' was measured at constant temperatures guaranteeing the occurrence of only pure martensitic or austenitic phase. The experiment was preceded by MT or RT for the measurement in the martensitic or austenitic phase respectively, to eliminate the ageing effect prior to the experiment. As shown earlier, the DSC results allow determination of the characteristic temperatures for the forward and reverse martensitic phase transformation. Measurements of elastic properties performed using DMA showed a significant improvement after all the post processing; the temperature hysteresis was observed and M_s , M_f , A_s , A_f temperatures were determined.

6.7 Summary

DSC graphs also show that the equiatomic composition was capable of producing peaks, in both heating and cooling curve in the as manufactured state. Ti rich composition of NiTi45 was also able to show some partial curve. In case of ternary alloy all samples showed visible peaks in the as manufacture state. After LSP it was found Ni rich composition of NiTi45 totally was unable to produce any visible spectrum. Whereas NiTi50 and NiTi45 were able to show some visible peaks overcoming the impinged compressive stress. TiNiCu5, TiNiCu10 produced good visible spectrums after LSP in ternary alloys. TiNiCu15 and TiNiCu20 managed to have some peaks to display. TiNiCu25 and TiNiCu30 completely didn't produce any peaks. After the final post processing technique of laser annealing, NiTi50, NiTi45 in binary and TiNiCu5, TiNiCu10 in ternary alloy showed visible peaks which are a clear indication of improved nature of the alloys than in the as manufactured state. TiNiCu15 also managed to have some visible curves. TiNiCu5 and TiNiCu10 showed better transformation peaks than the commercially available NiTi samples.

Finally the DMA results show only NiTi50, TiNiCu5 and TiNiCu10 were able to show good shape memory effect among the formed samples. TiNiCu5 seems to be more ductile among the samples with high percentage of storage modulus. TiNiCu10 stands second in displaying good ductility. NiTi50 also showed good shape memory properties. Hence the as manufactured samples were brought into better shape with the influence of post processing techniques and were able to have better SME in the samples developed by LAM.

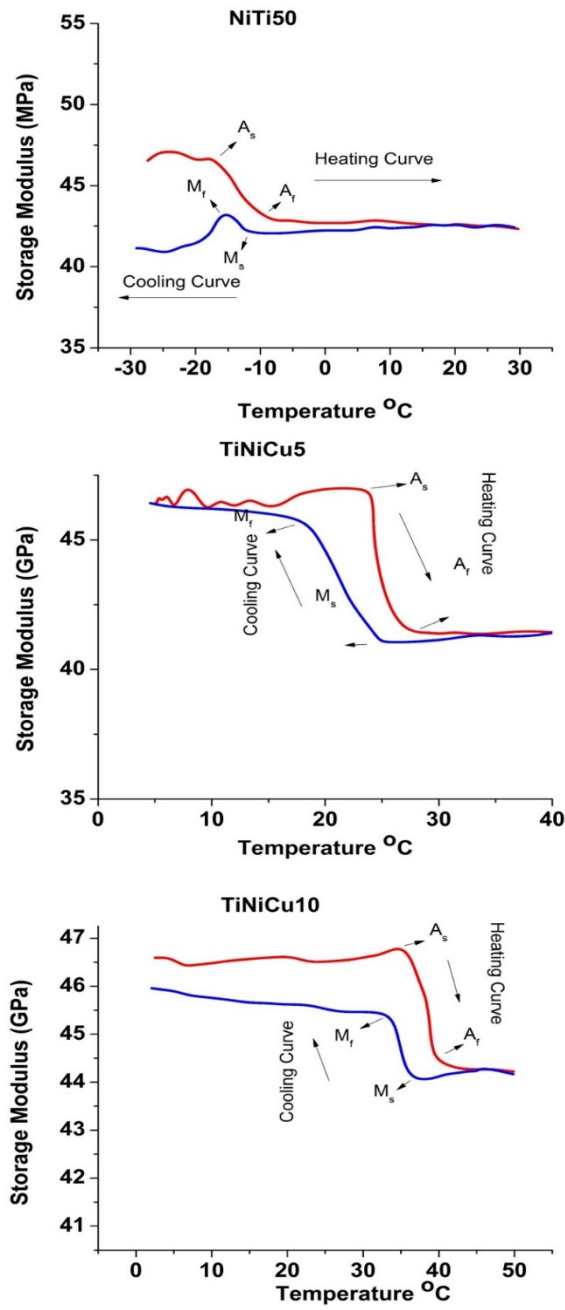


Fig 6.6 The DMA results of (a) NiTi50 (b) TiNiCu5 and (c) TiNiCu10 samples

Chapter 7

Conclusion and Future Scope of Work

7.1 Conclusions

Bulk SMA structures with binary and ternary alloy in different compositions were developed. Various characterization techniques were used to study the surface morphology, mechanical properties, crystalline properties and phase transformation properties. Post processing technique - LSP was deployed to overcome the problem of brittleness in the formed samples. The power of 1 GW/cm² was used for the process. After, LSP amorphization dominated in all samples. Hence, another post processing of laser annealing was deployed to overcome the issue. The surface annealing of NiTi samples were successfully performed at a laser energy density of 1100 mJ/cm². An increase in the grain size and surface roughness was observed. DSC results revealed the influence of laser annealing on the samples by visible phase transformation spectrums which was helpful to determine phase transformation temperatures precisely. All numerical studies were verified experimentally and reported in the corresponding sections in order to have a better process insight and good forecast about the processing to be done. Also the experimentation analysis being at par with the simulation results proved the accuracy of prediction. Finally, the influence of the post processing techniques in the shape memory properties of the samples were analyzed using DMA analyses. The results correlated with the DSC results and had a very minimum variation of less than 5°C. Hence the post processing techniques had successfully raised the quality of the developed samples in various aspects. Results of the present study are concluded as follows.

7.1.1 Development of bulk NiTi and TiNiCu structures with numerical and experimental study

Based on the experimental and numerical study binary and ternary bulk SMA were developed following conclusions are arrived at .

- i) Bulk SMA structures with binary alloy of and ternary alloy in different compositions can be successfully developed. Various characterization techniques were used to study the surface morphology, mechanical properties, crystalline properties and phase transformation properties. Among the formed samples NiTi50 and TiNiCu5 and TiNiCu10 were the best in binary and ternary alloys respectively.

- ii) The surface morphological results reveal the samples were closely packed with fine microstructures. The surface roughness of the developed samples were fine as well. The AFM results show the grain size of NiTi50, TiNiCu5 and TiNiCu10 are respectively.
- iii) The mechanical properties of the samples reveal the NiTi50 has a micro hardness of 250 VHN and ultimate strength of MPa. Whereas TiNiCu5 320 MPa and TiNiCu10 have
- iv) The crystalline nature of the three best samples were fine and visible spectrum was obtained for them. The martensite and austenite peak positions were

7.1.2 Laser shock peening of bulk NiTi and TiNiCu structures with numerical and experimental study

- i) The effect of LSP was very clearly observed on all three samples. The behavior of samples varied due to the compositional variations. The surface morphology showed general changes like increment in surface roughness and decrement in lots of peak structures. The microstructures were closely bonded for NiTi50, TiNiCu5 and TiNiCu10, sub sequentially there were no cracks formed on the surface due to LSP.
- ii) The XRD graphs showed the effect of amorphization within the samples as the peak intensity got highly reduced and peak width got broader after LSP. From the XRD graph it was clearly observed NiTi50 had the maximum amount of compressive stress, from its peak shift position
- iii) Similar to XRD, DSC graphs also show that NiTi50 , TiNiCu5 and TiNiCu10 compositions were capable of producing peaks, in both heating and cooling curve. Some of the compositions were not able to produce visible spectrum due to the effect of LSP.

7.1.3 Laser annealing of bulk NiTi and TiNiCu structures with numerical and experimental study

- i) LSP processed samples were dealt with laser annealing in order to overcome the problem of amorphization and recrystallize the formed samples. .
- ii) As an effect of laser annealing oxide layer formation was observed for binary NiTi alloy due to the incomplete transformation of martensite phase. But similar case was not visible in the ternary TiNiCu alloys. The effect of laser annealing was visible with smoother surface finish.
- iii) The increase in grain size of all samples were visible with AFM and XRD results. From the results effective influence of laser annealing was clearly seen.
- iv) As an effect of laser annealing narrow peaks were displayed in the XRD results. And the peaks have shifted very accurate to the position of perfect alloys.

- v) The DSC graphs showed three samples of NiTi50, TiNiCu5 and TiNiCu10 have peaks formed in them, whereas other samples failed to display the phase transformation peaks.

7.1.4 Shape memory characteristics analysis on the developed samples

- i) The results of DMA proved the presence of shape memory effect in the samples. The visible spectrum in the plot are clearly visible for binary NiTi50 sample and more clearly visible for ternary TiNiCu5, TiNiCu10.
- ii) The DMA results co-relate with the DSC results. The phase transformation temperatures have just a mild difference of less than 3°C between them.
- iii) The storage modulus capacity was high for TiNiCu5 and next was TiNiCu10 samples. Hence the option of choosing these two alloys for practical applications can give effective shape memory results.

7.2 SCOPE OF FUTURE WORK

- The methodology of developing bulk SMA using LAM and subsequent post processing techniques can be performed by developing other primary options of SMA like CuAlNi, CuZnAl.. etc
- The methodology of a laser annealing can be tried with picoseconds laser assisted annealing. This approach is expected to result in more intense laser annealing process with it's effect on SME would be really interesting, as the heat impact zone will be more narrow, due to shorter pulse width of the laser.
- The process of laser shock peening can be tried with higher power of 3-5 GW/cm², after the samples are well developed without any brittleness and porosity. The higher impact would be really interesting to study as its influence on SME has not yet been explored.
- Application of LAM developed bulk SMA can be utilized in practical problems of civil construction and machine tool design as good vibration dampers.

REFERENCES

- [1] A. AbuZaiter, Ee Leen Ng, Suhail Kazi, and Mohamed Sultan Mohamed Ali, 2015, Development of Miniature Stewart Platform Using TiNiCu Shape-Memory-Alloy Actuators, *Advances in Materials Science and Engineering*, <http://dx.doi.org/10.1155/2015/928139>
- [2] Andani MT et al., 2016, Achieving biocompatible stiffness in NiTi through additive manufacturing. *J Intell Mater Syst Struct*. DOI: 10.1177/1045389X16641199.
- [3] H. S. Bang, S. M. Joo, J. M. Kim and W.S. Chang: 2003, Mechanical Characteristics of resistance multispot welded joints, *Science and Technology of Welding and Joining*, 8, 369-376.
- [4] Bhargava P, Paul CP, Preme Singh CH, Mishra SK, Atul Kumar, Nagpure DC, et al. 2013, Tandem rapid manufacturing of inconol-625 using laser assisted and plasma transferred arc depositions. *Adv. Manuf*; 1:305–313.
- [5] Besseghini S. Villa E., Tuissi A. 1999, *Materials Science and Engineering A273–275*, 390–394.
- [6] M. Bram, A. Ahamad-Khanlou, A. Heckman, B. Fuchs, H.P. Buchkremer, D. Stover, 2002, Powder metallurgical fabrication process for NiTi shape memory alloys parts. *Mater.Sci.Eng A*;337, 254-63.
- [7] S. S. Brenner; *Journal of Applied Physics* 27 (1956) 1484
- [8] Bellouard Y, Lehnert, T, Bidaux, JE, et al. Local annealing of complex mechanical devices: a new approach for developing monolithic micro-devices. *Mater.Sci.Eng.A* 1999; 795:273-275.
- [9] Bormann T et al. 2012, Tailoring selective laser melting process parameters for NiTi implants. *J Mater Eng Perform*, 21(12), 2519–24.
- [10] Benxin Wu, Yung C. Shin. Laser pulse transmission through the water break down plasma in laser shock peening *APPLIED PHYSICS LETTERS* 88, 041116 (1-3) (2006).
- [11] M. Cai., Y.Q Fu, S. Sanjabi., Z.H, Barber, J.T Dickinson., 2007. Effects of composition on surface relief morphology in TiNiCu thin films. *Surf Coat Tech.* 201, 5843-5849.
- [12] A.T. Clare et al. 2008, Selective laser melting of high aspect ratio 3D nickel–titanium structures two way trained for MEMS applications. *Int J Mech Mater Des*, 4(2), 181–7.
- [13] Dadbakhsh S et al. 2014, Effect of SLM parameters on transformation temperatures of shape memory nickel titanium parts. *Adv Eng Mater*;16(9),1140–6.
- [14] de Wild M et al. 2014, Damping of selective-laser-melted NiTi for medical implants. *J Mater Eng Perform*;23(7),2614–9.

- [15] W.G Drossel, Tom Junker, André Bucht, Iñaki Navarro y de Sosa, Kenny Pagel, 2016, Evaluation of shape memory alloy bulk actuators for wear compensation in ball screw drives, IFAC-PapersOn Line 49-21, 088–094.
- [16] C. Constantinescu, N. Scarisoreanua, A. Moldovan, et al. 2007, Thin films of NdFeB deposited by PLD technique. *Appl.Surf Sci.*, 253, 8192–8196
- [17] C.Y. Chung, L. You, H.D Gu, et al. 1997, NiTiHf shape memory alloy thin films by laser ablation and sputtering. *Proceedings of China-Japan Bilateral Symposium on Shape memory Alloys*, Hanzou China, 96-101
- [18] C. Craciunescu, J. Li and M. Wuttig; *Scripta Materialia*, 48(1) (2003) 65.
- [19] H.Du, , Y.Fu , 2004. Deposition and characterization of Ti_{1-x}(Ni,Cu)_x shape memory alloy thin films. *Surf. Coat Tech.* 176, 182-187
- [20] T.W. Duerig K.N. Melton, D. Stockel, C.M. Wayman, 1990, *Engineering aspects of shape memory alloys* - London: Butterworth-Heinemann.
- [21] Elahinia et al. 2012, Manufacturing and processing of NiTi implants: A review, *Progress Mater Sci*, 57,911-946.
- [22] R. Fabbro, J. Fournier, P. Ballard, D. Devaux, J. Virmont. Physical study of laser-produced plasma in confined geometry. *Journal of Applied Physics* 68, 775-784 (1990).
- [23] Fatemeh Alijani, Rasool Amini, Mohammad Ghaffari, Morteza Alizadeh, Ali Kemal Okyay., 2014. Effect of milling time on the structure, micro-hardness, and thermal behavior of amorphous/nanocrystalline TiNiCu shape memory alloys developed by mechanical alloying. *Mater.Des.* 55, 373-380.
- [24] Y.Q. Fu, W.M. Hwang, H.J. Du, 2011. Stress induced texture and shape memory trench in TiNiCu films *THIN SOLID FILMS*. 519,5290–5296.
- [25] F. J. Gil, E. Solano, J. Penal, E. Engel, A. Mendoza, J. A. Planell, 2004, *J. Mater.Sci.Mater.Med.* 15, 1181
- [26] T.Goryczka, P.Ochin 2005, *Journal of Mater Process Technol* 162–163, 178–183.
- [27] T.Goryczka, , M.Karolus, , P .Ochin,, Morawiec, H., 2001. Martensites in NiTi and NiTiCu alloys-Structure of melt spun Ni₂₅Ti₅₀Cu₂₅ ribbons studied by X-ray diffraction. *J Phys Colloq.* 11 (8), 345-350
- [28] C. Grabe and O.T. Bruhns; *International Journal of Plasticity* 25(3) (2009) 513
- [29] H. Gedda., Powell J., Wahistrom G., Liet al. 2002, Energy redistribution during CO₂ laser cladding, *Journal of Laser Applications*, 14, 78-82.

- [30] I. Gibson, D.W. Rosen, B. Stucker. 2010, Additive manufacturing technologies. Springer;
- [31] O. P. Gupta: 2003, Finite and Boundary Element Methods in Engineering, Oxford and IBH Publications, New Delhi,.
- [32] C. Haberland et al.,2014, On the development of high quality NiTi shape memory and pseudoelastic parts by additive manufacturing. *Smart Mater Struct*, 23(10), 104002.
- [33] Habijan T et al. 2013, The biocompatibility of dense and porous nickel–titanium produced by selective laser melting. *Mater Sci Eng, C*;33(1), 419–26.
- [34] Hirschhorn, J.S., 1969. Introduction to powder metallurgy, first ed. American Powder Metallurgy Institute.
- [35] F.Hensel, ,C. Binroth, , G.Sepold, 1992, A Comparison of Powder and Wire-Fed Laser Beam Cladding”, *Proceeding of ECLAT '92*, 39-44.
- [36] He Q, Hong MH, Huang WM, et al. CO₂ laser annealing of sputtering deposited Ni-Ti shape memory thin films. *J. Micromech. Micro Engg.* 2004; 14: 950.
- [37] Hoffmann W et al. 2014 Rapid prototyped porous nickel–titanium scaffolds as bone substitutes. *J Tissue Eng*;5, 1-14.
- [38] L. Hou and D. S. Grumman; *Scripta Metallurgica*,33(6) (1995) 989
- [39] T. Honma, 1987, TiNi-based shape memory alloys, in *Shape memory alloys*, ed. H. Funakubo, New York: Gordon and Breach Science Publishers, p. 92.
- [40] A. Ishida, M. Sato, A. Takei and S. Miyazaki, 1995, Effect of heat treatment on shapememory behavior of Ti-rich Ti-Ni thin films, *Mater. Trans. JIM*, 36, 1349–1355
- [41] A. Ishida and V. Martynov,2002, Sputter-deposited shape-memory alloy thin films: propertiesand applications, *MRS Bulletin*, 27, 111–114.
- [42] Y. Kawamura, A. Gyobu, T. Saburi, M. Asai, 2000, Stucture of sputter-depositedTi–rich Ti–Ni alloy films, *Mater. Sci. Forum* 327–328, 303–306.
- [43] Kalainathan, S., Sathyajith, S., and Swaroop. S.,2012, “Effect of laser shot peening without coating on the surface properties and corrosion behavior of 316L steel,” *Opt Laser Eng.*, 50, pp. 1740-1745. DOI: 10.1016/j.optlaseng.2012.07.007.
- [44] A. Kruusing., 2008, *Handbook of Liquids Assisted Laser Processing*, Elsevier Ltd, Chap. 2. ISBN-13: 978-0-08-044498-7
- [45] S. Kajiwara, T. Kikuchi, K. Ogawa, T. Matsunaga and S. Miyazaki, 1996, Strengthening OfTi-Ni shape-memory films by coherent subnanometric plate precipitates, *Philos. Mag. Lett.*, 74, 137–144.

- [46] J. Laeng, Xiu Z, Xu X, Sun X, Ru H, Liu Y. 2007, Phase formation of Ni-Ti via solid state reaction. *Phys.Scr.T*, 129, 250-254.
- [47] Liu YS, Xu D, Jiang BH, et al. CO₂ laser annealing of sputtering deposited Ni-Ti shape memory thin films. *J.Micromech. Micro Engg* 2005;15:575
- [48] J. H. Lee, J. B. Park, G. F. Andreasen, and R. S. Lakes; *Journal of Biomedical Materials Research* 22 (1988) 573
- [49] S. Lee, Seung-Kook Ro, Jong-Kweon Park, 2016, Performance evaluation of a shape memory alloy tool holder for high-speed machining, *Int J Adv Manuf Technol*, 84, 717–725
- [50] Li YH, Meng FL, Qiu DL, et al. 2004, Grain size and its distribution in Ni-Ti thin films sputter-deposited on heated substrates. *Chin. Phys.*; 13:1315.
- [51] B.Y. Li, L.J. Rong, V.E. Gjunter, Y.Y Li., 2000, Porous Ni–Ti shape memory alloys produced by two different methods. *Z Metalkd*, 91, 291–5.
- [52] C. Li, Y. F Zheng. 2006, *Materials Letters* 60, 1646–1650
- [53] D.S. Li, Zhanng YP, Ma X, Zhang. 2009, Space-holder engineered porous NiTi Shape Memory alloys with improved pore characteristics and mechanical properties. *J.Alloys Compd*, 474, L1-L5.
- [54] H. Li, Zhi-qiang Liu, Jin-ping Ou, 2008, Experimental study of a simple reinforced concrete beam temporarily strengthened by SMA wires followed by permanent strengthening with CFRP plates, *Engineering Structures*, 30, 716-723.
- [55] C. Liang, 1990, The constitutive modeling of shape memory alloys, Virginia Polytechnic Institute and State University.
- [56] H. C. Lin, Shyi-Kaan Wu and J. C. Lin, 1992, A study of the martensitic transformation in Ti-rich TiNi alloys, *Proc. Int. Conf. on Martensitic Transformations (ICOMAT92)*, Monterey, 875–880.
- [57] A.M. Locci, R. Orru, G. Cuo, Z. A Munir, 2003, Field-activated pressure-assisted synthesis NiTi. *Intermetallics*, 48, 3895-3904
- [58] J.C.F. Millett, N.K. Bourne, G.T. Gray, Behavior of the shape memory alloy NiTi during one-dimensional shock loading. *J. Appl. Phys.* 92 (2002) 3107–3110.
- [59] C.F Marsden., A.F. Houdley.A., J.D Wagniere, 1990., "Characterization of laser cladding process", *Proceeding of ECLAT*, 90, 543-553.
- [60] Morales, M., Ocana, J.L., Molpeceres, C., Porro, J.A., Garcia- Beltran, A., 2008, "Model based optimization criteria for the generation of deep compressive residual stress fields in high elastic limit metallic alloys by ns-laser shock processing," *Surf Coat Technol.*, 202, pp. 2257-2262.

- [61] W. Maziarm, J. Dutkiewicz, J. VanHumbekbeck, T. Czeppe, 2004, Mechanically alloyed and hot pressed Ni-49.7Ti alloying showing martensitic transformation. *Mater.Sci.Eng.A*; 375-377,844-48.
- [62] K. Malukhin, Hankyu Sung, Kornel Ehmann 2012, A shape memory alloy based tool clamping device, *J.Mater.Process.Technol*, 212, 735-744.
- [63] Mullenix N, Povitsky A. Exploration of pulse timing for multiple laser hits within a combined heat transfer, phase change, and gas dynamics model for laser ablation. *Appl. Surf. Sci.* 2007; 253:6366-6370.
- [64] Mc Neese MD, D.C. Logovdas, T. C.Pollock. 2000, Processing of TiNi from elemental powders by hot isostatic pressing. *Mater.Sci.Eng.A*,280,334-48.
- [65] K. N. Melton and O. Mercier; *Acta Metallurgica* 27 (1) (1979) 137
- [66] H. Meier, C. Haberland, J. Frenzel, 2012, Structural and functional properties of NiTi shape memory alloys produced by selective laser melting. In: *Innovatedevelopments in design and manufacturing: advanced research in virtual and rapid prototyping*. p. 291–6.
- [67] S. Miyazaki, Y. Q. Fu and W. M. Huan, 2009, *Thin Film Shape Memory Alloys:Fundamentals and Device Applications*, Cambridge University Press New York, NY, USA.
- [68] S. Miyazaki and A. Ishida, 1994, Shape memory characteristics of sputter-deposited Ti-Ni thin films, *Mater. Trans. JIM*, 35, 14–19.
- [69] D.G. Morris, M.A. Moris, 1989, NiTi intermetallic by mixing, milling and interdiffusing elemental components. *Mater Science, Eng A*;110,139-49.
- [70] Montross, C. S., Wei, T., Ye, L., Clark, G., and Mai, Y.-W., 2002, “Laser Shock Processing and Its Effects on Microstructure and Properties of Metal Alloys: A Review,” *Int. J. Fatigue*, 24 10 , pp. 1021–1036.
- [71] T. Mousavi, M.H. Abbasi and F. Karimzadeh; *Materials Letters* 63(9-10) (2009) 786.
- [72] K. Otsuka; (1994)., *Shape Memory Materials*. International Academic, Beijing,
- [73] K. Otsuka, C. M. Wayman, 1998. *Shape Memory Materials* Cambridge: Cambridge University Press.
- [74] Ocelík, V., Bosgra, J., de Hosson, J.T.M.,2009. In-situ strain observation in high power laser cladding, *Surf. Coat. Tech.* 203, 3189–3196.
- [75] Palani IA, Nilesh J. Vasa, Singaperumal M. 2008. Crystallization and ablation in annealing of amorphous-Si thin film on glass and crystalline-Si substrates irradiated by third harmonics of Nd³⁺:YAG laser. *Mater. Sci. Semicond. Process.*; 11: 107-116.
- [76] X. Peng, W. Pi and J. Fan; *International Journal of Plasticity* 24(6) (2008) 966.

- [77] J. L. Pons; 2005, *Emerging Actuator Technologies: A Micromechatronic Approach*' John Wiley & sons Ltd. England.
- [78] Paul CP, Bhargava P, Atul Kumar, Pathak AK, Kukreja LM. 2012, Laser rapid manufacturing: technology, applications, modeling and future prospects. In: Paulo Davim J, editor. *Lasers in Manufacturing*, UK: ISTE-Wiley;, p.1-38.
- [79] C.P. Paul., H. Kumar, S.Thakur, A.K.Nath., 1997 ,Development of Mechanically vibrated gas assisted powder feeder for laser cladding, National Laser Symposium, PRL, Ahmedabad, Dec..
- [80] Ralf Hassdorf, Jurgen Feydt, Rene Pascal, Sigurd Theinhaus, Markus Boese, Tobias Sterzl, Bernhard Vinzek, Michael Moske., 2006. Phase formation and structural sequence of highly-oriented MBE- grown shape memory thin films. *Mater T JIM*. 43(5), 933-938.
- [81] J. N. Reddy, D. K. Gartling, 2000: *The Finite Element Method in Heat Transfer and Fluid Dynamics*, 2nd ed., CRC Press, Boca Raton, FL.
- [82] M.H. Ren, L.Wang, D.Xu, , B.C Cai,., 2000. Sputter-deposited TiNiCu shaped memory alloy thin films. *Mater. Des.*21, 583-586
- [83] Rösner, H., Schlomacher, P., Shelyakov, A.V., Glezer, A.M., 2000. Formation of TiCu plate-like precipitates in Ti50Ni25Cu25 shape memory alloys. *Scr Mater*. 43, 871-876.
- [84] Saedi S et al. 2016, The influence of heat treatment on the thermomechanical response of Ni-rich NiTi alloys manufactured by selective laser melting. *J AlloyCompd*;677, 204–10.
- [85] T. Saburi, 1998, Ti-Ni shape memory alloys, in *Shape Memory Materials*, ed. K. Otsuka and C. M. Wayman, Cambridge: Cambridge University Press, p. 49.
- [86] R. Santamarta, C.Segui, J.Pons, E. Cesari 1999, *Scripta Mater* 41, 867–872
- [87] R. Santamarta E. Cesari, J. Pons, T. Goryczka, 2004, *Metall. Mater. Trans.* 35A.,761–770.
- [88] T. Sawaguchi, G. Kaust'ater, A. Yawny, M. Wagner, G. Eggeler, 2003, *Metall. Mater. Trans.* A 34, 2847–2859.
- [89] Sadrnezhaad SK, Rezvani E, Sanjabi S, et al. 2009. Pulsed-Laser Annealing of Ni-Ti Shape Memory alloy thin film. *J.Mater. Sci. Technol*; 25:1.
- [90] J. A. Shaw and S. Kyriakides; *J. Mech. Phys. Solids* 43(8) (1995) 1243.
- [91] I. Shishkovsky, I. Yadroitsev, I.Smurov,2012, Direct selective laser melting of nitinol powder. *Phys Proc*,39, 447–54.

- [92] Jiang Shu-young, Zhang Yan-qiu. Microstructure evolution and deformation behavior of as-cast NiTi shape memory alloy under compression. *Trans.Nonferrous, Met. Soc.China* 2012;22:90-96.
- [93] D.Stoeckel ,2001, Forming NiTi – a challenge. In: Siegert K, editor. *New developments in forging technology*, 119–34.
- [94] S.Sun, Y. Durandet., T. M Brand., 2005, Parametric investigation of pulsed Nd:YAG laser cladding of Stellite 6 on stainless steel”, *Surface and Coatings Technology*, Vol. 194, 225–231.
- [95] Sun, G., Zhang, Y., Liu, C., Luo, K., Tao, X., Li, P., 2010. Microstructure and wear resistance enhancement of cast steel rolls by laser surface alloying NiCr–Cr₃C₂, *Mater.Des.*31, 2737–2744.
- [96] Suryanarayana, C., 2001. Mechanical alloying and milling. *Prog Mater Sci.* 46, 1-184.
- [97] T. Tadaki, K. Otsuka, K. Shimizu. **1988**, *Annual Review on Materials Science*,18, 25
- [98] Takashi Mineta , Tomoe Deguchi , Eiji Makino, Takahiro Kawashima , Takayuki Shibata., 2011.Fabrication of cylindrical micro actuator by etching of TiNiCu shape memory alloy tube. *Sens. Actuators, A.*,165,392–398.
- [99] P. Tautzenberger, G. RAU,1989, European Symposium on Martensitic transformations ESOMAT, 213-222.
- [100] E. Toyserkani, Amir khajepour, Steve Corbin. 2004, 3-D finite element modeling of laser cladding by powder injection: effects of pulse shaping on the process. *Opt. Laser Eng*; 41: 849-867.
- [101] A. Trivedi, S. Bag, A. De: 2007, Three Dimensional Transient Heat Conduction and Thermo Mechanical Analysis for Laser Spot Welding Using Adaptive Heat Source, *Science and Technology of Welding and Joining*, 12, 24-31.
- [102] Vamsi Krishna B, Susmita Bose, Amit Bandyopadhyay, 2007, Laser Processing of Net-Shape NiTi Shape Memory Alloy.*Metallurgical and Materials transactions.*;38A,1096-1103.
- [103] Van Humbeeck 1997, *J. J. Phys. IV France* 7., C5-3-C5-11
- [104] M.Valeanu, , M.Lucaci, , A.D Crisan,, M.Sofronie, , L. Leonat.,, V.Kuncser, 2011. Martensitic transformation of Ti₅₀Ni₃₀Cu₂₀ alloy prepared by powder metallurgy. *J Alloy Compd.* 501, 4495-4498.

- [105] P.A. Vetter., T.H Engel., J. Fontaine., 1994 ,Laser cladding: the relevant parameters for process control, Proceeding of SPIE, Vol. 2207,452-562.
- [106] Wei Ya, Pathiraj B, Shaojie Liu. 2D modelling of clad geometry and resulting thermal cycles during laser cladding. *J. Mater. Process. Technol* 2016; 230: 217-232.
- [107] Wang Xi, Yves Bellouard, Zhenyu Xue,et al. 2008. Thermal modelling of laser-annealing-induced crystallization of amorphous Ni-Ti thin films. *Appl. Phys.A*; 90: 689-694.
- [108] Wang X, Belloard Y, Vlassak JJ. Laser Annealing of amorphous Ni-Ti shape memory alloy thin films to locally induce shape memory properties. *Acta.Mater.* 2005; 53: 4955-4961.
- [109] J.M. Walker et al., 2016, Process development and characterization of additively manufactured nickel–titanium shape memory parts. *J Intell Mater Syst Struct*.DOI: 10.1177/1045389X16635848.
- [110] K. Weinert, V.Petzoldt 2004, Machining of NiTi based shape memory alloys. *Mater Sci Eng A*, 378,180–4.
- [111] Wirth C, Comte V, Lagneau C, Exbrayat P, Lissac M, Jaffrezic-Renault N, et al., 2005, Nitinol surface roughness modulates in vitro cell response: a comparison between fibroblasts and osteoblasts. *Mater.Sci.Eng C*;25:51–60
- [112] S.L. Wu, Chung CY, Liu XM, Chu PK, Ho JPY, Chu CL, et al. 2007, Pore formation mechanism and characterization of porous Niti shape memory alloys synthesized by capsule-free hot isostatic pressing.*Acta Mater*;,55,3437-3451.
- [113] S.L. Wu, Liu XM, ChuPK ,Chung CY, Chu CL, Yeung KWK. 2008, Phase transformation behavior of porous NiTi alloys fabricated by capsule-free hot isostatic pressing. *J.Alloys Compd*,449,139-143.
- [114] Xi Wang n, Weiguang Xia, Xianqian Wu, Yanpeng Wei, Chenguang Huang. Microstructure and mechanical properties of an austenite NiTi shape memory alloy treated with laser induced shock. *Materials Science & Engineering A* 578 (2013) 1–5.
- [115] Yeon-Wook Kim, Sang-Hoon Lee, Tae-Hyun Nam.,2007. Microstructure modifications of TiNiCu shape memory alloy strips fabricated by arc melt overflow process. *Phys. Scr.*T129, 245-249.

- [116] Yiliang Liao, Chang Ye, Huang Gao, Bong-Joong Kim Sergey Suslov Eric A. Stach and Gary J. Cheng, Dislocation pinning effects induced by nano-precipitates during warm laser shock peening: Dislocation dynamic simulation and experiments. JOURNAL OF APPLIED PHYSICS 110, 023518 1-8. (2011)
- [117] C. Ye, Sergey Suslov, Dong Lin, Yiliang Liao, Xueling Fei, and Gary J. Cheng. Microstructure and mechanical properties of copper subjected to cryogenic laser shock peening Journal of Applied Physics 110, 083504(1-8) (2011)
- [118] W.A.Y, Yusoff, A.J. Thomas, 2008, The effect of employing an effective laser sintering scanning strategy and energy density value on eliminating “orange peel” on a selective laser sintered part, Proc. International Association for Management of Technology (IAMOT).
- [119] Z. Zhang, J. Frenzel, K. Neuking, G. Eggeler, 2005, Acta Mater., 53, 3971–3985.
- [120] H.J Zhang, C.J Qiu,.,2006. A TiNiCu Thin Film Micropump Made by Magnetron Co-Sputtered Method. Mater T JIM.47(3), 532-535.